STUDIA UNIVERSITATIS
BABEŞ-BOLYAI

UNIVERSITATEA BABEŞ-BOLYAI
BABEŞ-BOLYAI TUDOMÁNYEGYETEM
BABEŞ-BOLYAI UNIVERSITÄT
BABEŞ-BOLYAI UNIVERSITY
TRADITIO ET EXCELLENTIA

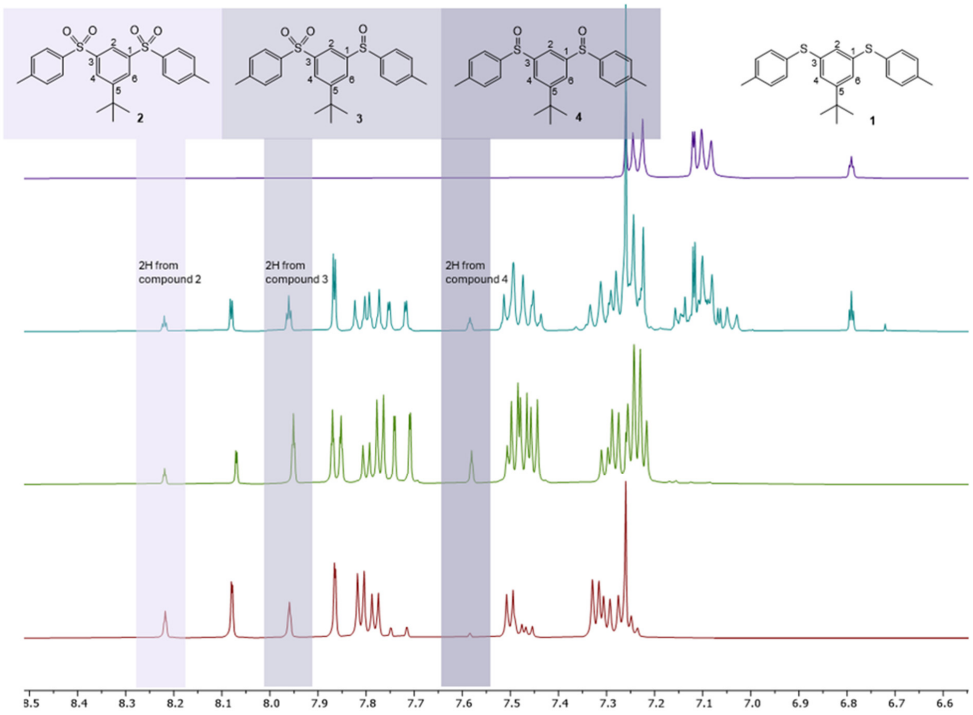

CHEMIA

1/2026

STUDIA
UNIVERSITATIS BABEŞ-BOLYAI
CHEMIA

1/2026

ISSN (print): 1224-7154
ISSN (online): 2065-9520; ISSN-L: 1224-7154

Published by Babeş-Bolyai University

https://studia.reviste.ubbcluj.ro/index.php/chemia/
studiachemia@ubbcluj.onmicrosoft.com

YEAR **Volume 71 (LXXI) 2026**
MONTH **March**
ISSUE **1**

PUBLISHED ONLINE: 2026-03-25
PUBLISHED PRINT: 2026-03-30
ISSUE DOI: 10.24193/subbchem.2026.1

S T U D I A
UNIVERSITATIS BABEŞ–BOLYAI
CHEMIA

1

CONTENT/ SOMMAIRE/ INHALT/ CUPRINS

Studia Universitatis Babes-Bolyai Chemia has been selected for coverage in Thomson Reuters products and custom information services. Beginning with V. 53 (1) 2008, this publication is indexed and abstracted in the following:

- Science Citation Index Expanded (also known as SciSearch®)
- Chemistry Citation Index®
- Journal Citation Reports/Science Edition

STUDIA UBB CHEMIA, LXXI, 1, 2026 (p. 7-18)
(RECOMMENDED CITATION)
DOI:10.24193/subbchem.2026.1.01

Dedicated to Professor Luminița Silaghi-Dumitrescu on the Occasion of Her 75th Anniversary

CATALYTIC SULFOXIDATION REACTIONS OF 1,3-BIS(PARA-TOLYL SULFIDE)-5-TERT-BUTYLBENZENE USING DECAVANADATE DERIVATIVES

Henrietta ALBERT-NAGY[a], Ioana SUCIU[a], Szidonia LAZSADI-RACZ[b], Meryem IDBOUMLIK[b,c], Mohammed LACHKAR[c], Gabriela NEMEȘ[b]*, Noemi DEAK[b]*

ABSTRACT. Catalytic sulfoxidation of 1,3-bis(*para*-tolyl sulfide)-5-*tert*-butylbenzene in order to obtain sulfones and sulfoxides, was carried out using three decavanadate ($V_{10}O_{28}$)$^{6-}$ containing catalysts. Reaction conditions were varied to evaluate different parameters of the process; the tested procedures followed the guidelines of green chemistry. To align with these principles, reaction parameters were optimized at room temperature using environmentally benign solvents, including methanol, ethanol, *iso*-propanol, water, and ethylene glycol, as well as their mixtures with toluene. In this study we present a fast and environmentally friendly procedure to obtain sulfonyl and sulfinyl containing compounds through sulfoxidation of bis-thioether 1,3-bis(*para*-tolyl sulfide)-5-*tert*-butylbenzene.

Keywords: *catalytic sulfoxidation, bis-thioether, sulfide oxidation, green chemistry*

[a] *Babeş-Bolyai University, Faculty of Chemistry and Chemical Engineering, Doctoral School of Chemistry, Cluj-Napoca 400028, Romania*
[b] *Babeş-Bolyai University, Faculty of Chemistry and Chemical Engineering, 11 Arany Janos str., RO-400028, Cluj-Napoca, Romania.*
[c] *Sidi Mohamed Ben Abdellah University, Faculty of Sciences, Engineering Laboratory of Organometallic, Molecular Materials, and Environment (LIMOME), Po. Box 1796 (Atlas), 30000, Fez, Morocco*
* *Corresponding authors: noemi.deak@ubbcluj.ro, gabriela.nemes@ubbcluj.ro*

INTRODUCTION

Compounds containing sulfonyl (−SO_2−) and/or sulfinyl (−SO−) moieties have a wide variety of applications,[1] for example playing important roles in organic synthesis transformations[2,3,4] or acting as ligands in the synthesis of transition metal complexes.[5] Sulfonyl and sulfinyl containing derivatives can also be found in biologically active compounds[6,7] or in materials with diverse properties.[8] For this reason, the efficient synthesis of such compounds is of interest for the scientific community. The introduction of the sulfonyl and sulfinyl groups can be realized through several well-known strategies,[9] among which one of the most representative being through the oxidation of the corresponding sulfide.[2,10] The sulfoxidation of thioethers is commonly achieved using oxidants like hydrogen peroxide (H_2O_2), meta-chloro-perbenzoic acid (*m*CPBA), oxone, HIO_4, etc. in various solvents.[11] This oxidation can be done through catalytic pathways as well.[12,13] Due to the importance and applicability of the topic, several catalytic derivatives are presented in the literature, with examples for different homogeneous and heterogeneous systems, most commonly employing catalysts based on tungsten, vanadium and titanium.[14,15,16] While there are several examples for sulfoxidation reactions of various sulfide containing substrates[12,13,14,15,16], there are very few examples where the substrates contains two or more sulfide moieties in their structure.

Our research group is also interested in the use of sulfur containing compounds, mainly for their role as pincer-type ligands in various p and d block elements-based derivatives.[17,18,19,20,21] Three compounds containing sulfonyl and sulfinyl groups were designed and used as O,C,O-chelating pincer ligands, one containing two sulfonyl groups,[19] a second one containing a sulfonyl and a sulfinyl group[21] and a third one containing two sulfinyl groups.[18] These sulfone and sulfoxide based compounds were successfully used for the stabilization of low valent group 14 elements and transition metal complexes.[17,18,19,20,21] Thus, we started to explore strategies for the synthesis of the sulfone and sulfoxide-based compounds that are in accordance with the principles of green chemistry. Recently, we presented the potential of decavanadate-containing materials as catalysts in the oxidation of diphenyl sulfide.[22] The obtained results showed that full conversion of the diphenyl sulfide substrate could be reached in a short reaction time (2 h), in solvents like methanol, ethanol, *iso*-propanol, with low catalyst loading (1.5 mol%). Moreover, good results were obtained in the recyclability test of the catalyst as well, observing full conversion of the substrate even after three runs.

Starting from these results, we continued the study in order to employ these catalytic systems in the oxidation of a bis-thioether, a compound that contains two sulfide moieties, namely 1,3-bis(*para*-tolyl sulfide)-5-*tert*-butylbenzene (further named bis-thioether **1**). We aimed to investigate and compare reaction conditions for the oxidation of bis-thioether **1** testing different solvents, catalysts and reaction times, with the purpose of finding a more environmentally friendly procedure.

RESULTS AND DISCUSSION

Based on the results obtained in our previous study for the oxidation of diphenyl sulfide,[22] we investigated the catalytic activity of decavanadate containing compounds in sulfoxidation reactions. Three decavanadate-based materials were used as catalysts to test their activity in oxidation reactions: tetraammonium decaaquadilithium decavanadate $\{Li_2(H_2O)_{10}\}(V_{10}O_{28})(NH_4)_4$ (**Cat.1**),[22] diethylenediammonium diammonium decavanadate tetrahydrate $(NH_4)_2(H_2en)_2\{V_{10}O_{28}\}\cdot 4H_2O$ (**Cat.2**)[23] and triethylenediammonium decavanadate hexahydrate $(H_2en)_3\{V_{10}O_{28}\}\cdot 6H_2O$ (**Cat.3**).[24] Full conversion of diphenyl sulfide was observed even after only two hours in methanol, ethanol, *iso*-propanol, and **Cat.1** showed good results in the recyclability test as well.[22]

These results represented the starting point in the investigation of the oxidation of 1,3-bis(*para*-tolyl sulfide)-5-*tert*-butylbenzene **1** (bis-thioether **1**), in order to obtain 1,3-bis{(4-methylphenyl)sulfonyl}-5-*tert*-butylbenzene (bis-sulfone **2**), 1-(*para*-tolylsulfinyl)-3-tosyl-5-*tert*-butylbenzene (sulfone-sulfoxide **3**) and 1,3-(*para*-tolylsulfinyl)-5-*tert*-butylbenzene (bis-sulfoxide **4**). (**Scheme 1.**)

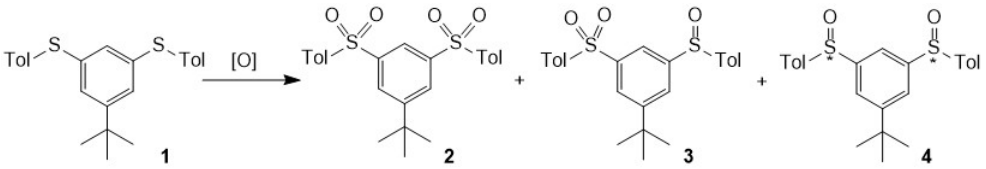

Scheme 1. Oxidation of 1,3-bis(*para*-tolyl sulfide)-5-*tert*-butylbenzene **1.**

Compounds **2** and **3** can be obtained through different pathways, presented in the literature.[19,20] Bis-sulfone **2** can be synthesized through a palladium catalysed cross-coupling reaction between 1,3-dibromo-5-*tert*-butylbenzene and sodium *para*-toluenesulfinate,[19] while sulfone-sulfoxide

3 can be obtained from 1-bromo-3-(*tert*-butyl)-5-(*para*-tolylsulfinyl)benzene and sodium *para*-toluene sulfinate with a palladium catalyzed coupling reaction.[20] Compounds **2** – **4** can also be obtained by the oxidation of bis-thioether **1** in two ways: one where the oxidation is done in anhydrous acetic acid media with hydrogen-peroxide as oxidant, and a second one using as oxidant *meta*-chloroperoxybenzoic acid (*m*CPBA) in dichloromethane (CH_2Cl_2).[18] In both cases the formation of all three products **2** – **4** can be observed and both oxidation methods have some disadvantages. Among the drawbacks is the use of a large amount of CH2Cl2 for the extraction of the products when oxidation is realized in anhydrous acetic acid with H_2O_2. Another inconvenience is the use of chlorinated solvents and the low atom economy of *m*CPBA in the second case. With the purpose of avoiding these drawbacks, the above-mentioned catalytic conditions, employed previously for the oxidation of diphenyl sulfide, were tested for the oxidation of bis-thioether **1** as well. The major challenge of this process is the presence of two sulfide groups in the molecule, that makes selectivity towards any of the expected compounds difficult to achieve.

In this work the oxidizing reaction of bis-thioether **1** (**Scheme 1.**) was tested with the previously mentioned catalysts **Cat.1-3**. One of the major considerations when selecting the reaction conditions was to comply as much as possible with the recommendations of green chemistry.[25] In the literature there are several guidelines available that help in planning and evaluating the chemical processes in a way to adhere as much as possible to the principles of green chemistry.[26,27,28] In the present case, parameters like atom economy, catalyst use, solvent safety and low energy use were considered.

Having these in mind, we developed a methodology considering the following criteria: the reaction should run at room temperature with the shortest possible reaction time, an easily handled oxidant should be used, solvents should be chosen in adherence to the solvent selection guidelines (factoring in safety, health and environmental effects), and high atom economy should be achieved. Therefore, in our tests, as the oxidizing agent an excess of 35% H_2O_2 solution was used, hydrogen peroxide being one of the most atom-economical choices and easy to handle. According to the selection guide of solvents[27,28] and taking into account the solvents usually used in sulfoxidation reactions, the following solvents were chosen for the experiments: ethanol (EtOH), methanol (MeOH), water (H_2O), ethylene glycol (EG), and isopropanol (*i*-PrOH).[27,28]

The oxidation reactions of bis-thioether **1** were followed using ^{1}H NMR spectroscopy, where compounds **1 – 4** exhibit characteristic signals. (**Figure 1.**)

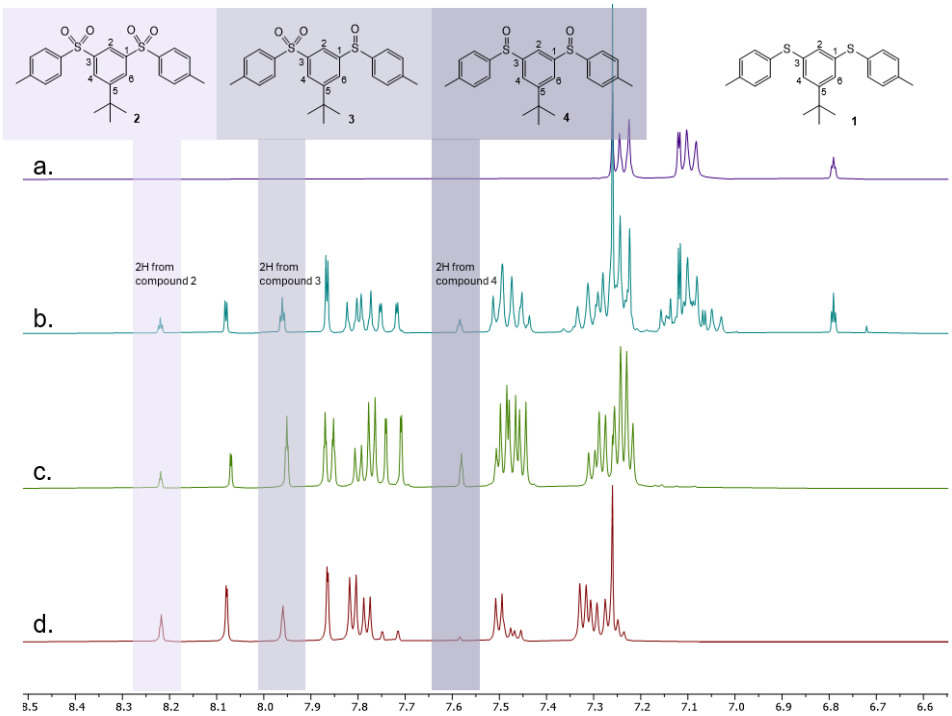

Figure 1. Example for the use of ^{1}H NMR spectroscopy for calculating the conversion and selectivity of the oxidation reactions. a. starting material b. **Cat.1**, EtOH, 48h c. **Cat.2**, H_2O, 48h d. **Cat.3**, *i*-PrOH, 48h ($CDCl_3$, 400.13 MHz)

Specifically, the conversion of the starting material bis-thioether **1** was monitored through the evolution of the distinctive triplet signal at δ 6.79 ppm (t, *J* = 1.65 Hz). The percentage of this signal, relative to the signals of the oxidation products (8.23 – 7.30 ppm), allowed for the calculation of the conversion. (**Figure 1.**)

The selectivity of the oxidation reaction towards the products bis-sulfone **2**, sulfone-sulfoxide **3**, and bis-sulfoxide **4**, was determined by calculating the percentage ratio of their respective characteristic signals. Using this method, the progress of oxidation, the overall conversion, and the product ratio could be determined. (**Figure 1.**)

The initial tests of sulfoxidation of bis-thioether **1**, after 2 and 24 h reaction time, showed no or very low conversion of the substrate. Thus, the first tests were conducted at 48 h reaction time, and the results are presented in **Table 1**.

Table 1. Experimental details, conversion and selectivity data for the oxidation reactions of compound **1.**

Nr.	Catalyst	Solvent	Conversion (%)*	Selectivity (%)*		
				2	**3**	**4**
1	**Cat.1**	MeOH	0	0	0	0
2		H_2O	**100**	21	51	28
3		EtOH	97	31	30	39
4		*i*-PrOH	**100**	20	38	42
5		EG	0	0	0	0
6	**Cat.2**	MeOH	0	0	0	0
7		H_2O	**100**	30	58	12
8		EtOH	72	23	47	30
9		*i*-PrOH	41	33	42	25
10		EG	0	0	0	0
11	**Cat.3**	MeOH	0	0	0	0
12		H_2O	**100**	75	25	0.00
13		EtOH	0	0	0	0
14		*i*-PrOH	**100**	36	49	15
15		EG	0	0	0	0
16	none[a,b]	MeOH	20	0	0	0
17	**Cat.3**[c]	MeOH	0	0	0	0

Reaction condition: 50 mg (0.27 mmol) bis-thioether **1**, 3 mL solvent, 1 mL H_2O_2 35% solution, 5 mg catalyst (1.5 mol%), room temperature, 48 hours. [a]no catalyst was used. [a]formation of an unidentified product was observed, based on ^{1}H NMR containing one sulfoxide and one sulfide group [c]no H_2O_2 was used
*without separation from reaction mixture, according to ^{1}H NMR measurements.

The catalytic oxidation efficiency of **Cat.1 – 3** was highly dependent on the reaction solvent. No substrate conversion was detected in either MeOH or EG with any of the catalysts, even after 48 h reaction time. However, complete conversion was achieved in H_2O with all three catalysts **Cat.1 – 3** and *i*-PrOH using catalysts **Cat.1** and **Cat.3** (**Table 1**). Conversions in EtOH were more variable, ranging from undetectable (**Table 1**, entry 14) to nearly quantitative depending on the specific catalyst (**Table 1**, entries 4

and 9). While overall selectivity for products **2 – 4** was generally low across the catalysts and conditions, a notable exception was the 75% selectivity for bis-sulfone **2** observed with **Cat.3** in H_2O (**Table 1**, entry 13). These results are somewhat different compared to the case when using diphenyl sulfide as a substrate in our previous study,[22] where full conversion was obtained every time in MeOH, EtOH, *i*-PrOH, and most of the time in H_2O and EG. This could be explained with the lower solubility of bis-thioether **1** compared to the diphenyl sulfide in the used polar solvents, but also with the presence of the two sulfide groups.

Given that bis-thioether **1** has a lower solubility in the polar solvents chosen for these oxidation reactions, adding an apolar solvent was needed to increase the solubility of the compound. Considering the solubility of compound **1** and the solvent selection guidelines,[19,27,28] toluene proved to be a suitable solvent to be used in the oxidation tests. Thus, toluene was added in a 1:5 ratio to the polar solvents (methanol, water, ethanol, isopropanol and ethylene-glycol) for further reactions. Two different reaction times were tested, 24 and 48 hours. The reactions were followed by ^{1}H NMR spectroscopy in order to calculate conversion and selectivity, the obtained results being presented in **Table 2**.

Adding toluene in a ratio of 1:5 to the different polar solvents (MeOH, H_2O, EtOH, *i*-PrOH and EG) increased the conversion in most cases, except EG and MeOH (**Table 2.**). In the case of EG and MeOH, although adding toluene helped, full conversion could be reached only with **Cat.1**, after 48 hours (**Table 2.**, entries 1 and 5). When it came to H_2O and *i*-PrOH the conversion was 100% in most cases after 48 hours, no matter what the catalyst was. When the reaction time was 24 hours, full conversion could be observed in toluene and H_2O solvent mixture for all three catalyst **Cat.1 – 3** (**Table 2.**, entries 17, 22, 27), while in toluene and *i*-PrOH **Cat.1** and **Cat.2** (**Table 2.**, entries 19, 24) led to the complete transformation of the substrate.

Considering the selectivity of the reactions, in most cases no clear majority was observed for either one of the products. However, in some examples, the formation of bis-sulfone **2** was preferred, after 24 hours using **Cat.1** in H_2O or **Cat.2** in *i*-PrOH. (**Table 2**, entries 17, 24) However, this could not be observed with the increased 48 hours reaction time. This difference can be explained with the stability of the catalytic systems in the alcoholic media.

Table 2. Experimental details, conversion and selectivity data for the oxidation reactions of compound **1** for 48 h and 24 h reaction time.

Nr.	Catalyst	Solvent	Reaction time (h)	Conversion (%)*	Selectivity (%)*		
					2	**3**	**4**
1	**Cat.1**	tol:MeOH	48	**100**	27	44	29
2		tol:H_2O		**100**	69	31	0
3		tol:EtOH		37	33	40	27
4		tol:*i*-PrOH		**100**	59	41	0
5		tol:EG		**100**	16	46	38
6	**Cat.2**	tol:MeOH	48	40	0	0	100
7		tol:H_2O		**100**	15	49	36
8		tol:EtOH		89	27	39	34
9		tol:*i*-PrOH		**100**	35	57	8
10		tol:EG		0	0	0	0
11	**Cat.3**	tol:MeOH	48	20	48	52	0
12		tol:H_2O		**100**	42	47	11
13		tol:EtOH		**100**	28	41	31
14		tol:*i*-PrOH		**100**	14	39	47
15		tol:EG		0	0	0	0
16	**Cat.1**	tol:MeOH	24	0	0	0	0
17		tol:H_2O		**100**	100	0	0
18		tol:EtOH		5[a]	0	0	0
19		tol:*i*-PrOH		**100**	23	49	27
20		tol:EG		**100**	23	62	25
21	**Cat.2**	tol:MeOH	24	37	0	47	53
22		tol:H_2O		**100**	29	48	18
23		tol:EtOH		33	11	30	59
24		tol:*i*-PrOH		**100**	100	0	0
25		tol:EG		20	60	18	22
26	**Cat.3**	tol:MeOH	24	49	0	0	4
27		tol:H_2O		**100**	29	48	23
28		tol:EtOH		18	0	0	100
29		tol:*i*-PrOH		74	12	32	56
30		tol:EG		0	0	0	0

Reaction condition: 50 mg (0.27 mmol) bis-thioether **1**, 3 mL solvent (toluene and polar solvent in a 1:5 ratio), 1 mL H_2O_2 35% solution, 5 mg catalyst (1.5 mol%), room temperature, 24 or 48 hours.

*without separation from reaction mixture, according to ^{1}H NMR measurements.

[a]formation of an unidentified product was observed, based on ^{1}H NMR containing one sulfoxide and one sulfide group

A reaction time of 2 hours was also tested. The calculated conversion and selectivity results are presented in **Table 3**.

Table 3. Experimental details, conversion and selectivity data for the oxidation reactions of compound **1** for 2 h reaction time

Nr.	Catalyst	Solvent	Conversion (%)*	Selectivity (%)*		
				2	**3**	**4**
1	**Cat.1**	tol:MeOH	0	0	0	0
2		tol:H_2O	**100**	38	36	26
3		tol:EtOH	15	33	56	12
4		tol:*i*-PrOH	10	0	29	71
5		tol:EG	0	0	0	0
6	**Cat.2**	tol:MeOH	0	0	0	0
7		tol:H_2O	**100**	38	57	5
8		tol:EtOH	34	0	20	80
9		tol:*i*-PrOH	31	0	21	79
10		tol:EG	0	0	0	0
11	**Cat.3**	tol:MeOH	35[a]	0	0	0
12		tol:H_2O	**100**	25	60	15
13		tol:EtOH	27[a]	6	10	15
14		tol:*i*-PrOH	50	19	32	49
15		tol:EG	25[a]	0	0	0
16	**Cat.2**[b]	H_2O, 1st run	**100**	17	59	24
17		H_2O, 2nd run	**100**	67	33	0
18		H_2O, 3rd run	**100**	31	56	13

Reaction condition: 50 mg (0.27 mmol) bis-thioether **1** , 3 mL solvent (toluene and polar solvent in a 1:5 ratio), 1 mL H_2O_2 35% solution, 5 mg catalyst (1.5 mol%), room temperature, 2 hours.

*without separation from reaction mixture, according to ^{1}H NMR measurements

[a]formation of an unidentified product was observed, based on ^{1}H NMR containing one sulfoxide and one sulfide group

[b]scale-up to 500 mg substrate and catalyst recyclability test

It was shown that, when using toluene and H_2O as solvent mixture, even after a 2 hours reaction time, full conversion can be obtained for all three catalyst **Cat.1 – 3**. When using other solvents (MeOH, EtOH, *i*-PrOH, EG) the conversion was usually lower than with the reaction time of 24 or 48 hours. When considering the selectivity, no clear preference towards products **2 – 4** was observed, all three being obtained in all cases.

A scale-up and catalyst recyclability test was carried out as well with **Cat.2**. Using 500 mg bis-thioether **1** in the toluene and H_2O solvent mixture full conversion of the substrate could be observed even after 3 runs, thus showing a robust, environmentally friendly and fast procedure to obtain the targeted compounds **2 – 4**.

CONCLUSIONS

In this study an efficient and environmentally benign method for the catalytic oxidation of bis-thioether **1** to its corresponding sulfone and sulfoxide derivatives was successfully developed using three decavanadate-based catalysts (**Cat.1**, **Cat.2**, **Cat.3**). The results of the present research indicate that using a mixture of toluene and water, full conversion of the substrate was obtained within two hours at room temperature, with a low catalyst loading and H_2O_2 as oxidant.

This methodology aligns with the principles of green chemistry by employing non-toxic solvents and H_2O_2 as oxidant, and represents a significant advancement over traditional oxidation techniques, which frequently rely on hazardous organic solvents and oxidants with low atom economy. The ability of the system to maintain high activity in aqueous-organic mixtures validates the feasibility of using water as a primary medium for oxidation of sulfides, aligning with the principles of green chemistry. Furthermore, this system proved to be scalable, and the catalyst displayed potential for recyclability.

The method described in this work is highly effective for achieving full conversion of a substrate containing two sulfide groups, even if selectivity towards any of the products is not observed. Future investigations will focus on tailoring the catalyst and the catalytic system to reach selectivity towards either sulfoxides or sulfones.

EXPERIMENTAL SECTION

General considerations

Compounds bis-thioether **1**[18] and catalysts **Cat.1 – 3** were prepared according to literature procedures.[22,23,24] All other chemicals were purchased from usual chemical suppliers and used as received. NMR spectra were recorded in deuterated chloroform on Bruker Avance 400 spectrometer (operating frequency of 400.13 MHz for ^{1}H). Chemical shifts are given in ppm relative to the solvent residual peak for the ^{1}H NMR spectra.

General procedure for catalytic oxidation

In a typical experiment 50 mg bis-thioether **1**, 3 mL solvent, 1 mL 35% H_2O_2 solution and 5 mg catalyst were added to a 25 mL one-necked round bottom flask and stirred at room temperature for different time periods (2, 24 or 48 hours). After adding 3 mL water, the phases were extracted with 5 mL ethyl-acetate two times. The organic phases were dried under vacuum and analyzed by ^{1}H NMR spectroscopy using $CDCl_3$ as solvent. Conversion was calculated in MestReNova software considering the sum of the integral for H2 of bis-thioether **1** (**Figure 1**), bis-sulfone **2**, sulfone-sulfoxide **3** and bis-sulfoxide **4** (**Figure 1**) 100, then using the normalized values as percentage of each signal, thus each compound. In a similar fashion, when calculating the selectivity, the sum of the integrals corresponding to H2 in compounds **2 – 4** (**Figure 1**) was set to 100.

ACKNOWLEDGMENTS

This work was supported by a grant of the Ministry of Research, Innovation and Digitization, CNCS – UEFISCDI, project number PN-IV-P2-2.1-TE-2023-0612, within PNCDI IV.

REFERENCES

1. M. Wang, X. Jiang, *ACS Sustainable Chem. Eng*. **2022**, *10*(2), 671–677.
2. S. Liang, K. Hofman, M. Friedrich, J. Keller, G. Manolikakes, *ChemSusChem* **2021**, *14*, 4878 – 4902.
3. J. Priego, O. García Mancheño, S. Cabrera, J. C. Carretero, *J. Org. Chem*. **2002**, *67*(4), 1346–1353.
4. G. Sipos, E. E. Drinkel, R. Dorta, *Chem. Soc. Rev*. **2015**, 44, 3834– 3860.
5. B. M. Trost, M. Rao, *Angew. Chem., Int. Ed*. **2015**, *54*, 5026– 5043.
6. E. A. Ilardi, E. Vitaku, J. T. Njardarson, *J. Med. Chem*. **2014**, *57*(7), 2832–2842.

7. X. Chen, H. Wu, C.-M. Park, T. H. Poole, G. Keceli, N. O. Devarie-Baez, A.W.Tsang, W. T. Lowther, L. B. Poole, S. B. King, M. Xian, C. M. Furdui, *ACS Chem. Biol.* **2017**, *12* (8), 2201–2208.
8. H. Mutlu, E. B. Ceper, X. Li, J. Yang, W. Dong, M. M. Ozmen, P. Theato, *Macromol. Rapid Commun*. **2018**, 1800650.
9. S. Patai, Z. Rappoport, C. J. M. Stirling, *The Chemistry of Sulphones and Sulphoxides*, Wiley, New York, **1988.**
10. E. Wojaczynska, J. Wojaczynski, *Chem. Rev.,* **2010**, *110*, 4303–4356.
11. J.-E. Bäckvall, *Modern Oxidation Methods*, Wiley-VCH, Weinheim, **2004.**
12. E. Wojaczyńska, J. Wojaczyński, *Chem. Rev*. **2020**, *120*(10), 4578–4611.
13. X. B. Liu, Q. Rong, J. Tan, C. Chen, Y. L. Hu, *Front. Chem*. **2022**, *9*, 798603.
14. J.-P. Cao, Y.-S. Xue, N.-F. Li, J.-J. Gong, R.-K. Kang, Y. Xu, *J. Am. Chem. Soc.* **2019**, *141*(49), 19487–19497.
15. W. Al-Maksoud, S. Daniele, A.B. Sorokin, *Green Chem*., **2008**, *10*, 447–451.
16. F. Rajabi, E. Vessally, R. Luque R, L. Voskressensky, *Molecular Catalysis*, **2021**, *515*, 111931.
17. N. Deak, D.Madec, G. Nemes, *Eur. J. Inorg. Chem*, **2020**, 2769-2790.
18. N. Deak, O. Thillaye du Boullay, S. Mallet-Ladeira, I.-T. Moraru, D. Madec, G.Nemes, *Eur. J. Inorg. Chem,* **2020**, 3729-3737.
19. N. Deak, P. M. Petrar, S. Mallet-Ladeira, L. Silaghi-Dumitrescu, G. Nemeş, D.Madec, *Chem. Eur. J.,* **2016**, *22*, 1349-1354.
20. N. Deak, O. Thillaye du Boullay, I.-T. Moraru, S. Mallet-Ladeira, D.Madec, G.Nemes, *Dalton Trans.*, **2019**, *48*, 2399-2406.
21. N. Deak, R. Septelean, I.-T. Moraru, S. Mallet-Ladeira, D. Madec, G. Nemes, *Studia UBB Chemia*, **2018**, *LXIII* (2), 105-115
22. N. Deak, M. Idboumlik, A. Soran, M. Lachkar, B. El Bali, G. Nemes; *Stud. Univ. Babes-Bolyai, Chem.,* **2024**, *69*, 7–23.
23. M. Idboumlik, M. Kadiri, N. Hamdi, M. Driouch, A.F.I. Ngopoh, I. Lakkab, E-E. Bendeif, M. Sfaira, B. El Bali, M. Lachkar, A. Zarrouk, *Mater. Chem. Phys*., **2022**, *287*, article no. 126211.
24. M. Idboumlik, I. Lakkab, S. Erraouan, N. Hamdi, M. Lachkar, M. Dusek, V. Eigner, B. El Bali, *J. Mol. Struct*., **2024**, *1312*, article no. 138551.
25. P. T. Anastas and J. C. Warner, *Green Chemistry: Theory and Practice*, Oxford University Press, **1998.**
26. A. M. Afanasenko, N. Deak, J. October, R. Sole, K. Barta, *Green Chem.*, **2025**, *27*, 5947-5981.
27. D. Prat, A. Wells, J. Hayler, H. Sneddon, C.R. McElroy, S. Abou-Shehadad, P.J.Dunn, *Green Chem.*, **2016**,*18*, 288-296.
28. D. Prat, J. Hayler, A. Wells, *Green Chem.*, **2014**, *16*, 4546-4551.

STUDIA UBB CHEMIA, LXXI, 1, 2026 (p. 19-30)
(RECOMMENDED CITATION)
DOI:10.24193/subbchem.2026.1.02

SYNTHESIS, CHARACTERIZATION AND *CIEL*a*b** COLOR SPACE STUDY OF TWO ECO-FRIENDLY DIRECT STILBENE AZOIC DYES

Maria Elena RADULESCU-GRAD[a], Simona POPA[b,*], Sorina BORAN[b], Giannin MOSOARCA[b]

ABSTRACT. The article presents the synthesis of two disazo-stilbene dyes with symmetrical structure. A non-carcinogen, non-mutagen/teratogen intermediate, 4,4'-diaminostilben-2,2'-disulfonic acid was used as central component and the 8-amino-1-naphtol-3,6-disulphonic acid and the 6-hydroxynaphthalene-2-sulphonic acid as coupling components respectively. To evaluate the characterization of the dyes, well known and applied methods were used TLC, UV-VIS and FT/IR spectroscopy. Color variations (ΔE**ab* and Δh*) were determined relative to a single standard, (C.I.77891 P.W.6). The results highlight a metamerism effect and good coloring properties of the studied dyes.

Keywords: *azo-stilbene dyes, CIEL*a*b* color space*

INTRODUCTION

As is known, azo dyes are synthetic dyes that contain one or more nitrogen-nitrogen double bonds called azo groups [1]. Because of their diverse colors and chemical stability, they are usually used in multiple industries to color textiles, paper, plastics, etc [2-5] and consider their photophysical properties and anti-bacterial activity, in medicine as well [6,7].

[a] *"Coriolan Dragulescu" Institute of Chemistry, Romanian Academy, Mihai Viteazu Bd. No. 24, 300223, Timisoara, Romania.*
[b] *Faculty of Chemical Engineering, Biotechnologies and Environmental Protection, Politehnica University Timisoara, V. Parvan Bd. No. 6, 300223 Timisoara, Romania.*
[*] *Corresponding author: simona.popa@upt.ro*

Due to the instability of the azo bonds existing in their structure, the degradation of the dyes can take place by photo-oxidation, photolysis, biodegradation, and chemical degradation [8,9]. Literature underlines that toxic amines can result from these degradation processes both for the dye molecules and for the intermediates used in their synthesis and, at consequence, their use may be restricted [10,11].

The researchers' efforts are now to find alternative dyes that use instead of benzidine, a diamine toxic intermediate having a carcinogen, mutagen/teratogen character, dyes with properties like the benzidine ones. The replacement for benzidine dyes represents a notable challenge, results in this area show that the 4,4'-diaminostilben-2,2'-disulfonic acid may offer a viable alternative as an intermediate in the synthesis of azo dyes. However, a limited number of studies are known in recent years regarding the synthesis of new dyes with azo-stilbene structure [12-15].

The basis of all color measurement systems is the one CIE proposed, *CIEL*a*b** space being a three-dimensional color model that represents all colors visible to the human eye, in cartesian and/or cylindrical coordinates. Therefore, any specific single color may be represented as a point in the three-dimensional color space, which is powerful and versatile at the same time, qualities that make it useful for a wide range of applications. The color difference equations may be developed and are generally based on the principle of calculating the distance in three-dimensional color space between two colors, for example between a sample and a standard [16-19].

This paper presents the synthesis, the characterization, and the colorimetric study of two eco-friendly disazo direct dyes with symmetrical structure derived from 4,4'-diaminostilbene-2,2'-disulphonic acid and containing 8-amino-1-naphthol-3,6-disulphonic acid and 6-hydroxynaphthalene-2-sulphonic acid respectively as coupling components.

To the best of our knowledge, the new approach of the color analysis performed upon direct stilbene azoic dyes, such in this paper, was not yet presented.

RESULTS AND DISCUSSION

Synthesis of the dyes

The synthesis of the dye I and II with structures shown in Scheme 1 involved the bis-diazotization of 4,4'-diaminostilbene-2,2'-disulphonic acid and the coupling reactions of the resultant bis–diazonium salt with 8-amino-1-naphthol-3,6-disulphonic acid and 6-hydroxynaphthalene-2-sulphonic acid respectively as coupling components in a 1:2 molar ratio.

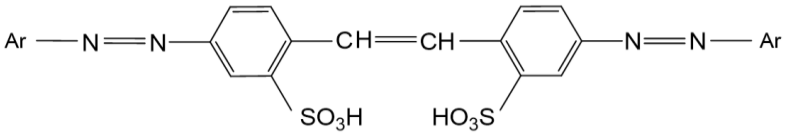

where the coupling component Ar:

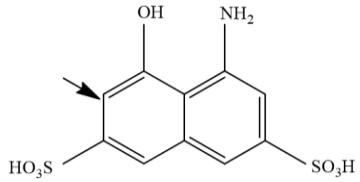

(a)

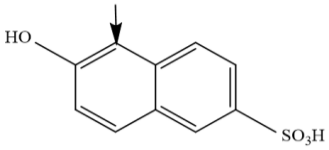

(b)

Scheme 1. Structures of the symmetrical azo-stilbene dyes Ar
(a) - (dye I); (b) - dye II

In the first step (diazotization), 4,4'-diaminostilbene-2,2' disulphonic acid was treated with sodium nitrite ($NaNO_2$) in an acidic hydrochloric acid (HCl) solution (see for details) [20]. This process creates the diazonium salt, which is the key component for dye formation.

In the second step (coupling), the diazonium salt solution was directly added to an alkaline solutions containing 8-amino-1-naphthol-3,6-disulphonic acid and 6-hydroxynaphthalene-2-sulphonic acid respectively (the coupling components). The optimal versions of the coupling process for the synthesis of dye I and II were established after several experimental attempts namely, the direct addition of the acid suspension of the bis-diazonium salt of 4,4'-diaminostilbene-2,2' -disulphonic acid to the basic solutions of the coupling components (8-amino-1-naphthol-3,6-disulphonic acid and 6-hydroxynaphthalene-2-sulphonic acid respectively) and vice versa. The reaction conditions were established knowing that coupling reactions with phenols and naphtols take place in a weakly alkaline medium and at low temperature.

Consequently, the reactions maintained at around 10°C and at a pH around 8, with the caution addition of Na_2CO_3 form the desired dyes' molecules. In order, to ensure the completion of the reactions, the mixtures were kept under stirring for 3.5 h for dye I and 3 h for dye II. The purification was performed by fractioned crystallization from dioxane:pyridine 90:10 (v:v), according to the solubility difference in the mixture' s corresponding components, of the synthesized dyes I and II respectively.

Characterization of the dyes

The thin layer chromatography (TLC) and the UV-VIS, FT/IR spectroscopy were used to establish the purity and the structure of the synthesized disazo dyes I and II.

According to the FT/IR spectra (Figure 1), the reaction products reveal two absorption bands, around 3500 cm^1 and 1380 cm^1, corresponding to the stretching and deformation vibrations respevtively of the hydroxyl group. At the same time dye I and II show an absorption band in the region of 1120-1187 cm^{-1} and absorption band in the region of 1070-1078 cm^{-1}, described by the asymmetric and symmetric stretching vibrations of the sulphonic function (-SO_3H). The medium stretching vibration band related to the olefinic bound was recorded for both studied dyes in the region 1630-1680 cm^{-1} In azo derivatives, the stretching vibration of the −N=N− bond generally appears in the IR region around: −N=N− stretching: ~1400–1500 cm^{-1} (sometimes reported up to 1600 cm^{-1}) But in symmetric azo derivatives, this band is very weak or even absent in IR, because the vibration does not produce a significant change in dipole moment. [21].

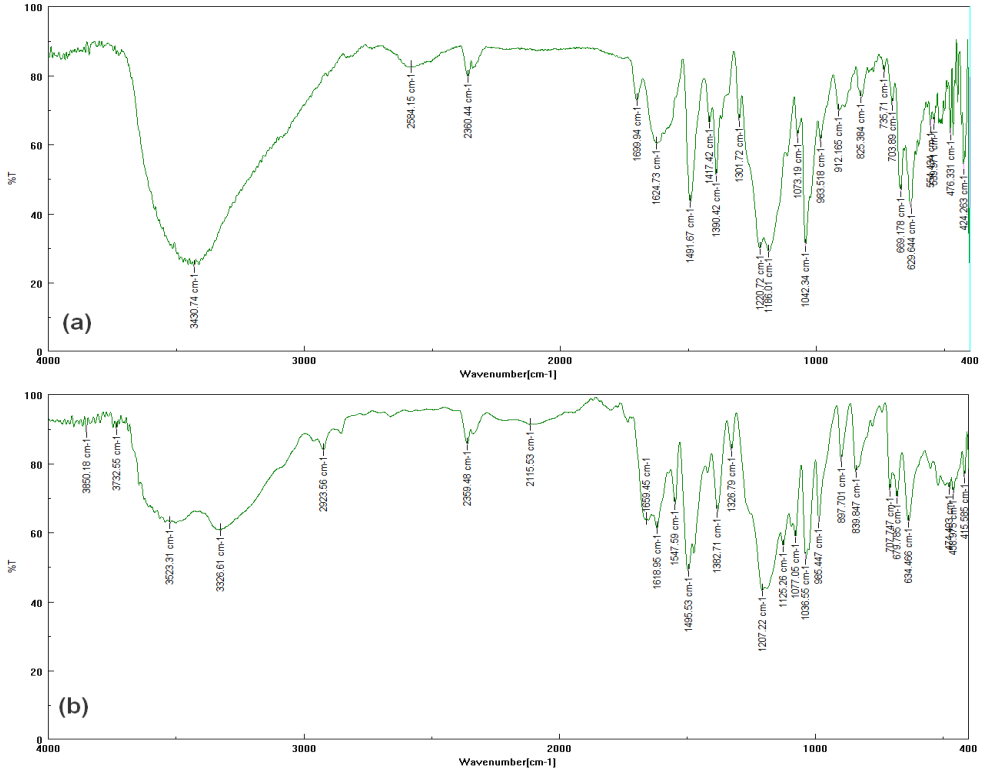

Figure 1. FTIR spectra for: (a) – dye I and (b) – dye II

The electronic spectra of the analyzed dyes exhibit in a 50% aqueous methanol (MeOH) solution an absorption namely, in the yellow region 560-590 nm for dye I and absorption in the green region 500-560nm for dye II as expected.

Colorimetric measurement of the dyes

The synthesized compounds, dye I and dye II, have extensive conjugation of the double bonds on their entire molecules. The presence of two naphthalene molecules, each containing an auxochrome hydroxyl group, in dye I in *α*-position and in dye II in *β*-position, is the reason why they have dark colors. Because dye I has also an auxochrome amino group on each naphthalene molecule, it presents a dark violet color comparative to dye II, which is dark purple.

To understand how concentration affects the dyes color, we mixed them at various concentrations with a water-based acrylic resin containing titanium dioxide (TiO_2) paste (C.I.77891 P.W.6). When the dyes concentrations increase, the material reflects less light, resulting in a darker or more intense color, an aspect presented by other authors as well. [22].

Using the reflectance spectra, the Kubelka-Munk equation (see Equation 1) one may determine a material's color strength across the visible spectrum. This equation allows us to calculate a value called "K/S" which indicates the relative intensity or strength of a material's color [23, 24].

$$\frac{K}{S} = \frac{(1-R)^2}{2R} \quad (1)$$

The equation considers three key factors that influence a material's color:

- Reflectance ratio (R) - which represents the proportion of light reflected by the material compared to the light that hits it. A lower reflectance ratio indicates that more light is absorbed by the material, potentially resulting in a more intense color.

- Absorbance coefficient (K) - which measures how strongly the material absorbs light at a specific wavelength. A higher absorbance coefficient means the material absorbs light more efficiently, contributing to a stronger color.

- Scattering coefficient (S) - which reflects how light gets dispersed within the material. A lower scattering coefficient allows for clearer light absorption and potentially a more vibrant color.

Figure 2 presents the results of these values for both dyes (I and II), showing that their color strength decreases with increasing their concentration in resin (2%, 5%, 8% and 15%). Similar results have been reported in other papers [23, 25-27].

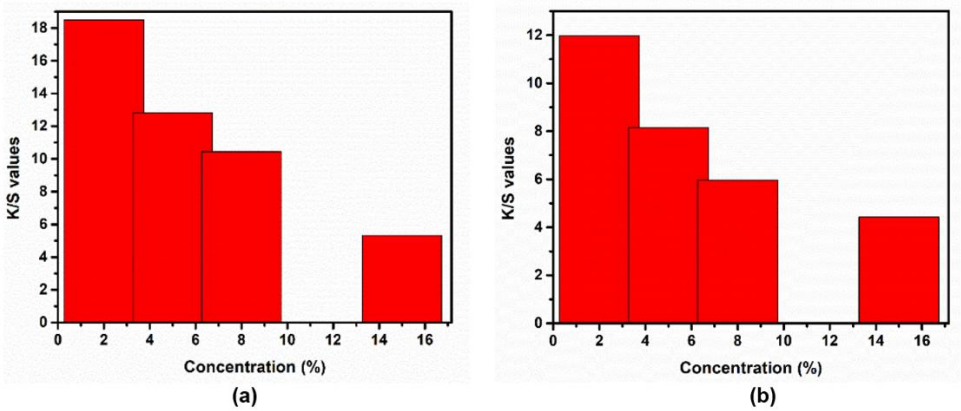

Figure 2. Color strength (K/S) at different compound concentrations (2%, 5%, 8% and 15%) in water-based acrylic resin, for dye I (a) and for dye II (b)

The colored resin samples containing dye I (Figure 3,a) show exactly what expected. As the amount of dye increases, the material becomes darker (lower *L** value). Additionally, the higher red (*a**) and yellow (*b**) values at higher dye concentrations tell us the color becomes a more intense violet.

The color parameters in the *CIEL*a*b** system for dye II are presented in Figure 3,b. It is observed that the lightness (*L**) decreases as the dye concentration increases in the water-based acrylic resin, and the (*a**) and (*b**) parameters reveal an intensification of the purple color under the same conditions mentioned above.

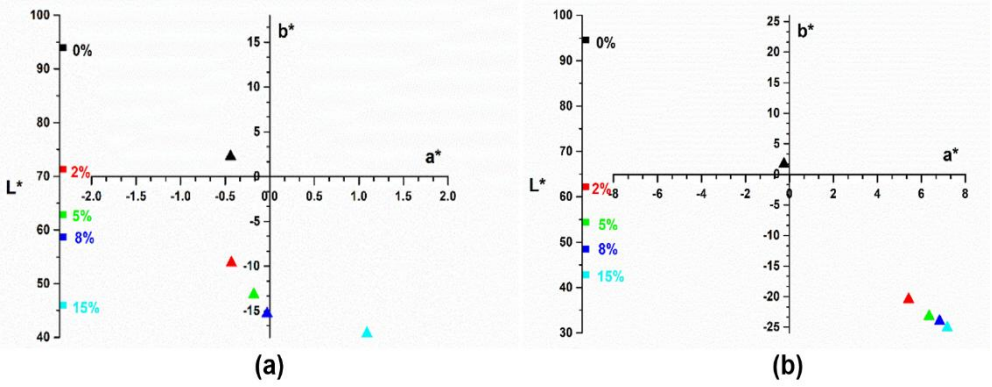

Figure 3. *CIEL*a*b** values of dye I (a) and dye II (b) in water-based acrylic resin at different concentrations

One can use a color measurement system to determine how different a sample's color is from a standard color. This overall difference is represented by ΔE**ab* (that is the distance between the two colors in a specific color space). Equation (2) allows us to calculate this overall difference. There are also ways to analyze specific aspects of the color difference: Saturation difference (ΔC*) calculated using equation (3), which tells us how much the colors differ in terms of their intensity or vibrancy. Equation (4) helps us determine the difference in the actual color "tone" (red, green, blue, etc.) between the sample and standard, represented by the hue difference (Δh*) [17, 22].

$$\Delta E^*_{ab} = \sqrt{(\Delta L^*)^2 + (\Delta a^*)^2 + (\Delta b^*)^2} \quad (2)$$

$$\Delta C^* = C^*_{sample} - C^*_{standard} \quad (3)$$

$$\Delta h^* = \sqrt{(\Delta E^*_{ab})^2 - (\Delta L^*)^2 - (\Delta C^*)^2} \quad (4)$$

The color differences mentioned above depend on the dye concentration as presented in Figure 4. As can be observed, their values increase with product concentration, with a tendency of higher limitation at higher concentrations, a fact also revealed in the literature [17, 27, 28].

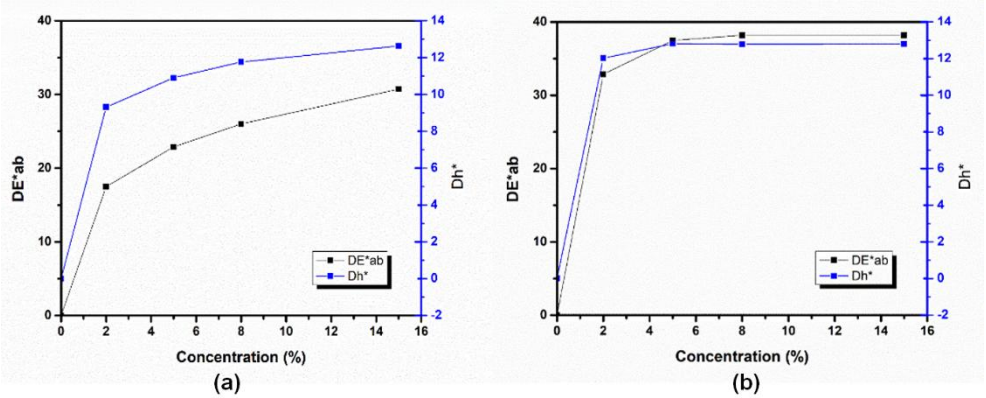

Figure 4. The total color difference (ΔE*ab) and hue difference (Δh*) of the dye I and dye II at different concentrations in water-based acrylic resin

Although the color of dye I gets more intense with increasing concentration under all three standard lighting conditions (CIE illuminants), Table 1 reveals an interesting detail. The specific shade of the dye appears

different depending on the light source. This phenomenon, where materials can appear to have different colors under different lighting conditions, is called, as known, *metamerism.*

Table 1. Effect of concentration and light source (D65, A, F2) on dye I color in resin

Color parameter	Concentration	D65		A		F2	
		Color	Value	Color	Value	Color	Value
L*	2%		71.33		70.56		70.39
a*			-0.43		-1.62		-0.1
b*			-9.63		-10.68		-11.65
L*	5%		62.84		61.79		61.64
a*			-0.18		-2.28		0.1
b*			-13.16		-14.47		-15.74
L*	8%		58.68		57.46		57.34
a*			-0.03		-2.85		0.26
b*			-15.31		-16.77		-18.25
L*	15%		46.05		44.3		44.69
a*			1.09		-3.22		1.1
b*			-17.53		-19.13		-20.68

A similar approach may be underlined for dye II, that can be seen in Table 2, the color changes under different illuminants. Based on these observations it was concluded that dye II exhibits a *metamerism* effect as well.

Table 2. Effect of concentration and light source (D65, A, F2) on dye II color in resin

Color parameter	Concentration	D65		A		F2	
		Color	Value	Color	Value	Color	Value
L*	2%		62.19		61.19		60.57
a*			5.42		2.18		3.98
b*			-20.46		-21.16		-24.12
L*	5%		54.42		53.23		52.63
a*			6.35		2.11		4.6
b*			-23.21		-24		-27.27
L*	8%		48.48		47.35		46.77
a*			6.83		2.4		4.9
b*			-23.01		-23.65		-26.95
L*	15%		42.78		41.82		41.36
a*			6.48		2.24		4.54
b*			-23.99		-20.99		-23.99

CONCLUSIONS

Considering that 4,4'-diaminostilben-2,2'-disulfonic acid may be a favorable alternative for benzidine, as intermediate, assignable to its low toxicity, as well as the possibility of extending the conjugation on the whole molecule was successfully employed to synthesize two eco-friendly symmetrical disazo-stilbene direct dyes. The used coupling components were 8-amino-1-naphtol-3,6-disulphonic acid and 6-hydroxynaphthalene-2-sulphonic acid respectively. The thin layer chromatography (TLC) was used to establish the purity of the dyes (I, II) and the UV-VIS, FT/IR spectroscopy data were useful for the confirmation of their structures. The new approach of the color analysis performed upon these direct dyes with azo-stilbene structure, using the *CIEL*a*b** color system, emphasizes the color properties of dyes, showing their dark color, one dark purple and the other dark violet, highlighting their good coloring properties and that metamerism effect is present for both dyes, as well. Attempts to use symmetric-structure azo-stilbene dyes in obtaining film-forming materials have led to encouraging results [29].

EXPERIMENTAL SECTION

Synthesis of the dyes

The protocol used to obtain the disazo direct stilbene dyes is also mentioned in the previously published papers [15].

The diazotization step:

A suspension of 1.95 g of 4,4′-diaminostilbene-2,2′-disulfonic acid (95%, 0.005 mol) was prepared in 25 mL of distilled water. To this mixture, 1.1 mL of 30% aqueous NaOH (0.01 mol) was added gradually, and the resulting solution was cooled to 5 °C. The sodium salt formed in situ was then acidified with 3 mL of 32% HCl (0.03 mol). Bis-diazotization of the resulting suspension was carried out by adding 0.71 g of solid $NaNO_2$ (98%, 0.0101 mol) at 5 °C while maintaining the pH at approximately 1. After the addition of $NaNO_2$, the reaction mixture was stirred for 1,5 hours to ensure complete diazotization. Excess nitrous acid was subsequently destroyed by treatment with urea.

The coupling step:

In an aqueous 10% NaOH solution were dissolved 3.54 g of 8-amino-1-naphtol-3,6-disulphonic acid and 2.48 g of 6-hydroxynaphthalene-2-sulphonic acid (98%, 0.011 mol), respectively. Further the diazonium salt solution was

directly added to an alkaline solutions containing 8-amino-1-naphthol-3,6-disulphonic acid and 6-hydroxynaphthalene-2-sulphonic acid respectively. By periodically adding a 10% aqueous Na_2CO_3 solution, the pH of the reaction mixture was maintained at approximately 8–8.5, and the temperature at about 8–10 °C**.** The progress of reaction was monitored by drop reaction (with an alkaline solution of 8-amino-1-naphtol-3,6-disulphonic acid respectively with the diazonium salt of 4-nitroaniline) and by TLC. In order, to ensure completion of the reactions, the mixtures were kept under stirring for 3.5 h for dye **I** and 3 h for dye **II**. The separation of the crude dyes was carried out by filtration. The purification of the dyes was carried out by recrystallization from a 90:10 (v:v) dioxane:pyridine mixture to obtain the pure products with yields of 80–82%.

Characterization of the dyes

The UV/VIS spectroscopy measurements were performed using a CECIL CE 7200 spectrophotometer in the 300–800 nm range, while the FT/IR (KBr) spectroscopy data were carried out on a JASCO FT/IR-4200 spectrometer in the 4000–400 cm^{-1} range.

For I: TLC (silicagel plates 60F−254:methyl−ethyl ketone:ammonia 25%:MeOH=2:3:2 (v:v:v)) (R_f: 0.77); VIS (50% aqueous MeOH) (λ_{max}/nm; lgε: 591; 4.40); IR (KBr) (v/cm^{-1}: 3430 (OH), 1185, 1073 (SO_3H), 1681(C=C)).

For dye II: TLC (silicagel plates 60F−254:methyl−ethyl ketone: ammonia 25%:MeOH=4:4:1.5 (v:v:v)) (R_f: 0.81); VIS (50% aqueous MeOH) (λ_{max}/nm; lgε : 542; 4.42); IR (KBr) (v/cm^{-1}: 3523 (OH), 1125, 1077 (SO_3H), 1640 (C=C)).

Colorimetric measurement of the dyes

Experimental details of the color analysis of the above-mentioned dyes may be found in previous published studies [15, 29]. The dyes were mixed in different concentrations (2%, 5%, 8% and 15%) with a water-based acrylic resin containing titanium dioxide (TiO_2) paste (C.I.77891 P.W.6) – the standard for all color analysis (0%). The mixtures were then applied on a white cellulosic support, and their color properties (L* - lightness; a* - the transition from green to red and b* - the transition from blue to yellow, as well as the Reflectance) were recorded using a MINOLTA CM 3220d spectrophotometer with the CIE D65 as the illuminant (natural day light) and the standard 10° observer function, and for thee metamerism effect determination, two other illuminants were used, namely A – warm light and F2 – cold light.

REFERENCES

1. H. Zollinger; *Color Chemistry: Syntheses, Properties and Applications of Organic Dyes and Pigments*, 3rd ed.; Wiley-VCH: Weinheim, Germany, **2003**.
2. A. Z. Omar; M. G. Mohamed; E. A. Homed; M. A. El-Atavy; *J. Saudi Chem.*, **2023**, *27(1)*, 101594.
3. A. Matei; C. Constantinescu; B. Mitu; M. Filipescu; V. Ion; I. Ionita; S. Brajnicov; A. P. Alloncle; P. Delaporte; A. Emandi; M. Dinescu; *Appl. Surf. Sci.*, **2015**, *336*, 200-205.
4. K. Yamjala; M. S Naiar; N. R. Ramisetti; *Food Chem.*, **2016**, *192*, 813–824.
5. S. Benkhaya; S. M'rabet; A. El-Harfi; *Heliyon*, **2020**, *6(1)*, e03271.
6. E. U. Mughal; Q. A. Raja; A. Y. A. Alzahrani; N. Naeem; A. Sadiq; E. Bozkurt; *Dyes Pigm.*, **2023**, *220*, 111762.
7. F. Eltaboni; N. Bader; R. El-Kailany; N. Elsharif; A. Ahhmida; *J. Chem. Rev.*, **2022**, *4(4)*, 313-330.
8. P. D. Josephy; E. Allen-Vercoe; *Food Chem Toxicol.*, **2023**, *178*, 113932.
9. T. Platzek; *Toxicol. Lett.*, **2013**, *221*, S53.
10. Bundesgesetzblatt; *Zweite Verordnung zur Änderung der Atomrechtlichen Verfahrensordnung*, nr. 82; Bonn, Germany, **1994**.
11. Bundesgesetzblatt; Vierte Verordnung zur Änderung der Bedarfsgegenständeverordnung, nr. 8; Bonn, Germany, **1995**.
12. Y. C. Chao; S. S. Yang; *Dyes Pigm.*, **1995**, *29(2)*, 131-138.
13. M. E. Grad; V. Rădiţoiu; L. Wagner; A. Rădiţoiu; A. X. Lupea; *Rev. Chim. (Bucharest)*, **2007**, *58(8)*, 786-790.
14. M. E. Grad; G. M. Simu; S. G. Muntean; G. Ilia; *J. Iran Chem Soc.*, **2013**, *10(4)*, 807-814.
15. M. E. Rădulescu-Grad; A. Visa; M. S. Milea; R. I. Lazău; S. Popa; S. Funar-Timofei; *J. Mol. Struct.*, **2020**, *1217*, 128380.
16. J. A. Paulo, D. I. Santos, *Ind. Crop. Prod.*, **2023**, *205*, 117513.
17. R. M. Christie; *Colour Chemistry*, 2nd ed.; The Royal Society of Chemistry: Cambridge, UK, **2013**.
18. S. Yufa; F. A. M. Al-Zahrani; L. Lin; *Dyes Pigm.*, **2023**, *208*, 110854.
19. J. Biswas; S. Yana; S. Gosh; *J. Non-Cryst. Solids.*, **2024**, *630*, 122890.
20. H. Sanielevici; F. Urseanu; *Sinteze de Coloranţi Azoici*, vol. 2; Ed. Tehnică: Bucureşti, Romania, **1987**.
21. A. E. Balaban; M. Banciu; I. Pogany; *Aplicatii ale metodelor fizice in chimia organica*; Ed. Didactică şi Pedagogică: Bucureşti, Romania, **1980**.
22. A. Raditoiu; V. Raditoiu; C. A. Nicolae; M. F. Raduly; V. Amariutei; L. E. Wagner; *Dyes Pigm.*, **2016**, *134*, 69-76.
23. R. Mia; M. Minhajul Islam; T. Ahmed, M. Azhar Waquar; N. Jahan Khanam; S. Sultana; M. Sajjadul Karim Bhuiyan; M. Nizam Uddin; *Clean. Eng. Technol.*, **2022**, *8*, 100471.

24. P. M. Bhate; R. V. Devi; R. Dugane; P. R. Hande; L. Shaikh; S. Vaidya; S. Masand; *Dyes Pigm.*, **2017**, *145*, 208-215.
25. D. R. Patel; B. M. Patel; N. B. Patel; K. C. Patel; *J. Saudi Chem. Soc.*, **2024**, *18(3)*, 245-254.
26. M. Filgueiras Rebelo de Matos; P. Quênia Muniz Bezerra; L. Conceição Argôlo Correia, V. Denise Nunes; A. de Oliveira Rios; J. Izabel Druzian; I. L. Nunes; *Food Chem.*, **2021**, *365*, 130446.
27. A. T. M. Gulam Moula; Md. Dulal Hosen; Md. Abu Bakar Siddiquee; Md. Abdul Momin; Z. Kaisar; Md. Abdullah Al Mamun; Md. Azharul Islam; *Heliyon*, **2022**, *8*, e11246.
28. M. Tousirot; W. Nowik, E. Hnawia, N. Lebouvier, A.E. Hay; A. de la Sayette; M.G. Dijoux-Franca; D. Cardon; M. Nour; *Dyes Pigm.*, **2014**, *102*, 278-284.
29. S. Popa; M.E. Radulescu-Grad; A. Perdivara; G. Mosoarca; *Sci. Rep.*, **2021**, *11*, 5889.

STUDIA UBB CHEMIA, LXXI, 1, 2026 (p. 31-41)
(RECOMMENDED CITATION)
DOI:10.24193/subbchem.2026.1.03

COPPER CHELATION BY SYRINGIC HYDRAZONES: A PROMISING STRATEGY FOR COMBATING OXIDATIVE STRESS-RELATED DISEASES

Nadji BELKHEIRI[a]

ABSTRACT. Oxidative stress is a critical factor in vascular damage and the development of diseases such as atherosclerosis. This study investigates the complexation properties of two syringic hydrazones, (E)-4-Hydroxy-3,5-dimethoxybenzaldehyde -1,3-benzothiazol-2-ylhydrazone **1** and (E)-4-Hydroxy-3,5-dimethoxybenzaldehyde phthalazin-1-ylhydrazone hydrochloride **2**, with copper ions ($CuSO_4 \cdot 5H_2O$ and $CuCl_2 \cdot 2H_2O$). Using UV spectrophotometry, we determined stability constants and stoichiometries of the complexes formed. Compound **1** forms three distinct types of complexes (ML, ML_2, and M_2L) with higher stability constants compared to those formed by compound **2**, particularly when using $CuCl_2 \cdot 2H_2O$. These findings extend our previous work, where syringic hydrazones demonstrated potent antioxidant properties through scavenging $DPPH^{\bullet}$ and $ABTS^{\bullet+}$ radicals, inhibiting superoxide anion generation, and reducing TBARS formation in human cell-mediated LDL oxidation. These results highlight the dual potential of syringic hydrazones as radical scavengers and metal chelators.

Keywords: *Antioxidant activity, ROS scavenging, metal chelation, UV spectrophotometry, Cu(II) complexes, stability constants*

INTRODUCTION

Oxidative stress underpins vascular damage and cardiovascular diseases, arising from an imbalance between reactive oxygen species (ROS) production and antioxidant defenses [1]. Cellular processes like mitochondrial

[a] Laboratory for Inorganic, Organic and Bio-Inspired Chemistry Research, Faculty of Exact Sciences and Computer Science, University of Djelfa, Algeria. Email: belkheirinadji@yahoo.fr

respiration and NADPH oxidase activity generate ROS, leading to lipid peroxidation, protein modifications, and cellular dysfunction [2, 3]. Transition metals, notably copper and iron, catalyze Fenton and Haber-Weiss reactions, producing hydroxyl radicals that exacerbate oxidative stress [4, 5]. Antioxidants mitigate this stress by scavenging free radicals or forming stable complexes with transition metals [6, 7].

Hydrazones, characterized by a C=N-NH bond, exhibit dual functionality as antioxidants and metal chelators [8, 9]. Our earlier work [11] demonstrated the potent antioxidant properties of syringic hydrazones through their scavenging effects on DPPH$^{\bullet}$ and ABTS$^{\bullet+}$ radicals, inhibition of superoxide anion generation, and reduction of TBARS formation during human cell-mediated LDL oxidation. Furthermore, these compounds effectively decreased protein carbonyl content in cells exposed to oxidized LDL, showcasing their carbonyl scavenger efficacy. However, their potential as metal chelators remained unexplored.

This study investigates the complexation behavior of two syringic hydrazones (E)-4-Hydroxy-3,5-dimethoxybenzaldehyde -1,3-benzothiazol-2-ylhydrazone **1** and (E)-4-Hydroxy-3,5-dimethoxybenzaldehyde phthalazin-1-ylhydrazone hydrochloride **2** with copper ions. Using UV spectrophotometry, we determined the stability constants and stoichiometries of the resulting complexes, providing insights into their therapeutic potential for oxidative stress-related diseases.

In our publication [11], we conducted a comprehensive physicochemical evaluation of syringic hydrazones, focusing on their antioxidant properties. The study revealed their potent scavenging effects on DPPH$^{\bullet}$ and ABTS$^{\bullet+}$ radicals, expressed as Trolox equivalent antioxidant capacity (TEAC). Additionally, these compounds inhibited superoxide anion ($O_2^{\bullet-}$) generation and reduced TBARS formation during human cell-mediated low-density lipoprotein (LDL) oxidation, highlighting their ability to protect against lipid peroxidation. Furthermore, their carbonyl scavenger efficacy was assessed by measuring the reduction of protein carbonyl content in cells challenged with oxidized LDL, demonstrating their protective role against protein oxidation. Despite these promising findings, the potential of syringic hydrazones as metal chelators was not explored, leaving a gap in understanding their full therapeutic potential.

This current study addresses this gap by investigating the complexation behavior of syringic hydrazones with copper ions, thereby expanding their application as dual-action agents capable of mitigating oxidative stress through both radical scavenging and metal sequestration.

RESULTS AND DISCUSSION

In this study, after synthesizing compounds **1** and **2**, we investigate the complexation behavior of two syringic hydrazones, designated as compounds **1** and **2**, with copper sulfate and copper chloride.

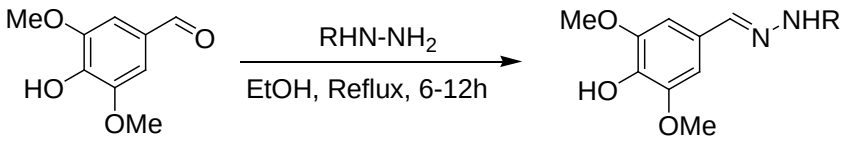

Cpd N°	R	Yield
1	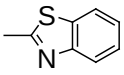	89%
2	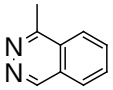	97%

Scheme 1. General synthesis of ligands **1** and **2**

Synthesis

The following **Table 1** present the spectroscopic analyses of compounds **1** and **2**, including RMN, IR, and UV techniques.

Table 1. Characterization of Compounds **1** and **2**

Compound	(E)-4-Hydroxy-3,5-dimethoxybenzaldehyde -1,3-benzothiazol-2-ylhydrazone (1)	(E)-4-Hydroxy-3,5-dimethoxybenzaldehyde phthalazin-1-ylhydrazone hydrochloride (2)
Yield (%)	97	75
Melting Point (°C)	219-221	154-156
IR Spectrum (KBr) v cm^{-1}	Peaks at 3543 (O-H); 3480 (N-H); 3185 (=C-H ethyl.); 3068 (C-H arom.); 2846 (C-H, O-CH_3); 1672 (C=N ethyl.); 1608 (C=C arom.); 1510 (C=C arom.), 1249 (O-C arom); 1219 (O-C), 1110 (O-C)	Peaks at 3415 (O-H); 1630 (C=N); 1619 (C=C); 1592 (C=C arom.); 1516 (C=C arom.); 1464 (C=C arom.); 1222 (C-O); 1122 (C-O)
^{1}H NMR (CD_3OD, 300 MHz)	3.97 (s, 6H, OCH_3); 6.94 (s, 2H, $H_{2,6}$);	3.84 (s, 6H, OCH_3); 7.38 (s, 2H, $H_{2,6}$); 8.15 (td, J = 8.2 Hz, J = 1.5, 1H, H_{11});

Compound	(E)-4-Hydroxy-3,5-dimethoxybenzaldehyde -1,3-benzothiazol-2-ylhydrazone (1)	(E)-4-Hydroxy-3,5-dimethoxybenzaldehyde phthalazin-1-ylhydrazone hydrochloride (2)
δ ppm	7.18 (t, 1H, J = 7.8 Hz, $H_{5'}$); 7.36 (t, 1H, J = 8.1 Hz, H_{11}); 7.56 (d, 1H, J = 8.1 Hz, H_{10}); 7.68 (d, 1H, J = 7.8 Hz, H_{13}); 7.90 (s, 1H, H_7).	8.21 (t, J = 8.2 Hz, 1H, H_{12}); 8.25 (d, J = 8.0 Hz, 1H, H_{13}); 8.98 (s, 1H, H_7); 9.04 (s, 1H, H_{15}); 9.23 (d, J = 7.6 Hz, 1H, H_{10})
UV Spectrum ((EtOH, 50 µM, 25°C)	λ = 342 nm, ε = 34,920 L mol^{-1} cm^{-1}	λ = 300 nm, ε = 13,220 L mol^{-1} cm^{-1}, λ = 372 nm, ε = 22,180 L mol^{-1} cm^{-1}

Complexation Studies by UV-Vis Spectrophotometry

The complexation behavior of syringic hydrazones **1** and **2** with copper(II) ions was investigated using UV-Vis spectrophotometric titrations. For each ligand, a solution in absolute ethanol (10^{-5} M) was titrated with incremental additions of an aqueous solution of the metal salt ($CuSO_4 \cdot 5H_2O$ or $CuCl_2 \cdot 2H_2O$, 10^{-3} M in deionized water). For compound **2**, which was isolated as a hydrochloride salt, the ethanolic medium was first neutralized by adding a few microliters of triethylamine (Et_3N) prior to titration. This ensured that complexation studies were performed under comparable, near-neutral pH conditions for both ligands.

The spectral evolution during the titration of **1** with both copper salts is shown in **Figure 1**. The addition of metal ions resulted in a significant bathochromic shift and changes in absorbance, indicating the formation of copper-ligand complexes. The presence of clear isosbestic points in the spectra (e.g., at ~370 nm and ~420 nm for **1** with $CuCl_2 \cdot 2H_2O$) confirms the existence of well-defined equilibria between distinct absorbing species.

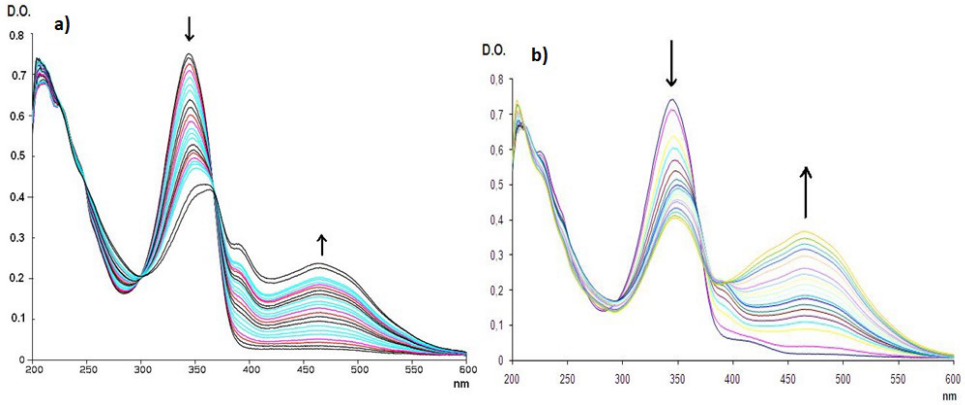

Figure 1. UV-Vis spectral changes during the titration of compound **1** (10^{-5} M in ethanol) with incremental additions of aqueous solutions of (a) $CuSO_4 \cdot 5H_2O$ and (b) $CuCl_2 \cdot 2H_2O$ (10^{-3} M in water). The arrows indicate the direction of spectral changes upon increasing metal concentration

Figure 2 displays the analogous spectral changes observed during the titration of compound **2** with $CuCl_2 \cdot 2H_2O$. A qualitatively similar, though less pronounced, variation in the absorbance spectra was observed upon complexation, suggesting the formation of weaker or fewer complexes compared to **1**.

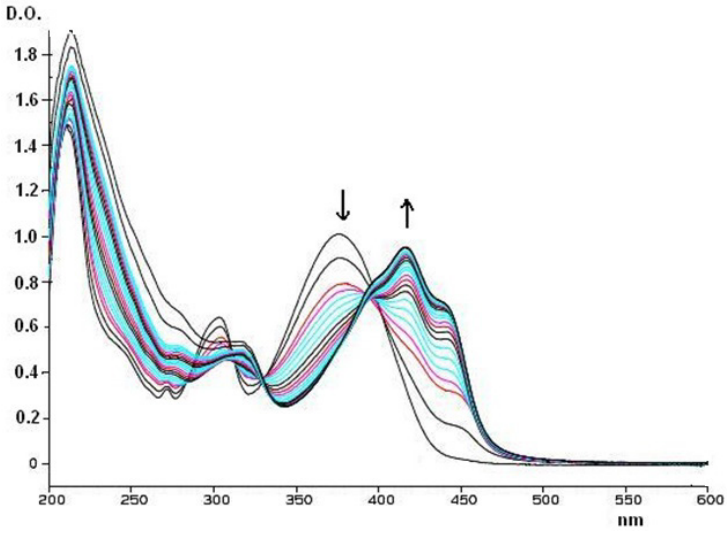

Figure 2. UV-Vis spectral changes during the titration of compound **2** (10^{-5} M in ethanol, neutralized with Et_3N) with incremental additions of an aqueous solution of $CuCl_2 \cdot 2H_2O$ (10^{-3} M in water)

Determination of Stability Constants

Stability constants and stoichiometries were determined using the STAR program [13], which performs global multi-wavelength fitting. Analysis was carried out over the wavelength ranges listed in Table 2. Various binding models (ML, ML_2, M_2L) were tested, and the best-fit model was selected based on minimal residual variance (S(A) < 0.005), satisfactory statistical parameters (χ^2 < 12.6, R(%) < 1%, kurtosis ≈ 3), and physical consistency.

The resulting formation constants are summarized in Table 2. Notably, **1** forms three complex types (ML, ML_2, M_2L) with significantly higher stability constants than **2**, especially when $CuCl_2 \cdot 2H_2O$ is used as the metal source. The exceptionally high value for the ML_2 species of **1** with $CuCl_2 \cdot 2H_2O$ (log β = 16.56 ± 0.01) indicates very strong chelation.

It should be noted that the reported stability constants are conditional values, valid under the specific experimental conditions (mixed ethanol–water medium, near-neutral pH after neutralization where applicable, and ambient temperature)

Table 2. Formation constants and statistical tests of complexes of **1** and **2** with $CuSO_4.5H_2O$ and $CuCl_2.2H_2O$

Compound	**1**	**1**	**2**	**2**
Metal source	$CuSO_4 \cdot 5H_2O$	$CuCl_2 \cdot 2H_2O$	$CuSO_4 \cdot 5H_2O$	$CuCl_2 \cdot 2H_2O$
λmax(nm)	340-487	330-540	370-455	395-450
Logβ ML	5.84±0.02	7.97±0.02	4.3±0.2	4.2±0.04
Logβ ML_2	10.76±0.08	16.56±0.01	-	8.4±0.1
Logβ M_2L	11.04±0.03	13.10±0.01	8.7±0.3	-
S(A) < 0.005	0.000577	0.0012	0.000991	0.000963
k2 < 12.6	7.4	11.3	8.96	6.9
R(%) < 1	0.46	0.85	0.64	0.34
Kurtosis ≈ 3	3.3	2.8	2.25	2.77

Complexation Behavior of Compound 1 vs. Compound 2

Compound **1** [(E)-4-Hydroxy-3,5-dimethoxybenzaldehyde -1,3-benzothiazol-2-ylhydrazone] exhibited markedly superior Cu^{2+}-binding ability compared to **2**, forming ML, ML_2, and M_2L species. This enhanced metal-chelating property may contribute to its observed antioxidant effects previously reported for **1** [11], as effective sequestration of redox-active copper reduces its participation in ROS-generating reactions.

By contrast, **2** formed fewer complexes and displayed lower stability constants, particularly with $CuSO_4 \cdot 5H_2O$. Interestingly, our earlier biological assays showed **2** to be more cytoprotective in certain in vitro models (TBARS and MTT) [11]. This apparent discrepancy may arise from structural differences: the benzothiazole moiety in **1** enhances electron donation and metal coordination, whereas the phthalazinyl group in **2** may favor alternative protective mechanisms, such as direct carbonyl scavenging or modulation of cellular pathways [12].

Interpretation of Stability Constants and Biological Implications

The stability constants (logβ) presented in Table 2 provide a quantitative measure of the affinity between the syringic hydrazones and copper ions. A higher logβ value indicates a more stable complex and a greater thermodynamic driving force for complex formation. The exceptionally high value for the **1**–$CuCl_2$ ML_2 complex (logβ = 16.56) signifies an extremely stable chelate, suggesting that compound **1** can effectively sequester Cu^{2+} ions even at low concentrations. In contrast, the significantly lower constants for compound **2** (e.g., logβ ML ≈ 4.2–4.3) reflect a weaker and more labile interaction. Qualitatively, this places the chelating strength of compound **1** on par with some known high-affinity copper chelators, while compound **2** functions as a much weaker binder. This distinction has direct implications for their potential biological activity: a chelator with relatively high affinity such as compound 1 has greater potential to sequester redox-active copper ions in a cellular environment, thereby inhibiting metal-catalyzed radical generation a key mechanism in mitigating oxidative stress-related damage.

Effect of Metal Source on Complexation Efficiency

The choice of copper salt significantly influenced complex stability. $CuCl_2 \cdot 2H_2O$ consistently yielded higher log β values than $CuSO_4 \cdot 5H_2O$, particularly for the ML_2 species of **1**. This may stem from chloride ions stabilizing specific coordination geometries or promoting mixed-ligand complexes [14,15]. The presence of two clear isosbestic points during titration with $CuCl_2 \cdot 2H_2O$ further supports stepwise, well-defined binding equilibria.

Implications for Antioxidant Activity

The dual role of syringic hydrazones as radical scavengers and metal chelators positions them as promising multifunctional agents against oxidative stress. They directly neutralize ROS (e.g., $O_2^{-\bullet}$, $ROO^{\bullet}$) while

simultaneously reducing metal-catalyzed hydroxyl radical formation [6,7]. The present physicochemical data complement our earlier findings [11] by providing a mechanistic basis for the contribution of copper chelation to overall antioxidant efficacy.

Structure-Activity Relationships

Spectroscopic and stability data highlight key structural features governing chelation. The hydroxyl and methoxy groups increase electron density at the binding site, while the planar benzothiazole ring in **1** likely facilitates favorable π-interactions [8,9]. In **2**, the bulkier phthalazinyl moiety may introduce steric hindrance, reducing metal accessibility. These insights underscore the value of targeted structural modification in future hydrazone design.

Clinical Relevance and Future Directions

The physicochemical insights gained from this study provide a foundation for future research into therapeutic strategies targeting oxidative stress-related diseases. Compounds with the ability to chelate transition metals, such as the syringic hydrazones studied here, represent an important class of molecules for further investigation in pathological contexts where metal ion dysregulation and ROS production are implicated, including atherosclerosis, neurodegenerative disorders, and cancer [5]. The dual functionality of syringic hydrazones, combining radical scavenging and metal chelation, makes them particularly interesting candidates for further structure-activity relationship studies and mechanistic exploration.

Future research should focus on evaluating the in vivo efficacy of these compounds in preclinical models of oxidative stress-related diseases. Investigations into their pharmacokinetic and pharmacodynamic profiles will provide critical insights into their suitability for clinical translation. Additionally, studies examining the synergistic effects of combining syringic hydrazones with existing antioxidant therapies may uncover new avenues for improving treatment outcomes [6].

In conclusion, this study provides a comprehensive analysis of the complexation behavior of syringic hydrazones with copper ions, highlighting their potential as therapeutic agents for combating oxidative stress. The superior metal-chelating ability of compound **1**, combined with its potent antioxidant properties, positions it as a lead candidate for further physicochemical and biological evaluation. Continued research in this area holds great promise for advancing our understanding of the role of metal ions in oxidative stress and developing innovative solutions to address this pressing health challenge.

CONCLUSIONS

This study demonstrates the ability of syringic hydrazones to form stable complexes with copper(II) ions. Compound **1** exhibited superior complexation, forming ML, ML_2, and M_2L species with higher stability constants than compound **2**, particularly when using $CuCl_2 \cdot 2H_2O$. These findings provide a physicochemical basis for understanding the metal-chelating capacity of these compounds, complementing their previously established radical-scavenging antioxidant activity.

The results highlight the dual functionality of syringic hydrazones and underscore the importance of structural features—such as the benzothiazole moiety in **1** in determining metal-binding affinity. Future work should focus on elucidating the molecular mechanisms underlying these differences and evaluating the efficacy of these chelators in biological models of oxidative stress.

EXPERIMENTAL SECTION

Synthesis of Compounds 1 and 2

Compounds **1** and **2** were synthesized according to the procedures outlined in **Scheme 1**. Commercially available syringaldehyde was refluxed in absolute ethanol with different hydrazines for 6-12 hours. The reaction was monitored by thin-layer chromatography (TLC) until completion. The solution was then cooled to room temperature, and the resulting precipitate was collected by filtration to provide the corresponding hydrazones as hydrochloride salts or non-salt forms, depending on the nature of the commercially available hydrazines [11].

The synthesis and full spectroscopic characterization (including ^{1}H NMR, ^{13}C NMR, IR, UV-Vis, and elemental analysis) of compounds **1** and **2** have been reported previously [11]. The ^{1}H and ^{13}C NMR spectra for both compounds are provided in the Supplementary Material.

Complexation

Compounds **1** and **2**, previously synthesized and fully characterized [11], were used without further purification and were of sufficient purity (>95% as assessed by NMR) for the spectrophotometric complexation studies

UV spectrophotometry was employed to study the complexation of **1** and **2** with Cu^{2+}. Solutions of the ligands (10^{-5} M) were prepared in ethanol,

and incremental volumes of $CuSO_4 \cdot 5H_2O$ or $CuCl_2 \cdot 2H_2O$ (10^{-3} M) were added. Spectra were recorded over the range of 200-600 nm after each addition. The presence of isobestic points confirmed the formation of specific equilibria between the ligand and metal complexes.

The stability constants were calculated using the STAR program [13], which evaluates the best fit between experimental and calculated spectra. Statistical tests were applied to validate the models:

- S(A): Must be < 0.005.
- R (%): Must be < 1%.
- Kurtosis: Should be around 3.
- χ^2 (Chi-Square): Must be < 12.6.

ACKNOWLEDGMENTS

We thank Ms. Chantal Carayon from the Laboratoire de Synthèse et Physico-Chimie de Molécules d'Intérêt Biologique (Toulouse) for her valuable contribution to the spectroscopic analysis and the study of copper complex formation.

REFERENCES

1. R. Shao; H. Chen; Q. Zheng; M. Yao; K. Li; Y. Cao; L. Jiang, Cell Biol. Int. **2024**, 48, 1781.
2. E. Niki, Dual Stressor Effects of Lipid Oxidation and Antioxidants, Academic Press, Cambridge, USA, **2020**, p 249.
3. Yu. S. Voronkova; O. S. Voronkova; V. A. Gorban; K. K. Holoborodko, J. Serb. Chem. Soc. **2018**, 29, 52.
4. M. A. Rajizadeh; R. Pourbabaki, Oxidative stress and exposure to metals. In Biochemical and Physiological Response During Oxidative Stress – From Invertebrates to Humans, IntechOpen, **2024**.
5. J. Zhang; C. Nie; J. Wang; L. Yang; X. Du; L. Liu; Y. Chen; Q. Yang; X. Zhu; Q. Li, Biomed. Pharmacother. **2024**, 177, 117112.
6. K. H. Lee; U. J. Kim; B. H. Lee; M. Cha, Free Radical Biol. Med. **2025**, 226, 143.
7. S. Bhattacharya, Antioxidants **2024**, 587, 612.
8. V. Kamat; K. D. Venuprasad; A. J. Shadakshari; R. S. Bhat; A. D'souza; S. Chapi; A. Kumar; P. V. Kuthe; M. Sankaranarayanan; K. N. Venugopala, J. Mol. Struct. **2024**, 1312, 138634.
9. C. Topkaya, Maced. J. Chem. Chem. Eng. **2024**, 43, 127.

10. H. M. Abd El-Lateef; T. El-Dabea; M. M. Khalaf; A. M. Abu-Dief, Antioxidants **2023**, 12, 213.
11. N. Belkheiri; B. Bouguerne; F. Bedos-Belval; H. Duran; C. Bernis; R. Salvayre; A. Nègre-Salvayre; M. Baltas, Eur. J. Med. Chem. **2010**, 45, 3019.
12. B. Halliwell; J. M. C. Gutteridge, Free Radicals in Biology and Medicine, 5th ed.; Oxford University Press: New York, USA, **2015**.
13. A. E. Martell; R. M. Smith, Critical Stability Constants; Plenum Press: New York, USA, **1974**.
14. I. Bertini; H. B. Gray; E. I. Stiefel; J. S. Valentine, Bioinorganic Chemistry; University Science Books: Sausalito, California, USA, **1994**.
15. J. L. Beltrán; R. Codony; M. D. Prat, Anal. Chim. Acta **1993**, 276, 441.

STUDIA UBB CHEMIA, LXXI, 1, 2026 (p. 43-56)
(RECOMMENDED CITATION)
DOI:10.24193/subbchem.2026.1.04

ENHANCING THE OPERATIONAL STABILITY OF RECOMBINANT PHENYLALANINE AMMONIA-LYASE IMMOBILIZED ON MAGNETIC NANOPARTICLES BY POST-ENTRAPMENT

Bálint ALÁCS[a], Anna ZRINYI[a], Evelin BELL[a,*]

ABSTRACT. Recombinant *Petroselinum crispum* phenylalanine ammonia-lyase (*Pc*PAL) was selectively immobilized on magnetic nanoparticles by metal affinity binding (IMAC) to create a well applicable biocatalyst. To overcome the stability limitations of coordination bond, two post-immobilization entrapment strategies were investigated: macroscopic entrapment in calcium-alginate hydrogel beads and also in sol–gel matrix. The catalytic efficiency and operational stability of the composite biocatalysts were evaluated in the ammonia elimination reaction of L-phenylalanine. The concentration of immobilized biocatalyst was optimized in the calcium-alginate stabilization. In the sol–gel shell formation the amount of tetraethyl ortosilicate (TEOS) and the combination with a less crosslinking capability dimethyldiethoxysilane (DMDEOS) was investigated. In the latter case the TEOS was used in 4 different ratios in the silane precursor mixture. While the best calcium-alginate beads (5 m/m% loading) provided a biocompatible environment, they suffered from mechanical instability and physical disintegration occur after four reaction cycles. In contrast, the optimized silica-coated nanobiocatalyst exhibited superior mechanical and chemical stability, preventing enzyme leaching and retaining over 80% of its initial activity after seven consecutive reaction cycles. These results demonstrate that individual particle encapsulation via a silica shell offers a more robust solution for the design of reusable magnetic biocatalysts than macroscopic hydrogel entrapment.

Keywords: *immobilized metal ion affinity chromatography, enzyme immobilization, sol-gel, alginate*

[a] *Department of Organic Chemistry and Technology, Faculty of Chemical Technology and Biotechnology, Budapest University of Technology and Economics, Műegyetem rkp. 3., H-1111 Budapest, Hungary*

* *Corresponding author: bell.evelin@vbk.bme.hu*

INTRODUCTION

Biocatalysis has been getting a growing focus in sustainable industrial chemistry, offering highly stereo- and regioselective routes to valuable compounds under mild reaction conditions [1–3]. Enzymes, such as phenylalanine ammonia-lyase (PAL), are widely used in the synthesis of pharmaceutical intermediates and amino acids [4]. However, the industrial application of soluble enzymes is often hampered by their high production costs, low stability under process conditions, and the difficulty of their recovery [5]. Enzyme immobilization provides a robust solution to these challenges, enabling facile separation, catalyst recycling, and often improved thermal and operational stability [6].

Among the various support materials, magnetic nanoparticles (MNPs) have gained significant attention due to their high specific surface area and the ease of separation using an external magnetic field, which eliminates the need for filtration or centrifugation [7,8]. Due to their advantageous applicability, they are also used in combined enzyme immobilization processes, such as in the formation of magnetic nanoparticle supported cross-linked enzyme aggregates [9]. For the immobilization of recombinant enzymes, Immobilized Metal Affinity Chromatography (IMAC) offers a unique advantage: It allows for the selective binding of histidine-tagged (His-tagged) proteins directly from crude cell lysates [10]. This “one-pot” purification and immobilization strategy significantly reduces the time and cost of biocatalyst preparation compared to traditional methods that require prior enzyme purification [11].

Despite its efficiency, traditional IMAC-based immobilization has limitations. The metal-coordination bond can be susceptible to ligand exchange or metal ion leaching during operation, leading to enzyme detachment and product contamination [12]. Furthermore, enzymes bound solely to the surface of nanoparticles remain exposed to shear forces and harsh solvent environments. To address these issues, post-immobilization stabilization strategies are required to shield the biocatalyst while maintaining the benefits of the magnetic support [13].

In this study, we present the development of robust magnetic nanoparticles-based biocatalysts using recombinant *Petroselinum crispum* phenylalanine ammonia-lyase [14] (*Pc*PAL) selectively immobilized via metal affinity binding. To overcome the stability limitations of simple surface binding, we investigated and compared two distinct entrapment strategies. The first approach involved the macroscopic entrapment of the enzyme-loaded nanoparticles into calcium-alginate beads to create a biocompatible diffusion barrier. In parallel, we examined microscopic encapsulation by forming a porous silica shell directly around the enzyme-coated nanoparticles, resulting in individual

core-shell nanostructures (Figure 1.). We examined the morphological properties of the resulting composites and evaluated their catalytic efficiency, kinetic parameters, and reusability in the ammonia elimination reaction of L-phenylalanine, resulting *(E)*-cinnamic acid [15]. Our results provide insights into the trade-offs between mass transfer limitations and structural stability in the design of magnetically separable biocatalysts.

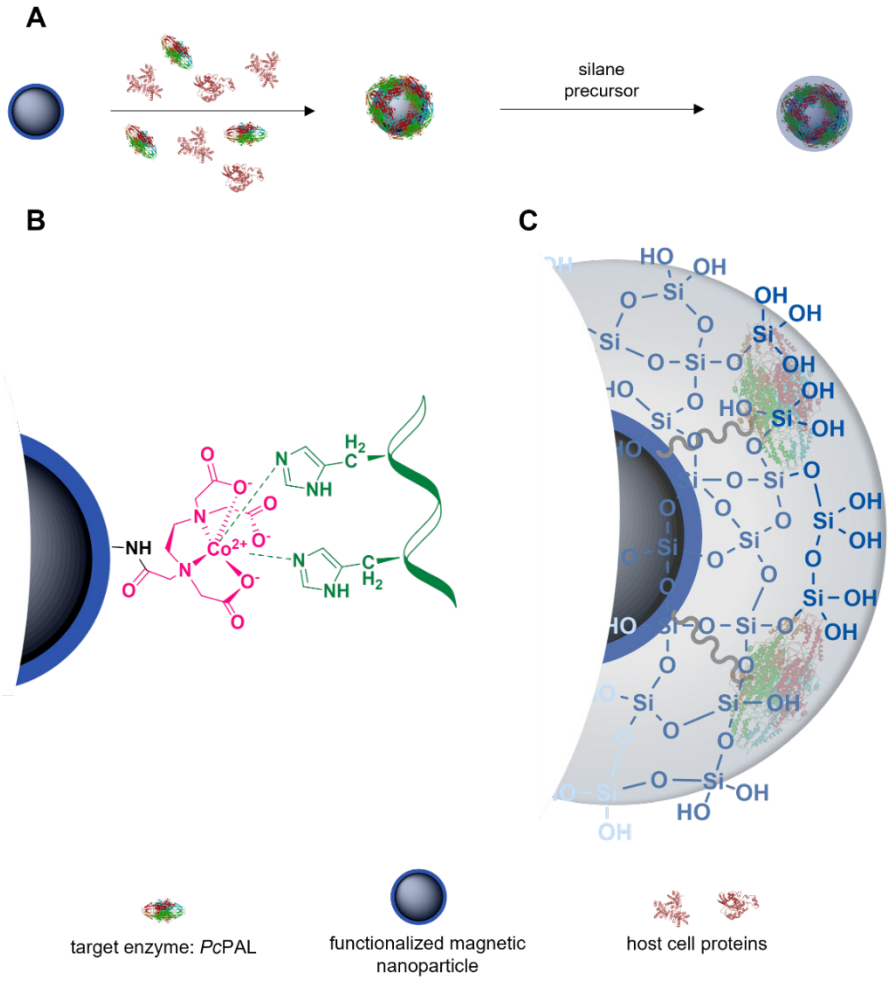

Figure 1. A: Scheme of selective enzyme immobilization and the entrapment of the biocatalyst in sol-gel matrix. **B:** Structure of the surface metal complex binding the histidine tagged protein. **C**: Silica sol-gel matrix entrapment of the *Pc*PAL complexed on the surface of the magnetic nanoparticles.

RESULTS AND DISCUSSION

The model enzyme, *Pc*PAL with histidine tag was immobilized from the cell lysate on high-capacity magnetic nanoparticles surface-modified with EDTA dianhydride and subsequently complexed with cobalt ions. The magnetic nanoparticles were used at maximum enzyme loading. The immobilization process was monitored in all cases by UV–Vis spectrophotometry, and the enzymatic activity of the supernatant was analyzed before and after the enzyme complexation.

The macroscopic entrapment was investigated by encapsulating the enzyme-loaded magnetic nanoparticles into calcium-alginate beads. Four different biocatalyst loading were tested: 0.5, 1, 5 10 m/m% (AG1–4). Uniform spherical beads were obtained as shown in Figure 2.

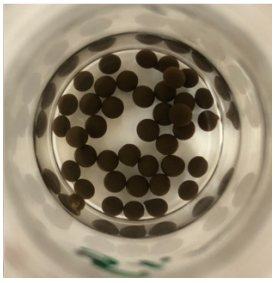

Figure 2. Photograph of the calcium-alginate beads containing entrapped magnetic nanoparticle biocatalysts.

The specific biocatalytic activity of the beads was evaluated in the ammonia elimination reaction (Figure 3.). Since the significant mass contribution of the hydrogel matrix naturally lowers the specific biocatalytic activity [U_B], the conversions of the 30 min reactions were considered for better comparison.

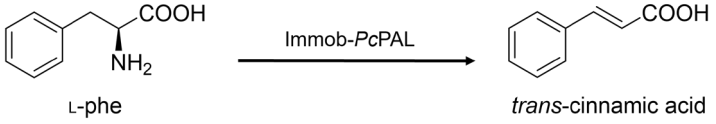

Figure 3. Biocatalytic reaction of immobilized *Pc*PAL.

The composite AG3 containing 5 m/m% *Pc*PAL complexed nanoparticles proved to be the optimal compromise. Increasing the particle loading to 10% (AG4) no longer improved the activity of the biocatalyst, suggesting that the alginate matrix limited the substrate and product diffusions or the more crowded distribution of the particles limited the enzyme conformational changes needed

to the catalytic activity (Table 1.). To verify the stabilizing effect of the alginate matrix, the beads were washed with 500 mM imidazole, which typically used for protein elution from IMAC resins. The specific biocatalytic activity of the imidazole fractions were tested in the ammonia elimination reaction also and detectable cinnamic acid formation was observed only in case of the non-stabilized biocatalysts confirming that the alginate matrix successfully entrapped the enzyme and prevented its leaching even if the His-tag–metal ion complex was disrupted.

Table 1. Specific biocatalytic activity and enzyme activity of the alginate-entrapped preparations at different loadings (AG1–AG4 represents 0,5; 1; 5; 10 m/m %). All the reactions were performed in triplicates, and the standard deviations were under 5%.

	U_B [U g^{-1}]	c [%]
MNP	76.50	23.0
AG1	0.09	2.2
AG2	0.15	3.6
AG3	**0.46**	10.3
AG4	0.48	13.1

Consequently, both entrapment strategies successfully stabilized the *Pc*PAL on the magnetic nanoparticle carrier. The core–shell silica method offering higher specific activity, while the alginate beads provided a macroscopically easier-to-handle formulation.

The sol–gel network formation was then carried out in an aqueous–alcoholic system, using tetraethyl orthosilicate (TEOS) as silane precursor. The effect of the amount of TEOS on catalytic activity was investigated first (27, 54, 107, and 215 µmol TEOS for 1 g magnetic nanoparticle; labeled as SG1-4). The matrix formation occurred overnight at room temperature. During the washing steps following network formation, it became apparent that increasing the TEOS content resulted in progressively more difficult magnetic separation of the catalyst. In addition, silica nanoparticles were formed that no longer contained embedded magnetic particles bearing the immobilized enzyme.

The biocatalytic activity of the stabilized biocatalyst was tested in the same ammonia elimination reaction as previously. The biocatalyst was measured as a suspension into the test reactions, and the exact catalyst

mass was determined retrospectively. The catalytic activity of the silica-coated nanoparticles showed a strong dependence on the precursor concentration, as illustrated in Figure 4.

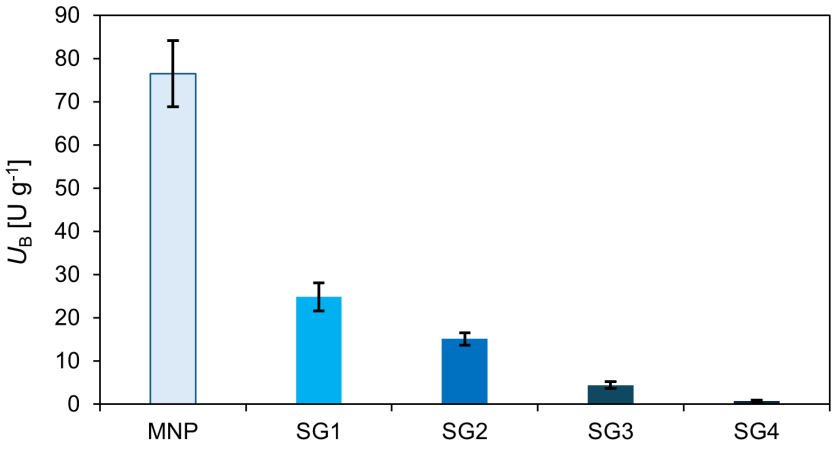

Figure 4. Effect of the silane precursor (TEOS) amount on the specific biocatalytic activity (U_B) of the silica-coated magnetic nanoparticles. (SG1–4 represent increasing TEOS loadings: 27, 54, 107, and 215 µmol TEOS for 1 g magnetic nanoparticle; MNP serves as the non-stabilized control). The measurements were performed in three replicates.

As expected, the formation of a thicker silica shell at higher TEOS loadings (SG3 and SG4) resulted in a dramatic decrease in specific biocatalytic activity, likely due to severe mass transfer limitations that hindered substrate diffusion to the active sites. The sample prepared with the lowest amount of silane (SG1) retained the highest activity; however, even this was significantly lower than that of the non-stabilized reference (MNP). Furthermore, drying the preparations under vacuum caused a substantial loss of activity, indicating the sensitivity of the enzyme to dehydration; therefore, all subsequent samples were stored in buffer suspension.

To improve the catalytic efficiency and alleviate diffusion barriers, the sol–gel matrix was modified by partially substituting TEOS with dimethyldiethoxysilane (DMDEOS). Since DMDEOS contains only two hydrolysable ethoxy groups (Figure 5.), it acts as silica network modifier, creating a less dense matrix.

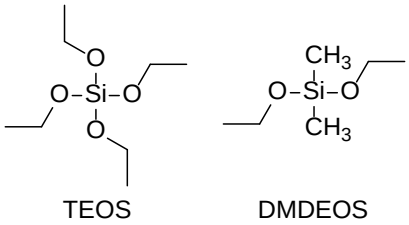

Figure 5. Chemical structures of the silane precursors used for the sol–gel coating: tetraethyl orthosilicate (TEOS) and dimethyldiethoxysilane (DMDEOS).

Optimization studies using the magnetic nanoparticles were performed by varying the TEOS concentration for the SG1 and SG2 precursor quantities. The quantitative results of this optimization are visualized in Figure 6.

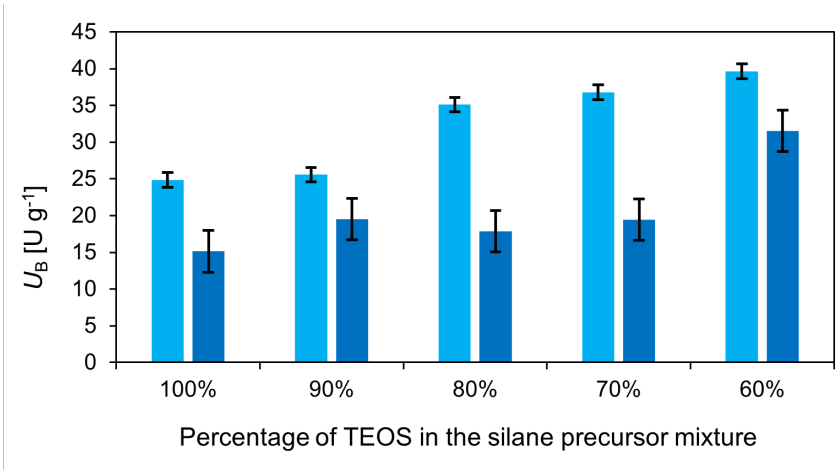

Figure 6. Influence of the TEOS concentration in the silane precursor mixture on the specific biocatalytic activity (■ 27; ■ 54 µmol silane precursor for 1 g magnetic nanoparticle). The measurements were performed in three replicates.

Our results revealed that increasing the DMDEOS ratio up to 40% the specific biocatalytic activity is enhanced. No significant difference was observed between the SG1 samples containing 80, 70 and 60% TEOS. Therefore, the further decrease of TEOS was not investigated. The optimized formulation (60% TEOS – 40% DMDEOS) achieved a specific biocatalytic activity of 39.6 U g^{-1}. Like the samples stabilized with alginate, the sol-gel matrix provided protection against leaching too; the enzymatic activity in the imidazole washing fractions of sol-gel stabilized MNP biocatalysts were not detectable compared to the free particles.

To assess the operational stability and industrial viability of biocatalysts, reusability studies were conducted using optimized preparations: the silica-coated composite (SG1-60 formulation) and the optimized alginate beads (5 m/m%, AG3). The non-stabilized, enzyme complexed MNP served as the control.

The biocatalysts were subjected to seven consecutive reaction cycles. Between cycles, the biocatalysts were magnetically separated and washed three times with buffer without drying. The operational stability results are presented in Figure 7.

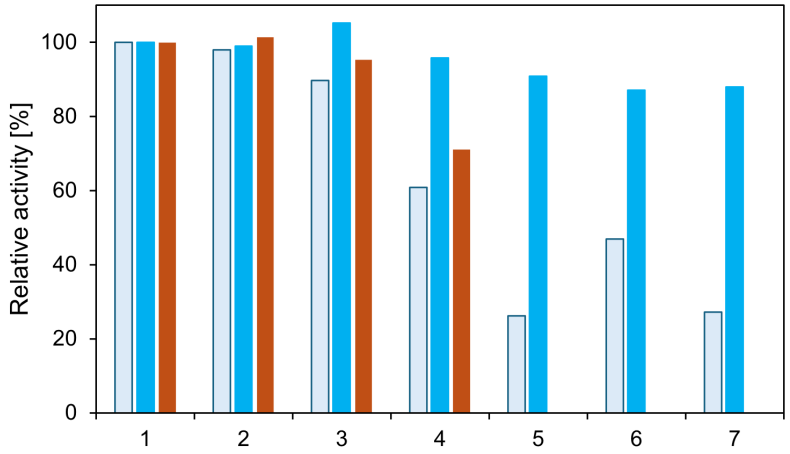

Figure 7. Reusability of the optimized stabilized biocatalysts (■ SG1-60; ■ AG3) compared to the non-stabilized reference (□ MNP) over seven consecutive reaction cycles.

A clear difference in mechanical and operational stability was observed between the carriers. The non-stabilized reference became increasingly difficult to handle after the first few cycles; significant catalyst mass loss was observed during the washing steps, which, combined with enzyme leaching, resulted in a rapid activity decrease, dropping to below 30% by the seventh cycle.

The alginate-entrapped biocatalyst initially performed well but suffered from physical-mechanical instability. As shown in Figure 5, the data series for the alginate beads ends after the fourth cycle. This is because the hydrogel beads began to disintegrate under the mechanical stress of the reaction stirring, making magnetic separation impossible and leading to the termination of the series.

In contrast, the silica-coated biocatalyst (SG1-60) showed high stability and resistance. The particles remained easily separable and chemically stable throughout the experiment. Most notably, the silica-stabilized catalyst retained

more than 80% of its initial activity even after the seventh cycle. This confirms that the porous silica shell not only prevents enzyme leaching, as proved by the imidazole wash tests, but also protects the enzyme from mechanical shear forces.

CONCLUSIONS

In this study, we successfully developed robust magnetic biocatalysts containing recombinant *Petroselinum crispum* phenylalanine ammonia-lyase (*Pc*PAL) to overcome the stability limitations of traditional metal affinity immobilization. We investigated and compared two post-immobilization entrapment strategies: microscopic encapsulation via a sol–gel silica shell and macroscopic entrapment in calcium-alginate hydrogel beads.

Our results demonstrated that the diffusion properties of the silica shell could be significantly improved by the addition of DMDEOS to the silane precursor mixture. The optimized shell formulation (60% TEOS – 40% DMDEOS) successfully balanced the transfer efficiency of small molecules with the enzyme protection, achieving a specific biocatalytic activity of 39.6 U g^{-1}. In case of the alginate entrapment the optimal 5 m/m% biocatalyst loading offered a facile method for creating larger, easy to use biocatalyst beads, but due to the high mass of alginate matrix a lower biocatalytic activity was earned.

The most significant difference between the two stabilized biocatalysts was observed in their operational stability. The alginate beads proved physically unstable under reaction conditions, disintegrating after four reuse cycles. However, the silica-coated nanobiocatalyst exhibited superior mechanical robustness and chemical stability. It completely prevented enzyme leaching and retained more than 80% of its initial catalytic activity even after seven consecutive reaction cycles. Therefore, the formation of a silica shell around the IMAC-immobilized enzyme represents a more effective strategy for the design of industrially viable, reusable magnetic biocatalysts compared to macroscopic hydrogel entrapment.

EXPERIMENTAL SECTION

Materials

Solvents and reagents were purchased from Sigma-Aldrich, Fluka, Merck, Alfa Aesar, Reanal, and Molar Chemicals. Chemicals used for protein analysis were products of Bio-Rad and Thermo Scientific.

The fermentation of the recombinant *Pc*PAL enzyme

Production of *Pc*PAL was achieved in *E. coli* Rosetta containing the recombinant pET19b plasmid with the gene of *Pc*PAL and 10 Histidine. LB-CarCA medium (5 mL; LB medium containing carbenicillin [50 mg L^{-1}], and chloramphenicol [30 mg L^{-1}]) was inoculated with one fresh colony from an overnight LB-CarCA agar plate and cells were grown overnight in shake flask (37 °C, at 200 rpm). Autoinduction medium (0.5 L: Na_2HPO_4, 6 g L^{-1}; KH_2PO_4, 3 g L^{-1}; tryptone, 20 g L^{-1}; yeast extract, 5 g L^{-1}; NaCl, 5 g L^{-1}; glycerol, 7.56 g L^{-1}; glucose, 0.5 g L^{-1}; lactose, 2 g L^{-1}) in a 2 L flask was inoculated with seed culture (2 mL) and was shaken for 16 h at 25 °C, 200 rpm. The cells were harvested by centrifugation (16,000 × g, 4 °C, 20 min), then suspended with 40 mL protease inhibitor containing lysis buffer (50 mM tris(hydroxymethyl)aminomethane, 150 mM NaCl, 0.5 mM EDTA, 2 mM phenylmethylsulfonyl fluoride, 1 mM tris(2-carboxyethyl)phosphine, 1 mM benzamidine). The cell disruption was done using ultrasound, then the media were centrifugated (20,000 × g, 4 °C, 20 min) resulting in the final cell lysate containing recombinant *Pc*PAL. To determine the target enzyme concentration as 1 mg mL^{-1} in the protein mixture a small sample of the cell lysate was purified with Ni Sepharose 6 Fast Flow (Merck GmbH) according to the description provided by the manufacturer.

Synthesis of Magnetic Nanoparticles (MNPs)

Magnetic nanoparticles were synthesized via a solvothermal method. Iron(III) chloride hexahydrate (3.36 g, 12.4 mmol) was dissolved in ethylene glycol (150 mL) via sonication. Subsequently, polyethylene glycol 4000 (12.0 g) and sodium acetate trihydrate (9.0 g, 66.4 mmol) were added to the solution. The mixture was sonicated until complete dissolution, then transferred to a stainless-steel autoclave and heated at 200 °C for 24 h. The resulting black suspension was magnetically separated using a neodymium magnet and the precipitate was washed thoroughly 3 times with distilled water (100 mL) and 3 times with 2-propanol (50 mL). The particles were dried in a fume hood until constant weight.

Preparation of Amine-Functionalized Nanoparticles

The dried magnetic nanoparticles (1500 mg) were dispersed in ethanol (15 mL) containing polyethylene glycol 400 (750 mg) by ultrasonication for 10 min. Ammonium hydroxide solution (35%, 135 µL) was added, and the suspension was shaken for 10 min. Subsequently, 3-(2-aminoethylamino)propyl-methyldimethoxysilane (320 µL, 1.5 mmol) was

added, and the reaction mixture was shaken at room temperature for 24 h. The functionalized particles were washed three times with 2-propanol (10 mL), magnetically separated, and dried in a vacuum chamber at room temperature for 2 hours.

Preparation of the Chelate-type Support

The amine-functionalized particles (200 mg) were dispersed in dimethylformamide (DMF, 7 mL) containing polyethylene glycol 400 (100 mg) via ultrasonication. EDTA-dianhydride (45.6 mg, 178 µmol) and *N*-ethyl-*N,N*-diisopropylamine (30 µL) were added to the suspension. The mixture was shaken at 60 °C for 24 h (600 rpm). Then, distilled water (200 µL) was added, and shaking continued for another 1 h at 60 °C. The particles were washed with acetonitrile (2 × 5 mL), 2-propanol (1 × 5 mL), and distilled water (1 × 5 mL). Finally, the particles were suspended in cobalt(II) chloride solution (5 mL, 50 mM) and were shaken for 30 min at room temperature, washed with distilled water (3 × 5 mL), 2-propanol (1 × 5 mL), and dried in a vacuum chamber at room temperature for 2 hours.

Enzyme Immobilization via IMAC

The cobalt-charged magnetic support (50 mg) was suspended in lysis buffer (5 mL; 50 mM Tris, 150 mM NaCl, pH 7.5) and mixed with the cell lysate (5 mL) containing the His-tagged *Pc*PAL enzyme. The suspension was shaken for 30 min at room temperature. The immobilization progress was monitored by measuring the activity of the supernatant; fresh lysate was added until saturation was reached. The immobilized biocatalyst was magnetically separated and washed sequentially with LS buffer (50 mM HEPES, 30 mM KCl, pH 7.5), HS buffer (50 mM HEPES, 300 mM KCl, pH 7.5), and Tris buffer (50 mM, pH 7.5).

Sol–Gel Silica Coating of the Biocatalyst

The immobilized biocatalyst suspension (1600 µL containing 10 mg particles) was mixed with polyethylene glycol 1000 solution (400 µL, 5 m/m% in 50 mM Tris buffer, pH 7.5). To this mixture, 2-propanol (250 µL) and the appropriate amount of silane precursors (see at Table 2 and 3.) were added. Polycondensation was initiated by adding NaF catalyst (20 µL, 1 M). After shaking for 24 h at room temperature, the silica-coated particles were magnetically separated and washed twice with 25% 2-propanol in Tris buffer, then stored in Tris buffer (50 mM, pH 7.5).

Table 2. Amount of TEOS during the silica shell optimization.

	SG1	**SG2**	**SG3**	**SG4**
TEOS [µL]	60	120	240	480

Table 3. Amounts of TEOS and DMDEOS during the second silica shell optimization.

			TEOS ratio [%]			
			90	**80**	**70**	**60**
SG1	**TEOS**	[µL]	54	48	42	36
	DMDEOS	[µL]	4.6	9.2	13.8	18.4
SG2	**TEOS**	[µL]	108	96	84	72
	DMDEOS	[µL]	9.2	18.4	27.6	36.9

Entrapment in Alginate Beads

The immobilized biocatalyst suspension (corresponding to 0.5–10 m/m% loading) was mixed with sodium alginate solution (1 g, 30 mg mL^{-1} in water) and 1000 µL Tris buffer (100 mM, pH 7.5). The mixture was homogenized by vortex and added dropwise into a 2% $CaCl_2$ solution using a syringe with a blunt-end needle. The resulting magnetic beads were separated, washed three times with Tris buffer (10 mL, 50 mM, pH 7.5), and stored at 4 °C.

Activity Measurements

The biocatalytic activity was determined in the ammonia elimination reaction of L-phenylalanine. The biocatalyst (2.5–5 mg) was added to L-phenylalanine solution (1 mL, 10 mM in 100 mM Tris buffer, pH 8.8) and shaken at 30 °C (600 rpm). Samples (20 µL) were taken after 30, 60 and 120 minutes, diluted with distilled water (280 µL), and the absorbance of the produced *trans*-cinnamic acid was measured at 290 nm using a microplate reader [Thermo Scientific Multiscan SkyHigh microplate reader, (Thermo Fisher Scientific Inc., Waltham, MA, USA)].

Characterization of the productivity and immobilization yield

To characterize the productivity of the different biocatalysts, the specific biocatalytic activity was calculated using the equation

$$U_B = n_P/(t \times m_B) \quad (1)$$

where n_P [μmol] is the amount of the product, t [min] is the reaction time and m_B [g] is the mass of the applied biocatalyst. To determine the ratio of immobilized target enzyme the activity of the crude cell lysate was measured before and after the immobilization process as well as the imidazole elution fractions during the washing steps.

ACKNOWLEDGMENTS

Balint Alacs acknowledges the support of Gedeon Richter Talentum Foundation.

REFERENCES

1. J. M. Guisan; F. López-Gallego; L. Betancor; C. Mateo; V. Grazu; G. Fernandez-Lorente; J. Rocha-Martin; J. M. Bolivar; K. Ovsejevi; C. Manta; et al. *Immobilization of Enzymes and Cells*; Guisan, J.M., Ed.; Methods in Molecular Biology; Humana Press: Totowa, NJ, **2013**; Vol. 1051; ISBN 978-1-62703-549-1.
2. Sheldon, R.A. Fundamentals of Green Chemistry: Efficiency in Reaction Design. *Chem. Soc. Rev*. **2012**, *41*, 1437–1451, doi:10.1039/C1CS15219J.
3. Bornscheuer, U.T.; Huisman, G.W.; Kazlauskas, R.J.; Lutz, S.; Moore, J.C.; Robins, K. Engineering the Third Wave of Biocatalysis. *Nature*, **2012**, *485*, 185–194, doi:10.1038/nature11117.
4. Cui, J.D.; Qiu, J.Q.; Fan, X.W.; Jia, S.R.; Tan, Z.L. Biotechnological Production and Applications of Microbial Phenylalanine Ammonia Lyase: A Recent Review. *Crit. Rev. Biotechnol.* **2014**, *34*, 258–268, doi:10.3109/07388551.2013.791660.
5. Datta, S.; Christena, L.R.; Rajaram, Y.R.S. Enzyme Immobilization: An Overview on Techniques and Support Materials. *3 Biotech*, **2013**, *3*, 1–9, doi:10.1007/s13205-012-0071-7.
6. Mateo, C.; Palomo, J.M.; Fernandez-Lorente, G.; Guisan, J.M.; Fernandez-Lafuente, R. Improvement of Enzyme Activity, Stability and Selectivity via Immobilization Techniques. *Enzyme Microb. Technol.,* **2007**, *40*, 1451–1463, doi:10.1016/j.enzmictec.2007.01.018.
7. Gupta, A.K.; Gupta, M. Synthesis and Surface Engineering of Iron Oxide Nanoparticles for Biomedical Applications. *Biomaterials*, **2005**, *26*, 3995–4021, doi:10.1016/j.biomaterials.2004.10.012.
8. Lu, A.-H.; Salabas, E.L.; Schüth, F. Magnetic Nanoparticles: Synthesis, Protection, Functionalization, and Application. *Angewandte Chemie International Edition,* **2007**, *46*, 1222–1244, doi:10.1002/anie.200602866.

9. Lucena, G.N.; Santos, C.C. dos; Pinto, G.C.; Piazza, R.D.; Guedes, W.N.; Jafelicci Júnior, M.; de Paula, A. V.; Marques, R.F.C. Synthesis and Characterization of Magnetic Cross-Linked Enzyme Aggregate and Its Evaluation of the Alternating Magnetic Field (AMF) Effects in the Catalytic Activity. *J. Magn. Magn. Mater.,* **2020**, *516*, 167326, doi:10.1016/j.jmmm.2020.167326.
10. Porath, J.; Carlsson, J.; Olsson, I.; Belfrage, G. Metal Chelate Affinity Chromatography, a New Approach to Protein Fractionation. *Nature*, **1975**, *258*, 598–599, doi:10.1038/258598a0.
11. Sánta-Bell; Molnár; Varga; Nagy; Hornyánszky; Paizs; Balogh-Weiser; Poppe "Fishing and Hunting"—Selective Immobilization of a Recombinant Phenylalanine Ammonia-Lyase from Fermentation Media. *Molecules*, **2019**, *24*, 4146, doi:10.3390/molecules24224146.
12. Cassimjee, K.E.; Kourist, R.; Lindberg, D.; Wittrup Larsen, M.; Thanh, N.H.; Widersten, M.; Bornscheuer, U.T.; Berglund, P. One-step Enzyme Extraction and Immobilization for Biocatalysis Applications. *Biotechnol. J.,* **2011**, *6*, 463–469, doi:10.1002/biot.201000357.
13. Weiser, D.; Nagy, F.; Bánóczi, G.; Oláh, M.; Farkas, A.; Szilágyi, A.; László, K.; Gellért, Á.; Marosi, G.; Kemény, S.; et al. Immobilization Engineering – How to Design Advanced Sol–Gel Systems for Biocatalysis? *Green Chemistry,* **2017**, *19*, 3927–3937, doi:10.1039/C7GC00896A.
14. Appert, C.; Logemann, E.; Hahlbrock, K.; Schmid, J.; Amrhein, N. Structural and Catalytic Properties of the Four Phenylalanine Ammonia-Lyase Isoenzymes from Parsley (Petroselinum Crispum Nym.). *Eur. J. Biochem.*, **1994**, *225*, 491–499, doi:10.1111/j.1432-1033.1994.00491.x.
15. Poppe, L.; Rétey, J. Friedel–Crafts-Type Mechanism for the Enzymatic Elimination of Ammonia from Histidine and Phenylalanine. *Angewandte Chemie International Edition,* **2005**, *44*, 3668–3688, doi:10.1002/anie.200461377.

STUDIA UBB CHEMIA, LXXI, 1, 2026 (p. 57-75)
(RECOMMENDED CITATION)
DOI:10.24193/subbchem.2026.1.05

CFD PARTICLE MODEL AND OPTIMIZATION OF THE REACTION OF SULFIDIC PELLETS WITH HYDROGEN

Vlad-Cristian SANDU[a], Alexandru-Constantin BOZONC[a], Ana-Maria CORMOS[a,*], Shareq Mohd NAZIR[b], Paul COBDEN[c]

ABSTRACT. A dynamic 2D CFD multilayer particle model was developed and simulated using COMSOL Multiphysics 6.3 to study desulfurization of copper sulfide (Cu_2S) with hydrogen (H_2). The model solved interstitial velocity and pressure fields in the gas phase coupled to transiently resolved species transport in both gas and solid phases, incorporating reduction kinetics and dynamic pellet porosity change. After model validation with experimental data from literature, a constricted optimization study was carried out to identify optimal conditions necessary to maximize Cu_2S conversion and H_2 utilization. The optimization solutions (i.e., 100% H_2 and 973 K) indicated that both high inlet mole fraction of H_2 and temperature improved the objective function steadily, highlighting the trade-off between maximizing conversion and minimizing H_2 slip. The current work can serve as a framework for reactor-scale simulations aimed at intensification and decarbonization of primary copper production.

Keywords: *copper sulfide, hydrogen desulfurization, CFD multilayer particle model, process optimization*

INTRODUCTION

Despite global initiatives to limit climate change, annual greenhouse gas (GHG) emissions continue to increase steadily every year. Energy-related carbon dioxide (CO_2) emissions reached an all-time high in 2024 of

[a] *Babeş-Bolyai University, Faculty of Chemistry and Chemical Engineering, 11 Arany Janos str., RO-400028, Cluj-Napoca, Romania.*
[b] *KTH Royal Institute of Technology, Department of Chemical Engineering, Brinellvägen 8, Stockholm, Sweden.*
[c] *Swerim AB, Box 812, 971 25 Luleå, Sweden.*
[*] *Corresponding author: ana.cormos@ubbcluj.ro*

37.8 Gt CO_2, 0.8% higher than the previous year, contributing to record concentrations of CO_2 in the atmosphere of 442.5 ppm [1]. Although emissions from industrial processes declined by 2.3% in 2024, further decarbonization of industry is necessary to stay within the proposed carbon budget to keep global warming from exceeding 1.5 °C above pre-industrial levels [2].

Copper (Cu) is an essential component in many technologies supporting global decarbonization, including renewable energy generation (i.e., PV panels and generators), energy storage (i.e., batteries), electric vehicles (i.e., motors and wiring), power transmission and distribution, etc. In 2024, the production of Cu accounted for 0.2% of global anthropogenic GHGs [3], although estimates see the Cu cycle contributing up to 2.7% by 2050 without efforts to reduce emissions [4]. The current demand for Cu at 25 Mt per year is projected to double by 2035 [5], with energy transition technologies accounting for half of the demand [6]. Consequently, the Cu sector is in the position of having to expand production to support the overall energy transition while also reducing its own emissions in accordance with global decarbonization goals.

There are two main routes for Cu production, pyrometallurgical and hydrometallurgical, depending on the properties of the raw material. Pyrometallurgy, accounting for around 80% of copper mine production, is the dominant route for sulfide ores, especially chalcopyrite, while hydrometallurgy is preferred for low-grade oxide ores and some secondary sulfides, since chalcopyrite is extremely difficult to dissolve in aqueous solutions [7]. The pyrometallurgical route, shown in Figure 1, is an inherently multi-stage process of higher complexity when compared to hydrometallurgy (i.e., leaching, extraction, stripping and electrowinning) which involves fewer high-temperature unit operations to produce high-purity copper cathodes from low-grade ores that pyrometallurgy cannot handle efficiently [8]. From an environmental perspective, pyrometallurgy must manage SO_2-rich off-gases from the smelting and converting stages by capturing and converting them into sulfuric acid. On the other hand, key environmental issues in hydrometallurgy include management of (i) solution acidity to protect groundwater by utilizing adequate liners and (ii) acid mist formation in the electrowinning stage by using ventilation systems or suppressants [9]. From an economic point of view, a higher capital investment is necessary for copper refinement via pyrometallurgy (i.e., fixed investment of 33,000 $ per annual t Cu produced) vs. the hydrometallurgical route (i.e., fixed investment of 3,550 $ per annual t Cu produced), attributed to much smaller infrastructure requirements for the latter [9]. Operating costs for both routes are mainly driven by electricity price, due to the power intensive smelting and electrowinning stages, with higher overall costs for pyrometallurgy (i.e., 6 $ per kg Cu produced) vs. hydrometallurgy (i.e., 2 $ per kg Cu) [9].

Production from primary sources via pyrometallurgy begins with extraction of Cu-bearing ores from mines, typically containing between 0.25 – 1 wt.% Cu. The sulfide ore is first crushed and ground, then subjected to flotation to obtain Cu concentrate with 20 – 40 wt.% Cu. The concentrate is then smelted in a flash furnace at temperatures of 1200 – 1300 °C, resulting in Cu matte containing 50 – 70 wt.% Cu. Subsequently, the matte is further refined and converted to blister Cu with 98.5 – 99.5 wt.% Cu. A final electrochemical process results in refined Cu cathodes with higher than 99.99% purity. In addition to raw ore, Cu scrap can be introduced into the pyrometallurgical production process at different stages, but can also be processed as a standalone feedstock in the production of refined Cu. The main benefits of using Cu scrap are (i) enables higher energy efficiency compared to mining and processing Cu ore, (ii) avoids emissions, (iii) circumvents wastes from mining, concentration, leaching and smelting stages, and (iv) lessens ore depletion and improves overall copper availability [10].

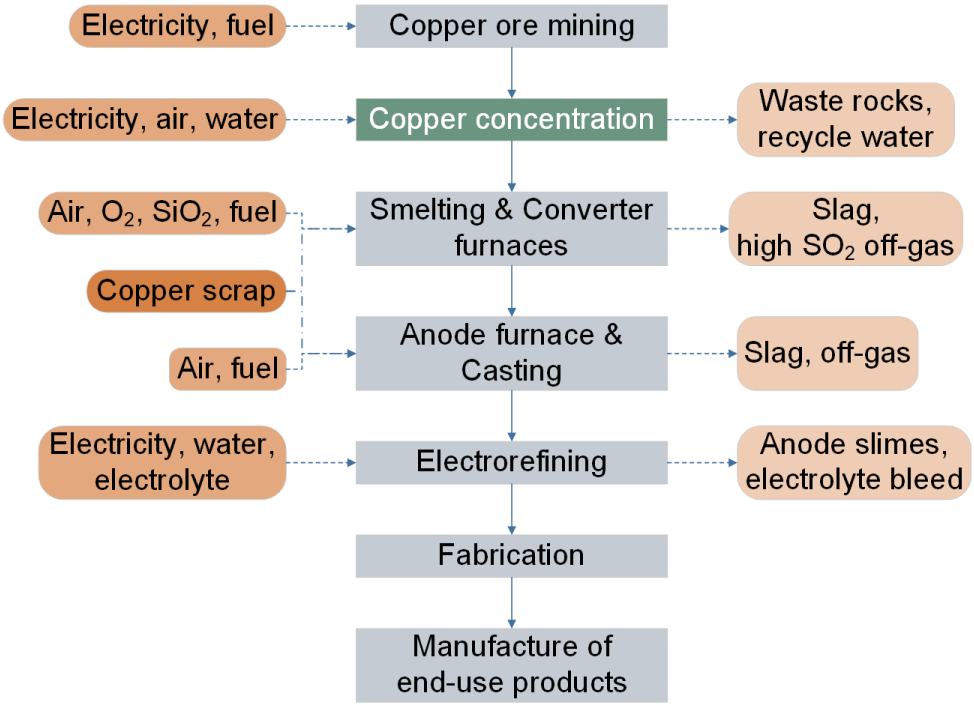

Figure 1. Pyrometallurgical production processes within the Cu value chain

The mining and concentration stages together account for about 65 – 80% of the total emissions from mine-to-copper cathode production. In addition, the flash smelting technology used in the pyrometallurgical route accounts for roughly 60% of primary Cu production [11]. However, as ore grades decline and concentrate quality becomes more heterogeneous, maintaining stable flash smelter operation becomes increasingly difficult, with adverse impacts on throughput, specific energy consumption and CO_2 emissions [12]. The most common copper-containing minerals are chalcopyrite ($CuFeS_2$) and chalcocite (Cu_2S), but their concentrations in the ore are low, ranging from 0.3 – 1.7 wt.% Cu [13]. In addition, typical Cu ore concentrates that are fed to smelters primarily contain $CuFeS_2$, iron sulfide (FeS_2), copper sulfide (CuS) and Cu_2S, with exact compositions depending on the source of ore [14]. Therefore, enhancing the quality of Cu concentrate before it enters the smelter is an attractive lever for decarbonization, as well as for improving operational stability and process efficiency. In this work we focus on developing particle scale models for a model compound present in copper concentrate and its reaction with hydrogen (H_2).

To date, modeling advances of pyrometallurgical Cu refinement have mainly targeted the smelting furnace, with particular focus on flash smelting furnaces (FSF). A thermodynamic model was developed by Li et al. [15] for Cu side-blown smelting to accurately predict the product composition and the distribution behavior of impurity elements under representative operating conditions. Solghar et al. [16] developed a thermochemical model of the FSF, assuming that all matte, slag, dust and gas phases were in thermal and chemical equilibriums and determined that rate of fuel consumption was heavily influenced by the variation in working parameters of the furnace. In addition, computational fluid dynamics (CFD) has been used to study the Cu FSF, with Kumar et al. [17] investigating the impact of process parameters on smelting operation considering the model domains as the reaction shaft and settler freeboard. Zhou et al. [18] utilized CFD to investigate how gas flows influence particle dispersion and combustion in copper FSF, revealing that large momentum ratio combined with large amounts of air was beneficial in dispersion of particles and led to quicker combustions. Urbaniak et al. [19] developed a model to investigate copper concentrate roasting within a fluidized bed-furnace during the smelting process, establishing that a deposit with 40 mm thickness determined a reduction by 80% in the absorbed energy by water from the bed. Furthermore, Zhu et al. [20] employed discrete element method (DEM) modeling to study segregation of copper concentrate particles in the feeding system of a FSF, highlighting that its reduction was possible by increasing sloping angle or narrowing chute width.

Since most published models on pyrometallurgical Cu refinement focus on the smelting stage, the pre-treatment of Cu ores to improve concentrate grade for smelting remains largely unexplored. In the current work, this gap is addressed by developing a particle-scale modeling framework for hydrogen-assisted desulfurization and upgrading of Cu concentrates, designed to be later coupled with reactor-scale simulations. Overall, this study provides (i) a validated CFD multilayer particle model for Cu_2S conversion using H_2, (ii) insight into coupled transport-reaction behavior within pellets that account for dynamic porosity, and (iii) optimization-based identification of operating windows to enhance Cu_2S conversion while improving H_2 utilization.

MODEL DEVELOPMENT

The current study considered Cu_2S as the representative copper sulfide component to establish a baseline and enable validation using available kinetic data for desulfurization of copper sulfates with H_2. Further implementation of model kinetics to other components will be extended to mixed phases once consistent kinetics are available. As such, a 2D CFD multilayer particle model was developed in COMSOL Multiphysics 6.3 to study the desulfurization of Cu_2S by H_2, leading to the following overall reaction between ore and H_2 (Eq. (1)):

$$Cu_2S\,(s) + H_2\,(g) \rightarrow 2Cu\,(s) + H_2S\,(g) \qquad \Delta H^0_{298} = +60\ kJ/mol \qquad (1)$$

Model kinetics

The intrinsic kinetics of hydrogen reduction of Cu_2S were studied by Sohn and Won [21], who derived a first-order reaction rate with respect to the solid reactant and H_2 concentrations. The experimental measurements were carried out at temperatures between 823 – 1023 K in a thermogravimetric analyzer. The reaction kinetics were measured using small particles to neglect interparticle diffusional effects, as well as thin pellets of various sizes and thickness values to ensure diffusional effects were minimal. The activation energies obtained from experiments with both powder and pellets were 92 kJ/mol, while the pre-exponential factor (k_0) was around two times higher for the porous pellets than the powder as an effect of increased surface area. Thus, the rate of conversion for the dense Cu_2S particles during H_2 reduction was expressed as Eq. (2), with k_0 as $2.23 \cdot 10^6$:

$$\frac{dX_{Cu_2S}}{dt} = k_0 \cdot e^{\left(-\frac{11{,}100}{T}\right)} \cdot c_{H_2} \cdot \left(1 - X_{Cu_2S}\right) \qquad (2)$$

Model geometry and mesh

The model consisted of two domains: a fluid domain representing the interstitial gas and a particle domain representing the solid ore (Figure 2). The transport of species was solved over time for both domains and was coupled with a momentum balance that was solved under steady-state conditions for the gas phase. The pellet bed, with a diameter of 3 cm, was represented by a single layer of particles in the radial direction and multiple layers in the axial direction. The pellets were positioned to maximize the contact area between particles and incoming reacting gas front (i.e., H_2), while respecting the prescribed bed porosity of 0.3 (i.e., void space). In addition, to avoid artificial boundary effects, fluid-only sections were implemented with the thickness of one particle layer at the inlet and outlet of the model domain.

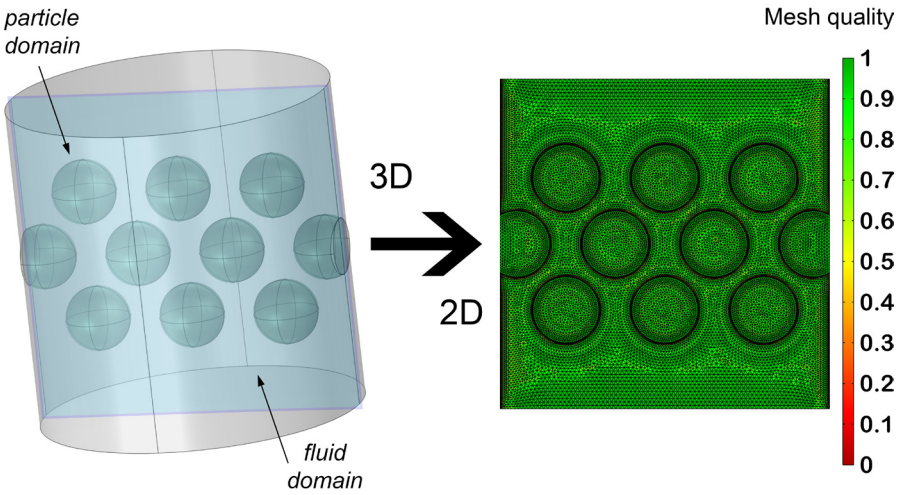

Figure 2. 3D to 2D geometry transition and 2D mesh quality (i.e., 1 meant best possible element)

To reduce model complexity, the initial 3D domain was sectioned and converted into a 2D particle-fluid model, significantly lowering the degrees of freedom and enabling investigation of operating conditions by optimization within reasonable computational times. In addition, since the dominant gradients were along the direction of flow and the bed structure was homogeneous in the out-of-plane direction, little accuracy was lost by neglecting the third dimension, while the essential transport and reaction phenomena were still captured. Mesh convergence was assessed based on the predicted pressure drop,

reaching a final mesh with 36,886 elements and an average element quality of 0.83, as indicated by the distribution shown in Figure 2, where quality was represented in terms of a dimensionless value between 0 (i.e., degenerated element) and 1 (i.e., best possible element).

Model parameters and operating conditions

The main operating conditions and parameters considered in this work are shown in Table 1. The simulations were based on the experimental conditions for which Sohn and Won [21] carried out their investigation on Cu_2S reduction by H_2.

Table 1. Operating conditions and parameters used in the particle model

Parameter	Value	Parameter	Value
Temperature	823 – 1023 [K]	Sample mass	20 – 60 [mg]
Gas pressure	0.86 [atm]	Pellet porosity	0.22 [-]
Flow rate	0.1 [dm^3/min]	Pellet diameter	3.11 [mm]

Model assumptions

The main assumptions considered when developing the multilayer particle model are shown below:

· The solid pellet ores were entirely composed of Cu_2S.
· The pellets were spherical with constant radii throughout the reaction.
· Diffusion was modeled using Fick's law with effective diffusivities.
· Incompressible laminar fluid flow was assumed for the gas phase.
· Isothermal conditions were assumed.

Model equations

The equations implemented in the 2D multilayer particle model are presented in Table 2. Species transport in the fluid domain was described by a time-dependent convection-diffusion equation (Eq. (3)), assuming Fickian diffusion with no reaction in the gas phase. Transport of gas species in the pellet domain was modeled by a diffusion-reaction equation (Eq. (4)), with effective diffusion (D_e) calculated using a Millington and Quirk relation, while the reaction rate term used the kinetics published by Sohn and Won [21] (Eq. (2)). Species transport for the solid components (Eq. (6)) only included a reaction term. The coupling between fluid and particle domains was implemented through a mass transfer boundary condition (Eq. (7)) at the interface, where

the mass transfer coefficient ($k_{m,i}$) was evaluated from the Sherwood number, diffusion coefficient and particle radius. Particle porosity was transiently calculated (Eq. (9)) by accounting for a shrinkage factor, estimated with the molar volumes of the solid components, and the conversion of the Cu_2S reactant. The Navier-Stokes equations in the x and y directions, coupled with the continuity equation, were used to describe momentum transport in the fluid domain. A stationary study solved incompressible laminar flow for the fluid domain, with Reynolds numbers confirming laminar flow in all cases, resulting in a velocity field that provided the convective term for the transient species transport, allowing the change of compositions for gas and solid components to be resolved in time. Consequently, the convective transport in the particles was assumed negligible and species transport was solved solely by diffusion-reaction.

Table 2. Equations implemented in the CFD multilayer particle model

Species transport in the fluid domain	
$\frac{\partial c_i}{\partial t} - \frac{\partial}{\partial x}\left(D_i \frac{\partial c_i}{\partial x}\right) - \frac{\partial}{\partial y}\left(D_i \frac{\partial c_i}{\partial y}\right) + u_x \frac{\partial c_i}{\partial x} + u_y \frac{\partial c_i}{\partial y} = 0$	(3)
Species transport in the pellet domain (for gas and solid phases)	
$\varepsilon_p \frac{\partial c_{i,p}}{\partial t} - \frac{\partial}{\partial x}\left(D_{e,i} \frac{\partial c_{i,p}}{\partial x}\right) - \frac{\partial}{\partial y}\left(D_{e,i} \frac{\partial c_{i,p}}{\partial y}\right) = R_i$	(4)
$D_{e,i} = \varepsilon_p^{4/3} \cdot D_i$	(5)
$(1 - \varepsilon_p) \frac{\partial c_{s,i}}{\partial t} = R_i$	(6)
$J_{i,p} = k_{m,i} \cdot (c_i - c_{i,p})$	(7)
$k_{m,i} = \frac{Sh \cdot D_i}{r_p}$	(8)
$\varepsilon_p = \varepsilon_{p,0} + \left(1 - \varepsilon_{p,0}\right) \cdot (1 - \Phi) \cdot X_{Cu_2S}$	(9)
$\Phi = \frac{2 \cdot V_{M,Cu}}{V_{M,Cu_2S}}$	(10)
Momentum transport in the fluid domain	
$\rho_f \left(u_x \frac{\partial u_x}{\partial x} + u_y \frac{\partial u_x}{\partial y}\right) = -\frac{\partial p}{\partial x} + \mu_f \left(\frac{\partial^2 u_x}{\partial x^2} + \frac{\partial^2 u_x}{\partial^2 y}\right)$	(11)
$\rho_f \left(u_x \frac{\partial u_y}{\partial x} + u_y \frac{\partial u_y}{\partial y}\right) = -\frac{\partial p}{\partial y} + \mu_f \left(\frac{\partial^2 u_y}{\partial x^2} + \frac{\partial^2 u_y}{\partial^2 y}\right)$	(12)
$\frac{\partial u_x}{\partial x} + \frac{\partial u_y}{\partial y} = 0$	(13)

Optimization study

A constrained optimization study was carried out to identify the operating conditions necessary to enable efficient desulfurization while preventing solid thermal degradation. The goal was to maximize overall hydrogen utilization with high Cu_2S conversion by identifying the optimal inlet hydrogen mole fraction and operating temperature as decision variables. The gradient-free Nelder-Mead method was chosen to solve the optimization problem with an optimality tolerance of 0.01 and 1000 maximum number of evaluations. Nelder-Mead is a derivative-free optimization method that considers a simplex of N+1 points, where N is the number of control variables, to perform reflections, expansions and contractions. This improves the worst point in the control variable space, and, consequently, the objective function. The main benefits to using Nelder-Mean in the current study were that (i) the simplex required less computational time than other-gradient free methods [22], and (ii) it was suitable due to the small number of decision variables in the objective function (i.e., 2).

RESULTS AND DISCUSSION

The multilayer model was validated using the experimental measurements presented by Sohn and Won [21]. Figure 3 shows experimentally measured Cu_2S conversion in time as function of time at various temperatures between 823 – 1023 K and a flowrate of 2 dm^3/min. Across all cases, higher overall conversion was achieved in less time at higher temperatures. The model reproduced the experimental conversion data well over the full temperature range with values for R^2 (coefficient of determination) higher than 0.9 and *RMSE* (root mean square error) values between 0.014 – 0.024 for conversion of Cu_2S.

Table 3. Accuracy of predicted conversion for variable temperatures

T [K]	823	868	921	973	1023
R^2	0.904	0.984	0.996	0.993	0.994
RMSE	0.022	0.015	0.014	0.024	0.022

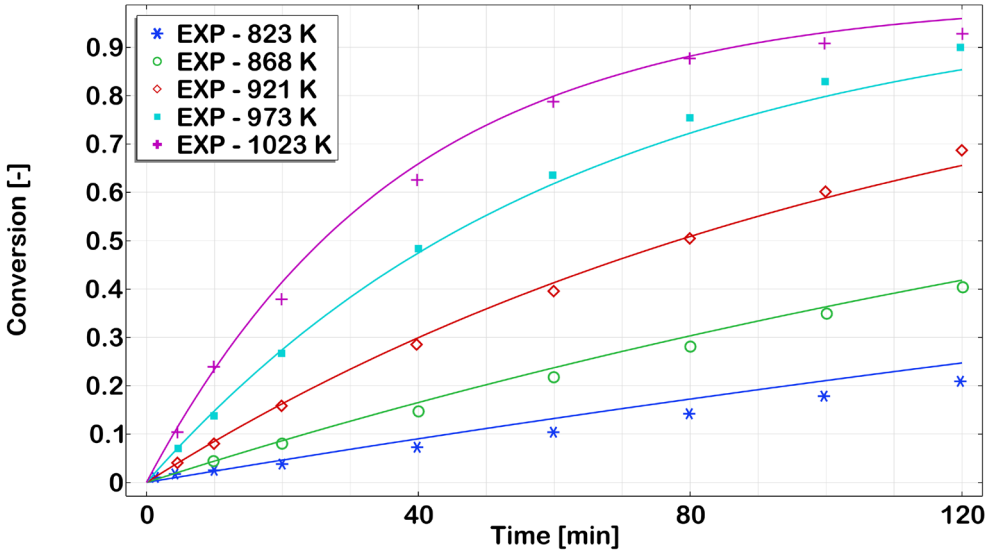

Figure 3. Experimental measurements [21] vs. CFD model predictions (lines) for conversion of Cu_2S in time at variable temperatures

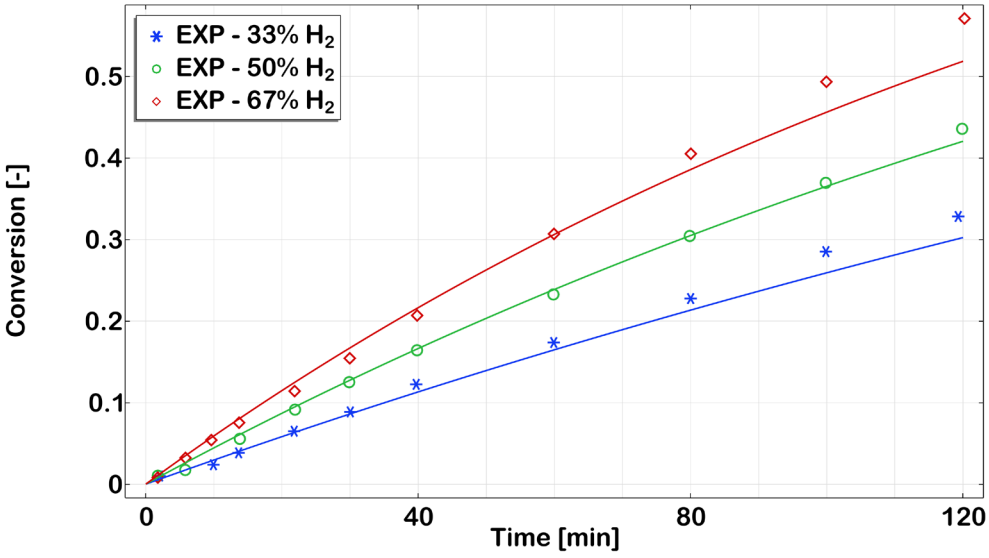

Figure 4. Experimental measurements [21] vs. CFD model predictions (lines) for conversion of Cu_2S in time at variable H_2 concentrations

Figure 4 shows experimentally measured Cu_2S conversion in time as function of three H_2 concentrations: 33%, 50% and 67%. The H_2 concentration was controlled using inert He gas, the total flowrate for the two components being 12 dm^3/min. Across all cases, higher overall conversion was achieved in less time at higher H_2 concentrations. The model exhibited good fit between measurements and predictions by yielding values for R^2 higher than 0.9 and *RMSE* values between 0.006 – 0.021 for conversion of Cu_2S.

Table 4. Accuracy of predicted conversion variable H_2 concentrations

cH_2 (%)	33	50	67
R^2	0.983	0.997	0.987
RMSE	0.013	0.006	0.021

Figure 5 presents the pressure loss distribution in the 2D particle-fluid domain. A gradual pressure drop was noticed closer towards the particle domains, while within the particle region, higher loss was seen around the narrow gaps between pellets. Overall, a small total pressure loss was predicted across the pellet domain, as expected for low-Reynolds laminar flow.

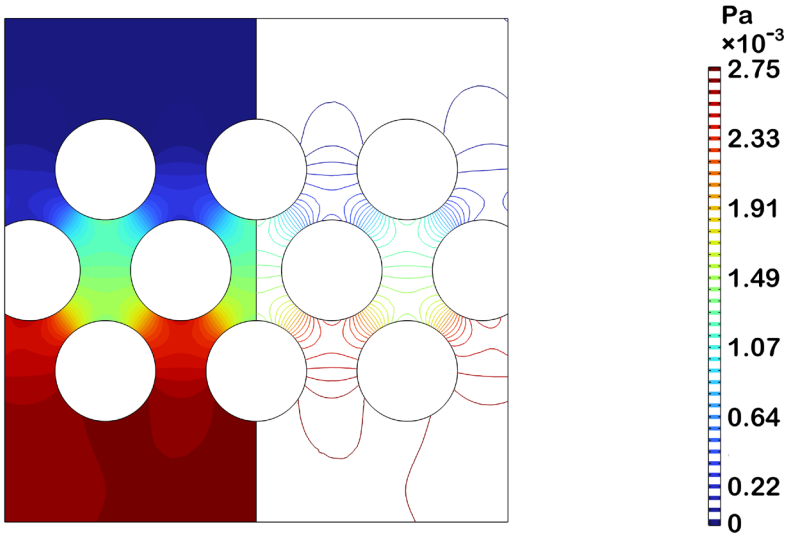

Figure 5. CFD model predicted pressure drop distribution

Figure 6 presents the velocity magnitude and streamlines in the 2D particle fluid domain. A fully developed laminar flow boundary condition was assumed at the inlet section. The narrow gaps between the pellets determined an acceleration of flow, reaching the highest velocities in these constricted areas, while a low-velocity zone was formed in the wakes. The streamlines illustrated the path of flow and indicated that no recirculation zones were formed, as expected for low-Reynolds laminar flow.

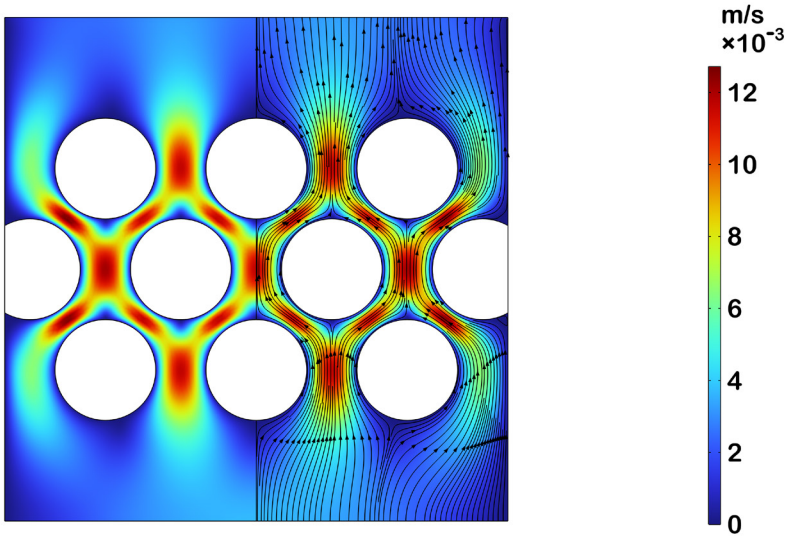

Figure 6. CFD model predicted velocity profile

Figure 7 presents the evolution in time of relative concentrations (i.e., gas concentration at time *t* for component *i* divided by total inflow concentration of gas) for all gas and solid components. The left panels show the gas-phase concentrations of H_2 and H_2S in the fluid-particle domains, while the right panels present the solid-phase concentrations of Cu_2S and Cu inside the pellets at different simulated times. At 0 s, before any gas was introduced to the domain, the pellet consisted entirely of Cu_2S. Over time, the H_2 gas penetrated the pellets forming H_2S, which then diffused through the particles toward the fluid domain. The Cu_2S depleted gradually from the outer regions where the H_2 diffused toward the pellet cores, with Cu being produced correspondingly from the surface inward.

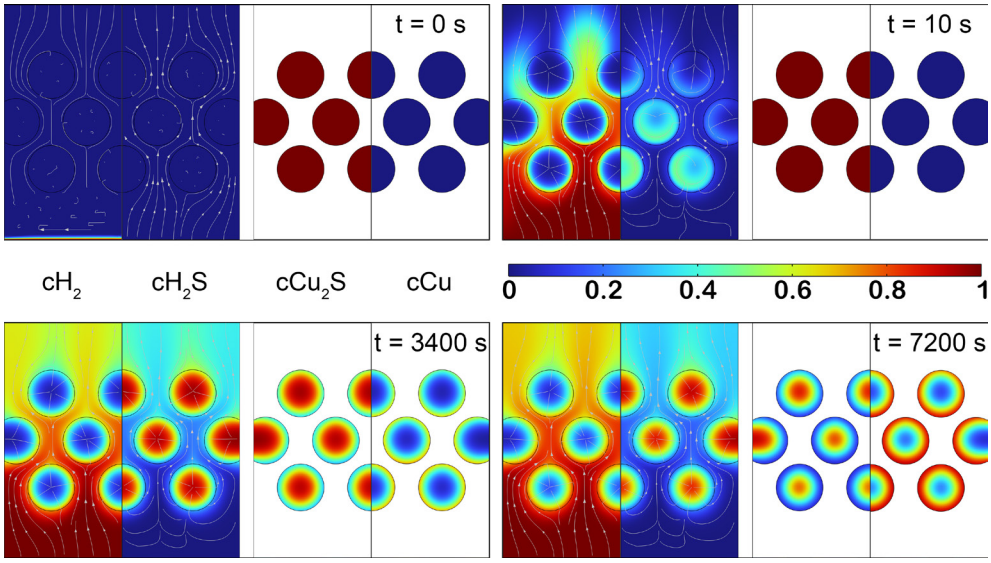

Figure 7. CFD model predicted concentration evolution for gases and solids

Figure 8 illustrates the change of particle porosity over time for a particle situated in the center of the fluid domain. The initial porosity was assumed to be completely uniform at 0.22 (i.e., void space). Shortly after H_2 penetration, a slight porosity change was seen at the edges, where reaction first took place. Further into the reduction reaction at 3600 s, a strong porosity gradient developed, with high porosity noticed in the outer shell, while porosity in the less reacted core barely changed. At 7200 s, the porosity increased throughout the entire pellet, forming a more compact inner region, reflecting the shrinkage of solid volume due to the progression of conversion inward toward the pellet core.

A multi-parameter optimization was performed to maximize a combined objective function (Eq. (14)) considering the average conversion of Cu_2S and overall hydrogen utilization. Two decision variables were considered: (i) inlet hydrogen mole fraction (y_{in,H_2}) and (ii) operating temperature (T) with an upper limit of 973 K imposed to avoid Cu sintering, observed to take place in the experimental measurements at higher temperatures [21].

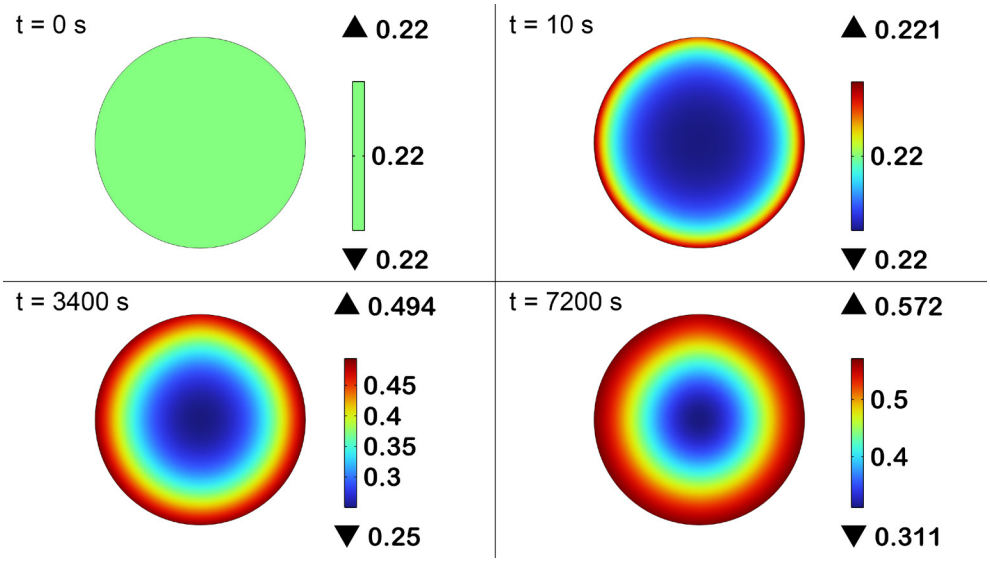

Figure 8. CFD model predicted pellet porosity change

The product form in the objective function (Eq. (14)) served to measure simultaneous improvement, such that *J* became high only for both high Cu_2S conversion and H_2 utilization, rather than for one term high and the other poor (e.g., high conversion but large H_2 slip). In addition, since *J* could become zero if either term approached zero, the form prevented reporting an optimal solution in which one key performance indicator collapsed to an unacceptable value (i.e., zero).

$$\max_{y_{in,H_2},T} J = \left(1 - \frac{c_{H_2}}{c_{in,H_2}}\right) \cdot \left(1 - \frac{w_{Cu_2S}}{w_{0,Cu_2S}}\right) \tag{14}$$

Subject to:

$$0.33 \leq y_{in,H_2} \leq 1$$
$$823\ \mathrm{K} \leq T \leq 973\ \mathrm{K}$$

The representative points of the converged optimal solutions are presented in Table 5. The two terms considered in the combined objective function Eq. (14) were intended to represent process performance (i.e., Cu_2S conversion) and resource efficiency (i.e., H_2 utilization). Generally, these two

quantities could be in trade-off: increase in H_2 driving force (i.e., higher H_2 inlet fraction) typically increases conversion based on the kinetic relationship published by Sohn and Won [21], but could also lead to unreacted H_2 in the outlet if the gas-solid contact time and transport limitations (i.e., high internal particle diffusion) prevented complete consumption of the reactant. However, within the parameter window considered here, matching the experimental conditions used for model validation, the combined objective function increased monotonically, resulting in a boundary solution as the optimal solution, rather than an interior optimum. Across all temperatures, the objective function increased consistently with y_{in,H_2}, indicating a strong dependence of reduction kinetics on H_2 availability. Higher H_2 partial pressure enhanced both fluid-particle interfacial transport and intraparticle reaction rates. In addition, the objective function also increased with temperature, enhancing reaction kinetics, which led to better conversion and improved H_2 usage. The highest value of the objective function achieved was 0.0705 obtained at 100% H_2 inflow composition and 973 K.

Although the temperature was allowed to vary between 823 – 973 K, the values reported in Table 5 correspond to the converged optimal solutions. To confirm that the solutions were not artifacts related to the initial simplex, the Nelder-Mead algorithm optimization was carried out using multiple starting points within the feasible temperature (i.e., 823 – 973 K) and hydrogen molar fraction (i.e., 0.33 – 1) boundaries. All runs converged to the same optimal conditions, indicating a global optimum, consistent with the steady increase of the objective function with temperature.

Table 5. Representative solutions calculated during optimization

Number	Variable 1 y_{in,H_2} [-]	Variable 2 T [K]	Objective function J
1	0.33	898	0.012
2	0.67	898	0.021
3	1.00	898	0.031
4	1.00	917	0.040
5	1.00	937	0.050
6	1.00	956	0.060
7	1.00	973	0.070 (optimum)

Figure 9 shows the change in time of H_2 utilization (U_{H_2}), the first term in Eq. (14), and Cu_2S conversion. A rapid decrease in U_{H_2} from 1 was noticed as H_2 was being consumed entirely, followed by a gradual approach to a low

value as H_2 slip increased, ending at 0.23 after 3600 s. In contrast, the Cu_2S conversion increased steadily, reaching 0.29 after 3600 s. The shape of the curves confirmed the expected interplay between reaction-diffusion within the pellets and illustrated the trade-off between minimizing H_2 slip and maximizing solid conversion.

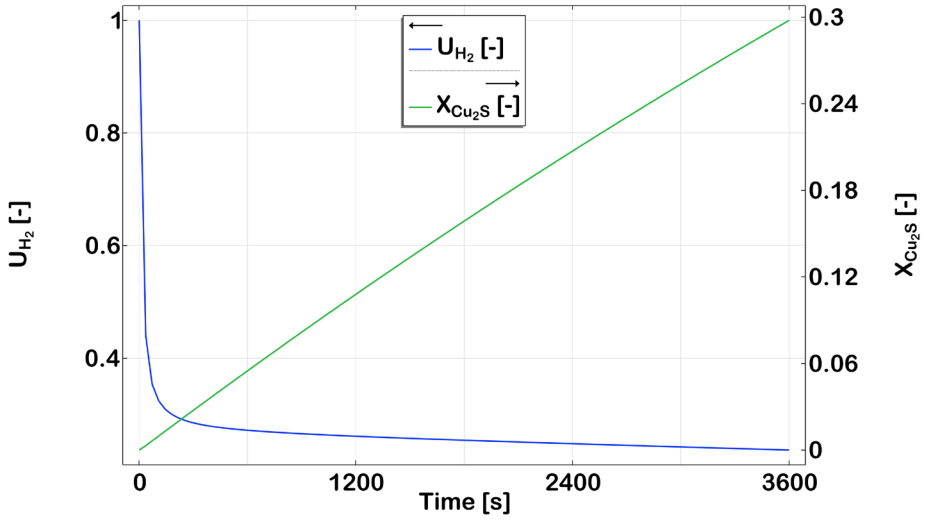

Figure 9. Evolution in time of the objective function during optimization

CONCLUSIONS

A 2D CFD multilayer particle model was developed to describe hydrogen-driven desulfurization of Cu ore concentrate, considering Cu_2S as the representative solid phase. The model coupled velocity and pressure profiles in the fluid domain to transiently solved species transport for both gas and solid components based on kinetic rates for desulfurization published by Sohn and Won [21], while also accounting for change of pellet porosity in time.

The model was validated with experimental data from literature [21], yielding R^2 coefficients higher than 0.9 and low *RMSE* values, thus confirming an accurate representation of the intraparticle diffusion-reaction mechanisms. The simulations solved spatial gradients for gas composition, solid conversion and porosity within the particle, as well as interstitial gas velocity and pressure fields, reflecting a limited decrease in total pressure through the multiplayer particle domain, as expected for the low-Reynolds laminar flow considered in this work.

An optimization study was conducted to identify the optimal inlet H_2 molar fraction and operating temperature necessary to maximize a combined objective function of H_2 utilization and Cu_2S conversion. The results demonstrated that both higher temperature and higher inlet mole fraction strongly promoted conversion and H_2 usage. The maximum was achieved at 100% H_2 and 973 K, highlighting the trade-off between maximizing conversion and minimizing H_2 slip.

The modeling framework developed in this work can be directly extended and coupled with reactor-scale CFD and process integration studies to support decarbonization of primary copper production. Overall, the results support decarbonization by identifying conditions that minimize H_2 slip, thus reducing upstream emissions associated with hydrogen production (e.g., GHGs to generate electricity for electrolysis) per t of Cu in hydrogen-based desulfurization.

ACKNOWLEDGMENTS

This research was supported by More4LessCu project (CETP-FP-2023-00394) which is funded within the Clean Energy Transition Partnership (CETP) programme, co-funded by the European Union. And was supported by a grant from the Ministry of Research, Innovation and Digitization, CNCS/CCCDI - UEFISCDI, project number ERANET-CETP-More4LessCu, within PNCDI IV.

NOMENCLATURE

c_i – concentration of species *i,* gas phase, fluid domain [mol/m^3]

$c_{i,p}$ – concentration of species *i,* gas phase, particle domain [mol/m^3]

$c_{s,i}$ – concentration of species *i,* solid phase, particle domain [mol/m^3]

D_i – molecular diffusion coefficient in the fluid domain [m^2/s]

$D_{e,i}$ – effective diffusion coefficient in the pellet [m^2/s]

J – objective function [-]

$J_{i,p}$ – mass flux across particle-fluid interface [kg/m^2/s]

k_0 – pre-exponential factor [m^3/mol/s]

$k_{m,i}$ – mass transfer coefficient of species *i* for film resistance [m/s]

p – relative pressure [Pa]

r_p – particle radius [m]

R_i – reaction rate term [mol/m^3/s]

R^2 – coefficient of determination [-]

Sh – Sherwood number [-]

t – time [s]

T – temperature [K]

u, v – gas velocity components in the x and y directions [m/s]

U_{H_2} – hydrogen utilization [-]

$V_{M,i}$ – molar volume of solid species i [m^3/mol]

x, y – spatial coordinates in the 2D domain

X_{Cu_2S} – conversion of solid component Cu_2S [-]

y_{in,H_2} – inlet hydrogen mole fraction [-]

ε_p – particle porosity (i.e., void space) [-]

Φ – shrinkage factor [-]

μ_f – fluid dynamic viscosity [Pa·s]

ρ_f – fluid density [kg/m^3]

CFD – computational fluid dynamics

GHG – greenhouse gas

RMSE – root mean square error

REFERENCES

1. International Energy Agency (IEA); Global Energy Review 2025, Paris, **2025**
2. M. Crippa; D. Guizzardi; F. Pagani; M. Banja; M. Muntean; GHG emissions of all world countries – 2025 Report, Luxembourg, **2025**
3. The Copper Mark (TCM); Decarbonizing the Copper Sector – Discussion Topics and Considerations for a 1.5 °C-aligned Trajectory and Target-setting Methodology, **2024**
4. T. Watari; S. Northey; D. Giurco; S. Hata; R. Yokoi; K. Nansai; et al.; Resources, Conservation and Recycling, **2022**, 179, 106118
5. International Copper Association (ICA); Copper — The Pathway to Net Zero, **2023**
6. S&P Global; The Future of Copper: Will the Looming Supply Gap Short-Circuit the Energy Transition?, **2022**
7. The Copper Mark (TCM); Decarbonizing the Copper Sector – Discussion Topics and Considerations for a 1.5 °C-aligned Trajectory and Target-setting Methodology, **2024**
8. International Copper Study Group (ICSG); The World Copper Factbook 2025, **2025**
9. International Finance Corporation (IFC); Net Zero Roadmap for Copper and Nickel Mining – Technical Report, **2023**
10. M. Chen; D. Sukhomlinov; P. Taskinen; J. Hamuyuni; M. Tiljander; M. Lindgren; et al.; Metallurgical and Materials Transactions B, **2025**, 56, 1897–1913
11. M. Li; Y. Feng; X. Chen; Metals, **2024**, 14, 840

12. A. A. Solghar; M. Abdolzadeh; Proceedings of the Institution of Mechanical Engineers, Part E: Journal of Process Mechanical Engineering, **2015**, 229, 11–24
13. S. Nirmal Kumar; B. Desai; V. Tathavadkar; Y. Patel; J. Patel; A. Singh; et al.; Mineral Processing and Extractive Metallurgy, **2023**, 132, 49–61
14. J. Zhou; J. Zhou; Z. Chen; Y. Mao; JOM, **2014**, 66, 1629–1637
15. R. Urbaniak; B. Hadała; R. Stanik; J. Konstanty; A. Olejnik; International Communications in Heat and Mass Transfer, **2024**, 108284
16. Z. Zhu; P. Zhou; Z. Chen; Z. Xiao; D. Wu; S. Kuang; Powder Technology, **2024**, 443, 119898
17. M. E. Schlesinger; K. C. Sole; W. G. Davenport; G. R. F. Alvear Flores; Extractive Metallurgy of Copper, 6th ed.; Elsevier, **2021**, 1–573
18. V. M. Sanchez-Corrales; J. A. Valera-Gonzalez; P. Flores-Perez; M. Perez-Tello; JOM, **2004**, 56, 29–32
19. H. Y. Sohn; S. Won; Metallurgical Transactions B, **1985**, 16, 831–839

STUDIA UBB CHEMIA, LXXI, 1, 2026 (p. 77-100)
(RECOMMENDED CITATION)
DOI:10.24193/subbchem.2026.1.06

NOVEL MATHEMATICAL MODEL WITH INTEGRATIVE OPTIMIZATION FOR MICROWAVE DRYING OF OLIVE LEAVES (*OLEA EUROPAEA*) TO ENHANCE BIOACTIVE COMPOUNDS PRESERVATION, ANTIOXIDANT ACTIVITY, AND ENERGY EFFICIENCY

Taous KADDOUR[a,*], Nassima CHAHER-BAZIZI[a], Farid CHEBROUK[b, c], Naima SAIDENE[a], Lamia HANIFI[a], Lydia KAROU[a], Mostapha BACHIR-BEY[a]

ABSTRACT. This study optimized the microwave drying of olive leaves by integrating mathematical modeling and proposing a novel drying model, along with a comprehensive analysis of energy efficiency and bioactive compound preservation. Experiments were conducted at microwave power levels ranging from 100 to 1000 W, assessing drying kinetics, energy efficiency, and retention of bioactive compounds. The optimal power of 700 W achieved a drying time of 21 minutes while preserving key bioactive compounds, with TPC, TFC, and antioxidant activity reaching 108.79 mg GAE/g DM, 12.12 mg RE/g DM, and 23.25 mg GAE/g DM, respectively. Several mathematical models from the literature were evaluated, and the Logarithmic, Modified Henderson–Pabis II, and Hii et al. models showed excellent agreement with the experimental data ($R^2 > 0.99$). The proposed new model also demonstrated strong predictive accuracy, with high R^2 values and low root mean square error and reduced chi-square (χ^2). The lowest specific energy consumption was 0.236×10^5 MJ/kg H_2O, accompanied by the highest energy efficiency. These results demonstrate that intermediate

[a] *Université de Bejaia, Faculté des Sciences de la Nature et de la Vie, Laboratoire de Biochimie Appliquée, 06000 Bejaia, Algeria*
[b] *Centre de Recherche Scientifique et Technique en Analyses Physico-Chimiques (CRAPC), BP384, Bou-Ismail, Tipaza 42004, Algeria*
[c] *Plateau Technique d'Analyses Physico-Chimiques, Route de Targa Ouzemmour 06000, Université de Bejaia, Algeria*
* *Corresponding author: taous.kaddour@univ-bejaia.dz*

microwave power provides an optimal balance between energy efficiency, processing time, and bioactive compound preservation, highlighting both practical and economic advantages for olive leaf drying.

Keywords: *Microwave drying, olive leaves, bioactive compounds, antioxidant activity, mathematical modeling, energy efficiency*

INTRODUCTION

Olea europaea L. is a species within the Oleaceae family, it is native to the Mediterranean region and is of significant economic and social importance. Historically, olive leaves have been used in traditional medicine to treat various conditions, including fevers, malaria, rheumatism, hypertension, diabetes, and cancer. Their extracts have garnered attention as natural additives in cosmetics, functional foods, and pharmaceuticals [1]. Fresh olive leaves generally need to be dried and ground before extraction to preserve bioactive compounds and ensure optimal extraction efficiency. This process prevents microbial and enzymatic degradation that could compromise the quality of the final product [2].

Several studies have investigated various methods for drying olive leaves, including air, convection, and solar drying [3–5]. However, these techniques exhibit notable limitations [6]. A high temperature during air drying can cause significant losses in polyphenols [7], particularly due to the degradation of compounds like oleuropein. Sun drying requires significant space and time, with minimal control over the process. Additionally, the leaves are exposed to dust and environmental contamination [8].

Modern drying methods, such as microwave drying, offer promising alternatives. Microwave drying generates volumetric heating, significantly shortening treatment time [9,10]. This minimizes the risk of alterations caused by prolonged heating in conventional processes. The combination of optimal heating power and shorter processing times helps preserve thermolabile compounds, maintain antioxidant activity, and reduce changes in the organoleptic and sensory properties of the products, particularly in terms of texture, color, taste, and aroma [11,12].

Despite its advantages, research on microwave drying remains limited, particularly regarding mathematical modeling and its impact on antioxidant preservation. Current models tend to overlook an integrated approach that could combine both mathematical modeling and the analysis of biological properties, which is crucial for improving outcomes [13].

This study presents an integrated approach to optimize microwave drying of olive leaves by combining mathematical modeling with an analysis of parameters influencing antioxidant retention. Thin-layer kinetic modeling is applied, testing 52 models to identify the best fit. A new drying kinetics model is proposed to improve the prediction of moisture removal dynamics and energy efficiency under varying microwave power levels. The study employs a multimodal approach, integrating advanced experimental techniques and detailed modeling of heat and mass transfer. Key parameters analyzed include drying time, microwave power, moisture content (MC), drying rates (DR), and effective moisture diffusivity (D_{eff}). Energy analysis includes activation energy (Ea), specific energy consumption (SECe), and energy efficiency (EE). Furthermore, the study evaluates both qualitative and quantitative properties of dried olive leaves, such as total phenolic content (TPC), total flavonoid content (TFC), and Radical scavenging activity (RSA), using principal component analysis (PCA) to explore relationships between drying conditions and product quality.

RESULTS AND DISCUSSION

Drying kinetics

In this study, the effect of varying microwave power levels on the drying of olive leaves was assessed, focusing on the relationship between relative moisture content and drying time. The drying curves obtained for each microwave power level are presented in Figure 1. These curves illustrate the evolution of MR in olive leaves over time (minutes) under different power settings: 100, 400, 700, and 1000 W. The variation in the time required to reach a constant weight of 7.55 ± 0.46 g is depicted. The results reveal a clear inverse correlation between microwave power and drying time. At 100 W, the drying time is 280 minutes. When the power is increased to 400 W, the drying time decreases to 31 minutes. Further power increases reduce the drying time to 21 minutes at 700 W and 19 minutes at 1000 W. An increase in microwave power leads to a significant reduction in the drying time of olive leaves, particularly between 100 W and 400 W. However, beyond 400 W, the effect on drying time becomes less pronounced, suggesting that an optimal power threshold exists around 700 and 1000 W.

These findings demonstrate that higher microwave power levels accelerate the drying process by enabling more efficient energy absorption by water molecules. In agreement with [14], our results show that increasing

power enhances the rate of moisture evaporation, thereby shortening drying times. However, while higher power levels lead to reduced drying durations, it is essential to monitor the potential effects on product quality [15].

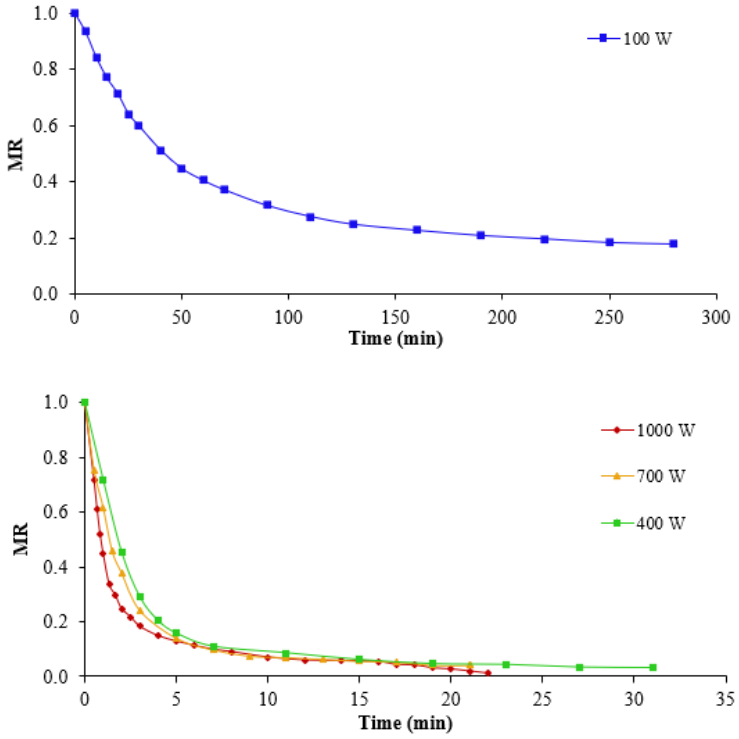

Figure 1. Evolution of the experimental moisture content with drying time for olive leaves at different microwave power levels

Mathematical modeling of drying kinetics

The drying kinetics of olive leaves were analyzed using 52 mathematical models to describe the MR over time under various microwave powers. The results, including statistical analyses and key metrics such as drying constants, model coefficients, R^2, χ^2, and RMSE for the best-performing models, are summarized in Appendix A.

The analysis showed that the Logarithmic, Modified Henderson and Pabis II, and the Modified Hii et al. models emerged as the best-fit models and the most effective based on their high R^2 values and the low χ^2 and

RMSE values. For these optimal models, R^2 values ranged from 0.999054 to 0.999937, χ^2 values ranged from 0.000015 to 0.002829, and RMSE values ranged from 0.002905 to 0.039889.

These results demonstrate the exceptional performance of the selected models in fitting the experimental data. The three models effectively predict the drying kinetics of olive leaves across various microwave power settings, providing a high degree of precision in simulating the drying dynamics. This accuracy suggests that these models are valuable tools for modeling and optimizing the drying process of olive leaves.

Compared to previous studies, our findings align with those reported by [16,17]. These studies validated the suitability of various models for defining drying curves of medicinal plants and crops dried in thin layers. Including the modified Henderson and Pabis models for *Piper umbellatum* L. leaves [18] and S. *terebinthifolius* leaves [19]. The Hii model has been validated as the best model for coriander leaves [20] and cocoa beans [21]. Additionally, the logarithmic model was applied to *Moringa oleifera* leaves [22], scent leaves, and lemon basil leaves [3].

Validation of the proposed model

In this study, a new double-exponential drying kinetics model was used. The constants a, b, c, K_1, and K_2 showed a strong correlation with the moisture ratio. The numerical values are summarized in Appendix A.

Residual analysis was performed to validate the proposed model. The results indicate an excellent correlation between the experimental and predicted data, with an R^2 value of 0.9992. Considering the overall fit, the residuals are very close to zero and randomly distributed, confirming the model's reliability. The RMSE values ranged from 0.00573 to 0.00985, while χ^2 values varied between 4.16×10^{-5} and 0.0002927, further demonstrating the model's high accuracy in fitting the experimental data.

Drying rates VS. moisture content

The drying rates of olive leaves as a function of moisture content are shown in Figure 2. The drying curves exhibit a sigmoidal shape, reflecting significant variations in the drying rate due to both moisture content and microwave power. Initially, the drying rate increases rapidly as microwave heating removes moisture, followed by a slower decline as the moisture content decreases and drying becomes less efficient.

The drying process can be divided into two distinct phases. During the initial heating phase, the drying rate increases significantly as the microwave power increases, particularly between 100 W and 400 W. At

100 W, the drying rate is 0.251 × 10^{-3} g water/g DM, while at 400 W, it increases to 5.238 × 10^{-3} g water/g DM, indicating a significant acceleration of moisture removal in the initial phase. At higher power levels (700 and 1000 W), the drying rates are similar with 9.143 × 10^{-3} and 10.551 × 10^{-3} g water/g DM, respectively. However, the increase in drying speed stabilizes beyond 400 W, indicating that the efficiency reaches a plateau at higher power levels rather than showing further significant improvements. Following this, in the decelerating phase, the drying rate decreases gradually. Notably, no constant-rate drying period is observed; all drying occurs during the falling-rate phase.

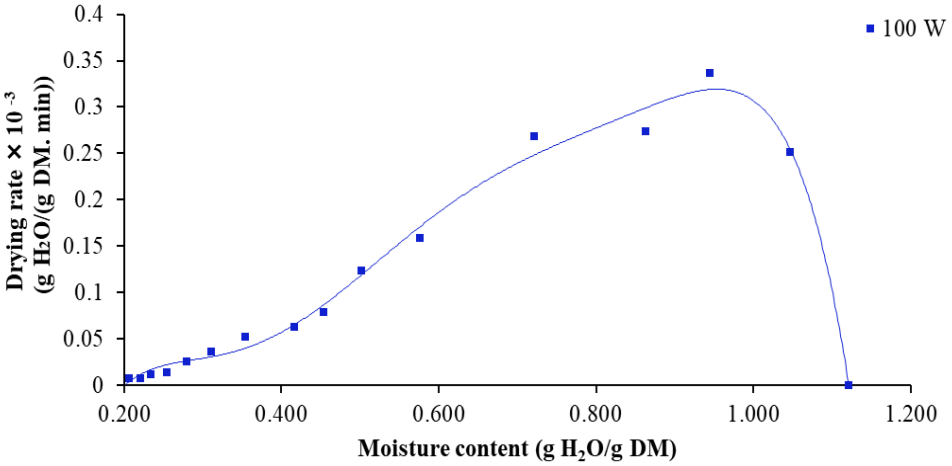

Figure 2. Variation of drying rate with moisture content of olive leaves dried at different microwave power levels

The average DR values recorded are 0.1097 × 10^{-3}, 1.274 × 10^{-3}, 1.7296 × 10^{-3}, and 2.1275 × 10^{-3} g water/ g DM. Sec for microwave powers of 100, 200, 400, and 1000 W, respectively. These results indicate that 700 W and 1000 W are the optimal power levels for rapid and efficient drying. The drying speed increases significantly between 100 W and 400 W, and then stabilizes at higher power levels, such as 700 W and 1000 W.

This behavior aligns with the principles of microwave drying, where higher microwave power enhances volumetric heating efficiency, accelerating heat and moisture transfer [23]. However, it is essential to monitor the temperature to prevent local overheating, which could potentially affect the bioactive properties of the leaves [24].

These findings are consistent with previous studies [25,26], affirming that microwave drying exhibits a characteristic model with an initial rapid drying phase followed by a period of decreasing rates, significantly influenced by microwave power. These observations highlight the importance of controlling microwave power to optimize the drying process while maintaining the quality of the final product [6].

Effective moisture diffusivity

Understanding the mass transfer mechanisms in materials subjected to microwave drying fundamentally relies on effective diffusivity. The values of D_{eff} were determined under different microwave power levels (100 W, 400 W, 700 W, and 1000 W) and are presented in Table 1.

Table 1: Impact of microwave power on diffusivity during olive leaf drying

Power (W)	D_{eff} 10^{-10} ± SD
100	0.78 ± 0.16 [c]
400	20.01 ± 2.83 [b]
700	22.1 ± 0.48 [b]
1000	30.78 ± 039 [a]

Distinct letters within each column indicate statistically significant differences according to the ANOVA followed by Tukey's post-hoc test ($p<0.05$). with the order reflecting the magnitude of the results ($a > b > c$)

The D_{eff} values obtained during microwave drying ranged from 0.78×10^{-10} to 30.78×10^{-10} m^2/s, depending on the applied power. This interval is consistent with biologically active dried products [27].

The D_{eff} values increased significantly with increasing microwave power, ranging from 0.78×10^{-10} m^2/s at 100 W to 30.78×10^{-10} m^2/s at 1000 W. Statistical analysis indicated significant differences among the different power levels. Specifically, the D_{eff} at 100 W was significantly lower than those observed at higher power levels (400 W, 700 W, and 1000 W), which showed substantial increases in diffusivity.

These findings are consistent with previous studies on microwave drying, where higher power levels increased moisture diffusivity due to enhanced energy transfer and water vaporization rates [28]. The rapid volumetric heating at higher powers promoted moisture migration, leading to greater D_{eff} values. The notable rise in D_{eff} at 1000 W indicates a stronger thermal gradient and higher vapor pressure within the olive leaf matrix,

facilitating more efficient moisture removal. This increase in D_{eff} can be explained by two key factors: reduced water viscosity and higher kinetic energy of water molecules at elevated power levels [29]. Microwave heating directly energizes water molecules, causing rapid temperature increases. However, careful control is necessary to prevent thermal imbalances, which could affect drying uniformity and product quality [28]. These results underscore the importance of optimizing microwave power for efficient drying.

Total energy balance

Activation energy

Figure 3 shows the relationship between effective moisture diffusivity and the sample ratio (m/P). This trend allows for the evaluation of different samples based on their moisture diffusivity throughout the drying process. The obtained values for the pre-exponential factors D_0 and Ea are 4.33×10^{-9} m^2/s and 26.94 W /g, respectively.

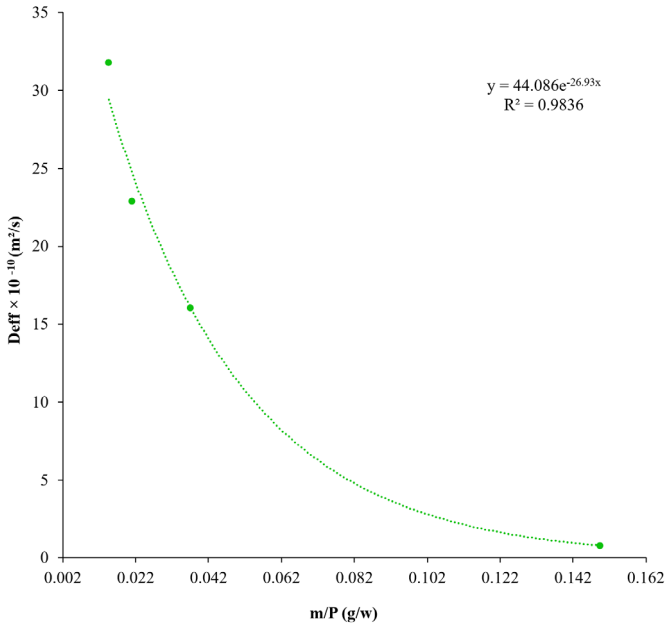

Figure 3. Arrhenius plot for calculating the drying activation energy of olive leaves

These results indicate a moderate activation energy, reflecting relatively efficient heat transfer within the material. The high diffusivity value highlights

the effectiveness of the microwave drying process, facilitating rapid moisture removal. This efficiency is crucial for achieving uniform drying and minimizing drying time, due to the process's homogeneity [30,31].

Similarly, previous studies in the literature revealed that the *Ea* value aligns with those reported for thermal diffusion processes in similar matrices, typically between 20 and 30 W/g. This consistency with previous studies supports the validity of the experimental method and conditions used [30].

Specific energy consumption and electrical energy

The results for specific energy consumption and energy efficiency at each power level for drying olive leaves are presented in Table 2. SEC values show statistically significant variation across power levels. The lowest SEC is observed at 700 W, with a value of 0.236×10^5 MJ/kg H_2O, suggesting that a moderate increase in power optimizes energy efficiency.

Table 2: Energy efficiency and specific energy consumption of olive leaf drying at different power levels

Power (W)	EE ± SD ($\times 10^{-2}$ %)	SEC ± SD ($\times 10^5$ MJ/kg H_2O)
100	133.506 ± 5.52 ^{d}	1.694 ± 0.0630 ^{a}
400	798.896 ± 7.37 ^{b}	0.283 ± 0.0352 ^{c}
700	963.824 ± 3.79 ^{a}	0.236 ± 0.0144 ^{c}
1000	219.837 ± 8.66 ^{c}	1.029 ± 0.0035 ^{b}

Values are expressed as mean ± standard deviation. Different letters within the same row indicate significant differences between treatments (ANOVA followed by Tukey's test $p<0.05$. a>b>c)

In contrast, higher SEC values at both lower (100 W) and higher (1000 W) power levels indicate inefficiencies, likely due to insufficient energy input at low power and excess thermal losses at high power. EE values vary significantly across power levels, with the highest efficiency observed at 700W, achieving 963.82×10^{-2} %. This suggests that intermediate power levels optimize energy use, while the lowest efficiency is seen at 100W, indicating a notable decrease in energy effectiveness at low power settings.

The results indicate that an intermediate power level of 700W balances energy input and process efficiency, minimizing SEC while maximizing EE. This inverse relationship between SEC and EE is consistent with previous studies showing that moderate power levels optimize energy use by balancing demand with evaporation rates [32–34].

Biological effect

Total phenolic content

Figure 4 illustrates the total phenolic content of olive leaves dried at various microwave powers. As the microwave power increased from 100 W to 700 W, TPC was significantly affected by the microwave power ($p < 0.05$), reaching a peak at 700 W with a value of 108.79 mg AGE/g DM.

However, a non-significant decrease was observed when the power increased from 700 W to 1000 W. These results might be due to the sensitivity of phenolic compounds to low microwave power (100 W), which requires a longer drying duration and might lead to increased degradation of these compounds. A moderate to high microwave power (700 and 1000 W) seems optimal for maximizing TPC. A similar trend has been observed in microwave drying, where an increase at higher power levels followed an initial decrease in total phenolic content [35], although beyond 500W, the TPC began to decline. Additionally, microwave drying of coriander leaves has demonstrated an enhancement in total phenolic content at higher power levels. Higher microwave power levels increase temperature and vapor pressure within plant tissues. This elevation may cause cell walls to rupture, facilitating the release of phenolic compounds, including those bound to the cell walls [13].

Total flavonoid content

Flavonoids are a diverse group of naturally occurring plant compounds known for their antioxidant properties. The effect of microwave drying on the flavonoid content of olive leaves was evaluated, with results shown in Figure 4. The data indicates that the average flavonoid concentrations ranged from 11.13 to 12.21 mg RE/g DM, depending on the microwave power levels applied. However, no statistically significant differences were observed between these values.

These findings suggest that variations in microwave power do not significantly impact the final flavonoid concentration in olive leaves. This is consistent with other studies on food products [18,36,37], which have also shown that changes in drying conditions, including microwave drying, do not substantially affect flavonoid content.

Radical scavenging activity

The antioxidant capacity of olive leaves dried under varying microwave power levels, assessed through the ABTS assay, is illustrated in Figure 4. The results showed that higher microwave power increased antioxidant activity,

with values of 23.25 and 23.49 mg GAE/g DM with no significant difference at 700 W and 1000 W, respectively. In contrast, at 100 W, antioxidant activity was lower, with values of 20.24 mg GAE/g DM.

The results show that higher microwave power levels enhance the preservation and activation of antioxidant compounds in olive leaves. At 700 W and 1000 W, antioxidant activity remained consistent, suggesting these power levels provide optimal conditions for maximizing antioxidant benefits.

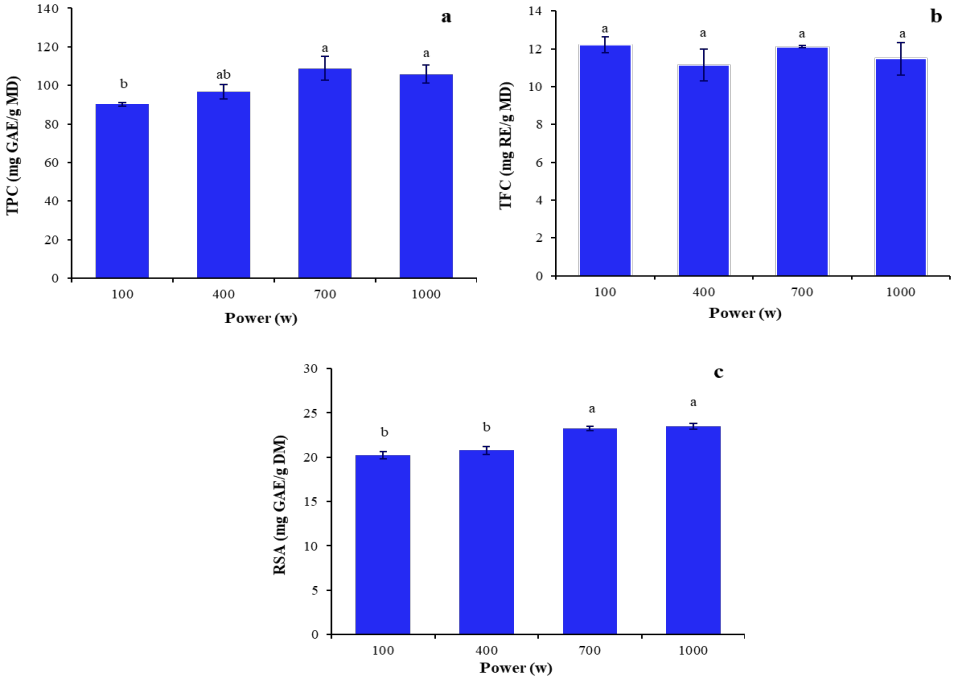

Figure 4. Impact of microwave drying power levels on TPC (a), TFC (b), and RSA (c) of olive leaves with different letters indicate significant differences between treatments (ANOVA followed by Tukey's test $p<0.05$, a>b>c)

This may be due to the reduced drying time and controlled thermal exposure, which minimize the degradation of bioactive compounds [8]. In contrast, at 100 W, lower antioxidant activity was observed, probably due to insufficient activation of bioactive compounds and potential degradation from prolonged exposure to lower power. Findings align with previous studies indicating that higher microwave power enhances the bioactive potential of plant material leaves [13,37].

Multivariate statistical analysis

Principal component analysis (PCA) was performed to reduce the dataset's dimensionality and highlight the key relationships among the studied variables (Figure 5). The analysis revealed that the first two components, PC1 and PC2, explained 72.1% and 15.5% of the total variance, respectively, cumulatively accounting for 87.6% of the variance. This high cumulative variance indicates the effectiveness of the dimensionality reduction in capturing the primary patterns within the data.

The loading plot demonstrated that PC1 was predominantly associated with RSA, TPC, and DPPH, all of which showed strong positive loadings. This finding highlights the significant contribution of higher phenolic content to antioxidant activity, consistent with the established role of phenolic compounds as key antioxidants. In contrast, PC2 exhibited weaker associations with TFC and drying time, suggesting that these parameters contributed less to the overall variance.

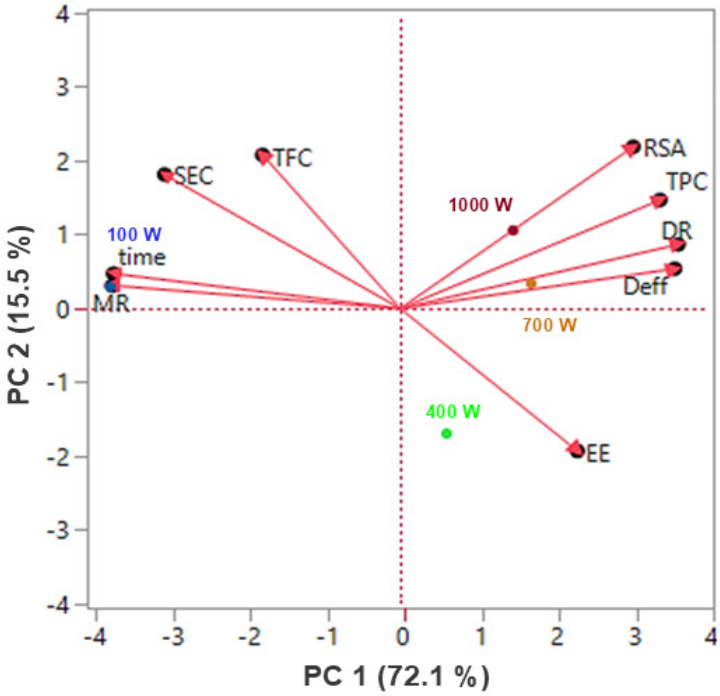

Figure 5. Principal component analysis of drying data for olive leaves
Biplot showing the relationships between principal components (PC1 and PC2) and the variables t, MR, DR, Deff, SEC, EE, TPC, TFC, and RSA across microwave power levels.

The score plot further revealed clear distinctions among samples processed at different microwave power levels. Samples treated at 700 W and 1000 W were clustered in the positive quadrant of PC1, reflecting higher TPC, RSA, and extraction efficiency (EE). These results underscore the benefits of higher microwave power in promoting the extraction of bioactive compounds. Conversely, samples processed at lower microwave power levels (100 W and 400 W) were positioned in the negative quadrants of PC1 and PC2, corresponding to lower phenolic content and antioxidant activity.

Correlations within the dataset further reinforced these trends. RSA exhibited strong positive correlations with TPC and EE, underscoring the role of extraction efficiency in determining antioxidant activity. On the other hand, drying time was negatively correlated with RSA and TPC, indicating that prolonged drying under lower power levels compromised the retention of bioactive compounds.

These findings highlight the importance of rapid, high-power drying techniques in preserving phenolic compounds and antioxidant properties.

CONCLUSIONS

This study optimized the microwave drying process of olive leaves by balancing drying power, time, bioactive compound preservation, and energy efficiency. The Logarithmic, Modified Henderson, Pabis II, and Hii et al. models demonstrated strong predictive accuracy for drying kinetics. Additionally, a new proposed model showed the best correlation with experimental data, confirmed by high R^2 values and low χ^2 and RMSE values.

Drying at 700 W and 1000 W preserved bioactive compounds effectively, with significant antioxidant retention. Principal component analysis confirmed that samples dried at these power levels exhibited higher bioactive compound extraction. Among these, 700 W for 21 minutes provided the best compromise, ensuring optimal compound preservation, superior energy efficiency, and economic feasibility. While 1000 W slightly reduced drying time (19 min), 700 W offered a more balanced approach, making it the most advantageous condition.

The novel proposed model holds great potential for designing and optimizing olive leaf drying processes. These findings highlight microwave drying as an efficient and sustainable technique for preserving bioactive compounds, with promising applications in functional foods and phyto-therapeutic sciences, reinforcing its industrial relevance.

EXPERIMENTAL SECTION

Chemicals and reagents

The reagents and chemicals used in this study were obtained from reputable sources. Folin-Ciocalteu's phenol reagent, sodium carbonate hydrate (Na_2CO_3), and aluminum chloride reagent ($AlCl_3$) were obtained from Chimoza (France). Gallic acid and rutin were obtained from Sigma-Aldrich (Germany). Methanol (CH_3OH), ethanol (C_2H_5OH), potassium persulfate, and 2,2-Azino-bis (3-ethylbenzothiazoline-6-sulfonic acid) diammonium salt (ABTS) were purchased from Biochem-Chemo Pharma (USA).

Initial moisture content

The initial moisture content (M_0) of fresh olive leaves was determined in triplicate. A 15 g sample was heated at 105 ± 2°C for 24 hours. The final moisture content was calculated based on the weight loss due to water evaporation, using the dry basis (db) method. This calculation was performed by determining the water weight on a dry basis, as described in Eq. 1.

$$M_{0,db}(g\ water/g\ \ dry\ matter) = \frac{W_i - W_f}{W_f} \quad (1)$$

Where M_0 is the initial moisture content (g), W_i is the initial weight of the sample (g) and W_f is the final weight of the sample (g).

Microwave drying experiments

The drying process was conducted using a digital microwave oven (Maxipower MASMO23S) with the following specifications: 230 V and a frequency of 50 Hz. The microwave's internal space measured 483 (W) * 281 (H) * 387 (D) mm and included a rotating glass plate with a diameter of 300 mm at the base. Drying experiments were performed at four different power levels: 100, 400, 700, and 1000 W, with both the power output and drying time adjusted via the microwave's digital control system.

During the trials, 15 g samples of olive leaves were arranged in a single layer on a glass plate and placed in the center of the microwave. Moisture loss was periodically assessed by weighing the samples at specific intervals: every 30 seconds at 1000 W, every 1 minute at 700 W, every 2 minutes at 400 W, and every 5 minutes at 100 W. A precision balance (AS 220.R2, Radwag, Radom, Poland) with an accuracy of 0.001 g was used for these measurements. Each experiment was replicated three times, and the average values were recorded. The heating continued until the samples reached equilibrium moisture, indicated by a constant weight of 7.55 ± 0.46 g.

Mathematical modeling of drying kinetics

Mathematical modeling is essential for accurately simulating drying kinetics and understanding the behavior of drying processes under specific conditions. This study employs 52 mathematical models (Table 3) to identify the most suitable models under varying drying powers. From the initial moisture content of olive leaves, the moisture content data at different time intervals, and the residual moisture contents, the dimensionless moisture ratio was calculated using Eq. 2.

$$MR = \frac{M_t - M_e}{M_0 - M_e} \quad (2)$$

Where MR is the moisture ratio, M_t, M_e, and M_0 refer to the moisture content at any time during drying (g H_2O/g DM), the equilibrium moisture content (g H_2O/g DM), and the initial moisture content (g H_2O/g DM), respectively.

Theoretically, equilibrium can only be reached after an infinitely long drying period. As a result, for extended drying times, the equilibrium moisture content (Me) is often disregarded and assumed to be zero. As a result, the moisture ratio can be simplified to Eq. 3 [34].

$$MR = M_t/M_0 \quad (3)$$

Table 3. Mathematical models adopted for curve fitting of drying data of olive leaves

	Name	***Mathematical equation***
1	*Ademiluyi Modified*	$MR = a.exp\ (-kt)^n$
2	*Aghbashlo et al.*	$MR = exp(-k_1t/1+k_2\ t)$
3	*Alibas*	$MR=a\ exp\ [(-kt)^n + bt\_]+g$
4	*Balbay and Şahin*	$MR = (1 - a)\ exp\ (-\ kt^n\ )+b$
5	*Chavez-Mendez et al.*	$MR = (1-[1-L_2]\ L_1t)^{1/(1-L2)}$
6	*Das et al.*	$MR = a.exp(-kt + b\sqrt{t})+c$
7	*Demir et al.*	$MR = a.exp\ (-kt)^{\ n} + b$
8	*Diffusion approach*	$MR = a.exp\ (-kt) + (1 - a)\ exp\ (-\ kbt)$
9	*Fernando and Amarasinghe*	$MR = 1 + at + bt^2 / (1 + ct)$
10	*Gauss*	$MR = a.exp\ (-(t+b)^2/2c^2)$
11	*Haghi and Angiz – I*	$MR = a.exp(-bt^n\ ) + ct^2 + dt + e$
12	*Haghi and Angiz – II*	$MR = a + bt + ct^2 + dt^3$
13	*Haghi and Angiz – III*	$MR = a + bt/\ (1 + ct + dt^2)$
14	*Haghi and Angiz – IV*	$MR = a.exp\ [-(t - b)^2/2c^2]$
15	*Hasibuan and Daud*	$MR = 1 - at^n\ exp\ (-kt^m)$
16	*Henderson and Henderson I*	$MR = c\ [exp\ (-bt) +1/9\ exp\ (-9kt)]$
17	*Henderson and Henderson II*	$MR = c\ exp\ (-bt) +1/9\ exp\ (-9kt)$

	Name	**Mathematical equation**
18	Henderson and Pabis	$MR = a.exp(-kt)$
19	Hii et al.	$MR= a.exp(-kt^n) + b.exp(-gt^n)$
20	Kaleta I	$MR = a\ exp(-kt^n) + (1-a)\ exp(-gt^n)$
21	Khazaei and Daneshmandi	$MR = a + exp(-bt) - ct$
22	Logarithmic (Asymptotic)	$MR = a.exp(-kt) + c$
23	Logistic	$MR =b/ (1+a\ exp(-kt)) +kt$
24	Meda et al.	$MR = a.exp(m+n)t^{1.5}$
25	Midilli	$MR = a.exp(-kt^n) + bt$
26	Modifie Henderson and Perry	$MR = a.exp(-kt^n)$
27	Modified drying	$MR = a+exp(-kt^n)$
28	Modified Henderson and Pabis I	$MR = a.exp(-kt) + b.exp(-gt) + c.exp(-ht)$
29	Modified Henderson and Pabis II	$MR = aexp(-kt^n) + bexp(-gt) + c\ exp(-ht)$
30	Modified Hii et al.	$MR = a\ exp(-kt^m) + c\ exp(-gt^n)$
31	Modified Midilli I	$MR = exp(-kt^n) + bt$
32	Modified Midilli II	$MR = exp(-kt) + bt$
33	Modified Midilli III	$MR = a.exp(-kt) + bt$
34	Modified Page equation V	$MR = exp[-(kt^n)]$
35	Modified Page equation-III	$MR = exp[-(-kt)^n]$
36	Modified Page equation-IV	$MR = a.exp[-(kt^n)]$
37	Modified Page equation-IX	$MR= k.exp[(-t/L^2)^n]$
38	Modified Page equation-VI	$MR = exp(kt^n)$
39	Modified Page equation-VII	$MR= exp[-k.(t/L^2)^n]$
40	Modified Page equation-VIII	$MR= exp\{-[k.(t/L^2)]^n\}$
41	Modified Page II	$MR = exp[\ -(kt)^n]$
42	Modified Two-term I	$MR = a\ exp(-kt) + (1 - a)\ exp(-kat)$
43	Modified Two-term II	$MR = a\ exp(kt) + (1 - a)\ exp(-gt)$
44	Verma et al	$MR = a\ exp(-kt) + (1- a)\ exp(-gt)$
45	Two-term exponential	$MR = a\ exp(-kt) + a\ exp(-gt)$
46	Modified Two-term V	$MR = a\ exp(-kt^n) + b\ exp(-gt)$
47	Multiple Multiplicative Factor	$MR= (a.b+c.t^d)/ (b+t^d)$
48	Newton	$MR = exp(-kt)$
49	Page	$MR = exp(-kt^n)$
50	Parabolic	$MR = c + bt + at^2$
51	Peleg	$MR = 1 - t/(a + bt)$
52	Regression I	$MR = exp(\ -(at^2+bt)\ )$
53	Proposed model	$MR=a+ b\ exp(-k_1t) +c\ exp(-k_2t)$

k. k_0. k_1. k_2. g: drying coefficients (1/min); a. b. c. d. e. L. L_1. L_2: coefficients of the equations; ^{n}. ^{m}: exponent; t - time (min); L: half of thickness (m)

Drying rate

The drying rate (DR) of olive leaves at different powers was calculated using Eq. 4.

$$DR = \frac{M_{t+dt} - M_t}{dt} \quad (4)$$

Where DR is the drying rate (g H_2O/g DM), Mt + dt is the MC at t + Δt (g H_2O/g DM), Mt is the moisture content (MC) at t (g H_2O/g DM), and dt is the difference in drying time (min).

The relationship between DR and time was analyzed through graphical plots to assess the drying behavior.

Effective moisture diffusivity

Effective diffusivity quantifies a material's ability to facilitate moisture movement from its interior to the surface, where evaporation occurs. This is based on thermodynamics and fluid kinetics, especially Fick's second law [38]. Understanding and measuring D_{eff} is essential for optimizing drying conditions, improving energy efficiency, and ensuring product quality. To calculate D_{eff}, the analytical solution of Fick's second law (Eq. 5) was applied, as described by Crank [39].

$$\frac{\partial M}{\partial t} = \frac{\partial_t}{\partial_x}\left(D_{eff}\frac{\partial M}{\partial_x}\right) \quad (5)$$

For extended drying periods, Eq. 6 can be simplified by considering only the first term of the series, resulting in Eq. 7.

$$MR = \frac{8}{\pi^2}\sum_{n=0}^{\infty}\frac{1}{(2n+1)^2}e^{\left(\frac{(2n+1)^2\pi^2}{4L^2}\right)D_{eff}t} \quad (6)$$

$$MR = \frac{8}{\pi^2}e^{\left(-\frac{\pi^2}{4L^2}D_{eff}\,t\right)} \quad (7)$$

where D_{eff} represents the effective moisture diffusivity (m^2/s), L refers the sample thickness (L = 2.211 ×10^{-3} m), and t represents the drying time (s)

A logarithmic form, Eq. 8, was therefore introduced, applicable when moisture diffusivity remains constant at each drying temperature, resulting in a linear relationship between the logarithmic moisture ratio and drying time. However, in our case, the experimental logarithmic drying curve is not linear. This suggests that the effective moisture diffusivity depends on moisture content, which is common for highly porous materials [20].

$$ln(MR) = \frac{8}{\pi^2} - \frac{\pi^2 D_{eff}t}{4L^2} \quad (8)$$

The plot of ln (MR) against drying time should produce a straight line with the following slope:

$$Slope = \left(\frac{\pi^2}{4L^2} D_{eff} \right) \quad (9)$$

Therefore, Eq. 10 is evaluated numerically for the Fourier number F_0 for diffusion.

$$F_0 = D_{eff} \times \frac{t}{L^2} = -0.101\ ln\ (MR) - 0.0213 \quad (10)$$

The effective moisture diffusivity was determined using Eq. 11 [40].

$$D_{eff} = \frac{F_0}{\left(\frac{t}{4L^2}\right)} = \frac{-0.101\ ln\ (MR) - 0.0213}{\left(\frac{t}{4L^2}\right)} \quad (11)$$

Activation energy

The activation energy (Ea) for the diffusion process during drying represents the energy required to initiate the movement of water from the material during the drying process [26], which describes the relationship between the D_{eff} and temperature. In microwave-assisted drying processes, the Arrhenius equation is often modified to incorporate the power of the microwave. [31] use the correlation between the effective diffusion coefficient and microwave power (m/P) to calculate Ea, as shown in Eq. 12.

$$D_{eff} = D_0\ e^{\left(\frac{-Ea\ m}{P}\right)} \quad (12)$$

Where Ea is the activation energy (W/g), m is the mass of the raw sample (g), D_{eff} is the effective diffusivity (m^2/s), D_0 is the pre-exponential factor (m^2/s), P is the power (W).

Energy consumption

Energy consumption during the drying process is a critical parameter that directly impacts the efficiency and cost-effectiveness of dehydration techniques, especially microwave drying. In this study, the energy consumption for drying olive leaves was assessed using specific energy consumption and electrical energy efficiency metrics The energy consumption required for the microwave drying was directly measured using a wattmeter (PEREL, E305EM6, Germany).

Specific electric energy consumption was determined using Eq. 13 to quantify the energy used to remove a kilogram of water from the sample. This index is crucial for assessing the efficiency of the drying process and optimizing energy usage.

$$SEC\left(\frac{\mathrm{MJ}}{\mathrm{kg}}\mathrm{H2O}\right) = \frac{3600\,E}{M_s(Xi - Xf)} \quad (13)$$

Where SEC is specific energy consumption, represented (kWh/kg water removed), E is the total energy consumed (kWh), and Ms (Xi-Xf) is the mass of water removed (kg).

Additionally, electrical energy was calculated using Eq. 14 to evaluate the proportion of energy effectively used to evaporate the water content from the sample.

$$EE\ (\%) = M_s(Xi - Xf)\ \frac{\Delta hv}{3600\ \times\ E} \times 100 \quad (14)$$

where EE is the electrical energy efficiency (%), M_s (Xi-Xf) is the mass of water removed (kg), Δhv is the enthalpy of evaporation of water (2257 kJ/kg at 100°C), and E is the total energy consumed (kWh).

Ultrasonic-assisted extraction of bioactive compounds

To extract the bioactive compounds from dried olive leaves at different powers, 2 g of olive leaf powder were combined with 25 mL of a 70:30 (v/v) ethanol-water. The mixture was subjected to ultrasound treatment with an ultrasonic bath (UCI-150, R. Espinar SL, Barcelona, Spain) operating at 40 kHz and a power of 400 W. The extraction was performed at 45°C for 10 minutes. The sample was centrifuged at 5000 × g for 10 min at 4°C, using a SIGMA 3–30K centrifuge (Germany), and the supernatant was recovered. The remaining pellet was reextracted using the same volume of solvent under the same conditions, and the extracts were combined. Ethanol was removed using a rotary evaporator, and the aqueous phase was subsequently lyophilized to obtain the dry extract.

Total phenolic content (TPC)

TPC of the olive leaf extracts was determined using the Folin-Ciocalteu method [41]. A 20 µL aliquot of the diluted extract was mixed with 100 µL of Folin-Ciocalteu reagent (diluted 1:10 with distilled water) and 80 µL of sodium carbonate solution (7.5%). The mixture was incubated at room temperature for 30 min, and the optical density was measured at 760 nm using a microplate reader (BioTek Synergy HTX). Results were expressed as gallic acid equivalents (mg GAE/g DM).

Total flavonoid content (TFC)

The aluminum chloride method determined the total flavonoid content [42]. A 100 µL aliquot of the diluted extract was mixed with 100 µL of $AlCl_3$ solution (2% in ethanol). After incubation at room temperature for 10 min, the absorbance was measured at 430 nm using a microplate reader. Results were expressed as rutin equivalents (mg RE/g DM).

Radical scavenging activity (RSA)

The ABTS assay was used to determine the antioxidant capacity of olive leaf extracts [43]. The ABTS radical cation was generated by reacting 7 mM ABTS with potassium persulfate and incubating the mixture in the dark for 12 hours. The resulting $ABTS^{\bullet+}$ solution was diluted with ethanol to achieve an absorbance of 0.70 ± 0.02 at 734 nm. A 20 µL aliquot of the diluted olive leaf extract was mixed with 180 µL of the $ABTS^{\bullet+}$ solution. After a 10-minute incubation period, the absorbance was measured at 734 nm using a microplate reader (BioTek Synergy HTX). The scavenging potential of the extracts was quantified as milligrams of gallic acid equivalent per gram of dry matter (mg GAE/DM).

Data analysis

Mathematical modeling and statistical analyses were performed using STATISTICA software 10.0. Drying kinetics were modeled through nonlinear regression, and the software provided key parameters, including the Root Mean Square Error (RMSE) using Eq. 15, coefficient of determination (R^2) derived from Eq. 16, and chi-square (χ^2) using Eq. 17. A new drying kinetics model was proposed and validated using JMP® Pro 14.0.0 software (SAS Institute Inc., USA) employing nonlinear regression and model optimization, along with Microsoft Excel (Microsoft Office 2019, USA) for additional data processing. Statistical significance was assessed using one-way analysis of variance (ANOVA) followed by Tukey's post-hoc test, with a significance level set at $P < 0.05$ [20].

$$RMSE = \sqrt{\sum_{i=1}^{N} \frac{\left(MR_{pre,i} - MR_{exp,j}\right)^2}{N}} \quad (15)$$

$$R^2 = \frac{\sum_{i=1}^{N}\left(MR_{exp,i} - \overline{MR}_{exp}\right)^2\left(MR_{pre,i} - \overline{MR}_{pre}\right)^2}{\sum_{i=1}^{N}\left(MR_{exp,i} - \overline{MR}_{exp}\right)^2 \sum_{i=1}^{N}\left(MR_{pre,i} - \overline{MR}_{pre}\right)^2} \quad (16)$$

$$\chi^2 = \sum_{i=1}^{N} \frac{\left(MR_{pre,i} - MR_{exp,j}\right)^2}{N - Z} \quad (17)$$

Where, $MR_{exp,i}$ is the experimental moisture ratio at observation, $MR_{pre,i}$ is the predicted moisture ratio at this observation, N is the number of experimental data points, and Z is the number of coefficients and constants.

Principal component analysis was conducted using XLSTAT software to assess a range of variables, including drying time, MR, DR, D_{eff}, SEC, EE, TPC, TFC, RSA.

ACKNOWLEDGMENTS

We express our gratitude to the Ministry of Higher Education and Scientific Research, particularly the Directorate-General for Scientific Research and Technological Development (DGRSDT). We also thank all members of the Laboratory of Applied Biochemistry for their support.

SUPPORTING INFORMATION

Appendix A is available to download: https://doi.org/10.5281/zenodo.19102031

REFERENCES

1. A. Silvestrini, C. Giordani, S. Bonacci, A. Giuliani, D. Ramini, G. Matacchione, J. Sabbatinelli, S. Di Valerio, D. Pacetti, A.D. Procopio, A. Procopio, M.R. Rippo, Anti-Inflammatory Effects of Olive Leaf Extract and Its Bioactive Compounds Oleacin and Oleuropein-Aglycone on Senescent Endothelial and Small Airway Epithelial Cells, *Antioxidants*. *12* (**2023**). https://doi.org/10.3390/antiox12081509.
2. S. Feng, C. Zhang, L. Liu, Z. Xu, T. Chen, L. Zhou, M. Yuan, T. Li, C. Ding, Comparison of phenolic compounds in olive leaves by different drying and storage methods, *Separations*. *8* (**2021**) 1–10. https://doi.org/10.3390/separations8090156.
3. N.N. Mbegbu, C.O. Nwajinka, D.O. Amaefule, Thin layer drying models and characteristics of scent leaves (Ocimum gratissimum) and lemon basil leaves (Ocimum africanum), *Heliyon*. *7* (**2021**) e05945. https://doi.org/10.1016/j.heliyon.2021.e05945.
4. A.E. Stępień, J. Gorzelany, N. Matłok, K. Lech, A. Figiel, The effect of drying methods on the energy consumption, bioactive potential and colour of dried leaves of Pink Rock Rose (Cistus creticus), *J. Food Sci. Technol. 56* (**2019**) 2386–2394. https://doi.org/10.1007/s13197-019-03656-2.
5. M. Popescu, P. Iancu, V. Plesu, C.S. Bildea, F.A. Manolache, Mathematical Modeling of Thin-Layer Drying Kinetics of Tomato Peels: Influence of Drying Temperature on the Energy Requirements and Extracts Quality, *Foods*. *12* (**2023**). https://doi.org/10.3390/foods12203883.

6. I.D. Boateng, D.A. Soetanto, X.M. Yang, C. Zhou, F.K. Saalia, F. Li, Effect of pulsed-vacuum, hot-air, infrared, and freeze-drying on drying kinetics, energy efficiency, and physicochemical properties of Ginkgo biloba L. seed, *J. Food Process Eng*. *44* (**2021**) 1–14. https://doi.org/10.1111/jfpe.13655.
7. A. Boukhiar, S. Benamara, Y. Bouchal, K. Touderte, S. Messouidi, High-temperature Thin-layer Drying Kinetic of Cultivated and Wild Algerian Olive Leaves Modeling and Effect on Oleuropein and Chlorophyll Contents, *Period. Polytech. Chem. Eng. 66* (**2022**) 660–674. https://doi.org/10.3311/PPch.20264.
8. J. Sánchez-García, S. Muñoz-Pina, J. García-Hernández, A. Heredia, A. Andrés, Impact of Air-Drying Temperature on Antioxidant Properties and ACE-Inhibiting Activity of Fungal Fermented Lentil Flour, *Foods. 12* (**2023**). https://doi.org/10.3390/foods12050999.
9. E.M. Ramírez, M. Brenes, C. Romero, E. Medina, Olive Leaf Processing for Infusion Purposes, *Foods. 12* (**2023**) 12–14. https://doi.org/10.3390/foods12030591.
10. A. Cagliari, T.R. Martiny, R. Nascimento, M.M. Morais, G.S. da Rosa, Effects of different drying conditions on bioactive potential of Brazilian olive leaf, Brazilian *J. Food Technol. 25* (**2022**) 1–16. https://doi.org/10.1590/1981-6723.14721.
11. N.A. AlFaris, J.Z. AlTamimi, L.A. AlMousa, F.A. AlGhamidi, N.A. Albaridi, Date-derived industries: A review of common products, manufacturing methods, and leading countries, *Emirates J. Food Agric. 34* (**2022**) 86–97. https://doi.org/10.9755/ejfa.2022.v34.i2.2825.
12. R. ElGamal, C. Song, A.M. Rayan, C. Liu, S. Al-Rejaie, G. ElMasry, Thermal Degradation of Bioactive Compounds during Drying Process of Horticultural and Agronomic Products: A Comprehensive Overview, *Agronomy. 13* (**2023**). https://doi.org/10.3390/agronomy13061580.
13. B.S. Kalsi, S. Singh, M.S. Alam, S. Bhatia, Microwave Drying Modelling of Stevia rebaudiana Leaves Using Artificial Neural Network and Its Effect on Color and Biochemical Attributes, *J. Food Qual. 2023* (**2023**). https://doi.org/10.1155/2023/2811491.
14. S. Swain, Mathematical Modelling of Microwave Assisted Dehydration of Osmotically Pretreated Yellow Sweet Pepper (Capsicum annum L), *J. Nutr. Heal. Food Eng. 1* (**2014**) 1–11. https://doi.org/10.15406/jnhfe.2014.01.00013.
15. T.P. Krishna Murthy, B. Manohar, Microwave drying of mango ginger (Curcuma amada Roxb): Prediction of drying kinetics by mathematical modelling and artificial neural network, *Int. J. Food Sci. Technol. 47* (**2012**) 1229–1236. https://doi.org/10.1111/j.1365-2621.2012.02963.x.
16. K. Ponkham, N. Meeso, S. Soponronnarit, S. Siriamornpun, Modeling of combined far-infrared radiation and air drying of a ring shaped-pineapple with/without shrinkage, *Food Bioprod. Process. 90* (**2012**) 155–164. https://doi.org/10.1016/j.fbp.2011.02.008.
17. Z. Erbay, F. Icier, Thin-layer drying behaviors of olive leaves (Olea europaea L.), *J. Food Process Eng. 33* (**2010**) 287–308. https://doi.org/10.1111/j.1745-4530.2008.00275.x.
18. L. do Nascimento Silveira Dorneles, A. Luís Duarte Goneli, C. Andrea Lima Cardoso, C. Bezerra da Silva, M. Rosemari Hauth, G. Cardoso Oba, V.

Schoeninger, Effect of air temperature and velocity on drying kinetics and essential oil composition of Piper umbellatum L. leaves, *Ind. Crops Prod. 142* (**2019**) 111846. https://doi.org/10.1016/j.indcrop.2019.111846.
19. A.L.D. Goneli, M. Do Carmo Vieira, H. da C. Benitez Vilhasanti, A. Alves Gonçalves, Mathematical modeling and effective diffusion of schinus terebinthifolius leaves during drying, *Pesqui. Agropecu. Trop. 44* (**2014**) 56–64. https://doi.org/10.1590/s1983-40632014000100005.
20. O.O. Olabinjo, A.I. Asamu, I.O. Filani, Mathematical modelling of drying kinetics of coriander leaves (Coriandrum sativum L.) using a convective dryer, *Ann. Food Sci. Technol. 21* (**2020**) 31–39.
21. C.L. Hii, C.L. Law, S. Suzannah, Drying kinetics of the individual layer of cocoa beans during heat pump drying, *J. Food Eng. 108* (**2012**) 276–282. https://doi.org/10.1016/j.jfoodeng.2011.08.017.
22. S. Ambawat, A. Sharma, R.K. Saini, Mathematical Modeling of Thin Layer Drying Kinetics and Moisture Diffusivity Study of Pretreated Moringa oleifera Leaves Using Fluidized Bed Dryer, *Processes. 10* (**2022**). https://doi.org/10.3390/pr10112464.
23. M.I.H. Khan, C.P. Batuwatta-Gamage, M.A. Karim, Y.T. Gu, Fundamental Understanding of Heat and Mass Transfer Processes for Physics-Informed Machine Learning-Based Drying Modelling, *Energies. 15* (**2022**).
24. J.-W. Dai, W. Qin, Z.-J. Wu, Y.-L. Bian, L.-H. Zhang, Drying Kinetics of Papaya Slices in Microwave Intermittent Dryer, *Proc. 2017 7th Int. Conf. Adv. Des. Manuf. Eng.* (ICADME 2017). *136* (**2017**) 177–182. https://doi.org/10.2991/icadme-17.2017.35.
25. [D. Kaur, A.A. Wani, D.S. Sogi, U.S. Shivhare, Sorption isotherms and drying characteristics of tomato peel isolated from tomato pomace, *Dry. Technol. 24* (**2006**) 1515–1520. https://doi.org/10.1080/07373930600961371.
26. S. Bennaceur, A. Berreghioua, L. Bennamoun, A. Mulet, B. Draoui, M. Abid, J.A. Carcel, Effect of ultrasound on henna leaves drying and extraction of lawsone: Experimental and modeling study, *Energies. 14* (2021). https://doi.org/10.3390/en14051329.
27. E.A.A. Elhussein, S. Şahin, Drying behaviour, effective diffusivity and energy of activation of olive leaves dried by microwave, vacuum and oven drying methods, *Heat Mass Transf. Und Stoffuebertragung. 54* (**2018**) 1901–1911. https://doi.org/10.1007/s00231-018-2278-6.
28. S. Karimi, N. Layeghinia, H. Abbasi, Microwave pretreatment followed by associated microwave-hot air drying of Gundelia tournefortii L.: drying kinetics, energy consumption and quality characteristics, *Heat Mass Transf. Und Stoffuebertragung. 57* (**2021**) 133–146. https://doi.org/10.1007/s00231-020-02948-0.
29. E. Demirhan, B. Özbek, Microwave-drying characteristics of basil, *J. Food Process. Preserv. 34* (**2010**) 476–494. https://doi.org/10.1111/j.1745-4549.2008.00352.x.
30. A. Madan, A. Pare, N.G.N. A, Mathematical Modelling of Thin-layer Drying Process of Bamboo (Bambusa bambos) Shoots at Varying Temperature, *Res. Rev. J. Bot. 3* (**2014**) 1–9. www.stmjournals.com.

31. A. Arslan, Y. Soysal, M. Keskin, Mathematical Modeling, Moisture Diffusion and Color Quality in Intermittent Microwave Drying of Organic and Conventional Sweet Red Peppers, *AgriEngineering. 2* (**2020**) 393–407. https://doi.org/10.3390/agriengineering2030027.
32. G. Huelsz, L. Urbiola-Soto, F. López-Alquicira, R. Rechtman, G. Hernández-Cruz, Total Energy Balance Method for Venting Electric Clothes Dryers, *Dry. Technol. 31* (**2013**) 576–586. https://doi.org/10.1080/07373937.2012.746977.
33. N.R. Nwakuba, V.C. Okafor, Energy Indices and Drying Behaviour of Alligator Pepper Pods (Aframomum Melegueta) as Influenced by Applied Microwave Power, *J. Energy Technol. Environ. 2* (**2020**) 74–93. https://doi.org/10.37933/nipes.e/2.2020.8.
34. S. Guemouni, K. Mouhoubi, F. Brahmi, F. Dahmoune, A. Belbahi, C. Benyoub, N. Adjeroud-Abdellatif, K. Atmani, H. Bakhouche, L. Boulekbache-Makhlouf, K. Madani, Convective and microwave drying kinetics and modeling of tomato slices, energy consumption, and efficiency, *J. Food Process Eng. 45* (**2022**). https://doi.org/10.1111/jfpe.14113.
35. B. Nayak, F. Dahmoune, K. Moussi, H. Remini, S. Dairi, O. Aoun, M. Khodir, Comparison of microwave, ultrasound and accelerated-assisted solvent extraction for recovery of polyphenols from Citrus sinensis peels, *Food Chem. 187* (**2015**) 507–516. https://doi.org/10.1016/j.foodchem.2015.04.081.
36. N. Vural, Z. Yilmazer Hitit, S. Ertunç, Multi-objective optimization of drying conditions for the Olea europaea L. leaves with NSGA-II, **2021**. https://doi.org/10.1111/jfpp.15625.
37. O. Content, M.K. Marevci, The Effect of Drying Methods and Extraction Techniques on (**2022**).
38. B. Ameri, S. Hanini, M. Boumahdi, Influence of drying methods on the thermodynamic parameters, effective moisture diffusion and drying rate of wastewater sewage sludge, *Renew. Energy. 147* (**2020**) 1107–1119. https://doi.org/10.1016/j.renene.2019.09.072.
39. J.W. Westwater, H.G. Drickamer, The Mathematics of Diffusion, *J. Am. Chem. Soc. 79* (**1957**) 1267–1268. https://doi.org/10.1021/ja01562a072.
40. H. Darvishi, J. Khodaei, M. Azadbakht, The parameters of mass transfer of convective drying in sliced melon, *Philipp. Agric. Sci. 98* (**2015**) 60–72.
41. S. Zaidi, N. Chaher-Bazizi, T. Kaddour, Z. Medjahed, N. Benaida-Debbache, Optimization of ultrasound-assisted extraction of phenolic compounds from Pistacia lentiscus with the study of their antioxidant and anti-inflammatory potential, *Sustain. Chem. Pharm. 41* (**2024**) 101678. https://doi.org/10.1016/j.scp.2024.101678.
42. N. Saidene, N. Chaher, B. Radia, K. Dina, A. Kilani, D. Atmani, Optimization of green ultrasound - assisted extraction of phenolic compounds from Crataegus laciniata leaves and assessing for antioxidant activity , enzyme inhibition , and UPLC - ESI - MS - MS guided identification of metabolites, *Chem. Pap.* (**2024**). https://doi.org/10.1007/s11696-024-03745-3.
43. L. Shi, W. Zhao, Z. Yang, V. Subbiah, H.A.R. Suleria, Extraction and characterization of phenolic compounds and their potential antioxidant activities, *Environ. Sci. Pollut. Res. 29* (**2022**) 81112–81129. https://doi.org/10.1007/s11356-022-23337-6.

STUDIA UBB CHEMIA, LXXI, 1, 2026 (p. 101-119)
(RECOMMENDED CITATION)
DOI:10.24193/subbchem.2026.1.07

EFFECT OF FLUID VISCOSITY ON FLUIDIZATION HYDRODYNAMICS AN EXPERIMENTAL AND COMPARATIVE STUDY

Nassima KECHROUD[a*], Hamid TIGHZERT[a]

ABSTRACT. In this study, we conducted an experimental investigation of the fluidization behavior of spherical glass particles with diameters *dp*=2 mm and *dp*=4 mm, using Newtonian fluids (aqueous sugar solutions). The influence of fluid viscosity on key global hydrodynamic characteristics of fluidization was examined, including the minimum fluidization velocity, the terminal settling velocity of the particles, and bed expansion. Experiments were carried out in a cylindrical glass column with an inner diameter of *D*=20 mm and a height of *H*=1500 mm.

The minimum fluidization velocity and bed expansion were determined experimentally for different solid–liquid systems. The experimental results were compared with various correlations from the literature. It was found that the results are in good agreement with some of these correlations, particularly for bed porosity values below 0.6.

Keywords: *Fluidization; Newtonian fluid; hydrodynamic; effect of viscosity; expansion; minimum fluidization velocity; terminal settling velocity.*

INTRODUCTION

A fluidized bed is a system widely used in chemical engineering, where solid particles are suspended by an upward-flowing fluid (gas or liquid) resulting in a fluid-like behavior known as fluidization. This process occurs when the upward drag force exerted by the fluid counterbalances the weight of the particles, allowing them to remain suspended. Compared to fixed beds,

[a] *Department of Process Engineering, Faculty of Technology, Environmental Engineering Laboratory, Abderrahmane Mira University, Bejaia, Algeria*
* *Corresponding author: nassima.kechroud@univ-bejaia.dz*

fluidized beds offer a significantly larger interfacial area between the solid particles and the fluid, enhancing phase interactions and transport processes [1-3]. This continuous movement promotes efficient heat and mass transfer, making fluidized beds highly suitable for a broad range of industrial applications. These include the chemical, petrochemical, pharmaceutical, metallurgical, biochemical, food processing, and waste treatment sectors, where fluidized beds are employed for operations such as particle coating, drying, combustion (fluidized-bed boilers), crystallization, and catalytic cracking [4]**.** Fluidized beds are also being examined for novel applications such as adsorption cooling and sustainable energy systems, demonstrating their ongoing industrial and environmental relevance [5].

The investigation of Newtonian fluidized bed hydrodynamics focuses on quantifying key parameters such as minimum fluidization velocity, pressure drop, and bed expansion. These are essential for the effective design, operation, and control of reactors. Over the past decades, considerable research has led to various empirical and semi-empirical correlations [2,6,7]. Despite the extensive development of this field, it remains of significant interest due to current industrial demands for improved energy efficiency, reduced costs, and stricter environmental regulations. In parallel, recent advances in computational fluid dynamics (CFD) and coupled CFD–Discrete Element Method (CFD-DEM) modeling have heightened the demand for high-quality experimental data to validate numerical predictions [8]. Accurate experimental characterization of Newtonian fluidized beds is therefore essential to improve existing correlations and to provide a reliable baseline for investigating more complex systems involving non-Newtonian fluids. In such systems, rheological effects strongly influence hydrodynamic behavior, making the prediction of key parameters, such as minimum fluidization velocity and bed expansion, considerably more challenging [4,9].

The main objective of the present study is to evaluate the influence of the rheological behavior of the fluid on key hydrodynamic characteristics, particularly the minimum fluidization velocity and bed expansion. The results obtained will be compared with established empirical correlations from the literature. Both minimum fluidization velocity and bed expansion are among the most influential parameters governing the dynamic behavior of fluidized beds. A comprehensive understanding of these factors is crucial in any effort to design predictive, adaptable, and efficient fluidized systems. This is precisely why the topic has long been, and continues to be, the subject of sustained research interest [10].

THEORETICAL BACKGROUND

Minimum Fluidization Velocity

The minimum fluidization point, marking the transition between a fixed and a fluidized bed, is typically characterized by the minimum fluidization velocity (U_{mf}) and the corresponding bed void fraction (ε_{mf}). Classical approaches, such as the Ergun correlation [1], estimate U_{mf} using fixed-bed equations while assuming specific values for ε_{mf} and the particle sphericity factor Φ. However, this method presents limitations, notably the need for parameters that are often difficult to determine experimentally. To address these issues, several researchers, including Riba et al. [11] and Coltters & Rivas [7], have developed simplified correlations.

Correlation of Riba et al. (1978)

Riba et al. [11] developed an empirical correlation to estimate the minimum fluidization velocity U_{mf} in fluidized beds. Their work aimed to improve the accuracy of predictions by taking into account a wide range of experimental conditions. The correlation relates U_{mf} to key physical properties such as particle diameter (d_p)**,** particle and fluid densities $(\rho_s; \rho_f)$, and fluid viscosity (μ):

$$Re_{mf} = 0.0154 \times Ga^{0.66} \times Mn^{0.7} \quad (1)$$

Where Re_{mf}, *Ga* and *Mv* are defined as:

$$Re_{mf} = \frac{\rho_f U_{mf} d_p}{\mu} ; Ga = \frac{d_p^3 \rho_f g}{\mu^2} ; Mn = \frac{\rho_s - \rho_f}{\rho_f} \quad (2)$$

Correlation of Coltters and Rivas (2004)

Coltters and Rivas (7] compiled 189 experimental measurements from the literature, covering approximately 89 different materials (sand, coal, polymers, glass, etc.) fluidized by a gas phase. For each material, the authors established a correlation that differs significantly from those commonly found in the literature. To predict the minimum fluidization velocity for glass particles with an average diameter between 569 µm and 3000 µm, the authors proposed the following correlation:

$$U_{mf} = (2.4624.10^{-3}) X^{(0.46942 \mp 0.01190)} \quad (3)$$

With:

$$X = \frac{d_p^2 (\rho_s - \rho_f) g}{\mu} . \left(\frac{\rho_s}{\rho_f}\right)^{1.23} \quad (4)$$

Porosity and Bed Expansion

Solid–liquid fluidized bed systems are characterized by a progressive and uniform expansion of the bed with increasing liquid velocity. This expansion is typically described in terms of bed porosity (or void fraction) *e*. The expansion process occurs between the minimum fluidization velocity and the terminal settling velocity of the particles, during which the bed height increases as a function of liquid velocity.

A widely used approach to determine the void fraction is based on measuring the expanded bed height, *H*.

$$\varepsilon = 1 - \frac{m_p}{HS\rho_S} \tag{5}$$

Where $\mathrm{m_p}$ is the mass of solid particles (kg), S is the cross-sectional area of the column (m²), and ρ_s is the density of solid particles (kg/m³).

Several correlations have been developed to describe the expansion of solid–liquid fluidized beds. Some of these take into account the terminal settling velocity of the particles (U_t), while others are based on different variables.

Correlations Independent of U_t

Correlation of Wen & Yu (1966)

Among the researchers who have contributed to improving the modeling of liquid fluidized bed expansion, Wen and Yu [2] are frequently cited. Based on a force balance during bed expansion, these authors proposed the following theoretical model:

$$\varepsilon^{-4,7} = \frac{Ga.Mn}{18\,Re + 2{,}7Re^{1{,}687}} \tag{6}$$

Correlation of Miura et al. (2000)

Miura et al. [9] examined the expansion characteristics of a fluidized bed composed of 3 mm glass beads using water and aqueous glycerol solutions as the fluidizing media. For a terminal Reynolds number ranging from 8.14 to 3947, the authors proposed the following correlation:

$$\varepsilon = \left(\left(18\frac{\mu U}{d_p^2} + 3\sqrt{\frac{\mu\rho_f U^3}{d_p^3}} + 0.3\frac{\rho_f U^2}{d_p} \right) \frac{1}{(\rho_s - \rho_f)g} \right)^{0{,}208} \tag{7}$$

Correlations Dependent of U_t

Richardson and Zaki [6] described bed expansion using a correlation between the bed porosity ε and the ratio of the superficial liquid velocity U to the terminal settling velocity U_t of an individual particle, as given by the following expression :

$$\frac{U}{U_t} = \varepsilon^Z \tag{8}$$

Where *Z* is the fluidization index (also known as the Richardson–Zaki exponent), which depends on the particle Reynolds number during settling (Re_t) and the particle-to-column diameter ratio ($\frac{d_p}{D}$). The value of Z is determined using the empirical correlations listed in Table 1.

Table 1: Empirical values of *Z* and applicable Re_t ranges

Correlation	Reynolds number
$z = 4.65 + 19.5\left(\frac{dp}{D}\right)$	$Re_t < 0{,}2$
$z = \left(4.45 + 18\frac{dp}{D}\right) Re_t^{-0.03}$	$0.2 < Re_t < 1$
$z = \left(4.45 + 18\frac{dp}{D}\right) Re_t^{-0,1}$	$1 < Re_t < 200$
$z = 4.45\ Re_t^{-0.1}$	$200 < Re_t < 500$
$z = 2.4$	$500 < Re_t$

Among the different formulas proposed to calculate the terminal Reynolds number (Re_t) or the terminal settling velocity (U_t), those developed by Lali et al. [12] are especially noteworthy. To study how the walls of a container affect the settling speed of particles in water–glycerol mixtures, the authors carried out experiments using nine vertical columns with diameters ranging from 0.9 to 20 cm. They used spherical particles made of glass and steel, with densities of 2500 kg/m³ and 1180 kg/m³, respectively. The particle diameters ranged from 1.2 to 25 mm for glass and from 0.8 to 20 mm for steel. This gave particle-to-column diameter ratios ($\frac{d_p}{D}$) between 0.05 and 0.78.

The authors proposed formulas that cover a wide range of infinite Reynolds numbers (Re_∞), which are listed in Table 2. These correlations allow for the estimation of $Re_¥$ (or $U_¥$) based solely on the Archimedes number.

Table 2: Correlations of Lali et al. (1989)

Correlations	Values of Re_∞	Values of *Ar*
$Re_\infty = \frac{Ar}{18}$	$Re_\infty < 1$	$Ar < 1.8$
$Re_\infty = \left(\frac{Ar}{18}\right)^{0,8}$	$1 < Re_\infty < 56$	$1.8 < Ar < 2600$
$Re_\infty = 0.45 \acute{} Ar^{0,61}$	$56 < Re_\infty < 1000$	$2.6 \acute{} 10^3 < Ar < 3.3 \acute{} 10^5$
$Re_\infty = 1.732 \acute{} Ar^{0,50}$	$Re_¥ > 10^3$	$Ar > 3.3 \acute{} 10^5$

Zigrang and Sylvester [13], building upon the work of Barnea & Mizrahi [14] and Barnea & Mednick [15] on solid–fluid suspensions, proposed an explicit equation for the particle settling velocity in solid–fluid systems. Their equation is expressed in terms of $Re_¥$ and the Archimedes number Ar:

$$Re_t = 1.8329 \acute{} Ar^{1/2} + 29.025 - \left(106.4 \acute{} Ar^{1/2} + 842.45\right)^{1/2} \quad (9)$$

RESULTS AND DISCUSSION

The different systems studied, as well as the ranges of velocity and porosity explored, are summarized in Tables 3 and 4.

It should be noted that the dimensionless Archimedes number (Ar), particle Reynolds number (Rep), Galileo number (Ga), and density ratio (Mv) presented in these tables are calculated using the mean diameter and density of the spherical glass particles studied:

$$Ar = \frac{dp^3 \rho_f (\rho_s - \rho_f) g}{\mu^2}\ ; \quad Ga = \frac{dp^3 \rho_f^2}{\mu^2}\ ; \quad Re_p = \frac{\rho_f U dp}{\mu}\ ; \quad Mn = \frac{(\rho_s - \rho_f)}{\rho_f}$$

Table 3: Experimental study parameters for particles with a diameter of d_p = 2mm and a density of r_p=2554 kg/m^3

m (Pa.s)	r_f (kg/m^3)	U(m/s)	Re	e	Ar	Ga	Mn
0.001	1000	0.014-0.106	28 - 212	0.40-0.76	122000	78480	1.55
0.002	1040	0.0017–0.0427	2 - 46	0.40- 0.58	32833	22554	1.46
0.006	1060	0.014-0.091	29 -196	0.40-0.69	3570	2533	1.41

Table 4: Experimental study parameters for particles with a diameter of d_p = 4mm and a density of r_p=2564 kg/m^3

m(Pa.s)	r_f (kg/m^3)	U(m/s)	Re	e	Ar	Ga	Mn
0.001	1000	0.098-0.024	94-393	0.40-0.64	982000	627840	1.56
0.002	1040	0.091–0.014	29-196	0.40-0.69	264401	180431	1.46
0.006	1060	0.003-0.052	2- 8	0.40-0.59	28754	20266	1.41

Determination of the Minimum Fluidization Velocity

To experimentally determine the minimum fluidization velocity for a given fluid–solid system, we adopted the standard method commonly used [2,16], which involves analyzing the ΔP–U plot. This method requires plotting the pressure drop (ΔP) as a function of the superficial velocity (U) in the fixed bed region and identifying its intersection with the line representing the constant pressure drop in the fluidized bed. For the six (sphere–fluid) systems studied, we plotted the variations in pressure drop as a function of the fluid superficial velocity and graphically determined the minimum fluidization velocity. Measurements were carried out by progressively increasing the flow rate up to the maximum fluidization limit, followed by a gradual decrease in flow rate. As shown in Figure 1, the minimum fluidization velocity corresponds to the point marking the transition between the fixed and fluidized states.

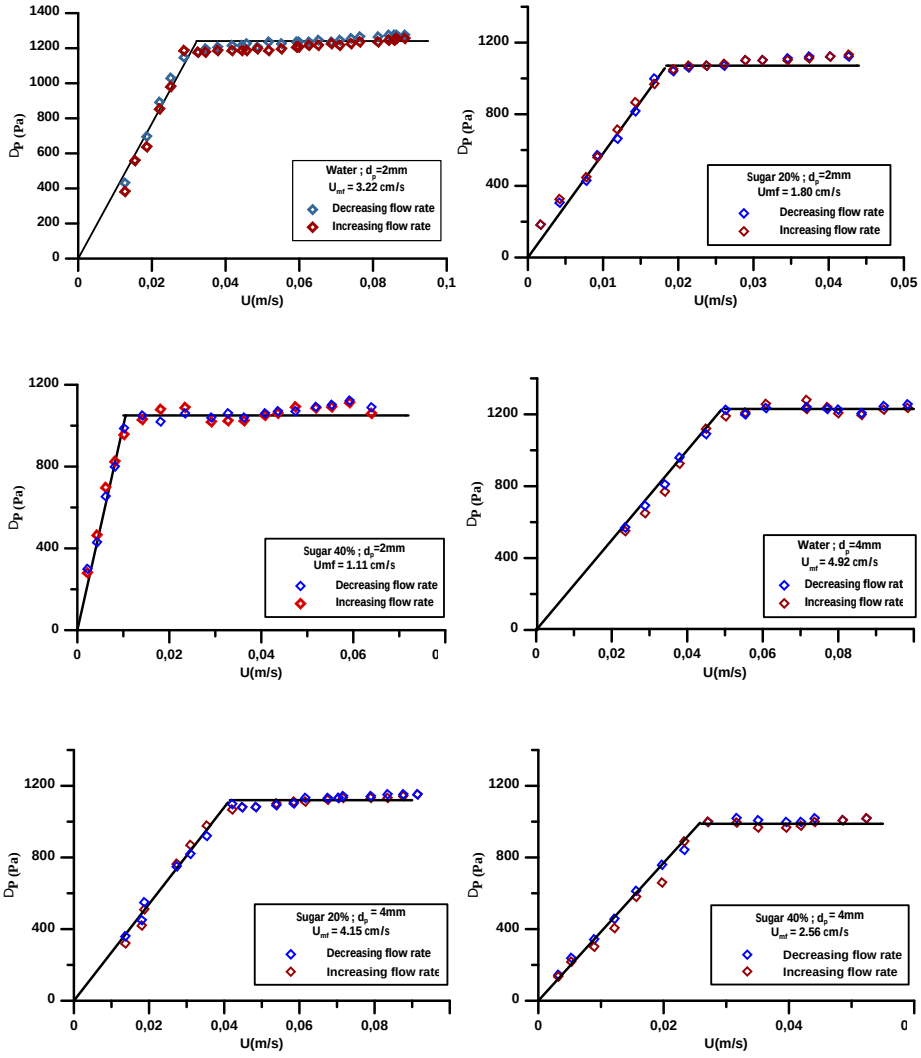

Figure 1: Pressure drop as a function of the fluid superficial velocity

The results are summarized in Table 5.

Table 5: Experimental values of the minimum fluidization velocity for all systems studied

d_p (mm)	μ (Pa.s)	ρ_f (kg/m^3)	U_{mf} (cm/s)
2	0.001	1000	3.22
	0.002	1040	1.80
	0.006	1060	1.11
4	0,001	1000	4.92
	0,002	1040	4.15
	0,006	1060	2.56

The results show that as the viscosity of the solution increases, the minimum fluidization velocity (U_{mf}) decreases. This decrease in U_{mf} can be explained by the fact that viscous forces become significant enough to support the apparent weight of the particles, making it possible to suspend them at lower flow rates.

Comparaison to the Litterature

Because fluidized bed flows involve complex phenomena, a full theoretical explanation is not provided here. Instead, we focus on using mathematical expressions that best describe the observed hydrodynamic behavior. To this end, the experimental results obtained in the present study are compared with those predicted by correlations from the literature.

We compared our experimental results with the minimum fluidization velocities predicted by two empirical correlations of Riba et al. [11] and Coltters and Rivas [7]. These predictions were compared to our experimental data by calculating the relative differences between the U_{mf} values given by the correlations and those measured in the experiments. Table 6 shows the average relative deviation, calculated using the following equation [10]:

$$E\,(\%) = \frac{\left|\left(U_{mf}\right)_{exp} - \left(U_{mf}\right)_{cal}\right|}{\left(\frac{\left(U_{mf}\right)_{exp} + \left(U_{mf}\right)_{cal}}{2}\right)} \times 100 \qquad (10)$$

Table 6: Relative deviations between the experimental minimum fluidization velocity and the values calculated using literature correlations for Newtonian fluidization

d_p (mm)	μ (Pa.s)	$U_{mf\ exp}$ (cm/s)	Riba et al. (1978)			Coltters and Rivas (2004)		
			Re_{mf}	U_{mf} (cm/s)	E%	Re_{mf}	U_{mf} (cm/s)	E%
2	0.001	3.22	35.59	1.78	57.63	58.40	2.92	9.78
	0.002	1.80	14.99	1.44	22.15	21.17	2.03	12.27
	0.006	1.11	3.45	0.98	11.78	4.22	1.19	8.18
4	0.001	4.92	141.02	3.52	33.02	225.33	5.63	13.51
	0.002	4.18	59.12	2.84	37.40	81.67	3.93	5.53
	0.006	2.56	13.67	1.93	28.14	16.27	2.30	10.59

The results obtained show that the accuracy of the correlation by Coltters and Rivas [7] is significantly higher than that of Riba et al. [11], as the observed relative deviations do not exceed 14%.

Bed Expansion and Porosity

Figure 2 shows the evolution of porosity as a function of fluid flow velocity. The porosity values obtained during increasing and decreasing flow rates exhibit minimal discrepancy, with the relative deviation across all systems investigated remaining below 0.1%. Up to the minimum fluidization velocity, porosity remains nearly constant. Beyond this threshold, a gradual increase in porosity is observed with increasing velocity, indicating a progressive expansion of the particle bed.

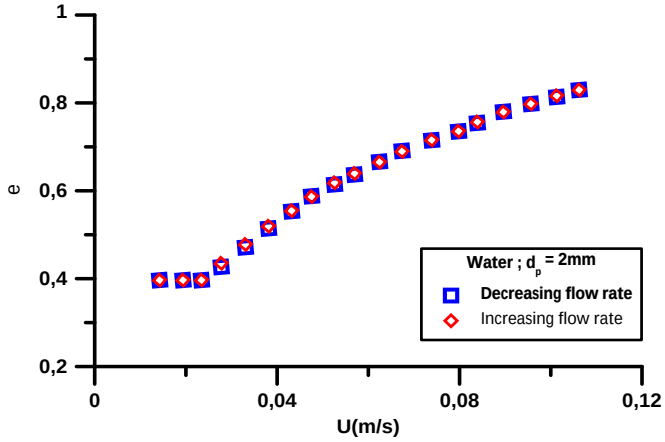

Figure 2: Exemple of the variation of bed porosity as a function of fluid velocity

Effect of Fluid Viscosity on Bed Expansion

Figure 3 presents the variation of porosity as a function of fluid velocity for the three Newtonian fluids investigated: water, and aqueous sugar solutions at 20 wt% and 40 wt%.

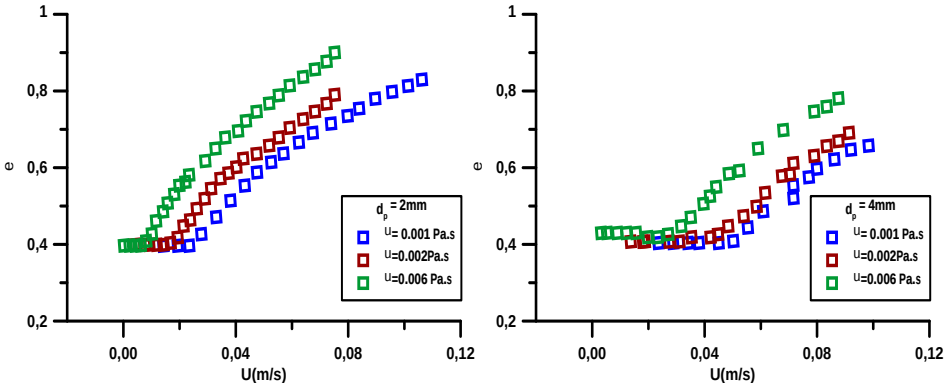

Figure 3: The effect of dynamic viscosity on the porosity evolution of the fluidized bed

It is observed that, for a given flow velocity, the porosity increases with the viscosity of the fluid. Similar observations were reported by Miura et al. [9] in their study on aqueous glycerol solutions (60%, 75%, and 83% by mass).

Correlations involving Ut

A large number of correlations reported in the literature involve the terminal settling velocity U_t. In general, the expansion behavior of fluidized beds is commonly described by the Richardson and Zaki [6] correlation:

$$\frac{U}{U_t} = \varepsilon^Z \qquad (11)$$

Richardson and Zaki [6] demonstrated that the parameter Z, often referred to as the fluidization index, depends solely on wall effects in both laminar and turbulent regimes. In the intermediate regime, however, Z is influenced by both wall effects and the settling Reynolds number Re_t, which is based on the settling velocity of an isolated particle.

To determine the expansion characteristics as predicted by the Richardson and Zaki [6] model, we used the experimental values of U_t obtained in the present study (see Figure 4). The parameter Z was calculated using the correlation proposed by Garside and Al-Dibouni [17].

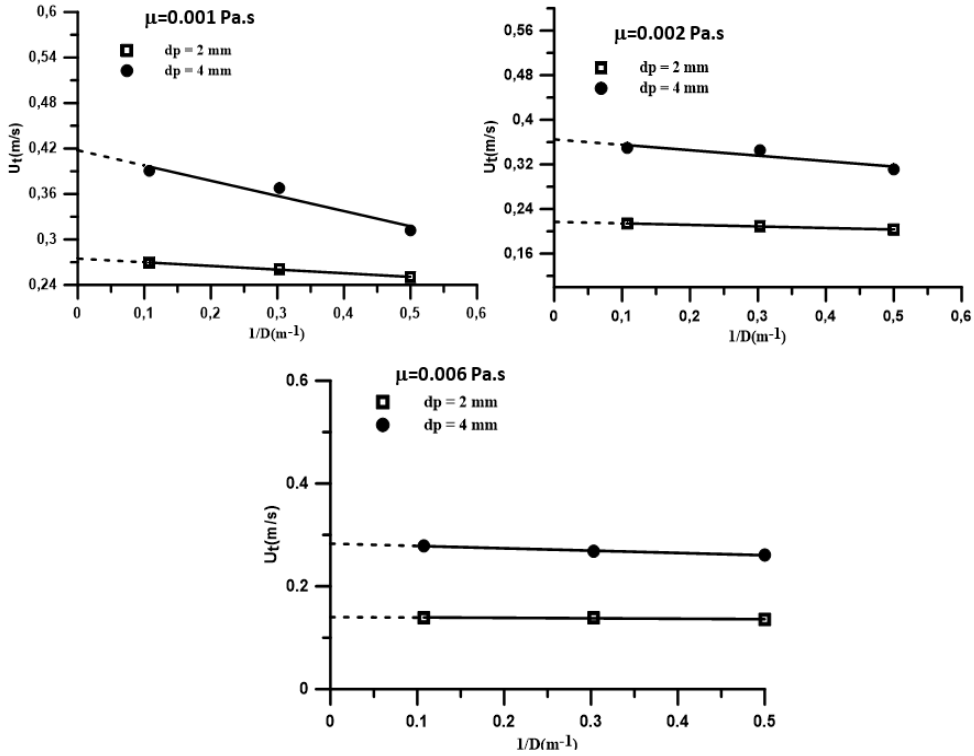

Figure 4: Variation of particle settling velocity with test column diameter

Based on the obtained graphs, the variation appears to be quasi-linear. Consequently, it is relatively easy to determine, by extrapolation, the particle settling velocity in the absence of wall effects U_∞ (corresponding to $D \rightarrow \infty$). The values thus obtained are presented in the following table.

Table 7: Experimental Values of U_∞

r_f (kg/m^3)	m (Pa.s)	d_p = 2 mm		d_p = 4 mm	
		U_∞ (m/s)	Rep_∞	U_∞ (cm/s)	Rep_∞
1000	0.001	0.27	550	0.43	1672
1040	0.002	0.22	232	0.36	783
1060	0.006	0.14	50	0.28	205

Our experimental results were compared with the predictions from the correlations proposed by Lali et al. [12] and Zigrang & Sylvester [13]. The results of this comparison are summarized in the table below.

Table 8: U_∞ Values calculated from selected correlations and comparison with experimental Data

d_p = 2 mm							
ρ_f (kg/m^3)	μ (Pa.s)	U_∞ (m/s)	Rep_∞	Zigrang & Sylvester (1981)		Lali et al. (1989)	
				Rep_∞	E(%)	Rep_∞	E(%)
1000	0.001	0.27	550	474	15	570	4
1040	0.002	0.22	232	219	6	256	10
1060	0.006	0.14	50	54	7	66	28
d_p = 4 mm							
1000	1	0.43	1672	1519	10	2034	20
1040	1,94	0.36	783	736	6	914	15
1060	5,9	0.28	205	202	1	236	14

In light of these results, it can be observed that the Rep_∞ values predicted by the correlation of Zigrang and Sylvester [13] are in better agreement with the experimental values obtained in the present study.

To evaluate the expansion behavior as predicted by the Richardson and Zaki [6] correlation, the experimental terminal velocities (U_t) measured in this study were used. The parameter Z was calculated using the correlation proposed by Garside and Al-Dibouni [17], and the corresponding values are presented in Table 9.

Table 9: Experimental values of U_t and fluidization indices

μ (Pa.s)	d_p = 2 mm			d_p = 4 mm		
	U_t (m/s)	Re_t	Z	U_t (m/s)	Re_t	Z
0.001	0.27	550	2.81	0.43	1672	2.76
0.002	0.22	232	2.90	0.36	783	2.79
0.006	0.14	50	3.27	0.28	205	2.92

Comparison of Fluidized Bed Expansion with Literature Correlations

Figure 5 shows the variation of bed porosity as a function of superficial fluid velocity for the different systems studied, along with predictions obtained from the correlations of Miura et al. [9], Wen and Yu [2], and Richardson and Zaki [6].

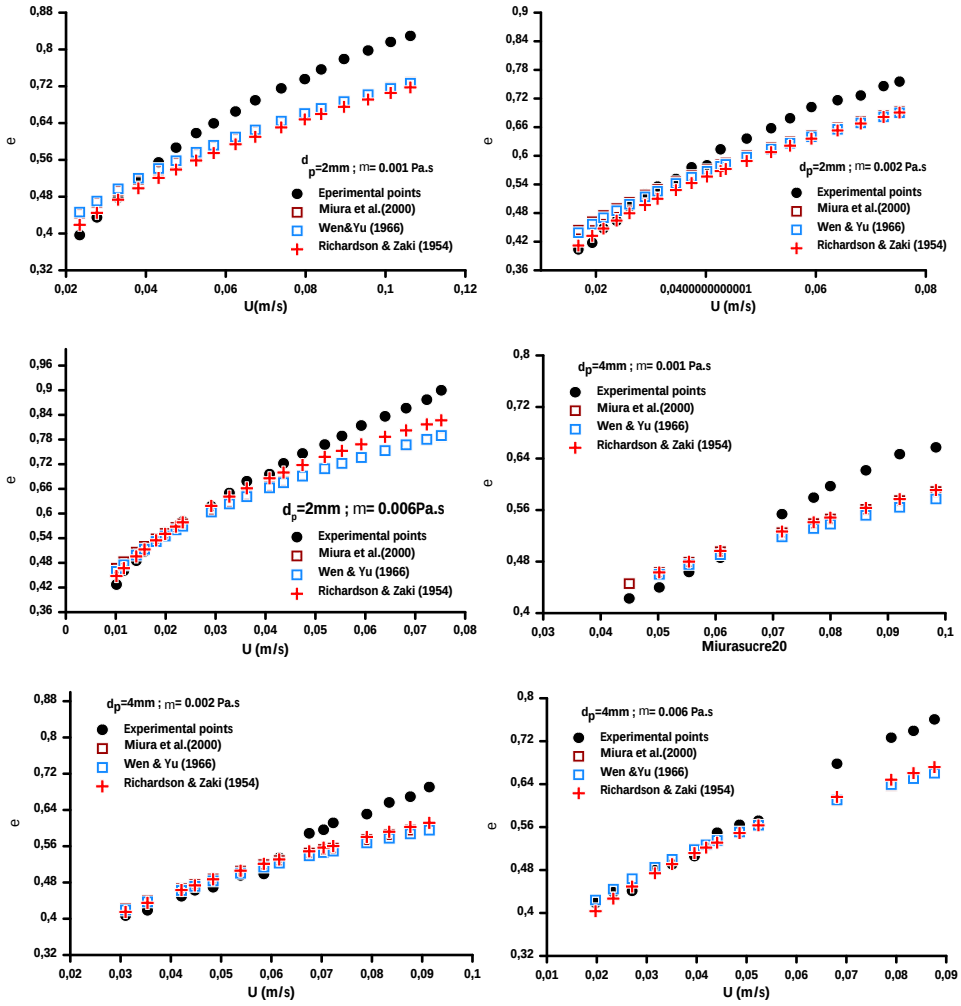

Figure 5: Comparison of bed expansion data with correlations from the literature

To identify the range of porosity in which the predictions can be considered highly satisfactory, the Root Mean Square Error (RMSE) was calculated between the experimental values and those predicted by the selected correlations for each solid–fluid system. The RMSE is computed using the following equation [18]:

$$RMSE = \left(\sum_{i=1}^{n}\left(\frac{\left(\varepsilon_{iexp}-\varepsilon_{ical}\right)^2}{n}\right)\right)^{1/2} \quad (11)$$

where ε_{iexp} denotes the experimental value, ε_{ical} the simulated value, and n the total number of values.

The results, summarized in Tables 10 and 11, show that the RMSE values are highly satisfactory for porosity values below 0.6. However, from ε = 0.6 onwards, the deviation between the calculated and experimental porosity values becomes more significant across all the systems studied.

Table 10: Root mean square errors by porosity range between experimental bed porosity values and those calculated using the selected correlations (for d_p = 2 mm)

RMSE						
m **(Pa.s)**	**0.001**		**0.002**		**0.006**	
Bed Porosity	$\varepsilon < 0.6$	$\varepsilon > 0.6$	$\varepsilon < 0.6$	$\varepsilon > 0.6$	$\varepsilon < 0.6$	$\varepsilon > 0.6$
Miura et al. (2000)	0.03	0.08	0.02	0.05	0.02	0.07
Wen & Yu (1966)	0.03	0.08	0.02	0.05	0.01	0.07
Richardson &Zaki (1954)	0.03	0.09	0.02	0.06	0.01	0.04

Table 11: Root mean square errors by porosity range between experimental bed porosity values and those calculated using the selected correlations (for d_p = 4 mm)

RMSE						
m **(Pa.s)**	**0.001**		**0.002**		**0.006**	
Bed Porosity	$\varepsilon < 0.6$	$\varepsilon > 0.6$	$\varepsilon < 0.6$	$\varepsilon > 0.6$	$\varepsilon < 0.6$	$\varepsilon > 0.6$
Miura et al. (2000)	0.03	0.07	0.02	0.07	0.01	0.09
Wen & Yu (1966)	0.03	0.08	0.02	0.08	0.02	0.08
Richardson &Zaki (1954)	0.03	0.06	0.02	0.06	0.01	0.07

CONCLUSION

In this study, experiments were conducted on a liquid–solid fluidized bed using a glass column with an internal diameter of 2 mm and a height of 150 mm. Glass particles with diameters of 2 mm and 4 mm were fluidized using tap water and aqueous sugar solutions at concentrations of 20 wt% and 40 wt%, maintained at 20 ± 1 °C. The minimum fluidization velocity (U_{mf}) and bed porosity were determined under various operating conditions. Results indicate that U_{mf} decreases with increasing fluid viscosity. The experimental U_{mf} values showed the best agreement with the correlation proposed by Coltters and Rivas [7], with mean relative deviations below 15%. For a given superficial velocity, bed porosity increased with fluid viscosity. Although the Richardson and Zaki [6] correlation, which requires knowledge of the particle terminal settling velocity, provided accurate porosity predictions for values below 0.6, this study demonstrates that such measurements are not essential. In fact, the correlations proposed by Wen and Yu [2] and Miura et al. [9], which do not require settling velocity data, yielded predictions in close agreement with experimental values. These findings confirm that accurate estimation of bed expansion can be achieved without prior knowledge of terminal settling velocity, thereby simplifying the hydrodynamic modeling of liquid–solid fluidized systems.

Future work could extend this study to a broader range of particle and column sizes, as well as to non-Newtonian fluids, thereby broadening the scope of the present results and generating a valuable dataset for establishing correlations and supporting simulation and modeling studies.

EXPERIMENTAL FLUIDIZED BED SETUP

The fluidization of spherical particles using a Newtonian aqueous sugar solution was studied using the experimental setup shown in figure 6-a). The setup consists of a cylindrical glass column (1) with an inner diameter of 2 cm and a height of 150 cm. Different particle beds were placed inside the column, supported by a liquid distributor (2) made of a fine-mesh grid. Since liquid flow can be uneven (following preferential paths), a flow-stabilizing section is positioned before the fluidization column. This homogenization section (3) has the same diameter as the column and a height of 12 cm.

The liquid is circulated from a supply tank (4) using a centrifugal pump (5) with a flow rate of 35 L/min. A thermostat (6), placed directly in the liquid, is used to monitor the temperature. The pipe feeding the column includes a bypass valve (7)

that redirects excess liquid back to the tank if necessary. Two flowmeters (8), installed in parallel after the pump, measure the flow rate. After passing through the column, the liquid flows back to the tank via a conical outlet (collector) (9). The conical shape helps minimize air bubble formation during discharge. The liquid returns to the tank through a small-diameter tube to ensure a steady flow. At the top, a fine-mesh grid (10) separates the return path from the main column. The experimental setup also includes a manometer (11) for measuring pressure within the fluidized bed. A metal ruler (12), marked with a scale, is used to measure the bed expansion.

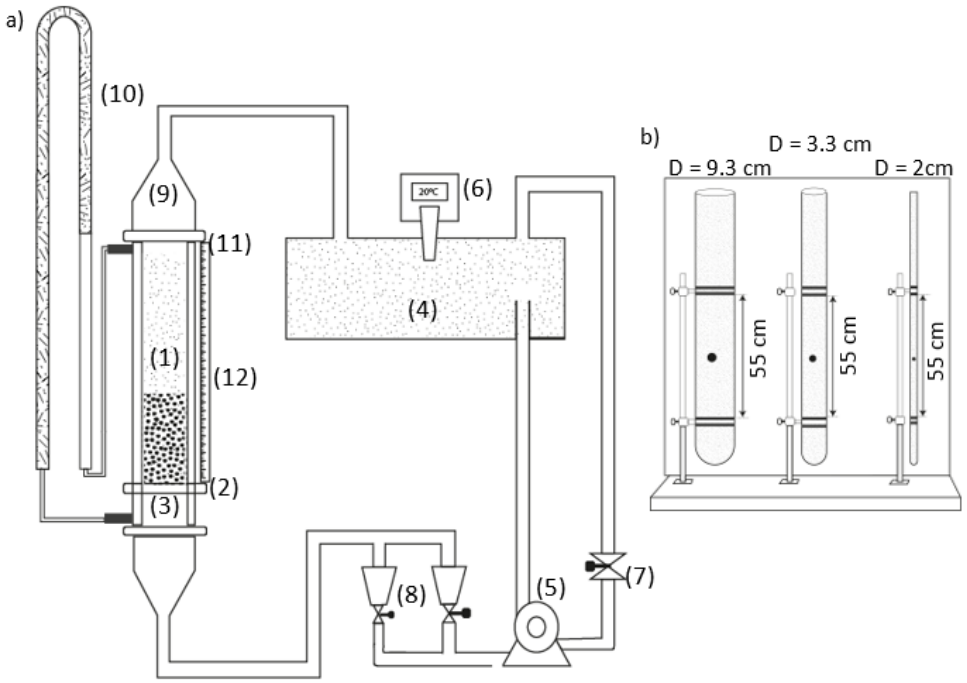

Figure 6: Experimental setup

(1) Test colmun; (2): Liquid distributor; (3): Homogenisation section; (4): Tank; (5): Pump; (6): Themostat; (7): Bypass; (8): Flowmeters; (9): Collector; (10): Manometric rule; (11): Fine-mesh grid; (12): Metal ruler.

The solid particles used in this study are glass spheres, with their physical properties listed in table 12. The fluids used consist of water and Newtonian aqueous sugar solutions containing 20% and 40% sugar by mass. These solutions were prepared by dissolving the appropriate amount of commercial sugar in water under constant stirring until complete dissolution

was achieved. The prepared solutions were then left to stand for 24 hours to allow any entrapped air to escape. The viscosities of the sugar solutions were measured using a HAAKE rheometer equipped with a Couette geometry (two concentric rotating cylinders. Since viscosity is highly sensitive to temperature, the measurement temperature was carefully controlled and is reported to ensure the reliability of the results. The values presented in Table 12 represent the average of three independent measurements for each solution.

Table 12: Fluid and solid properties

Solid properties			
***dp* (mm)**	2	4	
ρ_s (kg/m^3)	2554	2564	
Fluid properties			
Fluid	**Water**	**Sugar solution at 20% w/w**	**Sugar solution at 40% w/w**
ρ_f (kg/m^3)	1000	1040	1060
μ (Pa.s)	0.001	0.002	0.006

To determine the terminal settling velocity of the studied glass particles, experiments were conducted using three vertical columns with internal diameters of 2.0 cm, 3.3 cm, and 9.3 cm (see Figure 6-b)). After thorough cleaning, each column was filled with the test liquid and allowed to stand for approximately 12 hours to eliminate any trapped air bubbles and to ensure uniform fluid conditions. Simultaneously, the glass particles were immersed in the same liquid for about 6 hours to achieve complete wetting and thermal equilibrium. During the measurements, a single particle was released as close as possible to the central axis of the column. The descent time (*t*) was recorded between two fixed positions: 10 cm below the liquid surface and 10 cm above the bottom of the column, in order to minimize entrance and wall effects. The effective falling distance was *L*=55cm. Each test was performed in random order, and multiple repetitions were carried out to minimize measurement uncertainty. For each set of conditions, the reported terminal settling velocity corresponds to the average of at least 20 individual measurements and was calculated using the equation:

$$U_t = \frac{L}{t} \tag{12}$$

ACKNOWLEDGMENTS

The authors are grateful for the financial support of the Ministry of Higher Studies and Scientific Research of Algeria.

REFERENCES

1. S. Ergun**;** *Chemical Engineering Progress,* **1952**, *48*, 89–94.
2. C. Y. Wen; Y. H. Yu; *Chemical Engineering Progress Symposium Series*, **1966**, *62*, 100–111.
3. J. Balag; D. A. T. Franco; V. G. Miral; V. Reyes; L. J. Tongco; E. C. R. Lopez; *Engineering Proceedings*, **2023**, *56*, 62.
4. A. H. Darweesh; M. M. Weis; *Advanced Mechanical and Materials Engineering,* **2024**, *41*, 39–46.
5. Ł. Lasek; A. Zylka; J. Krzywański; D. Skrobek; K. Sztekler; W. Nowak; *Energies*, **2023**, *16*, 7311.
6. J. F. Richardson; W. N. Zaki; *Transactions of the Institution of Chemical Engineers*, **1954**, *32*, 35–53.
7. R. Coltters; A. L. Rivas; *Powder Technology*, **2004**, *147*, 34–48.
8. M. J. A. de Munck; E. A. J. F. Peters; J. A. M. Kuipers; *Industrial & Engineering Chemistry Research,* **2023**, *62*, 16687–16701.
9. H. Miura; T. Takahashi; J. Ichikawa; Y. Kawase; *Powder Technology,* **2001**, *117*, 239–246.
10. A. Kaur; A. Sobti; R. K. Wanchoo; *Industrial & Engineering Chemistry Research*, **2023**, *62*, 18704–18719.
11. J. P. Riba; R. Routié; J. P. Couderc; *Canadian Journal of Chemical Engineering,* **1978**, *56*, 26–30.
12. A. M. Lali; A. S. Khare; J. B. Joshi; K. D. P. Nigam; *Powder Technology*, **1989**, *57*, 39–50.
13. D. J. Zigrang; N. D. Sylvester; *AIChE Journal,* **1981**, *27*, 1043–1044.
14. E. Barnea; J. Mizrahi; *Chemical Engineering Journal*, **1973**, *5*, 171–189.
15. E. Barnea; R. L. Mednick; *Chemical Engineering Journal,* **1978**, *15*, 215–227.
16. L. D. Boset; Z. A. Debele; A. W. Koroso; *Journal of Heat and Mass Transfer Research*, **2025**, in press.
17. J. Garside; M. R. Al-Dibouni; *Industrial & Engineering Chemistry Process Design and Development,* **1977**, *16*, 206–214.
18. S. P. Neill; M. R. Hashemi; Fundamentals of Ocean Renewable Energy, **2018**.

STUDIA UBB CHEMIA, LXXI, 1, 2026 (p. 121-140)
(RECOMMENDED CITATION)
DOI:10.24193/subbchem.2026.1.08

GROUNDWATER QUALITY ASSESSMENT IN THE SUBURBAN LOCALITIES OF HADAPSAR, PUNE USING WQI METHODOLOGY

Amol PAWAR[a,*], Satyam SHAH[b], Shreyash DHANKUDE[a], Rani CHAVAN[a], Neha CHABUKSWAR[a]

ABSTRACT. Water Quality Index (WQI) approach has been utilized in this study to evaluate groundwater quality in suburban areas of Hadapsar, Pune, India. From borewells and open wells in Hadapsar and nearby area. Thirty-two groundwater samples were gathered. Physicochemical analysis revealed that calcium was the major cation, followed by magnesium, sodium, and potassium, while bicarbonate was the dominant anion. For Mg, K, electrical conductivity, total dissolved solids, some samples have been above allowable levels. 68.75% of samples were of good quality for drinking, according to WQI values, while 28.12% of samples have been of outstanding quality. Indicators of irrigation water quality, including the MH (Magnesium Hazard), SSP (Soluble Sodium Percentage), Percent Sodium (%Na), RSC (Residual Sodium Carbonate), and SAR (Sodium Adsorption Ratio), demonstrated that groundwater was suitable for irrigation with negligible risks related to sodium, salinity, and carbonate contents. This research highlights the significance of regular monitoring as well as analysis of groundwater resources in rapidly urbanizing areas to ensure sustainability and safety of drinking and irrigation purposes. These results offer important new information about pollution control methods, sustainable urban planning, and the management of water resources in Pune's expanding periphery.

Keywords: *Water samples, Water quality Index, Groundwater quality, Physicochemical analysis*

[a] *Department of Chemistry, S. M. Joshi College, Hadapsar, Pune, Maharashtra, 411028, India.*
[b] *School of Geography, Geology and the Environment, University of Leicester, Leicester, LE1 7RH, United Kingdom.*
[*] *Corresponding author: amolpawarmay@gmail.com*

INTRODUCTION

The life cycle on Earth depends heavily on water [1]. Clean water is must for healthier and sustainable growth of society, that leads growth and development of society [2]. Groundwater quality is an important aspect of environmental health and safety [3]. It is a significant supply of water for everyday tasks and drinking [4]. Rapid urbanization has increasingly strained groundwater resources that affect not only major metropolitan areas but also rapidly growing suburban regions [5], [6]. Infrastructural development often ignores the regulatory guidelines of local authorities [7], [8].

According to [9], the WQI is a useful tool for comprehending a region's water quality and presentation. A comprehensive evaluation of water quality, especially for everyday utilization, can be obtained by combining multiple physicochemical factors into single WQI value [9], [10]. Regular monitoring and analysis using the WQI provide important information for identifying potential health hazards, spotting pollution patterns, and enabling timely updates [11], [12]. Evaluation is essential to guaranteeing the sustainability and safety of groundwater resources in rapidly urbanizing places like Hadapsar [13], [14], [15].

Numerous recent studies have employed the Water Quality Index (WQI) approach to evaluate groundwater quality for drinking and irrigation purposes. For instance, [16] applied WQI for assessing spatial-temporal variability in groundwater quality in urban regions of China, while [17] examined drinking water risks in peri-urban India using integrated WQI and health risk models. [18] conducted a comprehensive hydro chemical and WQI-based assessment in a rapidly urbanizing area of China. Similarly, [19] and [20] evaluated groundwater suitability in Indian semi-arid zones using WQI, identifying geogenic and anthropogenic contamination sources. [21] and [22] integrated WQI with GIS to map groundwater risk zones in Iran. In African contexts, [23] and [24] analyzed WQI to understand domestic water quality issues in fast-developing urban clusters. Studies by [25] and [26] highlighted the significance of combining WQI with multivariate analysis to determine pollution hotspots and seasonal trends in groundwater. Collectively, these studies underscore the versatility of the WQI method and its growing relevance in assessing groundwater sustainability under the pressures of urbanization and changing land-use dynamics.

Hadapsar area is located in eastern region of Pune, Maharashtra. this is one such area which is experiencing rapid urban growth [17]. Traditionally, an agriculturally dominated area, Hadapsar, has undergone a drastic transformation in recent years, providing a way to residential complexes, industrial setups, and commercial zone development [27]. Concerns about how urbanization may affect groundwater quality have been raised by this quick development, which has altered environment [28], [29].

Some research has broadly carried out studies on groundwater pollution in Pune's urban and industrial areas, but there is still a lack of specific research on suburban areas, such as Hadapsar. Unchecked borehole drilling, industrial effluents, poor sewage disposal, and agricultural runoff are among the factors that play key roles in possible contamination [30], [31].

This study aims to analyze groundwater quality and key physicochemical parameters to evaluate its suitability for domestic use through the application of the Water Quality Index (WQI) methodology. The specific objectives are:

(i) To assess important physicochemical characteristics of water samples collected from various locations in Hadapsar, Pune,

(ii) To compute WQI values and classify water quality into standard categories,

(iii) To examine spatial variations in groundwater quality, and

(iv) To identify potential health hazards and likely sources of contamination.

The present study offers a focused, micro-level assessment of groundwater quality in a rapidly urbanizing suburban environment. Its findings provide important insight into the consequences of unplanned urban development on groundwater resources and highlight the need for timely, sustainable water management interventions.

RESULTS AND DISCUSSION

Physicochemical Characteristics

Physicochemical characterization of groundwater samples from study area showed that calcium (Ca) was the major cation, with the secondary presence of Mg, Na (sodium), potassium (K) in order Ca>Mg>Na>K. The sequence of prevalence for anions was HCO_3^- > SO_4^{2-} > Cl^- > CO_3^{2-}. Only one sample had calcium content above the desirable limit of 75 mg/L, though all samples remained within the permissible limit of 200 mg/L as per IS-10500 (2012). As for magnesium, the limit was 30 mg/L and was found to be above that in 7 out of 32 samples (21.88%). Sodium and potassium values fell within the normal ranges, with all potassium concentrations falling below the desirable 12 mg per L. Concentrations of bicarbonate (HCO_3^-) in the samples were usually high but still in the range allowed for drinking water. The quantities of sulfate and chloride were also intermediate; none of the samples had more than 250 mg per L of Cl^-, maximum permitted quantity. The carbonate levels in every sample were remained within the permissible limit of 200 mg per L.

The measured pH values ranged from 6.52-9.28. 24 (75.0%) of the 32 samples were alkaline (pH>7), suggesting the presence of bicarbonates

and carbonates, while the rest had values close to neutral pH. EC (Electrical conductivity) values ranged among 205 and 1284 µS per cm; 5 samples (15.62%) were above the maximum threshold of 1000 µS per cm, indicating an elevated ionic concentration. About this, TDS, determined as EC × 0.64, were also above the preferable maximum of 500 mg per L in 6 samples (18.75%), providing further evidence on possible salinity hazards in these zones.

The above samples indicate that a few samples of groundwater are outside the permissible limit for drinking water purposes regarding Mg, TDS, K, EC, suggesting some local contamination or mineral enrichment. These fluctuations could require further hydrogeochemical assessment to pinpoint their origin.

Table 1. Location of sample sites along with Water Quality Parameters

Sample No.	Latitude / Longitude	pH / Chloride	Ca / Mg	CO_3 / HCO_3	Hardness / Alkalinity	Conductivity / TDS	Na / K	SO_4	WQI
1	18.497174 / 73.934576	7.04 / 9.94	44.6 / 19.1	87.8 / 106.2	189.81 / 233.38	640 / 409.6	10.44 / 6.12	34.92	54.37
2	18.487805 / 74.01365	7.76 / 8.87	27.6 / 19.6	86 / 111.5	149.36 / 234.73	1140 / 729.6	14.9 / 7.24	40.95	79.16
3	18.493754 / 73.967801	7.58 / 26.98	43.2 / 21.75	122.6 / 141.5	197.175 / 320.32	389 / 248.96	7.72 / 4.61	37.89	54.27
4	18.493744 / 73.967827	7.58 / 15.26	35.3 / 20.7	109.7 / 122.7	173.12 / 283.41	205 / 131.2	5.3 / 1.89	32.28	42.06
5	18.525787 / 73.965504	7.58 / 26.98	38.4 / 16.4	104.5 / 134.9	163.24 / 284.74	356 / 227.84	6.34 / 3.11	31.62	48.65
6	18.525842 / 73.965479	9.25 / 34.43	44.6 / 26.6	121.4 / 155.6	220.56 / 329.87	690 / 441.6	12.22 / 6.02	38.46	82.22
7	18.499294 / 73.941778	7.55 / 12.42	24.2 / 13.95	63.7 / 89.8	117.695 / 179.77	540 / 345.6	5.78 / 3.85	44.55	47.19
8	18.534004 / 73.960113	9.12 / 34.43	45 / 36.85	139.5 / 169.4	263.585 / 371.35	364 / 232.96	4.98 / 2.81	38.91	71.66
9	18.523169 / 74.046821	9.21 / 34.43	71.8 / 26.8	143.7 / 169.2	289.38 / 378.19	1284 / 821.76	15.64 / 8.37	28.08	113.83
10	18.508222 / 73.944074	7.33 / 13.49	39.4 / 29.4	102.5 / 134.8	219.04 / 281.33	620 / 396.8	10.22 / 5.85	32.19	59.81
11	18.483405 / 73.943921	9.28 / 34.43	41.2 / 20.7	108.7 / 131.9	187.87 / 289.28	1090 / 697.6	11.72 / 6.13	44.76	95.59
12	18.48217 / 74.069897	7.45 / 12.78	56.4 / 31.4	136.5 / 168.7	269.74 / 365.78	1154 / 738.56	15.26 / 8.24	41.67	92.1
13	18.471187 / 74.012055	7.88 / 11.05	49.2 / 39.2	127.4 / 153.5	283.72 / 338.15	540 / 345.6	5.68 / 1.91	31.62	67.25
14	18.470367 / 74.020537	7.28 / 5.68	57 / 32	149.5 / 176.4	273.7 / 393.76	450 / 288	6.38 / 4.73	27.96	61.72
15	18.492168 / 73.930348	7.44 / 13.49	11.4 / 11.05	58.7 / 81.3	73.805 / 164.47	1022 / 654.08	12.66 / 7.11	38.73	63.3

Sample No.	Latitude / Longitude	pH / Chloride	Ca / Mg	CO_3 / HCO_3	Hardness / Alkalinity	Conductivity / TDS	Na / K	SO_4	WQI
16	18.486715 / 73.928698	7.08 / 11.05	27 / 37.45	75.2 / 135.3	221.045 / 236.23	579 / 370.56	11.74 / 6.34	34.89	52.97
17	18.474994 / 73.931796	6.83 / 9.58	71.1 / 18.9	86.1 / 146.4	255.24 / 263.5	647 / 414.08	12.42 / 5.87	30.93	64.07
18	18.486775 / 73.928716	7.02 / 11.71	49.15 / 29.1	119.7 / 194.8	242.185 / 359.17	745 / 476.8	4.32 / 4.21	46.53	69.36
19	18.484753 / 74.020967	7.03 / 9.63	27 / 16	82.8 / 119.3	133.1 / 235.79	302 / 193.28	10.64 / 6.88	29.64	36.64
20	18.511188 / 73.937074	7.05 / 10.46	62 / 23.5	129.2 / 188.2	251.35 / 369.6	780 / 499.2	16.44 / 7.18	37.62	72.56
21	18.500888 / 73.934659	8.06 / 22.18	38.5 / 19	80.2 / 127.9	174.15 / 238.5	485 / 310.4	7.78 / 6.23	32.94	55.44
22	18.510911 / 73.937315	6.88 / 19.62	46.5 / 15	88.7 / 115.7	177.75 / 242.67	694 / 444.16	11.82 / 4.97	23.94	59.16
23	18.493237 / 73.93134	7.72 / 28.13	41 / 27	79.8 / 117.4	213.2 / 229.23	648 / 414.72	5.74 / 3.87	25.23	60.48
24	18.503082 / 73.922765	6.76 / 27.82	42 / 18.35	87.3 / 114.8	180.235 / 239.6	483 / 309.12	14.74 / 5.84	31.29	53.49
25	18.480802 / 74.023642	6.73 / 16.23	39.2 / 20.55	73.9 / 122.5	182.255 / 223.58	380 / 243.2	16.9 / 7.48	25.56	48.2
26	18.485944 / 73.951982	6.52 / 9.65	38.25 / 17.45	72.8 / 119.3	167.17 / 219.12	436 / 279.04	9.52 / 6.36	34.77	54.52
27	18.490853 / 73.949474	7.18 / 12.17	52.5 / 40.5	144.5 / 182.4	297.3 / 390.34	871 / 557.44	5.38 / 4.66	38.04	80.08
28	18.510252 / 73.934581	6.87 / 10.2	48 / 22.5	88.1 / 134.6	212.25 / 257.16	387 / 247.68	15.04 / 7.11	29.46	48.88
29	18.484477 / 73.954496	7.14 / 14.63	36 / 11	71.9 / 102.5	135.1 / 203.85	328 / 209.92	12.68 / 8.31	33.42	37.51
30	18.482676 / 73.945038	7.58 / 11.35	22.5 / 8	58.6 / 84.9	89.05 / 167.26	289 / 184.96	16.78 / 4.96	32.43	34.41
31	18.52308 / 74.047846	6.67 / 13.16	30.2 / 12	71.3 / 94.6	124.7 / 196.37	261 / 167.04	13.82 / 4.52	22.29	39.63
32	18.497815 / 73.939729	6.68 / 12.32	76 / 36	173.8 / 209.3	337.6 / 461.22	742 / 474.88	10.36 / 8.33	28.86	87.6

Water Quality Index (WQI) Assessment

Table 1 presents WQI values derived from analyzed groundwater samples. According to the classification outlined in Table 1, of the 32 samples, 9 (28.12%) exhibited a WQI of less than 50, categorizing them as "excellent" for drinking purposes. The remaining 22 samples (68.75%) had WQI values ranging from 50 to 100, which are considered "good" quality drinking water according to the WQI criteria. 1 sample (3.12%) had WQI values ranging from 100 to 200, classifying them as "poor" water. Notably, none of the samples

analyzed in this study exceeded a WQI of 200, indicating the absence of "very poor," or "unsuitable" water types within research area. Together, these findings suggest that groundwater in area is generally of good drinking quality, with a notable portion of the samples displaying excellent water quality.

Table 2. Water Quality Index (WQI) Categories of Samples from the Study Area

WQI Class	WQI Category	No. of Water Samples	% of Samples
< 50	Excellent water	9	28.12%
50–100	Good water	22	68.75%
100–200	Poor water	01	3.12%
200–300	Very poor water	0	0.0%
> 300	Unsuitable for drinking use	0	0.0%

Enhanced Parameter Exceedance Analysis

Quantitative analysis of parameter exceedances reveals critical insights beyond descriptive statistics (Figure 1) 7 out of 32 samples (21.88%) had magnesium concentrations over the IS 10500:2012 acceptable limit of 30 mg/L, making it the main water quality issue that needs to be addressed right now. Electrical conductivity exceeded 1000 µS/cm in 5 samples (15.62%), while pH values exceeded 8.5 in 4 samples (12.5%). TDS values exceeded 500 mg/L in 6 samples (18.75%), indicating elevated dissolved solids concentration in these locations

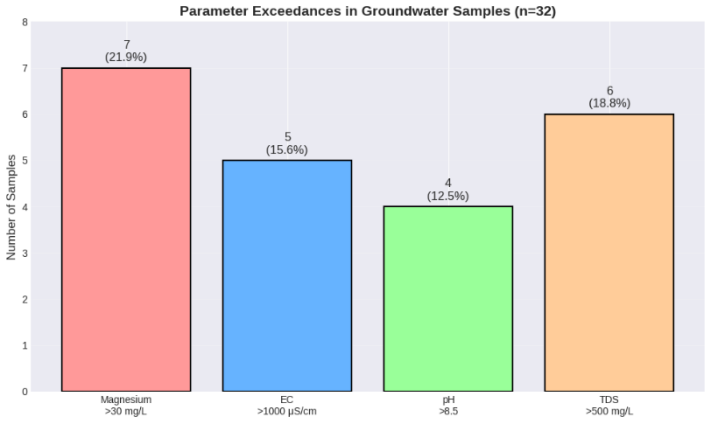

Figure 1. Parameter exceedances in groundwater samples (n=32) showing magnesium (7 samples, 21.88%), electrical conductivity (5 samples, 15.62%), pH (4 samples, 12.50%), and TDS (6 samples, 18.75%) exceeding IS 10500:2012 permissible limits

Preponderance of magnesium exceedance suggests systematic geological impacts, which are probably caused by anthropogenic inputs from farming practices or the breakdown of magnesium-bearing minerals in the Deccan Trap basalt bedrock. This finding necessitates targeted water treatment strategies focusing on magnesium removal for affected wells.

WQI Distribution and Statistical Characteristics

Detailed statistical analysis confirms that 9 samples (28.12%) exhibit excellent water quality (WQI <50), while 22 samples (68.75%) demonstrate good quality (WQI 50-100) (Figure 3). The WQI values range from 34.41 to 113.83 with a mean of 62.29 and median of 60.14.

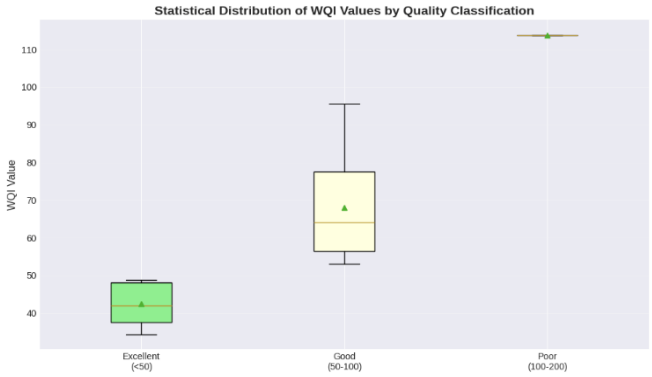

Figure 2. Box plot showing statistical distribution of WQI values across three quality categories: Excellent (n = 9, 28.12%), Good (n = 22, 68.75%), and Poor (n = 1, 3.12%) for 32 groundwater samples.

The box plot analysis (Figure 2) reveals distinct separation between excellent and good quality categories, with no intermediate values between 48-50 range. The Deccan Trap basalt bedrock's breakdown of magnesium-bearing minerals or anthropogenic inputs from farming methods are likely the causes of the prevalence of magnesium exceedance, which indicates systematic geological influences.

Hydrochemical Parameter Relationships

Correlation analysis validates key hydro chemical relationships governing water quality in research area (Figure 3). The TDS = EC x 0.64 equation used in this investigation is empirically supported by strong positive correlation among TDS and EC (r = 1.00). WQI demonstrates significant correlations with TDS (r=0.86), EC (r=0.86), magnesium content (r=0.53), establishing these as primary controlling parameters.

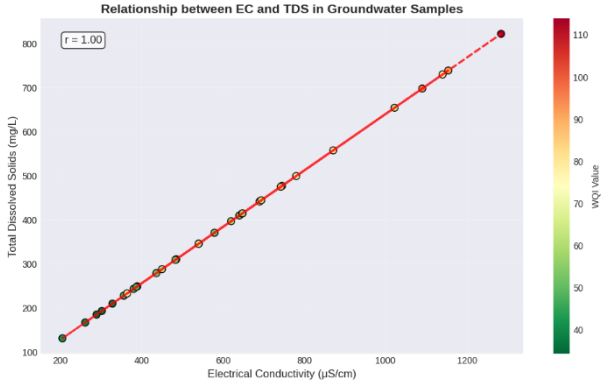

Figure 3. Scatter plot showing perfect correlation (r = 1.00) between electrical conductivity and total dissolved solids in 32 groundwater samples, with points coloured by WQI values. The red dashed line represents the regression equation TDS = EC × 0.64

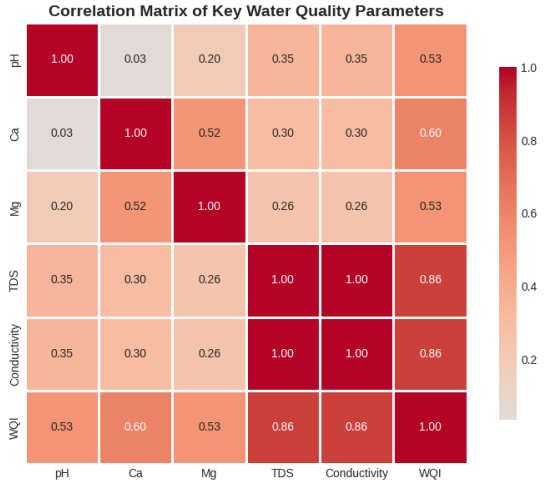

Figure 4. Correlation matrix showing relationships between water quality parameters (n=32), with notable correlations: EC-TDS (r=1.00), WQI-EC (r=0.86), WQI-TDS (r=0.86), and WQI-Mg (r=0.53).

The TDS versus EC scatter plot (Figure 4) not only validates the conversion formula but identifies potential analytical outliers requiring verification. Samples exhibiting higher WQI values consistently display elevated EC and TDS concentrations, confirming the WQI methodology's effectiveness in capturing overall water quality degradation.

Multiple Parameter Exceedance Patterns

Analysis of simultaneous parameter exceedances reveals that 37.5% of samples exceed limits for multiple parameters, suggesting systematic rather than random contamination sources (Figure 5). This pattern indicates that affected locations require comprehensive management interventions addressing multiple water quality aspects simultaneously.

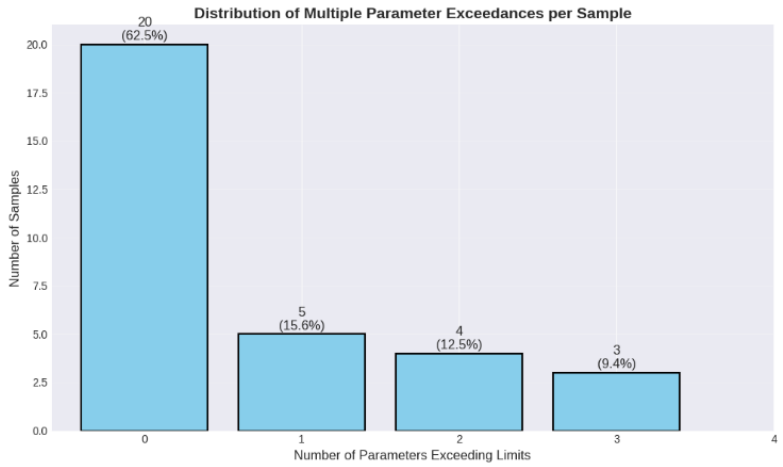

Figure 5. Distribution of samples by number of parameter exceedances showing 20 samples (62.5%) with no exceedances, 5 samples (15.6%) with one exceedance, 4 samples (12.5%) with two exceedances, and 3 samples (9.4%) with three exceedances.

The spatial clustering of multiple exceedances in specific zones supports the hypothesis that localized factors-including land use intensity, geological variations, or proximity to contamination sources-significantly effect groundwater quality across the research area.

Irrigation Water Quality Indices (IWQI)

Assessing groundwater for irrigation is particularly crucial since irrigation water may introduce soluble salts to the soil and root zone, which could negatively impact crop output and soil structure. The region's suitability for irrigation was assessed using a variety of measures, including SAR, RSC, SSP, MH, and %Na. These indices can be helpful in assessing the potential threat of high sodium and magnesium levels to soil permeability, infiltration capacity, as well as agricultural sustainability in long run. Table 3 lists obtained values of these parameters together with their interpretations in terms of general classification schemes.

Table 3. Irrigation Water Quality Indices of Hadapsar area

Sample	SAR	RSC	Na%	MH (%)	SSP (%)
1	0.33	0.87	16.67	41.39	16.81
2	0.53	1.70	25.44	53.93	25.41
3	0.24	2.46	12.69	45.36	12.66
4	0.18	2.20	8.71	49.16	8.63
5	0.22	2.43	11.86	41.32	11.75
6	0.36	2.18	15.97	49.58	15.98
7	0.23	1.24	16.01	48.73	15.99
8	0.13	2.15	6.4	57.45	6.39
9	0.40	1.77	16.02	38.10	16.07
10	0.30	1.24	14.42	55.16	14.50
11	0.37	2.03	17.83	45.31	17.97
12	0.40	1.92	16.69	47.86	16.74
13	0.15	1.08	5.8	56.78	5.72
14	0.17	2.40	8.3	48.07	8.66
15	0.64	1.81	32.62	61.51	38.22
16	0.34	0.30	14.36	69.58	15.86
17	0.34	0.17	14.12	30.47	14.14
18	0.12	2.34	7.81	49.40	7.68
19	0.40	2.05	20.56	49.42	23.42
20	0.45	2.36	17.84	38.46	17.72
21	0.26	1.28	15.94	44.86	15.87
22	0.39	1.30	17.63	34.72	17.77
23	0.17	0.32	9.53	52.06	9.49
24	0.48	1.19	20.19	41.87	20.68
25	0.54	0.82	19.34	46.36	23.46
26	0.32	1.04	18.14	42.93	18.11
27	0.14	1.85	7.56	55.98	7.35
28	0.45	0.90	19.33	43.59	19.34
29	0.47	1.37	26.29	33.50	26.55
30	0.77	1.56	32.78	36.96	35.58
31	0.54	1.43	26.52	39.58	25.02
32	0.25	2.47	10.84	43.85	11.49

Sodium Adsorption Ratio (SAR) and Other Irrigation Indices

All 32 of the groundwater samples that were examined had SAR between 0.12 and 0.77, which showed that they were completely suitable for irrigation. According to [35] , SAR values below 10 signify excellent irrigation water with a minimal sodium hazard. Consequently, all samples were classified within the 'excellent' category concerning alkali hazards. Sodium, a significant factor in soil dispersion and reduced permeability, posed no immediate risk at the observed levels.

Other irrigation quality parameters were evaluated in addition to SAR. RSC levels varied from 0.17 to 2.47 meq/L, and 29 out of 32 samples (90.6%) were within the safe limit (<2.5 meq/L), indicating minimal risk of carbonate precipitation that could affect soil structure.

The %Na values ranged from 5.8% to 32.78%, and 24 out of 32 samples (84.4%) were in excellent standard and remaining samples are suitable for irrigation in terms of sodium content. Since too much sodium can negatively affect crop health and soil permeability, all of the samples are suitable for irrigation.

According to the SSP values, which ranged from 5.72% to 38.22%, All samples were excellent and within the safe range (<40%), classifying them as ‘excellent’ for irrigation use.

However, Magnesium Hazard (MH) values indicated that 8 out of 32 samples (25%) exceeded the critical threshold of 50%, potentially contributing to adverse effects such as soil compaction and reduced aeration.

Other irrigation quality parameters were evaluated in addition to SAR. With 32 samples (100%) falling inside the safe limit (<2.5 meq per L), RSC levels varied from 0.17 to 2.47 meq per L, suggesting that there is little chance that carbonate precipitation may alter soil texture. Since too much sodium can negatively affect crop health and soil permeability, 32 samples have been deemed appropriate for irrigation, depending on %Na readings, which ranged from 5.8% to 32.78%.

According to the SSP values, which ranged from 5.72% to 38.22%., 81% of samples have been classified as ‘excellent’ for use in irrigation. Similarly, Magnesium Hazard (MH) values showed that a few samples slightly exceeded the critical limit of 50%, potentially leading to soil compaction and reduced aeration. However, the Electrical Conductivity (EC) values were within acceptable irrigation thresholds in 74% of the samples, reflecting a low salinity hazard for most samples.

Overall, the research area's groundwater showed good to exceptional quality for irrigation, with low hazards related to salinity, carbonate concentration, and sodium.

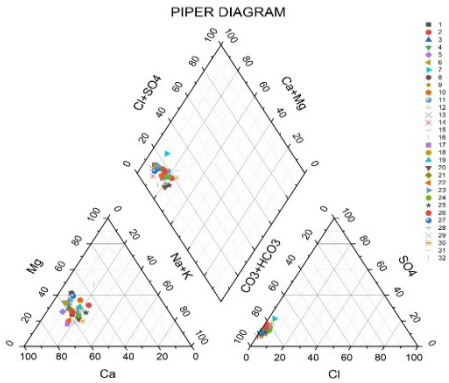

Figure 6. Piper trilinear diagram showing hydro chemical classification of 32 groundwater samples, with predominant Ca-Mg-HCO_3 water type indicating freshwater quality with temporary hardness

Hydro chemical Species Interpretation Using Piper Diagram

Hydro chemical facies in research area have been categorized, and the groundwater types were interpreted using Piper (1944) trilinear diagram (Figure 7). Five different hydro chemical facies were discovered by analyzing the geographical distribution of main anions and cations in groundwater samples: Ca–Mg–SO_4, Ca–Mg–HCO_3, Ca–Cl. 2 mixed water types were also identified: Na–Ca–HCO_3, Ca–Na–HCO_3–SO_4. Ca–Mg–HCO_3 water type was the most prevalent, indicating that majority of groundwater is of freshwater quality with temporary hardness, typically associated with shallow aquifers of recent recharge origin. These facies generally result from a dissolution of carbonate minerals involving calcite or dolomite, that occurs when infiltrating rainwater, enriched with atmospheric and soil-derived CO_2, percolates into the subsurface and chemically interacts with carbonate-bearing strata (Freeze and Cherry, 1979). The resulting reaction leads to elevated concentrations of Ca^{2+} and HCO_3^-, along with a modest increase in groundwater pH. The existence of mixed water types, including Na–Ca–HCO_3, Ca–Na–HCO_3–SO_4, indicates areas of anthropogenic influence and chemical change. These kinds might arise as a result of cation exchange activities in the aquifer system, in which groundwater's Ca, Mg are replaced by Na in soil matrix. This transformation marks a transition from pristine Ca–HCO_3 water to more evolved facies, influenced either by ion exchange or agricultural and domestic return flows. The rare presence of Ca–Cl, Ca–Mg–SO_4 types in a few samples could be attributed to localized influences involving industrial discharge, fertilization, or lithological heterogeneity, indicating some spatial variability in hydrogeochemical processes. Overall, Piper diagram confirms that groundwater

chemistry in the research area predominantly reflects natural geochemical weathering of carbonate rocks, with pockets of evolving water chemistry driven by ion exchange reactions and anthropogenic activities.

Spatial Distribution Patterns

The spatial distribution of WQI values (Figure 8) reveals distinct geographical patterns in groundwater quality across the study area. Notably, samples with higher WQI values (>80) show spatial clustering, particularly in the eastern sector (longitude >74.02) and northern areas (latitude >18.51). This clustering pattern suggests localized contamination sources rather than uniform distribution, supporting the hypothesis that specific land use activities or geological variations significantly influence groundwater quality. The sample with the highest WQI (113.83) is located at the northeastern extent of the study area, while excellent quality samples (WQI <50) are predominantly found in the central and southwestern zones

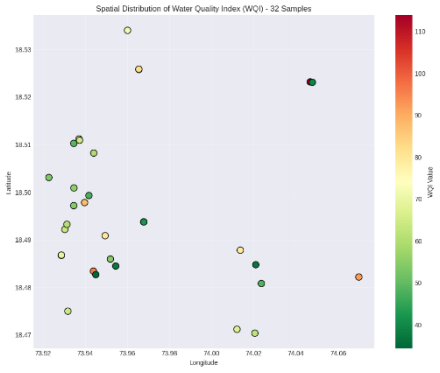

Figure 7. Spatial distribution of Water Quality Index values across 32 sampling locations in Hadapsar area. The color gradient from green (excellent quality, WQI <50) through yellow (good quality, WQI 50-100) to red (poor quality, WQI >100) reveals distinct spatial clustering, with higher WQI values concentrated in the eastern and northern portions of the study area.

This spatial pattern has important implications for targeted groundwater management strategies. The identification of contamination hotspots in the eastern and northern sectors aligns with objective (iii) of this study to examine spatial variations in groundwater quality. These findings suggest that monitoring efforts and remediation strategies should prioritize these high-WQI zones, particularly sample location 9 (WQI 113.83) in the northeastern sector. The central and southwestern zones with excellent water quality could serve as reference areas for understanding baseline conditions and may represent zones less impacted by urbanization pressures.

CONCLUSIONS

WQI methodology has been utilised to evaluate groundwater quality in Hadapsar, Pune, India, suburbs. From borewells and open wells in Hadapsar and nearby area, thirty-two groundwater samples were gathered. Physicochemical analysis revealed that calcium was the major cation, followed by magnesium, sodium, and potassium, while bicarbonate was the dominant anion. Some samples exceeded permissible limits for Mg, EC and TDS. Enhanced statistical analysis confirms that 28.12% of samples exhibit excellent quality (WQI <50) and 68.75% demonstrate good quality (WQI 50-100), with mean WQI of 62.29 indicating generally acceptable water quality with significant spatial variability. Groundwater was deemed appropriate for irrigation with low risks related to sodium, salinity, and carbonate concentrations, according to irrigation water quality indicators that included the SAR, RSC, %Na, SSP, MH.

The most significant finding is that magnesium exceedance affects 21.88% of samples, representing the primary water quality challenge requiring immediate intervention through targeted treatment strategies. Secondary concerns include EC issues in 15.62% of samples and pH exceedances in 12.50% of locations. Correlation analysis validates the analytical methodology and identifies EC, TDS, and magnesium as primary drivers of overall water quality assessment. The distinct bimodal WQI distribution indicates discrete hydrogeochemical regimes, suggesting that water quality is controlled by specific geological or anthropogenic factors rather than gradual contamination processes.

These enhanced analytical findings provide a quantitative basis for prioritising water treatment interventions and establishing monitoring protocols for sustainable groundwater management in rapidly urbanising suburban areas. The integrated geospatial-statistical approach demonstrates significant value for comprehensive water quality assessment beyond traditional physicochemical analysis alone.

EXPERIMENTAL SECTION

Materials and methods

Study area

Hadapsar is on eastern side of Pune city, Maharashtra, India, located between 18.50°N and 18.55°N latitude and 73.95°E and 74.00°E longitude. Hadapsar was once a rural territory that has evolved into a fast-paced peripheral center with high-density residential development, commercial complexes, IT

parks, and upcoming industrial areas. The area experiences scorching summers, mild winters, and modest monsoon rainfall of 750 mm annually due to its tropical semi-arid environment. Hadapsar has a comparatively flat topography with scattered embankments and is lined by seasonal streams and low-lying catchments. The area falls in the upper Bhima Basin and is primarily underlain by the Deccan Trap basalt. It also hosts aquifers in weathered and fractured zones.

Groundwater is available under semi-confined conditions, mainly in fractured basalt, weathered zones, and periodic grainy patches in surface drainage. For groundwater quality variation estimation, 32 sampling locations (borewells and open wells) were chosen from Hadapsar and nearby area, representing a representative series of land use patterns from core residential to transitional fringe areas.

Sampling

Thirty-two groundwater samples were obtained from five sampling locations. The sampled specimens were referred to with site information and geographic coordinates. The samples were transferred to pre-cleaned polyethene bottles to avoid contamination. Each sample was kept in ice boxes at 4 °C until analysis to avoid any chemical modification.

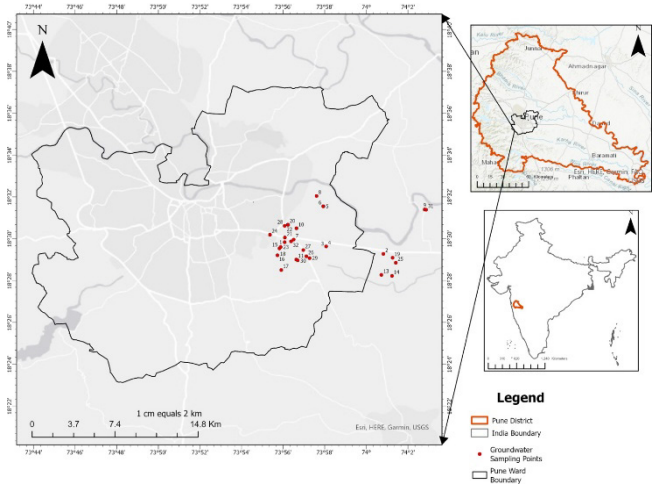

Figure 8. Location map showing groundwater sampling sites across Hadapsar, Fursungi, Manjari, and Sasane Nagar localities, Pune, Maharashtra, India. The main map displays the study area with 32 sampling locations (red dots) overlaid on Pune Ward Boundary. The upper right inset map showing regional context of Pune District within Maharashtra state, India. Lower right inset map provides national context, shows location of Maharashtra within India.

Sample collection and analysis followed Standard Methods for Examination of Water or Wastewater Guidelines of the APHA [32]. Physicochemical characteristics have also been analyzed. These involve TDS (total dissolved solids), pH, electrical conductivity (EC), Mg^{2+} (magnesium), Ca^{2+} (calcium), sodium (Na^{+}), potassium (K^{+}), carbonate (CO^{-2-}), Cl^{-} (chloride), HCO_3^{-} (bicarbonate), sulfate (SO^{-2-}).

Prior to each set of measurements, instruments such as pH meters, EC meters, and TDS meters were calibrated using standard buffer and conductivity solutions. Analytical precision was maintained by conducting all measurements in triplicate. Flame photometric and titrimetric analyses were validated with certified reference standards. Blank and spiked samples were incorporated as quality controls during titration to assess contamination and method accuracy. All physicochemical parameters fell within the detectable ranges of the instruments employed, and the methodology ensures the reproducibility, transparency, and reliability of the reported results.

Table 4. Overview of Analytical Techniques Employed: Parameter Assessment and Permissible WHO [33] and IS 10500:2012 [34] Limits in this Research

Parameter	Analytical Method	Instrument Used	Reagent/Formula	Unit	WHO Standard (2017)	IS 10500: 2012
pH	Electrometric Method (Direct in situ)	Digital pH Meter	-	-	6.5–8.5	6.5–8.5
Electrical Conductivity (EC)	Conductometric Method (Direct in situ)	Digital Conductivity Meter	-	µS/cm	500 (desirable)	1500 (max)
Total Dissolved Solids (TDS)	By EC × 0.64	Calculated	-	mg/L	500 (desirable)	2000 (max)
Calcium (Ca^{2+})	EDTA Titrimetric Method	Titration	EDTA-NaOH	mg/L	75 (desirable)	75–200
Magnesium (Mg^{2+})	EDTA Titrimetric Method	Titration	EDTA, NH_4OH, NH_4Cl	mg/L	30	30–100
Total Hardness	EDTA Titrimetric Method	Titration	2.5 (Ca) + 4.1 (Mg)	mg/L as $CaCO_3$	200 (desirable)	200–600
Sodium (Na^{+})	Flame Photometric Method	Systronics Flame Photometer 128	-	mg/L	200	No guideline

Parameter	Analytical Method	Instrument Used	Reagent/Formula	Unit	WHO Standard (2017)	IS 10500: 2012
Potassium (K^+)	Flame Photometric Method	Systronics Flame Photometer 128	- -	mg/L	-	-
Chloride (Cl^-)	Argentometric Titration	Titration	$AgNO_3$	mg/L	250	250–1000
Bicarbonate (HCO_3^-)	Acid Titration	Titration		mg/L	-	-
Carbonate (CO_3^{2-})	Acid Titration	Titration		mg/L	-	-
Alkalinity	Titrimetric Method	Titration	$HCO_3^- + 2CO_3^{2-} + OH^- - H^+$	mg/L	200 (desirable)	200–600
Sulfate (SO_4^{2-})	Spectrometric Method	UV-1800 spectrophotometer (Shimadzu)		mg/L	250	200–400

Water quality index (WQI)

WQI is widely utilized technique that provides single score that indicates the water's overall quality. WQI is useful indication of water quality for range of applications, including irrigation, drinking, as well as residential water suitability. In current research, WQI has been calculated following recommendations of the Indian Standard IS10500 (2012). The analysis used the weighted arithmetic index approach, which assigns higher weights to parameters that have more serious health implications. Weights wi assigned to every parameter are inverse of their standard allowable tolerances.

The WQI was determined using the following water quality parameters provided in (Table 4). WQI has been determined using equation below:

$$WQI = \sum_{i=1}^{n} \text{Wi qi}$$

Where: qi=quality rating of the ith parameter, wi=unit weight of parameter i , Unit weight (Wi) of every parameter has been calculated as Wi=k/Si Where: Si=standard permissible value of the ith parameter, k=proportionality constant (k=1/Σ(1/Si)).

Quality rating (qi) is expressed as qi= (Va − Vi)/ (Si − Vi) ×100. where Si is the standard acceptable limit as per IS:10500 (2012), Va is actual concentration of the parameter as determined by analysis, and Vi is ideal value (zero for most parameters, except pH, which is seven).

Table 5. Assigned Weights (wi) and Standard Limits (Si) for Water Quality Index Calculation

Parameter	Standard Limit (Si)	Assigned Weight (wi)	Relative Weight (Wi = wi /31)
pH	6.5–8.5	4	0.129
Calcium (Ca)	75 mg/L	2	0.065
Magnesium (Mg)	50 mg/L	1	0.032
Hardness	300 mg/L	3	0.097
CO3	200 mg/L	2	0.065
HCO3	200 mg/L	1	0.032
Alkalinity	200 mg/L	3	0.097
Chloride	250 mg/L	3	0.097
TDS	500 mg/L	5	0.161
EC	500 µS/cm	4	0.129
Sodium (Na)	200 mg/L	2	0.065
Sulphate	250 mg/L	4	0.129
Total		34	1

Suitability of Groundwater for Irrigation: To determine if groundwater is suitable for irrigation, several indices were computed. We computed the SAR, %Na, RSC, SSP, MH. Both indices show how soil permeability and plant health are affected by quantities of sodium, calcium, carbonate, magnesium, bicarbonate. The required input parameters were determined from the values obtained by measuring the Na+, Ca2+, Mg2+, CO32-, HCO3-, EC, TDS, and total hardness. Table 6 provides a summary of the formulas for these irrigation indices.

Table 6. The equations and classification standards applied for calculating the irrigation water quality indices.

Index	Formula	Parameters Used	Acceptable Limit	Reference
Sodium Adsorption Ratio (SAR)	$SAR = Na^+ / \sqrt{(Ca^{2+} + Mg^{2+})/2}$	Na^+, Ca^{2+}, Mg^{2+}	<10: Excellent; 10–18: Good; 18–26: Doubtful; >26: Unsuitable	[35]
Soluble Sodium Percentage (SSP)	$SSP = (Na^+ \times 100) / (Ca^{2+} + Mg^{2+} + Na^+ + K^+)$	Na^+, K^+, Ca^{2+}, Mg^{2+}	<50%: Safe; >60%: Unsuitable	[36]
Residual Sodium Carbonate (RSC)	$RSC = (CO_3^{2-} + HCO_3^-) - (Ca^{2+} + Mg^{2+})$	CO_3^{2-}, HCO_3^-, Ca^{2+}, Mg^{2+}	<1.25: Safe; 1.25–2.5: Marginal; >2.5: Unsuitable	[37]
Magnesium Hazard (MH)	$MH = (Mg^{2+} \times 100) / (Ca^{2+} + Mg^{2+})$	Mg^{2+}, Ca^{2+}	<50%: Suitable; >50%: Unsuitable	[38]
Percent Sodium (%Na)	$\%Na = (Na^+ + K^+) \times 100 / (Ca^{2+} + Mg^{2+} + Na^+ + K^+)$	Na^+, K^+, Ca^{2+}, Mg^{2+}	<60%: Suitable; >60%: Unsuitable	[36]

Geospatial and Statistical Analysis

To complement traditional physicochemical analysis, geospatial and statistical methods were employed. Sampling locations (n=32) were georeferenced and mapped in ArcGIS Pro to evaluate spatial distribution and network adequacy. Statistical analyses included descriptive metrics, correlation matrices, and exceedance quantification. Data visualization using Python (matplotlib, seaborn) facilitated interpretation of spatial variability, parameter interactions, and exceedance severity, enhancing the WQI-based assessment.

ACKNOWLEDGMENTS

We are thankful to Prof. Dr R. K. Jadhav, Head, Department of Chemistry, S. M. Joshi College, Hadapsar, Pune, Maharashtra, India, and Dr S. T. Salunkhe, Principal, S. M. Joshi College, Hadapsar, Pune, Maharashtra, India, for their support.

REFERENCES

[1] F. Westall; A. Brack; Space Sci. Rev., **2018**, 214.
[2] B. F. Milan; Sustain. Water Resour. Manag., **2017**, 3, 479–489.
[3] Y. Abduljaleel; et al.; Environ. Sci. Pollut. Res., **2024**, 31, 19185–19205.
[4] F. Liu; P. Zhen; S. Wang; Environ. Sci. Pollut. Res., **2022**, 29, 17655–17670.
[5] M. K. Jat; D. Khare; P. K. Garg; Environmentalist, **2009**, 29, 17–32.
[6] S. Gopinath; K. Srinivasamoorthy; K. Saravanan; R. Prakash; D. Karunanidhi; Hum. Ecol. Risk Assess., **2019**, 25, 314–334.
[7] M. Pandith; R. D. Kaplay; S. S. Potdar; H. Sangnor; A. D. Rao; Environ. Monit. Assess., **2017**, 189.
[8] D. J. Lapworth; et al.; Appl. Geochem., **2021**, 133, 105092.
[9] A. H. Ismail; D. Robescu; Environ. Eng. Manag. J., **2019**, 18, 1727–1737.
[10] Yisa; Am. J. Appl. Sci., **2010**, 7, 453–458.
[11] Z. Gao; Y. Liu; N. Li; K. Ma; Water Resour. Manage., **2022**, 36, 2685–2702.
[12] M. Ruhela; S. Bhardwaj; S. P. Gaurishankar; F. Ahamad; R. Bhutiani; ECJ, **2024**, 25, 604–610.
[13] E. Asadi; et al.; Sustainability, **2019**, 12, 177.
[14] D. E. Alexakis; Hydrology, **2021**, 8, 90.
[15] A. Asadollahi; A. Sohrabifar; A. B. Ghimire; B. Poudel; S. Shin; Environ. Prot. Res., **2024**, 1–15.
[16] Y. Xiong; et al.; Sustainability, **2023**, 15, 14477.
[17] L. N. Kantakumar; S. Kumar; K. Schneider; Eur. J. Remote Sens., **2019**, 52, 26–41.
[18] X. Hu; et al.; J. Water Process Eng., **2024**, 63, 105440.
[19] A. Yadav; A. Raj; B. Yadav; J. Environ. Manag., **2024**, 370, 122903.

[20] D. Thakur; A. Sharma; P. Goel; A. Thakur; M. Raturi; Groundw. Sustain. Dev., **2023**, 22, 100969.
[21] S. Lotfinasabasl; A. Gohardoust; F. Dargahian; S. Zandifar; Sci. Rep., **2025**, 15.
[22] Z. Karimzadeh Motlagh; R. Derakhshani; M. H. Sayadi; Groundw. Sustain. Dev., **2023**, 23, 101037.
[23] C. O. Unigwe; J. C. Egbueri; Environ. Dev. Sustain., **2023**, 25, 686–707.
[24] M. O. Abdus-Salam; et al.; Discov. Water, **2024**, 4.
[25] S. Barathkumar; et al.; Desalin. Water Treat., **2025**, 322, 101047.
[26] R. C. Karangoda; K. G. N. Nanayakkara; Groundw. Sustain. Dev., **2023**, 21, 100910.
[27] L. Zhang; et al.; Sci. Adv., **2022**, 8.
[28] H. H. Khan; A. Khan; S. Ahmed; J. Perrin; Environ. Earth Sci., **2011**, 63, 1289–1302.
[29] R. S. Gabor; et al.; Environ. Sci. Technol., **2017**, 51, 9477–9487.
[30] S. Kurwadkar; S. R. Kanel; A. Nakarmi; Water Environ. Res., **2020**, 92, 1659–1668.
[31] E. C. Edwards; et al.; J. Contam. Hydrol., **2022**, 246, 103964.
[32] American Public Health Association; American Water Works Association; Water Environment Federation; Standard methods for the examination of water and wastewater, Washington (D.C.), **2012**.
[33] World Health Organization; Guidelines for drinking-water quality, 4th ed., Geneva, **2017**.
[34] Bureau of Indian Standards (BIS); Drinking Water Standards (IS: 10500: 2012), **2012**.
[35] L. A. Richards; USDA Agriculture Handbook No. 60, **1954**.
[36] L. V. Wilcox; USDA Circular 969, Washington, DC, **1955**.
[37] E. M. Eaton; Soil Sci., **1950**, 69, 123–133.
[38] I. Szabolcs; C. Darab; Proc. 8th Int. Congr. ISSS, **1964**, 2, 803–812.

STUDIA UBB CHEMIA, LXXI, 1, 2026 (p. 141-161)
(RECOMMENDED CITATION)
DOI:10.24193/subbchem.2026.1.09

LITHIUM AND SELENIUM CONCENTRATIONS IN THE DRINKING WATERS OF A MOUNTAINOUS VILLAGE (SĂCALU DE PĂDURE): POTENTIAL RELATIONSHIP TO RESIDUAL THYROID PATHOLOGY (PRELIMINARY RESEARCH)

Mária Melinda VARGA[a*], Attila CSISZÉR[b], Réka BARABÁS[c], Imre Zoltán KUN[d]

ABSTRACT. The lithium excess and selenium deficiency in the body can lead to thyroid disorders (goiter and hypothyroidism). We hypothesize that these elements can contribute to the persistence of thyroid pathology after the universal salt iodination introduced in 2002−2003 in Romania. The concentrations of lithium, selenium, and other micro- and macro-elements, as well as anions, were measured in the well waters used for drinking in the mountain village of Săcalu de Pădure, Upper Mureș Valley. Li concentrations (13 measures), ranging from 9.7 to 69 µg/L, generally exceeded the non-regulatory Health-Based Screening Level (HBSL) of 10 µg/L by 2 to 7 times, sustaining the contribution of Li excess to residual thyroid pathology. Additionally, these waters may be effective in treating mania, suicidal tendencies, Alzheimer's disease, and migraine. The selenium levels, measured in this and 5 surrounding localities (11 assays), were very low, under the detection limit. While the maximum limit for selenium content in drinking water is 20 µg/L (OG 7/2023), no lower limit has been established. Urinary iodine excretion, measured in 22 randomly selected residents, had normal values (100-350 µg/L) in most cases (90.9%), indicating an adequate iodine supply and excluding the iodine role in the residual thyroid pathology.

Keywords: *lithium, selenium, goiter, hypothyroidism, psychiatric use*

[a] *Petru Maior College, Reghin; Faculty of Chemistry and Chemical Engineering, Babeș-Bolyai University, Cluj-Napoca, Romania*
[b] *Regional Center of the National Institute of Public Health, Târgu Mureș, Romania. Email: attila.csiszer@insp.gov.ro*
[c] *Babeș-Bolyai University, Faculty of Chemistry and Chemical Engineering, Department of Chemistry and Chemical Engineering of Hungarian Line of Study, Cluj-Napoca, Romania. Email: reka.barabas@ubbcluj.ro*
[d] *Doctoral School, George Emil Palade University of Medicine, Pharmacy, Science and Technology, Târgu Mureș, Romania. Email: kunimre@gmail.com*
** Corresponding author: vargamariamelinda@yahoo.com*

INTRODUCTION

Data from the 2002−2004 period showed that in Romania, a moderate iodine deficiency exists in 80% of the counties (especially in rural regions), with a prevalence of endemic goiter ranging from 0% to 40% and reduced urinary iodine excretion (UIE) in two-thirds of the studied persons [1]. The introduction of universal and mandatory salt iodination in 2002−2003 eliminated the moderate/mild iodine deficiency that had been typical until then, thus significantly reducing the incidence of goiter and associated thyroid pathology (IDD − Iodine Deficiency Disorders). However, this aim was not achieved in some mountainous areas and among pregnant women. For this program to work effectively and remain sustainable and reliable, it must be followed periodically, especially under the conditions mentioned. Such local controls were carried out by the medical staff of Endocrinology Clinic Târgu Mureș in Mureș Valley (in 1999) and Gurghiu Valley (in 2006 and 2013) [1, 2, 3, 4].

The goals of our research are, on the one hand, to conduct this control, which has not been conducted in the last 11 years, and to identify the factors that maintain residual thyroid pathology in this locality. At the same time, we strive to improve local health parameters by recognizing and treating the existing disorders. Considering that excess lithium (Li) and/or selenium (Se) deficiency in the body can cause thyroid disorders (goiter, hypothyroidism), we hypothesized that these elements may play a significant role in the residual thyroid pathology that persists after the general iodination of table salt from 2002−2003. To investigate this, we measured the presence and concentrations of lithium, selenium, and other micro- and macroelements, as well as some anions (see Table 8), in the drinking water from one of the mountain villages in the Upper Mureș Valley, Săcalu de Pădure.

Regarding the biological properties of lithium, it is worth noting that its exact molecular function is not fully understood. Perhaps because of this uncertainty, the WHO does not currently consider it an essential nutrient [5]. However, several studies found a correlation between higher levels of lithium in the diet and lower risks of dementia, Alzheimer's disease, and suicide. Recently, the adults' daily requirement of Li was estimated at 1 mg, amounts we naturally consume without dietary supplements. The primary dietary sources of Li are cereals, potatoes, tomatoes, cabbage, and mineral waters from specific locations [6, 7]. According to estimates, cereal grains and vegetables can provide between 66 and 90% of the daily Li consumed [8]. Animal-derived foods, drinking water, and beverages supply the remainder.

Li concentrations measured in *drinking waters* in *various countries* varied by three orders of magnitude, and the published mean concentrations ranged from 0.48 to 56 µg/L [12]. Several other studies [9, 10] examined the Li content of groundwater (bank-filtrated and karst waters) and surface

waters (rivers, lakes, open reservoirs) used to supply drinking water in the *United States*. Li concentrations in groundwater ranged between *1 and 396 µg/L (median 8.1 µg/L) for public supply wells and 1–1700 µg/L (median 6 µg/L) for domestic supply wells nationwide.* Sharma et al. [10] investigated the presence of Li in water sources (ground and surface water) across the United States in 21 drinking water facilities. In groundwater, Li concentrations ranged from 0.9 to 161 µg/L (median 13.9 µg/L), and in surface water, they ranged from 0.5 to 130 µg/L (median 3.9 µg/L). Li in drinking water is not regulated in the United States. Still, the United States Geological Survey (USGS), in collaboration with the U.S. Environmental Protection Agency (US-EPA), provides a non-regulatory Health-Based Screening Level (HBSL) of 10 µg/L, which provides a human health context for Li in drinking water sources. Li levels were higher than the HBSL of 10 µg/L in 56% of the groundwater and 13% of the surface water [10]. The authors also discovered a strong correlation between Li and Na concentrations. Additionally, the Li concentration in source water and treated drinking water was remarkably similar. A 2023 review article presents a meta-analysis of 76 papers on Li concentrations, stratified by water resource type and country subgroups, using a random effects model (REM) [11]. The overall pooled concentration of Li was 5.374 µg/L (95 % CI: 5.261–5.487 µg/L). The pooled concentration of Li in groundwater (40.407 µg/L) was 14.53 times that of surface water (2.785 µg/L). The highest water Li content was attributed to Mexico (2,209.05 µg/L), Bolivia (1,444.05 µg/L), Iraq (1,350 µg/L), and Argentina (516.39 µg/L). At the same time, the lowest water Li content was associated with Morocco (1.20 µg/L), Spain (0.46 µg/L), and India (0.13 µg/L). Dobosy et al. (2023) [12] found in Hungary that Li concentrations in bank-filtrated river water, surface water from open reservoirs, and groundwater varied between 0.90–4.23, 2.12–11.7, and 1.11–31.4 µg/L, respectively, while the median values were 3.52, 5.02, and 8.55 µg/L, respectively. In bottled Hungarian mineral waters, concentrations ranged from 4.2 to 209 µg/L, with a median of 17.8 µg/L. Additionally, only a correlation between Li and K concentrations was found. At ten sampling locations in the Hungarian segment of the Danube River, the mean and median lithium concentrations were 2.78 and 2.64 µg/L, respectively. In Romania, in the Dobrogea region, half of the studied waters had Li concentration ranging 3.00−12.2 µg/L, while in the Banat region, between 1.40-1.46 µg/L. Despite the high Li content in soil, Li was mainly unavailable for plant uptake and bioaccumulation [13]. Iordache et al. (2024) [14] found Li concentrations in bottled and spring water between 0.06–1.557 and 0.09–984 µg/L, respectively, and a strong positive correlation among Li, Na, and Mg. Li exceeded the Health-Based Screening Level (HBSL) in 41.37% and 19% of bottled and spring water samples, respectively. Their results showed that the Li values in drinking waters were extremely high in Covasna County,

and high in Harghita and Mureș Counties. Romania does not have a maximum allowed concentration of lithium in drinking water [15], as do the European Union and the WHO. Due to the high-water consumption of the hydrothermal recycling process for spent Li batteries, Li concentrations are expected to rise, particularly in rivers where treated industrial wastewater is discharged.

Regarding the *biological effects* of lithium, its neuroprotective and regenerative properties can be stressed [16]. Due to its normothymic effects, Li has been commonly used in psychiatry since 1949, mainly for bipolar disorders, treating acute mania and manic episodes [17, 18]. The typical therapeutic oral dosages of lithium carbonate per day vary from 600 to 1200 mg [19]. Using highly bioavailable orotate chelate, a low-dose Li therapy was also developed [20]. Several studies have investigated the relationship between Li concentration in drinking water and the risk of suicide, homicide, and arrest rate for drug use [21−24]. Most of these studies indicate a link between higher Li concentrations in drinking water and a lower risk of suicide [12]. It has been observed that the suicide rate is significantly reduced when drinking water with a high lithium content [12]. It can also have anti-osteoporosis effects. Recently, lithium in drinking water was linked to generally reduced cancer risk [25]. Long-term lithium exposure via drinking water was reported to potentially disrupt thyroid function in a study conducted in the Puna region in Argentina, where local lithium in drinking water ranged from 8 to 1.005 µg/L [12, 26, 46]. In the thyroid gland, lithium (e g, in the form of carbonate) inhibits iodine uptake, the coupling of iodotyrosines, proteolysis, and thus hormone secretion. In the periphery, it blocks the formation of active T3 from T4 by inhibiting the 5'-deiodinase enzyme that activates it. Its spectrum of action is narrow; therefore, it is used successfully only for short-term thyroid inhibition, under lithium control (0.8-1.0 mmol/L content in the blood), mainly in iodine-induced severe hyperthyroidism [27, 28]. Because it inhibits ADH action in the kidney, it can be used to treat water intoxication ('water poisoning,' Schwartz-Bartter syndrome) when used to induce diabetes insipidus. Its effect on the bone marrow can be beneficial in some circumstances, stimulating leukopoiesis. It must be stressed that it is contraindicated in pregnant women because it can cause fetal developmental abnormalities (Ebstein anomaly). Of the lithium salts, lithium carbonate (Li_2CO_3) and lithium citrate ($Li_3C_6H_5O_7$) are most used. The active moiety of these salts is the lithium ion: Li^+.

Selenium is an essential mineral that is naturally present in many foods and added to others; it is also available as a dietary supplement. Selenium is a constituent of 25 selenoproteins, including thioredoxin reductases, glutathione peroxidases, and selenoprotein P [29]. Selenoproteins play critical roles in thyroid hormone metabolism, DNA synthesis, reproduction, and protection from oxidative damage and infection [30, 31]. It exerts a general antioxidant effect. Selenium concentration is higher in the thyroid gland than in

any other organ and plays essential roles in thyroid hormone synthesis and metabolism [32]. Selenoproteins play critical roles in the conversion of T4 to the active T3 (acting in the opposite direction to that of Li), via 5'-deiodinase, which is rich in selenoproteins. In the structure of the iodothyronine deiodinases, Se is incorporated as selenocystein [33]. In addition, the selenoproteins glutathione peroxidase and thioredoxin reductase help protect the thyroid gland from the hydrogen peroxide produced during thyroid hormone synthesis [32, 34]. Selenium is frequently used in autoimmune thyroiditis (Hashimoto), reduces TPOAb levels, and is effective in mild forms of hypothyroidism [33, 35−37]. Selenium may reduce the risk of cardiovascular mortality associated with selenium deficiency. Both its low and high serum levels were associated with depression [38]. In Romania, the maximum allowed concentration for selenium in drinking waters is 20 µg/L [15].

RESULTS AND DISCUSSION

Săcalu de Pădure is a village of 301 people [39] in the Upper Mureș Valley, and it is administratively part of Brâncovenești. This village is not supplied with tap water, so the residents obtain water for their needs from their own wells or other local sources, e g, the two wells in the center. In the villages Brâncovenești and Lueriu, the residents use tap water.

Clinical examinations. Twenty-three subjects, randomly selected and of different ages, were clinically examined: 14 women and nine men. We found thyroid pathology in 11 cases, which means 47.82% suffering from some form of thyroid disease: most of them (9 persons) have various degrees of goiter, some (5) hypothyroidism, one chronic autoimmune thyroiditis, and one papillary thyroid cancer (the latter was operated on and irradiated). Some patients are suffering from combined disorders. At the same time, we found psychological symptoms in 8 persons (34.78%): severe depression, bipolar disorders with repeated, persistent periods of depression, and generalized anxiety disorders with panic attacks.

Determination of urinary iodine excretion (UIE) was conducted on 22 residents in August 2024 in Săcalu de Pădure. The participants were randomly allocated. The average UIE value was 208.09 ± 67.38 µg/L, the median 190 µg/L.

Table 1. The indicators of iodine status (August 2024)

Iodine status indicators (µg/L)	Săcalu de Pădure
Average UIE	208.09
Average ± SD	208.09 ± 67.38
Median value of UIE	190

Table 2. Percentage distribution of UIE

UIE values (µg/L)	>350	100−350	<100	<50
Percentage distribution (in parentheses, the number of subjects)	9.09% (2/22)	90.90% (20/22)	0% (0/22)	0% (0/22)

As Table 2 shows, most cases (90.9%) have normal (100-350 µg/L) [5] values. None of the values were below 100 µg/L, indicating iodine deficiency, and only two exceeded 350 µg/L, pleading for excessive iodine intake. These results suggest *an adequate iodine supply*; there were no cases of UIE below 100 µg/L. The two high values (>350 µg/L, i e 9.09%) suggest even *excessive iodine intake.* This can be attributed to significant environmental exposure to iodine, primarily through alimentation. Thus, monitoring iodine supplementation is essential not only to detect iodine deficiency but also to avoid excessive iodine intake, which can promote the development of certain diseases, including hypothyroidism, hyperthyroidism, autoimmune thyroiditis, and perhaps thyroid cancer [5].

Table 3. Distribution of subjects by age

Age distribution	<20	20-30	30-40	40-50	50-60	60-70	70-80	80-90
Nr. of subjects	3	2	2	4	5	2	2	2

Table 4. Distribution by gender

Woman (number/percentage)	14	63.63%
Man (number/percentage)	8	36.36%

In 1999, the staff of the Endocrinology Clinic from Târgu Mureș (Balázs et al.) showed a moderate iodine deficiency in a group of 508 schoolchildren in the Upper Mureș Valley (around the town of Deda): average UIE was 59.95 ± 30.22 mg/L, while the estimated mean value of UIE was 52.29 µg/L [3]. After that, in 2006 and then in 2013, Kun et al. carried out similar tests in Gurghiu Valley, finding a gradual improvement in the iodine deficiency. In 2006, the UIE was 85.37±60.05 µg/L, with a mean of 74.88 µg/L, confirming a slight iodine deficiency; 30.8% of the children had a normal value. In 68.1% of children, urinary iodine levels did not reach the usual lower limit (100 µg/L), while in 30.3%, they did not even reach 50 µg/L. With

slight differences among the three investigated locations (Caşva, Glăjărie, Largă), hypothyroidism due to iodine deficiency was present in 15% of the examined schoolchildren (11 clinical forms and nine subclinical forms) [1]. In 2013, the average UIE for 120 children from the Gurghiu Valley was 345.15±201.40 µg/L. The mean UIE was 297.5 µg/L, with individual urinary iodine levels differing significantly (SD ± 197.13 µg/L*)*. Urinary iodine levels exceeded the normal range (> 350 µg/L) in 35.83% of children. These high values indicate excessive iodine intake [5].

Table 5. Comparison of iodine status (reflected by UIE) and thyroid pathology in the Upper Mureș and Gurghiu Valley between the years 1999 -2024

Year	Geographical zone, authors	UIE Mean ±SD(µg/L)	Median (µg/L)	Iodine status	Thyroid changes
1999	Mureș Valley (Balázs et al.) [3]	59.95 ± 30.22	52.29	moderate iodine deficiency	33.7% goiter
2006	Gurghiu Valley (Kun et al.) [1].	85.37 ± 60.05	74.88	slight iodine deficiency, 68% reduced iodine intake	15% hypothyroidism (11 overt, 9 subclinical form), 20% goiter
2013	Gurghiu Valley (Kun et al.) [5].	345.15 ± 201.40	297.5	excessive iodine intake in 36% of children	7% subclinical hypothyroidism 6% goiter, autoimmunity increases
2024	Săcalu de Pădure (Varga, Kun et al.)	208 ± 67	190	adequate iodine intake	goiter (total: 9), 56%; (>Gr.1/a: 5), 31%; hypothyroidism (2), 12.5%; cancer (1), 6.25%, from 16 subjects

Nearly 11 years have passed since the last study, underscoring the need for a new understanding of thyroid pathology that remains relevant today, even if it has decreased in both number and significance. Despite the use of iodized salt, thyroid pathology can still be found in the Upper Mureș Valley, though to a much lesser extent. Our survey shows that iodine coverage improved significantly after the introduction of universal use of iodized table salt in 2002-2003, compared with earlier results. Mountain settlements known to be mildly/moderately deficient in iodine have now become iodine sufficient. Looking to the future, we must emphasize the importance of

constant and accurate monitoring. Given that iodine deficiency has practically disappeared, other factors may explain the persistence of thyroid pathology, such as excessive lithium exposure and/or selenium deficiency.

The lithium concentrations in drinking water. Measured in Săcalu de Pădure wells, the Li-concentrations showed relatively high values compared to other settlements of Upper Mureș Valley, such as Lueriu and Brâncovenești (Table 6). Similarly, when we compare these values with the Li-concentrations measured in different areas of Romania [13, 14], in Hungary [12], and in other parts of the world [10, 11, 26], they can be classified as relatively high. It can be assumed that the geological conditions (clay soil) in Săcalu de Pădure are such that the wells may even have a composition close to mineral water, with a relatively elevated lithium content.

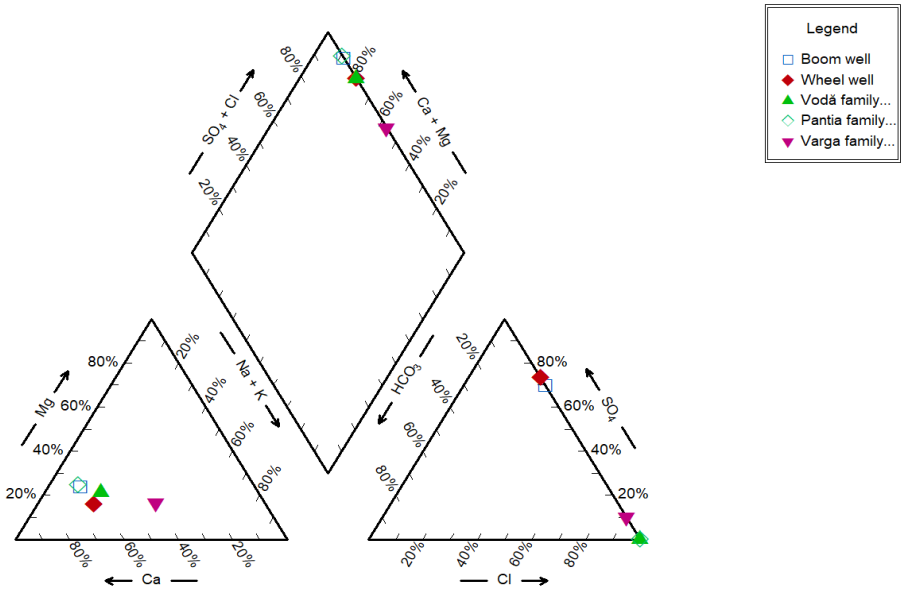

Figure 1. Piper diagram

To determine the water typology, the Piper diagram and the Gibbs plot are employed in several studies to analyze the hydrochemical facies and the correlation among groundwater chemistry and geomorphological processes [40, 41]. The Piper diagram shows that in the cation triangle, all points cluster toward the calcium corner, with only small contributions from magnesium and very low sodium–potassium levels, indicating a clear Ca-dominant character.

Figure 2. Map of the settlements: Săcalu de Pădure, Lueriu, Brâncovenești

Table 6. Lithium concentrations in drinking water. Comparison of the values in Săcalu de Pădure with the data of surrounding settlements (Lueriu, Brâncovenești)

Maximum value of lithium (µg/L) allowed in drinking water [10, 12, 42]:10 µg/L					
No.	Settlement	Origin of sampling	2024 Nov.	2025 April	2025 May
1	Săcalu de Pădure	Central boom well	24.74	22	25.9
2		Central wheel well	38.44	-	-
3		V. family well	25.56	24.5	-
4		P. family well	31.92	-	-
5		B. V. family well	-	40.3	-
6		B. V. family well, Glodeșel 1	-	10	-
7		Glodeșel 2 (Fountain Valley)	-	9.7	-
8		S. C. family well, 96 m deep drilled fountain	-	69	-
Other settlements					
9	Lueriu	tap water (mains)	1.66	-	-
10	Brâncovenești	well water (M. V. well)	1.04	-	-

‘’**–** “: not measured.

Table 6 shows that the Li values found in Săcalu de Pădure wells are higher than those in the surrounding localities of Lueriu and Brâncovenești. Lithium concentrations measured in the wells of Săcalu de Pădure ranged between 9.7 and 69 µg/L (the latter, highest value, was found in the water of a drilled well); three Li values measured at several-month intervals in the water of the central boom wells provided concordant results. Similar concordance can be seen in the case of V. family’s well.

Table 7. Li concentration indicators

Indicators (µg/L)	Săcalu de Pădure	Other settlements
Average	29.09	1.35
Average ±SD	29.09 ± 11.5	1.35 ± 0.35
Median value	25.56	1.35

Although there is no legal limit for lithium [12, 42], the water cannot be considered usual [43, 44], as it generally exceeds the 10 µg/L limit by 2−7 times. Related to this limit, we already mentioned in the introduction that, in Romania, as in the whole of Europe, Li in drinking water is not regulated. The situation is similar in the United States, where a *non-regulatory Health-Based Screening Level* (HBSL) *of 10 µg/L* for Li in drinking water sources has been accepted [10]. This value was later generally accepted as the maximum limit in drinking water. Considering the daily water consumption of 2 liters (as indicated in literature), this means a lithium intake of approximately 20-140 µg/day [42]. Of course, food sources also contribute significantly to its total daily intake.

Until now, the inhibitory effect of Li on *thyroid function* was known only at high therapeutic doses (0.6-1.2 g/day). It can be assumed that long-term intake, even at low doses, may elicit a similar effect, as has already been demonstrated in psychiatry. The literature is scarce regarding the possible role of Li-excess in the persistence of postiodination residual goiters and the associated pathological changes. In this sens two important sources should be mentioned: Stewart A.G. and Pharoah P.O.D. [45], called to attention to this possibility (1996), and the study of Broberg K. et al. (2011), and Concha G. et al. (2010), conducted in Puna region in Argentina − where local lithium in drinking water ranged from 8 to 1.005 µg/L −, concluding: exposure to lithium via drinking water and other environmental sources may affect thyroid function, consistent with known side effects of medical treatment with lithium. This emphasizes *the need to screen for lithium in all drinking water sources* [26, 46]. In high daily doses (e. g., Li carbonate 0.6-1.2 g), used in bipolar disorders, lithium can inhibit all steps of thyroid hormone biosynthesis, as well as their secretion in the bloodstream. Similarly, lithium inhibits 5'-deiodinase, blocking the conversion of T4 to active T3. Its clinical application for the treatment of hyperthyroidism is limited by the side effects observed at these doses; it is used mainly in special circumstances for thyrotoxic states. For the subtle mechanism of lithium's thyroid effects, it is assumed that in the formation of the goiter, in addition to hypothyroidism, which leads to the hyperstimulation of TSH secretion, lithium affects the

insulin-like growth factor, tyrosine kinase, and Wnt, exerting its effect on beta-catenin pathways, too [44, 47, 48]. It is not yet known whether lithium can induce autoimmune thyroiditis [48], but there is much data in this respect.

In addition to the observed thyroid changes, Li may also induce many *neuropsychological* and psychiatric effects. The daily intake of 20-140 µg in Săcalu de Pădure corresponds to low and slightly higher doses exerting different psychological actions [42]. In tiny doses, Li can be used for suicide prevention and dementia prevention (threshold for anti-aggressive/anti-impulsive effects may occur at 0.0008 mEq/L in the blood). Recently, it was supposed that the reduction of testosterone secretion in men also contributes to the acute anti-aggressive effects [49]. It was demonstrated that as the dose increases, not only does the strength of the effect increase, but its *quality* also changes. This can be imagined as follows: increasing the dose will cause lithium to act on more attack points [50]. The effect does not always increase linearly with dose; the relationship can be exponential or sigmoidal. Many factors influence the strength of the effect, but the importance of elimination must be emphasized. Given that there is a long-term and permanent intake, lithium – even in small daily amounts – can accumulate in the body and cause long-lasting effects. At the same time, natural lithium in drinking water *can increase lifespan.*

Regarding the *neuropsychiatric* effects of Li, it was mentioned that its principal therapeutic utilization is for bipolar disorders (usually in daily doses between 0.6-1.2 g), acutely in the manic phase, and chronically for preventing recurrences of these disorders. In chronic, permanent use, it can cause depression, too. This latter effect can be attributed to the induced hypothyroidism and neurobiological alterations resulting from chronic exposure. Low levels of lithium cause mood swings, but very high levels can cause severe poisoning [51].

The subtle *mechanisms of action of lithium in the CNS have* not been elucidated. It is now likely that, first, it affects the secondary messenger processes of neurotransmitters, the current fashionable hypothesis being that it acts through *phosphoinositide,* that can affect myoinositide depletion, thereby enhancing synaptogenesis [43, 52]. Similarly, Li reduces phosphoinositide levels in cell membranes and, consequently, the formation of second messengers, inositol triphosphate and diacylglycerol, thereby reducing the sensitivity of different brain structures to neurotransmitters and hormones in acute manic states. Lithium can affect a wide range of levels, from macroscopic brain structures to intracellular organelles. Modulation of neurotransmission is essential to its mechanism of action; thus, it inhibits dopaminergic and NMDA (glutamate)-ergic transmission and stimulates *GABA*-ergic transmission. It exerts a neuroprotective effect by influencing brain-derived neurotrophic factor (BDNF) and B-cellCLL/lymphoma (Bcl-2), with antiapoptotic actions. At

trace doses (i e, nanolithium), it may act mainly by inhibiting glycogen synthase kinase-3 beta (GSK-3β) [49]. Li acts as a neuroprotective agent against neurodegeneration by preventing inflammation, oxidative stress, apoptosis, and mitochondrial dysfunction using PI3/Akt/GSK3β and PI3/Akt/CREB/BDNF signaling pathways [16]. Regarding the molecular mechanism of Li action, it may exert its effects by directly altering the fate of sodium ions. Even if not perfectly, it can replace sodium ions and influence their movement back and forth during cell firing. This is directly related to the assumption that the main characteristic of lithium is a membrane-stabilizing effect.

From a biological point of view, lithium can be considered a double-edged sword: it is required in small quantities for the normal course of certain biochemical processes, but in large quantities, it has harmful effects: depression, ataxia, tremor, thyroid failure, diabetes insipidus, kidney lesions up to kidney failure, cardiovascular disorders (e.g. cardiac arrhythmias), and metabolic disorders, liver damage, etc. [4, 53, 54]. The inhibitory effect of lithium excess on the thyroid can probably be prevented – at least partially – by selenium supplementation, since both act, inter alia, at the level of the *5'-deiodinase* enzyme, Li inhibiting, and Se stimulating it. The competition between the two elements has already been proven in some aspects in animal experiments [55]. Similarly, some authors have found that Li can interact with Mg ions. Experimental studies showed an activation of thyroid gland synthetic activity by ingestion of magnesium chloride [56]. Mg can indirectly influence deiodination, which catalyzes the conversion of T4 to the more active T3 form [57]. Recently, Ahmed et al. (2025) [58] observed that neonatal hypothyroidism induced by lithium exposure via breast milk could be minimized with iodine supplements, as iodine successfully competed with Li. This may be another way to prevent the adverse thyroid effects of Li excess, in states without pregnancy, too.

Selenium concentration in drinking water. The selenium concentration in drinking water (mains, spring, and stream water) in Săcalu de Pădure, Brâncovenești, and in four localities situated in Gurghiu Valley (Gurghiu, Caşva, Largă, and Glăjărie), a total of 11 measures, was below the limit of quantification (LOQ=2.32 µg/L). However, this result is not consistent with a Se deficiency in the human body, because the intake of Se is attributed mainly to the alimentary route: consumption of selenium-containing foods, food supplements, dairy products, drinking water, multivitamins, and other selenium-containing medicines. So, our current studies are not suitable for answering this problem. Nevertheless, as a first step in the research, we measured its concentrations in drinking water, noting that this question can be answered only by measuring Se serum levels in the future. The maximum limit for selenium in drinking water was 10 µg/L until 2022; it has now been raised to 20 µg/L [15]. There is no established lower limit for its normal concentration because the amount of

selenium in water depends on soil composition. Since elemental selenium is not or only slightly soluble in water, how much is dissolved from rocks under given soil conditions depends on the oxidation state. The selenium concentration in drinking water is low − usually between 0.006 and 10 µg/L − and, on average, does not exceed 3 µg/L. Thus, the relative contribution of drinking water to daily selenium intake is considered not significant compared to that from food, even in regions with high selenium content (e g China, approx. 50 µg/L). Selenites and selenates are generally the more mobile selenium compounds that are soluble in water. The release of these compounds into water is also significantly influenced by soil pH. Magnesium deficiency impacts the bioavailability and tissue distribution of selenium, resulting in reduced levels [59].

Other micro- and macroelements, and anions in drinking waters:

Table 8. Concentrations of macro-, microelements, and anions in the tested waters

µg/l mg/L [15, 60, 61]	Maximum value allowed in drinking water	Săcalu de Pădure				Brânco-venești	LOD, LOQ mg/L µg/L
		Boom well	Wheel well	V. family well	P. family well	V. family well	
K	− mg/L	29.60	53.80	33.70	11.90	4.87	LOD=0.038
Na	200 mg/L	15.1	16.60	21.74	21.8	115	LOD=0.032
Ca	− mg/L	150	125	99.50	148	94.70	LOD=0.039
Mg	− mg/L	18.3	11.1	10.05	20.08	13.7	LOD=0.023
Al	200 µg/L	<LOQ	<LOQ	<LOQ	<LOQ	−	LOQ=5.3
Cr	0.05 mg/L	<LOD	<LOD	<LOD	<LOD	<LOD	LOD=0.048
Mn	0.05 mg/L	<LOD	<LOD	<LOD	<LOD	<LOD	LOD=0.015
Fe	0.2 mg/L	<LOD	0.09	<LOD	<LOD	<LOD	LOD=0.066
Ni	20 µg/L	6.72	5.72	5.63	7.02	−	LOQ=1.41
Cu	2 mg/L	<LOD	<LOD	0.08	<LOD	<LOD	LOD=0.038
Zn	5 mg/L	<LOD	<LOD	0.058	0.011	<LOD	LOD=0.004
Cd	5 µg/L	<LOQ	<LOQ	<LOQ	<LOQ	−	LOQ=0.84
Pb	5 µg/L	<LOQ	<LOQ	<LOQ	<LOQ	−	LOQ=1.53
F^-	1.5 mg/L	0.10	0.09	0.26	0.11	0.09	LOQ=0.05
Cl^-	250 mg/L	41.9	26.2	27	45.7	390	LOQ=0.05
NO_2^-	0.5 mg/L	<LOQ	<LOQ	<LOQ	<LOQ	<LOQ	LOQ=0.05
NO_3^-	50 mg/L	51.9	15.9	11	15.2	16.6	LOQ=0.05
PO_4^{3-}	0.5 mg/L	<LOQ	2.03	0.079	<LOQ	<LOQ	LOQ=0.05
SO_4^{2-}	250 mg/L	130	96.5	77.4	150	56.4	LOQ=0.05

LOD − Limit of detection; LOQ − Limit of quantification; "− ": Not measured.

For the elements and anions K, Na, Ca, Mg, Al, Cr, Mn, Fe, Ni, Cu, Cd, Pb, F-, Cl-, NO_2^-, NO_3^-, and SO_4^{2-}, the maximum values allowed in drinking water were taken from OG 7/2023. For the elements K, Ca, and Mg, there are no legally established maximum concentration limits. These ions are considered essential minerals and part of natural water hardness. The maximum concentrations of Zn and PO_4^{3-} in drinking water are not specified in the legal regulations [15]. Their mentioned upper normal concentrations are cited from other sources [60, 61].

The measured *Ca- and Mg*-concentrations (ranging between 99.5−150, and 10.05−20.08 mg/L, respectively) are comparable with those of some known bottled mineral waters (e g, Biborțeni – from Bățanii, source F1, Sâncrai, Borsec, Stânceni, Poiana Negrii, Aqua Carpatica, etc.) [62]. The Ca and Mg have a natural sedative effect helpful in the prevention and treatment of depression and stress reactions [63, 64]. Both elements play a fundamental role in the intrinsic functions of living cells, particularly in their excitability and motility. Both are necessary for bone health. Hypocalcemia induces neuromuscular hyperexcitation, which can progress to tetanic convulsions. Similarly, hypomagnesemia increases neuromuscular excitability, causes insulin resistance, and perhaps depression. Mg is needed for the activation of over 600 enzymes in the body [65, 66]. *Chloride* ions are present in higher concentrations in the water of the V.M. family well in Brâncovenești, which the proximity of the salt lake can probably explain. In this sense, Na has a relatively high concentration compared to other water sources.

The increased *phosphate* content detected in the wheel well can promote algae growth in the water. The pollution of the Săcalu de Pădure waters is primarily reflected in the increased *nitrate* content of the boom well. This excess is especially dangerous for infants, who may suffer from methemoglobinemia, as nitrates are converted into nitrites in the digestive system, which, when bound to hemoglobin, disrupt oxygen binding. This can lead to a hypoxic state in infants, which manifests itself in a blue discoloration. In adults, it causes stomach irritation. It should be noted that the two wells in the center of Săcalu de Pădure are currently under warning due to contamination: *Not suitable for human consumption!* But this is not indicated in the other wells in the settlement!

LIMITATIONS OF THE STUDY

Although the study was conducted using a rigorous methodology, certain limitations should be acknowledged. The applied random method for subject selection, the partially identical subjects across the different

groups, the relatively small sample size, and the various times of determination could influence the results. Similarly, we do not know the conditions before the introduction of iodination in different settlements, only the global situation of the Upper Mureș Valley. Nevertheless, it can be assumed that iodine deficiency was more severe in the mountainous region (Săcalu de Pădure) than in the flat areas (Brâncovenești, Lueriu). Due to time and resource constraints, the study focused only on the most relevant variables. Yet, the results provide valuable insights into the investigated phenomenon and serve as a basis for further research.

CONCLUSIONS

The relatively high lithium content (between 9.7 − 69 µg/L) of the drinking water in Săcalu de Pădure, Romania, exceeding generally 2−7 times the non-regulatory Health-Based Screening Level of 10 µg/L − considered its maximum standard limit − may contribute to the residual thyroid pathology, given that the iodine supply was found to be normal. It is true that until now, thyroid disorders (hypothyroidism and goiter) have only been detected after larger, therapeutic doses of lithium (typically Li carbonate 600-1200 mg/day, used primarily in bipolar disorders, and rarely in thyrotoxic states), but it can be assumed that the constant intake of small amounts of lithium (20−140 µg/day) can induce similar changes, too. This has already been demonstrated in connection with the psychological effects of lithium used in very low doses. This study cannot address the possible role of selenium deficiency in this process, as selenium is mainly obtained from food rather than drinking water. Residual goiter and related disorders should be treated according to well-established therapeutic guidelines.

EXPERIMENTAL SECTION

The clinical examinations, consisting of a brief familial and personal history, general clinical and endocrine examinations (mainly thyroid), were performed on 23 randomly allocated persons. This exam was conducted by a member of the authors (KIZ), who has practiced endocrinology for more than 4 decades.

Urinary iodine excretion (UIE). The standard Sandell-Kolthoff method was used to determine urinary iodine excretion in 22 residents randomly allocated at the Regional Center of the National Institute of Public Health, Târgu Mureș.

Sample collection and storage. The locations of county seats, the water wells, are illustrated in image 1. Water samples were collected from Săcalu de Pădure and the surrounding localities (Lueriu and Brâncovenești) at multiple time points − November 2024, and April and May 2025 − for comparative analysis. The samples were collected unfiltered in clean plastic bottles that had been rinsed three times with the local sampling water before collection, without any preservation steps. The water samples were stored at refrigeration temperatures (1–2 months) until laboratory processing. The samples were transported in a cooler bag to maintain the appropriate temperature throughout transit.

Reagents and solution. A multielement standard solution IV (1000 mg L^{-1}, Merck, Darmstadt, Germany) was used to prepare the calibration solutions by dilution with 2% (v/v) HNO_3. Nitric acid 63% (m/m) for analysis (Merck, Darmstadt, Germany) was used to prepare the 2% (v/v) HNO_3 blank solution by dilution with double-distilled water produced using a Cyclon bidistiller (Fistreem International, Cambridge, UK).

Sample preparation. Samples were filtered through 4 µm ashless filter paper (Macherey-Nagel, Düren, Germany). Aliquots of 125 mL were evaporated to dryness on a sand bath (ST 82, Gestigkeit Harry GmbH, Düsseldorf, Germany), then taken up with 5 mL of 65% (m/m) HNO_3 and diluted to volume in 25 mL volumetric flasks, resulting in a five-fold preconcentration of the sample.

Instrumentation. Lithium concentrations in the water samples were determined using high-resolution continuum source flame atomic absorption spectrometry on a ContraAA 300 spectrometer (Analytik Jena, Jena, Germany) equipped with a Xe short-arc lamp and an air-acetylene flame. The working conditions employed were those recommended by the manufacturer: 670.784 nm analytical line, air-acetylene flow rate of 70 L/h, and a burner height of 6 mm. Calibration curves were constructed in the range of 0–1 mg L^{-1} Li (n = 6) using peak height measurements, with signals obtained by 5-pixel integration of the analytical line, yielding an R^2 of 0.9999. The limit of detection (LOD) of the method was 0.074 µg/L, calculated using the 3σ criterion based on the standard deviation of 11 blank sample measurements and the calibration curve slope, considering the 5-fold preconcentration of the samples. Measures were first taken in November 2024, and subsequently in April and May 2025; in April 2025, the determinations were extended to the other wells in the village.

The technique used to analyze the anions was ion chromatography. These measurements were performed on an IC 761 Compact type, manufactured by Methrom A. G. (Switzerland). The eluent used was 0.0027 mol-1 sodium carbonate and 0.001 mol-1 sodium bicarbonate. The mobile phase speed

was 0.7 ml/min. The calibration curve was prepared using a 1000 mg/L multicomponent standard solution (NO_3^-, SO_4^{2-}, Cl^-, F^-, PO_4^{3-}). A separate standard stock solution was prepared for the determination of nitrite. All reagents were Sigma-Aldrich brand.

Selenium concentration in drinking water was determined with an inductively coupled plasma mass spectrometer (UltraMass 700, Varian, Australia) at the Regional Center of the National Institute of Public Health in Târgu Mureș. An internal standard of 89Y at 100 ppb was used. Limit of quantification (LOQ): 2,32 µg/L.

ACKNOWLEDGMENTS

We would like to thank Enikő Covaci, Timea Lakatos, and Norbert Muntean for conducting the macro- and microelement analyses and the lithium and anion determinations. We also gratefully acknowledge the support of the Tempus Public Foundation and of Collegium Talentum Competition. Ethical approval no. 11277/23.09.2025 was obtained from Mureș County Public Health Directorate.

REFERENCES

1. I.Z. Kun; Zs. Szántó; J. Balázs; A. Năsălean; C. Gliga; *Hot Topics in Endocrine and Endocrine-Related Diseases***,** Chapter 4: Detection of iodine deficiency disorders (goiter and hypothyroidism) in schoolchildren living in endemic mountainous regions, after the implementation of universal alimentary salt-iodization; In: Fedele M. (ed.); Publisher Intech; **2013,** e-book, pp. 101-128
2. H. Zier; *Lucrare de diplomă* (in Hungarian) - Államvizsga dolgozat, UMPhST, Târgu-Mureș, **2015**.
3. J. Balázs; I.Z. Kun; C. Buksa; L. Coroş; G. Vasilescu; A. Năsălean; *Revista de Medicină şi Farmacie,* Study of endemic goiter, chronic thyroiditis, thyroid function in correlation with iodine intake at schoolchildren living in the superior hydrographic basin of the river Mureş (in Romanian); **2000**/b, *46*, pp. 240-244.
4. Zs. Szántó; I.Z. Kun; I. Pașcanu; M. Kolcsár; Zs. Réti; *Klinikai endocrinologia*, Ed. Univ. Press, Târgu-Mureș, Romania, **2015**, pp. 46-49, 51-64, 68, 71-73, 76-80, 81-88, 89-94.
5. WHO; UNICEF; ICCIDD; *WHO* Assessment of iodine deficiency disorders and monitoring their elimination, Geneva, **2007**, pp. 1-97.
6. M. Długaszek; A. Kłos; J. Bertrandt; Podaż; *Litu w całodziennych racjach pokarmowych studentów*; **2012**.
7. C. Voica; C. Roba; A. M. Iordache; *Anal. Lett.;* Lithium levels in food from the Romanian market by inductively coupled plasma-mass spectrometry (ICP-MS): A pilot study; **2021**, 54, 242–254.

8. D.Szklarska; P.Rzymski; *Biol. Trace Elem. Res.;* Is lithium a micronutrient? From biological activity and epidemiological observation to food fortification; **2019**,189, 18–27.
9. B. D. Lindsey; K. Belitz; C. A. Cravotta; P. L. Toccalino; N. M. Dubrovsky; *Sci. Total Environ.* Lithium in groundwater is used in the United States for the drinking-water supply, **2021**, 767, 144691. D. Szklarska; P. Rzymski; *Biol. Trace Elem. Res.;* Is lithium a micronutrient? From biological activity and epidemiological observation to food fortification; **2019**, 189.
10. N. Sharma; P. Westerhoff; C. Zeng; *Chemosphere;* Lithium occurrence in drinking water sources of the United States; **2022**, 305, 135458.
11. T. Mahmudiono; Y. Fakhri; H. Daraei; F. Mehri; M. Einolghozati; S. Mohamadi; A.M. Khaneghah; *Rev. Environ. Health;* The concentration of Lithium in water resources: A systematic review, meta-analysis, and health risk assessment*;* **2023**, 39(4):667-677. doi: 10.1515/reveh-2023-0025
12. P. Dobosy; Á. Illés; A. Endrédi; G. Záray; *Sci. Rep.;* Lithium concentration in tap water, bottled mineral water, and Danube River water in Hungary, www.nature.com/, **2023**; 13:12543. https://doi.org/10.1038/s 41598-023-38864-6
13. A.I. Török; A. Moldovan; E.A. Levei; O. Cadar; C. Tănăselia; O.T. Moldovan; *Materials*; Assessment of Lithium, Macro- and Microelements in Water, Soil and Plant Samples from Karst Areas in Romania*,* **2021,** 14, 4002. DOI:10.3390/ma14144002
14. A. M. Iordache; C. Voica; C. Roba; C. Nechita; *Front. Public Health*, Evaluation of potential human health risks associated with Li and their relationship with Na, K, Mg, and Ca in Romania's nationwide drinking water, **2024,** p 1-12, DOI:0.3389/fpubh. 2024.1456640
15. Guvernul României - Ordonanţă nr. 7/2023 din 18 ianuarie 2023 *Ordonanţa nr. 7/**2023*** privind calitatea apei destinate consumului uman.
16. F. Ghanaatfar; A. Ghanaatfar; P. Isapour; N. Farokhi; S. Bozorgniahosseini; M. Javadi; M. Gholami; L. Ulloa; N. Coleman-Fuller; M. Motaghinejad; *Fundam. Clin. Pharmacol.*; Is lithium neuroprotective? An updated mechanistic illustrated review, **2022,** 37 (1):4-30. https://doi.org/10.1111/fcp.12826
17. M. L. Bourgeois; M. Masson; *The Science and Practice of Lithium Therapy;* Springer International Publishing, Cham; The history of lithium in medicine and psychiatry. **2017***;* 181–188; https://doi.org/10.1007/978-3-319-45923-3_10.
18. M. Vosahlikova; P.Svoboda; *Acta Neurobiol. Exp.;*Lithium–therapeutic tool endowed with multiple beneficial effects caused by various mechanisms; **2016**, 76, 1–19.
19. W. Young; *Cell Transplant;* Review of lithium effects on brain and blood, **2009**, 18, 951–975.
20. H. A. Nieper; *Agressologie;* The clinical applications of lithium orotate: A two-year study; **1973,** 14, 407–411.
21. M. Helbich; M. Leitner; N. D. Kapusta; *Br. J. Psychiatry;* Lithium in drinking water and suicide mortality: Interplay with lithium prescriptions; **2015**, 207, 64–71.
22. V. Liaugaudaite; N. Mickuviene; N. Raskauskiene; R. Naginiene; L. Sher; J. *Trace Elem. Med Biol*.; Lithium levels in the public drinking water supply and risk of suicide: A pilot study, **2017**, 43, 197–201.

23. P. Oliveira; J. Zagalo; N. Madeira; O. Neves; *Acta Med. Port.;* Lithium in public drinking water and suicide mortality in Portugal: Initial approach, **2019**, 32, 47–52.
24. P. Araya; C. Martínez; J. Barros; *Front. Public Health*; Lithium in drinking water as a public policy for suicide prevention: Relevance and considerations, **2022**, 10, 805774.
25. G. Mukherjee; *Medscape*; Lithium in Drinking Water Linked to Reduced Cancer Risk**, 2025**, March 12.
26. K. Broberg; G. Concha; K. Engström; M. Lindvall; M. Grandér; M. Vahter; *Environ Health Perspect;* Lithium in drinking water and thyroid function; **2011**,119:827–30. doi: 10.1289/ehp.1002678
27. I.Z. Kun; Zs. Szántó; T. Bartók; C. C. Pop Radu, I. Pascanu; *Endocrine Abstracts;* The use of lithium and perchlorate therapy in exceptional cases of hyperthyroidism; **2011**, 26 P376.
28. Ü. Çavdar; Ö. Eren; S. Karaıslı; M.S. Ertürk, B.Ö. Pamuk; *Clin Endocrinol (Oxf);* Safety and Effectiveness of Lithium Therapy in Patients with Graves' Disease; **2025** Dec;103(6):883-887. doi: 10.1111/cen.70022. Epub 2025 Aug 18. PMID: 40826817.
29. V.N. Gladyshev; E.S. Arnér; M.J. Berry; R Brigelius-Flohé; E.A. Bruford; et al.; *J Biol Chem;* Selenoprotein Gene Nomenclature, **2016**; 291:24036-40.
30. L.K. Hong; A.M. Diamond; Selenium, In: Marriott BP; Birt DF; V.A. Stallings; A. A Yates; eds. *Present Knowledge in Nutrition*. 11th ed. Cambridge, MA: Academic Press; **2020**,443-56.
31. X.G. Lei; M. Rayman; R.A. Sunde; Selenium. In: Tucker KL, C.A. Ross, G.L. Jensen; R. Torger-Decker; C.P. Duggan, eds. *Modern Nutrition in Health and Disease*. 12th ed. Burlington, MA: Jones & Bartlett Learning. In press. **2024**.
32. M. Ventura; M. Melo; F. Carrilho; *Int J Endocrinol;* Selenium and Thyroid Disease: From Pathophysiology to Treatment; **2017**;1297658.
33. A.M. Shulhai; R. Rotondo; M. Petraroli; V. Patianna; B. Predieri; L. Lughetti; S. Esposito; M.E. Street; *Nutrients;* The Role of Nutrition on Thyroid Function; **2024,** 16, 2496. https://doi.org/10.3390/nu16152496
34. M. P. Rayman; *Lancet;* Selenium and human health; ***2012***; 379:1256-68.
35. Zs. Szántó., I.Z. Kun; I. Kun; *OrvTudErt.;* Szelénkezelés idült autoimmun pajzsmirigybetegségekben. **2013,** Aprilie.
36. X.Q. Kong; G.Y. Qiu; Z.B. Yang; Z.X Tan; X.Q. Quan; *Medicine;* Clinical efficacy of selenium supplementation in patients with Hashimoto thyroiditis: A systematic review and meta-analysis; **2023**, 102, e3379.
37. V.V. Huwiler; S. Maissen-Abgottspon; Z. Stanga; S. Mühlebach; R. Trepp; L. Bally, A. Bano; *Thyroid*; Selenium Supplementation in Patients with Hashimoto Thyroiditis: A Systematic Review and Meta-Analysis of Randomized Clinical Trials., 34 (3): 295-313. **2024**. DOI: 10.1089/thy.2023.0556
38. L. A. Colangelo; K. He; M. A. Whooley; M. L Daviglus; S. Morris; K. Liu; *Neurotoxicology;* Selenium exposure and depressive symptoms: the Coronary Artery Risk Development in Young Adults Trace Element Study; **2014** Feb 20; 41:167–174. doi: 10.1016/j.neuro.2014.02.003
39. www.recensamant.ro

40. K.P. Kom; B. Gurugnanam; V. Sunitha; Y.S. Reddy; A.K. Kadam; *Int. J. Energy. Res*.; Hydrogeochemical assessment of groundwater quality for drinking and irrigation purposes in western Coimbatore, South India, **2022**, 6, 475–494.
41. A. Alqarawy; M. El Osta; M. Masoud; S. Elsayed; M. Gad; *Water;* Use of hyperspectral reflectance and water quality indices to assess groundwater quality for drinking in arid regions, Saudi Arabia, **2022**, 14, 2311.
42. M. Adeel; M. Zain; N. Shakoor; M. A. Ahmad; I. Azeem; M. A. Aziz; R. X. Supe Tulcan; A. Rathore; M. Tahir; R. Horton; M. Xu; R. Yuku; *Clean Water*; Global navigation of Lithium in water bodies and emerging human health crisis, *published* in partnership with King Fahd University of Petroleum and Minerals, **2023**, 6, 33.
43. G. S. Malhi; M. Tanious; et al*.; CNS drugs;* Potential mechanisms of action of lithium in bipolar disorder, **2013,** 27(2), pp. 135-153.
44. J.H. Lazarus; *Best Pract. Res. Clin. Endocrinol. Metab.*; Lithium and thyroid**; 2009**, 23, pp 723.
45. A.G Stewart; P.O.D Pharoah; *Environ. Geochem Health*; Clinical and epidemiological correlates of iodine deficiency disorders. From: Appleton, J. D., Fuge, R. & McCall, G. J. H. (eds), Geological Society Special Publication, **1996,** No. 113, pp. 223-230.
46. G. Concha; K. Broberg; M. Grandér; A. Cardozo; B. Palm; M. Vahter; *Environ. Sci. Technol*. High-level exposure to Lithium, boron, cesium, and arsenic via drinking water in the Andes of northern Argentina; 2010, 44:6875–80, doi: 10.1021/es1010384
47. A.S. Rao; N. Kremenevskaja; J. Resch; G. Brabant; *Eur. J. Endocrinol*; Lithium stimulates proliferation in cultured thyrocytes by activating Wnt/beta-catenin signalling, **2005**, 153:929.
48. M. I. Surks; *UpToDate;* Lithium and the thyroid, **2024**.09.29
49. T. Terao; H. Hirakawa; M. Muronaga; T. Izumi; K. Kohno; *Pharmaceuticals*; Trace Lithium for Suicide Prevention and Dementia Prevention, A Qualitative Review., **2024**, 17, 1486. https://doi.org/10.3390/ph17111486
50. M. M. Varga; A. Csiszér; R. Barabás; I. Z. Kun; *Book of abstracts* No. 7/2024 George Emil Palade University of Medicine, Pharmacy, Science, and Technology of Târgu Mureș. University Days December 9-13, 2024, Lithium excess in drinking waters of a mountainous village (Săcalu de Pădure), a potential determining factor for remnant thyroid pathology, Târgu Mureș. Scientific Session of University Academic Staff. International Conference of PhD Students and Young Doctors, page 182.
51. N. Shakoor; M. Adeel; M. Arslan Ahmad; M. Zain, U. Waheed; R. A. Javaid; F. U. Haider; I. Azeem; P. Zhou; Y. Li; G. Jilani; M. Xu; J. Rinklebe; Y. Rui; *Environ. Sci. Ecotechnology*; Reimagining safe lithium applications in the living environment and its impacts on human, animal, and plant system, **2023**, 15, 100252
52. J. H. Kim; S. A. Thayer; *Mol. Pharmacol.;* Lithium Increases Synapse Formation between Hippocampal Neurons by Depleting Phosphoinositides,**2009,** 75: 1021–1030.
53. A. H. Young; *Br J Psychiatry*; More good news about the magic ion: lithium may prevent dementia, **2011**, 198, 336–337.

54. S. Yacobi; A. Ornoy; *Isr J Psychiatry Relat Sci*;Is lithium a real teratogen? What can we conclude from the prospective versus retrospective studies?, **2008**,45 (2),95–106
55. M. Kiełczykowska; J. Kocot, J. Kurzepa, A. Lewandowska, R. Żelazowska, I. Musik; *Biol Trace Elem Res.;* Could Selenium Administration Alleviate the Disturbances of Blood Parameters Caused by Lithium Administration in Rats?, **2014**, 158:359–364.
56. R.V Yanko; E.G. Chaka; M.I. Levashov; *Clin. Exp. Morphol.;* Histomorphological changes in the thyroid gland of rats after magnesium chloride ingestion; **2019**, 8, 41–47.
57. B.R. Kolanu; S. Vadakedath; V. Boddula; V. Kandi; *Cureus;* Activities of Serum Magnesium and Thyroid Hormones in Pre-, Peri-, and Post-menopausal Women. **2020,** 12, e6554.
58. I. Ahmed. et al., *J Trace Elem Med Bio;* Minimizing neonatal hypothyroidism induced by lithium exposure through breast milk; 2025, 89, 127653. https://doi.org/10.1016/j.jtemb.2025.127653
59. A.O. Ige; R.N. Chidi; E.E. Egbeluya; R.O. Jubreel; B.O. Adele; E. O. Adewoye; *Heliyon;* Amelioration of thyroid dysfunction by magnesium in experimental diabetes may also prevent diabetes-induced renal impairment; **2019**, 5, e01660.
60. WHO; *A global overview of national regulation and standards for drinking water quality,* second edition, **2021**,
61. *Legea* nr. 458/2002 privind calitatea apei potabile
62. K. Bodor; Zs. Bodor; A. Szép; R. Szép; *J. Food Compos. Anal.;* Classification and hierarchical cluster analysis of principal Romanian bottled mineral waters, **2021** July, Volume *100,* 103903, https://doi.org/10.1016/j.jfca.2021.103903
63. M.J. Alkhatatbeh; H. N. Khwaileh; K. K. Abdul-Razzak*; Public Health Nutr.*; High prevalence of low dairy calcium intake and association with insomnia, anxiety, depression, and musculoskeletal pain in university students from Jordan; **2020**, 24(7), 1778–1786 doi:10.1017/S1368980020002888
64. A. Kowalczyk; A.J. Paczek; P. Dyczek; W. Staniszewska; J. Hofman; S. Lach I. Bednarek; *J. Educ. Health Sport*; Magnesium and Mental Health: A Review of Its Role in Anxiety, Sleep Disorders and Depression; **2025**; 83:66774. eISSN 23918306
65. Z. Majewska; K. Orywal; *Int. J. Mol. Sci;* Mineral Homeostasis and Depression: Implications for Prevention and Therapeutic Support − A Narrative Review; **2025**, 26, 6637. https://doi.org/10.3390/ijms26146637
66. A. J. Paczek; P. Dyczek; W. Staniszewska; J. Hofman; S. Lach; I. Bednarek; *J. Educ. Health Sport*; Magnesium and Mental Health: A Review of Its Role in Anxiety, Sleep Disorders and Depression, **2025**; 83:66774. eISSN 2391-8306. https://apcz.umk.pl/JEHS/article/view/66774. https://doi.org/10.12775/JEHS.2025. 3.66774.

STUDIA UBB CHEMIA, LXXI, 1, 2026(p. 163-174)
(RECOMMENDED CITATION)
DOI:10.24193/subbchem.2026.1.10

NEW PURIFICATION APPROACH AND THE ANTICANCER ACTIVITY OF PHENOLIC COMPOUNDS FROM *MANGIFERA INDICA* LEAVES CULTIVATED IN IRAQ

Jameelah Kadhim TAHER AL-ISAWI[a], Rafal Ismael ALI[b], Doaa Khalid MEZAAL[c], Dhafir T.A. AL-HEETIMI[a*]

ABSTRACT. Cancer continues to be a primary cause of death globally, prompting the investigation of effective natural therapeutic agents. *Mangifera indica* L. (mango) leaves are notable for their abundant bioactive compounds, especially polyphenols. This study investigated the extraction, purification, and anticancer properties of polyphenolic compounds from *M. indica* L. leaves cultivated in Iraq. The research employed systematic extraction procedures using methanol followed by purification through Sephadex LH60 column chromatography. Phytochemical analysis and High-Performance Liquid Chromatography (HPLC) characterization revealed significant concentrations of bioactive compounds, with mangiferin (49.8 mg/L) being the predominant polyphenolic constituent, alongside other compounds including apigenin (40.5 mg/L), ferulic acid (36.5 mg/L), and kaempferol (28.9 mg/L). The cytotoxic potential of methanolic extract of *M. indica* diphenyltetrazolium bromide (MTT) assay. The results demonstrated that the cytotoxic effect is dependent on dose, with maximum cell death (68.33%) observed at 1000 µg/mL concentration. The extract exhibited a moderate cytotoxic effect with a half-inhibitory concentration (IC_{50}) value of 132.4 µg/mL. The observed anticancer activity is attributed to the synergistic effects of various polyphenolic compounds, particularly mangiferin, which triggers apoptosis through both intrinsic and extrinsic pathways. These findings suggest that *M. indica* leaf extract could be a promising source of natural anticancer agents.

Keywords: *Mangifera indica L., mangiferin, MTT, HRT-18*

[a] *Department of Chemistry, College of Education for Pure Science Ibn Al-Haitham, University of Baghdad, Baghdad, Iraq.*
[b] *Tropical-Biological Research Unit, College of Science, University of Baghdad, Baghdad, Iraq.*
[c] *Biochemical Engineering Department, Al-Khwarizmi College of Engineering, University of Baghdad, Baghdad, Iraq.*
[*] *Corresponding author: dhafir.t.a@ihcoedu.uobaghdad.edu.iq, dhafir1973@gmail.com*

INTRODUCTION

The rising cancer incidence in the world has heightened the quest for new therapeutic agents available in nature, especially those found in plants [1]. For many years, medicinal plants have been valued for their rich content of bioactive substances, and phenolic compounds, in particular, are now viewed as strong prospects for use in creating new anticancer therapies [2]. One such plant is the *Mangifera indica* L. (mango), which is a member of the family Anacardiaceae and has attracted considerable attention in the scientific world because of its rich phytochemical composition and its traditional usage as a medicine [3]. *M. indica* L. is considered one of the key tropical fruits in the world, which is assumed to have Asian roots [4]. Human beings use both the ripe and the unripe mangoes in pickles, juice, oils, nectar, powder, sauce, cereal flakes and jam [5]. Mango fruit, peel, and flesh are known to be highly rich in fiber, vitamins C and A, essential amino acids, and polyphenols [6]. Mango seeds have been termed as a great source of polyphenols [7]. Although consumption of mango fruit as a food item is widely common, various parts of mango trees have been used in medicine since ancient times, predominantly in the Southeast Asian countries, with recent uses in Iraq [8]. Although the fruit of *M. indica* L. is a valuable source of economic growth; its leaves were traditionally used to treat diabetes [9], hypertension [10] and other inflammatory diseases [11].

Phenolic compounds represent one of the most homogenous groups of plant secondary metabolites [12] that include simple phenols, phenolic acids, flavonoids and more complex polyphenolic compounds [13]. They consist of one or more aromatic rings that have hydroxyl groups, which give them antioxidant potential [14]. The phytochemical research on *M. indica* L. leaves has revealed a number of phenolic groups, such as mangiferin, gallic acid, quercetin and different gallotannins [15].

The anticancer effects of phenolic compounds have been shown to have a promising future based on several mechanisms such as antioxidant activity, cell cycle control, apoptosis and cellular pathways control and modulation [16]. The molecular pathway that uses phenolic compounds to exert an anticancer effect is usually a multifaceted one. These are neutralization of reactive oxygen species [17], inhibition of pro-inflammatory mediators [18], control of cell cycle checkpoint proteins [19] and activation of caspase-dependent apoptotic pathway [20]. Kim *et al* demonstrated that the ethanolic extract of *M. indica* peel can trigger apoptosis in human cervical cancer HeLa cells through upregulation of apoptosis-related proteins expression, including Bax, Bcl-2, Bid, and caspases (3, 8, and 9) [21].

This study presents the first comprehensive characterization of Iraqi-cultivated *M. indica* leaf polyphenols, employing two-step Sephadex LH60 purification, HPLC analysis and cytotoxicity against HRT-18 colon cancer cells, expanding *M. indica* therapeutic applications while validating Middle Eastern cultivar bioactivity potential.

RESULTS AND DISCUSSION

Extraction of *M. Indica* L. Leaves

The leaves of *M. indica* L. were subjected to a series of extraction and purification processes for the isolation of polyphenols. Results in Table (1), exhibit that the resulted yield from the final purification step of *M. indica* methanolic extract (MI-ME) was 1.3 g. All fractions collected from Sephadex LH60 (2 × 30 cm) final purification step were detected positive for the presence of polyphenols.

Table 1. The total weight and yield of following *M. indica* L. leaves extraction and purification.

Steps	Weight	Yield (%)
M. indica L. Leaves	50 g	----
Methanolic Extraction	3.8 g	7.6
Sephadex LH60 (2 × 20 cm)	2.6 g	68.4
Sephadex LH60 (2 × 30 cm)	1.3 g	50.0

Sephadex LH60 is a size exclusion medium that is based on hydroxypropylated dextran, which offers an effective means of purifying phenols in alcoholic extracts of plants. Its unique cross-linked structure and optimal distribution of pore sizes make it highly efficient in separation of polyphenolic chemicals in terms of their molecular weights. The hydrophobic nature of LH60 enables strong interactions with phenolic compounds in an operation in organic solvents like ethanol or methanol [22].

Phytochemical Analysis of MI-ME

The crude MI- ME was measured quantitatively on the content of polyphenols, quantities of alkaloids and flavonoids. The crude MI-ME according to results was positive in polyphenols because of the reaction of

the bluish green color. The appearance of yellow color reaction was followed by the detection of flavonoids in MI-ME. Secondly, the presence of alkaloids was also detected by the presence of both white and brown precipitates that were obtained after the addition of Mayer and Wagner reagents, respectively.

M. indica L. has numerous bioactive chemicals that are mainly polyphenols and terpenoids in leaves [23]. Its main phenolic compounds include mangiferin (xanthone C-glycoside), gallic acid, quercetin glycosides as well as catechins [24]. In addition, triterpenes cycloartenol, friedelin and lupeol are very abundant in the leaves. Analysis of phytochemicals always indicates that it contains alkaloids, tannins, saponins, and flavonoids [25]. These chemicals vary in their concentration according to environmental factors, maturity of the leaves and methods of extracting them. The active components make the leaves supplement the already known antioxidant, anti-inflammatory, and antibacterial activity.

HPLC analysis revealed that the majority of purified MI-ME contained polyphenolic phytochemical constituents (Table 2). These phenolic compounds include apigenin, chlorogenic acid, ferulic acid, gallic acid, mangiferin, kaempferol, quercetin and rosmarinic acid with different concentration range between (20.6 for quercetin to 49.8 ppm for mangiferin).

Table 2. Mean ± SD concentration (mg/L) of polyphenolic compounds HPLC quantified using HPLC (*n* = 3).

Name	Mean Concentration ± SD (mg/L)
Apigenin	40.5±4.73
Chlorogenic acid	22.5±1.62
Ferulic acid	36.5±2.66
Mangiferin	49.8±5.09
Kaempferol	28.9±2.41
Quercetin	20.6±2.83
rosmarinic acid	24.6±3.37
Gallic acid	25.7±2.19

SD: Standard Deviation

The leaves of *M. indica* L. are characterized by a substantial array of polyphenolic chemicals, with mangiferin as the principal C-glucosylxanthone, Phytochemical investigations have identified substantial levels of flavonoids, including quercetin, kaempferol derivatives, and gallotannins [26]. Figure (1) presents the HPLC results, indicating the presence of several phenolic acids—including gallic, protocatechuic, and ellagic acids—that contribute to

the extract's antioxidant activity. [27]. Recent research employing liquid chromatography/mass spectrometry has discovered new polyphenolic chemicals, such as benzophenone derivatives and intricate gallotannins [24].

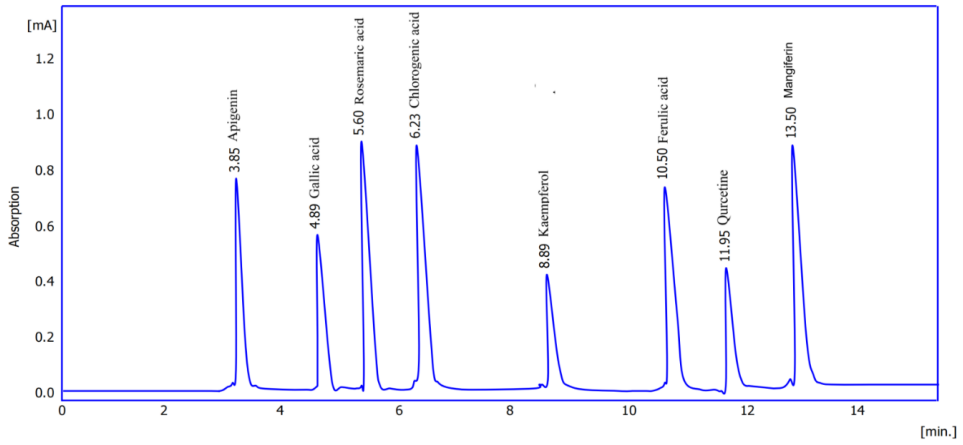

Result chromatography Table (Uncal - F:\ sample 1)

No	Reten. Time [min]	Area [mAU.s]	Height [mAU]	Area [%]	Height [%]	W 05 [min]	Compound Name
1	3.85	7542.59	795.85	13.25	13.24	0.20	Apigenin
2	4.89	5214.98	586.49	9.59	9.33	0.12	Gallic acid
3	5.60	15985.64	850.49	15.98	15.48	0.25	Rosemaric acid
4	6.23	16995.24	850.66	15.77	15.74	0.25	Chlorogenic acid
5	8.89	2011.45	395.44	7.35	7.65	0.12	Kaempferol
6	10.50	9630.31	784.11	14.56	14.26	0.20	Ferulic acid
7	11.95	2589.67	390.65	7.44	7.30	0.14	Qurcetine
8	13.50	17854.66	854.99	15.59	15.42	0.25	Mangiferin
	Total	77824.78	5508.86	100.00	100.00		

Figure1. HPLC Analysis several phenolic acids.

The polyphenolic concentrations identified in this study demonstrate both consistency and variation compared to previously reported values from different geographical origins. Zhang et al., 2012 reported that mangiferin contents analyzed in *M. indica* from China were 5.04 to 18.95 mg/g, confirming mangiferin as the predominant xanthone across cultivars [28]. In another study, the concentration of both gallic acid and quercetin showed great variation in different mango cultivars from Spain with 16-500 µg/mL and 16-800 µg/mL, respectively [29].

The inclusion of these bioactive chemicals enhances the extract's therapeutic potential, demonstrating notable antioxidant, anti-inflammatory, and antibacterial properties. The synergistic interactions among these polyphenolic chemicals augment their biological performance, especially in free radical scavenging and enzyme inhibitory activities.

Cytotoxic Activity of Purified MI-ME Against HRT-18 Cancer Cells

The potential anticancer activity of purified MI-ME rich with phenolic compounds was investigated using MTT cytotoxic assay against HRT-18 cell line. Figure (2) shows the effect of MI-ME on the HRT-18 cell line at different concentrations. The results indicate that the cytotoxicity of MI-ME against HRT-18 cells increases by increasing the concentration in dose-dependent pattern. The highest killing activity observed at 1000 µg/mL concentration, with a value of 68.33% and the lowest cytotoxicity was at concentration 31.2 µg/mL, with a value of 17.54%. Both concentrations, 1000 and 500 µg/mL, showed no significant differences in inhibiting HRT-18 cell viability, however, significant ($p < 0.05$) differences were observed with 250, 125, 62.5 and 31.2 µg/mL. The increase in cytotoxicity with increasing dose indicates the toxic effect of the MI-ME on the cell viability.

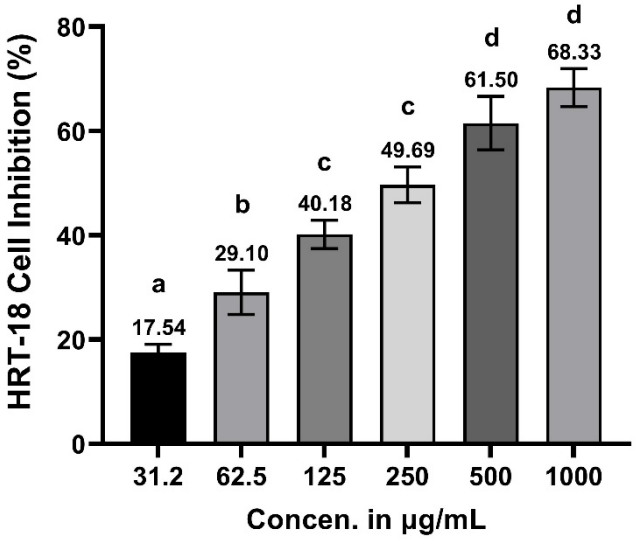

Figure 2. Cytotoxic activity of MI-ME against HRT-18 cell line. Different letters (a, b, c and d) considered significantly different at $p < 0.05$.

The IC_{50} which represents the concentration of purified MI-ME that inhibits cell growth by 50%. As illustrates in Figure (3), the calculated IC_{50} was 132.4 µg/mL, indicating that the extract exhibits a moderate cytotoxic effect on the HRT-18 cells line.

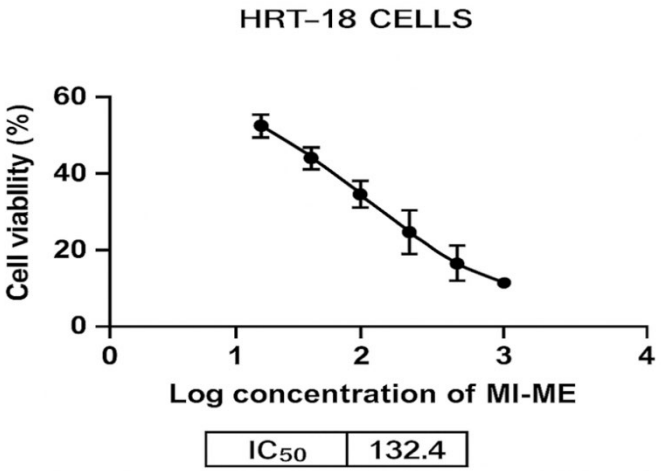

Figure 3. IC_{50} of purified MI-ME on HRT-18 cell line.

The cytotoxic properties of *M. indica* L. leaf extract have been thoroughly investigated, revealing notable antiproliferative effects due to its abundant polyphenolic content [30]. A study by Yehia and Altwaim indicated the cytotoxic activity of ethanolic extract of *M. indica* collected from Saudi Arabia with IC_{50} of 41.2 and 44.7 µg/mL against MCF-7 and HeLa cell lines [31]. While mango cultivars from Costa Rica showed a moderate cytotoxic activity against AGS, HepG2 and SW620 cancer cell lines with IC_{50} range of 138–175 µg/mL [32]. Mangiferin, the principal bioactive molecule, demonstrates specific cytotoxicity towards diverse cancer cell types via several routes. Research indicates that these polyphenols induce apoptosis through both intrinsic and extrinsic mechanisms, as seen by elevated activity of caspase-3, -8, and -9 [29]. The antiproliferative potential of gallotannins derived from mango seed extract against a spectrum of cancer cell lines, including liver, breast, and leukemia was investigated [33]. Vermerris and Nicholson indicated that proanthocyanidins and tannins have the potential to prevent digestive and other internal organ cancers [33]. The combined activities of quercetin derivatives and gallotannins augment the extract's antiproliferative capacity via ROS-mediated pathways and DNA fragmentation [30].

Many studies have also indicated an investigation the effect of an extract on other breast cancer cells lines like MDA-MB-231 and MCF-7. Also, Phenolic compounds of *M. indica* extract shown inhibition of proliferation of cancer cell, sometimes involving the induction of cell cycle arrest and apoptosis of many cancer cell lines types like Lung Cancer cell cines (A-549), Leukemia: Cell lines (Molt-4 and HL-60), Cervical Cancer (HeLa cells), Prostate Cancer (LnCap) and Gastric Cancer (AGS).

CONCLUSION

This study provides new insights including: (1) first comprehensive phytochemical characterization of Iraqi *M. indica* cultivar, (2) innovative two-step Sephadex LH60 purification methodology, and (3) first anticancer evaluation against HRT-18 colon cancer cells. Findings correlate with established mangiferin dominance and polyphenolic diversity while revealing regional quantitative variations and expanding therapeutic applications. The findings in this study indicate potential anticancer activity of methanolic extract of *M. indica* leaves but further investigation into other cancer models and *in vivo* systems are needed.

MATERIALS AND METHODS

Methanolic Extraction of *M. INDICA* L. Leaves (MI-ME)

The leaves of *M. indica* L. were collected from local mango farms in April 2024. The leaves were washed with tap water to remove impurities and air dried. The dried leaves crushed and powdered using electrical blender then 50 g of dried leaves were mixed with 450 mL from absolute methanol in ratio of 1:9 respectively. The mixture was subjected to constant mixing using shaker incubator (120 rpm) at room temperature for one week. After the end of maceration, the plant parts removed from the extract by filtration using filter paper (Whatman No. 1). The solvent was removed under vacuum by evaporation in rotary evaporator at 40°C, and the dried crude extract was stored at 4°C in refrigerator.

Separation and Purification of Polyphenols from MI-ME

Column chromatography of the polyphenols was conducted based on the method outlined by Harborne [34]. The dried powder of MI-ME obtained from extraction method was dissolved in 5 mL methanol and introduced into an open glass column (2 × 20 cm) filled with Sephadex LH60 previously equilibrated with 70% methanol. The elution was collected in 25 separated tubes each tube was filled with 5 mL of the eluent at a rate of 0.5 mL/min. All fractions were tested for $FeCl_3$ (1%) solution as a colorimetric method for polyphenols identification. Only positive tubes for $FeCl_3$ were collected and dried in dry oven at 40°C. The dried powder was subjected to a second round of purification using Sephadex LH60 (2 × 30 cm) column using the same conditions. A total of 20 tubes were collected and all tubes were tested for $FeCl_3$ 1% solution for polyphenols identification, and only the positive tubes were collected and dried.

Phytochemical Analysis

1. Detection of Polyphenols

Aliquot of 3 mL of sample was mixed with 2 mL of 1% $FeCl_3$, %; the appearance of bluish green color indicated the presence of phenols.

2. Detection of Alkaloids

An amount of 0.5 g of MI-ME was dissolved in 2.5 mL of distilled water acidified with 4% hydrochloric acid and 0.5 mL of the mixture was tested in a watch glass with each of the following reagents. First, Mayer reagent (1.36 g $HgCl_2$ and 5.0 g KI in 100 mL DW), the appearance of white precipitate indicated the presence of alkaloids. Second, Wagner reagent (2.5 g iodine and 12.5 g KI in 250 mL DW), the appearance of brown precipitate indicated the presence of alkaloids.

3. Detection of Flavonoids

Flavonoids were detected according to the method previously described [35]. In brief, one gram of MI-ME was suspended in 1 mL of 95% ethanol (Solution A). One volume of solution A was mixed with 1 volume of solution B (consist of 1 mL of ethyl alcohol (50%) and 1 mL of 50% potassium hydroxide). The appearance of yellow color after mixing of equal amounts of solution (A) and (B) indicated the presence of flavonoids.

High Performance Liquid Chromatography (HPLC)

MI-ME (10 µL) was automatically injected, and chromatographic separation was performed on a Poroshell 120 EC-C18 column (100 × 2.1 mm, 1.9 µm) with a flow rate of 0.3 mL/min. The mobile phase was made up of water with 0.5% formic acid (solvent A) and acetonitrile and methanol (80:20, v/v) as solvent B. Gradient elution was performed as follows: 0-1 min at 15% B to 20% B, 12 min at 50% B, 15 min at 60% B, 17.0-19.0 min at 95% B, and 19.0-20.0 min at 15% B, with a total run time of approximately 1 hour. The column temperature remained at 40°C.The study was performed in both positive and negative ionization modes, employing dynamic multiple reaction monitoring with a dwell time of 0.02 second. Each analysis was repeated three times.

Cell Line

HRT-18 colon cancer cell line was kindly provided from Biotechnology Research Center – Al-Nahrain University, Baghdad, Iraq.

The cells were cultured in Dulbecco's Modified Eagle Medium (DMEM) (Sigma, USA) media supplemented with 10% fetal bovine serum, 100 units/mL penicillin, and 100 µg/mL streptomycin. The cells were maintained at 37°C and 5% CO_2 environment. When cells reached 80% confluency, a brief trypsinization was performed for 2 – 3 min followed by culturing into a new flask [36].

MTT Experiment

A uniform volume of HRT-18 cell suspension (2×10^4 cells/mL) was added to the selected wells of a 96-well sterile tissue culture plate. The filter-sterilized (using Millipore Filter, 0.22 µm) MI-ME polyphenols (Dissolved in DMSO) was added to the wells of a microtiter plate to obtain final concentrations ranging from 0 to 1000 µg/mL in DMEM. The cells exposed to purified polyphenols of MI-ME were incubated in a CO_2 incubator at 37°C with 95% humidity for a duration of 24 h. After incubation, DMEM (100 µl) was removed from each well, and 20 µL of freshly prepared MTT (5 mg/mL in distilled water) was added. The wells were then incubated for 4 h at 37°C in a CO_2 incubator. Subsequently, the DMEM with MTT was entirely removed. The purple product generated by the cells in each well was obtained by adding dimethyl sulfoxide (100 µL/well), and the absorbance at 570 nm was measured with an Enzyme Linked Immunosorbent Assay (ELISA) reader [37]. Each concentration was tested in triplicate, and the IC_{50} was calculated following the MTT assay using GraphPad Prism (version 6) through the following equation:

$$Y= D+A-D / 1+10^{(X-logC) B}$$

Where Y: response, X: dose, D, A, C and B are constants.

STATISTICAL ANALYSIS

The data obtained was statically analyzed using one-way ANOVA with GraphPad Prism 6. The values were presented as the mean ± SD of triplicate measurements. Significant differences were adjusted at $p < 0.05$.

REFERENCES

1. J.K.T. Al-Isawi; A.M. Mohammed; D.T. Al-Heetimi; *Studia UBB Chemia*, **2023**, *68(2)*,131-144.
2. Z.A. Thabit ; Iraqi J. Sci,**2018**, *59* ,38-43.
3. M.K. Ediriweera; K.H. Tennekoon; S.R., Samarakoon; *eCAM.*, **2017**, *2017*(1), 6949835.
4. A. Sherman; M. Rubinstein; R. Eshed; M.Benita; M. Ish-Shalom; M. Sharabi-Schwager; *BMC Plant Biol.* **2015**, *15*,1-11
5. V.R. Lebaka; Y-J. Wee; W. Ye; M. Korivi; *Int. J. Environ. Res. Public Health*, **2021**,*18(2)* 741.
6. J.F. Ekorong Akouan Anta; P.D. Mbougueng; E.Durand; B. Baréa; P. Villeneuve; R. Ndjouenkeu; *JBAPN*, **2018**, *8(1)*,51-63.
7. D. Alshammaa;*Int J Curr Microbiol Appl Sci,*2016,*5*,163-73.
8. Infante-Garcia C, Jose Ramos-Rodriguez J, Marin-Zambrana Y, Teresa Fernandez-Ponce M, Casas L, Mantell C, *Brain Pathol*., **2017**,*27(4)*,499-507.
9. S.N. Ronchi; G.A. Brasil; A.M. do Nascimentode; E.M. Lima; R. Scherer; H.B. Costa; W. Romão; G.A.P. Boëchat; D. Lenz; M. Fronza; N.S. Bissoli, *Ther. adv. cardiovasc. dis.*, **2015**,*9(5)*,244-256.
10. T. Khumpook; S. Saenphet; Y. Tragoolpua; K. Saenphet, *Comp. Clin. Path.*, **2019**, *28* ,157-164.
11. T.M. Flayyih; A.A. Almarie, *Iraqi J. Sci.*, **2023**,*64(5)*,2215-2222.
12. A.M. Delgado; M. Issaoui; N. Chammem, *J. AOAC Int.*, **2019**, *102(5)*,1356-1364.
13. M. Olszowy, *Plant Physiol. Biochem.*, **2019**,*144*,135-143.
14. J. Pan; X. Yi; S. Zhang; J. Cheng; Y. Wang; C. Liu; X. He, *Ind. Crops Prod.*, **2018**,*111*,400-406.
15. F.M. Roleira; E.J. Tavares-da-Silva; C.L. Varela; S.C. Costa; T. Silva; J. Garrido; F. Borges, *Food Chem.*, **2015**, *183*,235-58.
16. S. Dutta; P. Sadhukhan; S. Saha; P.C. Sil, *ROS*, **2017**, *3*, 81-95.
17. V.B. Tatipamula; B. Kukavica, *Cell Biochem. Funct.*, **2021**, *39(8)*, 926-944.
18. H. Abbaszadeh; B. Keikhaei; S. Mottaghi, *Phytother. Res.*, **2019**, *33(8)*, 2002-2014.
19. B.H. Do; N.S. Hoang; T.P.T. Nguyen; N.Q.C. Ho; T.L. Le; C.C. Doan, *Nutr. Cancer.*, **2021**, *73(5)*, 869-888.
20. H. Kim; H. Kim; A. Mosaddik; R., Gyawali; K.S. Ahn; S.K. Cho, *Food Chem.*, **2012**, *133*(2), 416-422.
21. J.B. Harborne; *Phytochemical methods: a guide to modern techniques of plant analysis*,3rd ed; Chapman and Hall, London, UK, **1998**.
22. S.E. Quintana; S. Salas; L.A. García-Zapateiro, *J. Sci. Food Agric.*, **2021**, *101(15)*, 6186-6192.
23. M. Kumar; V. Saurabh; M. Tomar; M. Hasan; S. Changan; M. Sasi; C. Maheshwari; U. Prajapati; S. Singh; R.K. Prajapat; S. Dhumal, *Antioxidants*, **2021**, *10*(2)299, 1-23

24. D. Yadav; A.K. Pal; S.P. Singh; K. Sati, *Crop Research*, **2022**, *57*(1and2), 79-95.
25. B.G. Oliveira; H.B. Costa; J.A. Ventura; T.P. Kondratyuk; M.E. Barroso; R.M. Correia; E.F. Pimentel; F.E. Pinto; D.C. Endringer; W. Romão, *Food Chem.*, **2016**, *204*, 37-45.
26. Z. Hayat; T. Riaz; K. Saleem; K. Akram; H. Ur Rehman; M. Azam, *Separations*, **2023**, *10*(7)376, 1-14.
27. B. Mirza; C.R. Croley; M. Ahmad; J. Pumarol; N. Das; G. Sethi; A. Bishayee, *Crit. Rev. Food Sci. Nutr.*, **2021** *61(13)*, 2125-2151.
28. X. Zhang; B. Su; J. Li; Y. Li; D. Lu; K. Zhu; H. Pei; M. Zhao; *Journal of Chromatographic Science*, **2014**. 52(1): p. 1-4.
29. J. E. Ramirez; R. Zambrano; B. Sepúlveda; M. J. Simirgiotis; *Molecules*, **2014**. 19, 438-458.
30. K.M. Yap; M. Sekar; L.J. Seow; S.H. Gan; S.R. Bonam; N.N.I. Mat Rani; P.T. Lum; V. Subramaniyan; Y.S. Wu; N.K. Fuloria; S. Fuloria, *Breast Cancer: Targets Ther.*, **2021**, *13*, 471-503.
31. R. S. Yehia and S. A. Altwaim; *Plants,* **2023**, 12, 1539.
32. M. Navarro; E. Arnaez; I. Moreira; S. Quesada; G. Azofeifa; K. Wilhelm; F. Vargas; P. Chen; *Foods* **2019**, 8, 384.
33. C. Torres-León; M.T.D.S. Correia; M.G. Carneiro-Da-Cunha; L.Serna-Cock; J. Ventura-Sobrevilla; J.A. Ascacio-Valdés; C.N. Aguilar; Mango seed byproduct: A sustainable source of bioactive phytochemicals and important functional properties,1st ed In *Bioprocessing of Agri-Food Residues for Production of Bioproducts*, Apple Academic Press, London, UK, **2021**, pp. 33-60.
34. A.J. Harborne F.O. Phytochemical methods: a guide to modern techniques of plant analysis: Chapman and Hall; **1998**.
35. W. Vermerris; R. Nicholson; W. Vermerris; R. Nicholson; *Phenolic compounds and their effects on human health*, Springer Netherlands, **2006**, pp. 235-255.
36. A.Z. Al-Saffar; N.A. Hadi; H.M. Khalaf, *IJFMT*, **2020**, *14*(3), 2493-2499.
37. S.M. Akram; A.Z. Al-Saffar; N.A. Hadi; S.M. Akram, *Life Sci.*, **2022**, *311*, p. 121163.

STUDIA UBB CHEMIA, LXXI, 1, 2026(p. 175-192)
(RECOMMENDED CITATION)
DOI:10.24193/subbchem.2026.1.11

PHYTOCHEMICAL ANALYSIS, ANTIOXIDANT, ANTI-INFLAMMATORY AND IMMUNOMODULATORY EFFECTS OF METHANOLIC EXTRACT OF *JUNIPERUS PHOENICEA*

Nassrine KAHIA[a], Nacer AMRAOUI[a,*], Salma BERRI[a], Zineddine BOUTEFAHA[a], Noureddine BELATTAR[a], Mosaad Attia ABDEL-WAHHAB[b], Lekhmici ARRAR[a]

ABSTRACT. This work aims to evaluate the antioxidant, anti-inflammatory and immunomodulatory effects of *Juniperus phoenicea* extract. Polyphenol and flavonoid contents were estimated using colorimetric methods. The antioxidant potential was assessed using 2, 2-diphenyl-l-picrylhy- drazyl (DPPH) radical scavenging, iron chelation, and anti-hemolytic assays. Croton oil-induced ear edema and carrageenan-induced paw edema models were used to evaluate the anti-inflammatory activity. Furthermore, the hemagglutination test was used to assess the immunomodulatory activity. The total polyphenol and flavonoid contents in this extract were 138.15 ± 11.87 µg GAE/mg and 27.5 ± 1.2 µg QE/mg of dry extract, respectively. The methanolic extract exhibited a strong scavenging activity against DPPH radical (IC_{50} = 0.051 ± 0.002 mg/mL), while in iron chelation it presented low activity (EC_{50} = 3.61 ± 0.46 mg/mL) compared to the standard EDTA. The results showed that *J. phoenicea* extract exhibited high protection of erythrocytes in 2, 2′,-azobis (2 amidinopropane) dihydrochloride (AAPH)-induced hemolysis. Treatment with *J. phoenicea* extract (200 and 400 mg/kg) exhibited significant anti-edematogenic in both inflammatory models induced by croton oil and carrageenan. However, these doses did not show any significant increase/decrease on the antibody titer. This study indicates that *J. phoenicea* extract possesses antioxidant and anti-inflammatory effects, confirming the use of this plant in folk medicine.

Keywords: *DPPH, flavonoids, hemagglutination, iron chelation, Juniperus phoenicea, polyphenols.*

[a] *Laboratory of Applied Biochemistry, Faculty of Nature and Life Sciences, Setif 1 University Ferhat Abbas, Setif 19000, Algeria*
[b] *Food Toxicology and Contaminants Department, National Research Centre, Dokki, Cairo, Egypt*
* *Corresponding author*: *n.amraoui@univ-setif.dz*

INTRODUCTION

Oxidative stress (OS) arises from an imbalance between the synthesis of reactive oxygen species (ROS) and the capacity of the biological system's ability to neutralize them [1]. ROS are reactive molecules that include both radicals, which have a single unpaired electron, such as the superoxide radical anion ($O_2^{\bullet-}$), and non-radical species such as hydrogen peroxide (H_2O_2) [2]. Excessive production of ROS causes lipid peroxidation as well as DNA and protein damage [3]. Moreover, it has been demonstrated that an excess of ROS is known to promote the production of pro-inflammatory cytokines, transcription factors, and chemokines, ultimately leading to tissue damage [4].

Inflammation is a complex reaction to injury, infection, or tissue damage. It is often associated with pain, fever, swelling, and redness. Moreover, it can cause physiological dysfunction [5]. In this context, acute inflammation is a swift biological response that plays a crucial role in wound healing, however, chronic inflammation is a prolonged, long-lasting condition that arises in diseases such as rheumatoid arthritis, osteoarthritis, and cancer [6].

The immune system plays a crucial role in defending the body against harmful microorganisms. Once the immune system is stimulated, it responds promptly by synthesizing a range of cytokines, chemokines, and inflammatory mediators [7]. Immunomodulators are substances that regulate the immune system, by either enhancing or suppressing its activity [8]. They are essential for managing inflammatory and immune-related diseases, which result from immune system disorders [9].

Although a wide range of anti-inflammatory and immunomodulatory drugs are available, their prolonged use is often restricted by severe adverse effects and high costs, which pose a challenge to effective disease management. Consequently, research is actively underway to find suitable alternatives to these conventional treatments [10].The significance of herbal remedies for human health is attracting more attention, generating increased interest in plant-based traditional medicine. Scientists and researchers are exploring the antioxidant properties of plants as they have the potential to reduce oxidative damage that may trigger multiple diseases [11]. Plants serve as an immense source of therapeutic and pharmaceutical substances due to their abundance of bioactive compounds with medicinal properties [12]. *J. phoenicea* is a native tree of the Cupressaceae family, found in the Mediterranean basin. It predominantly grows in the mountains of Algeria [13]. This plant has traditionally been used to treat rheumatism, diabetes, urinary tract diseases, and bronchopulmonary conditions, as well as to enhance appetite [14].

Most studies on Algerian *J. phoenicea* focus on its antioxidant and anti-inflammatory activities *in vitro*. For instance, research by Ghouti et al. [13] and Zemmouli et al. [15] indicates that both aqueous and hydroethanolic *J. phoenicea* extracts exhibit antioxidant and anti-inflammatory properties. However, no available reports exist on its immunomodulatory effects or *in vivo* anti-inflammatory activity.

Therefore, the present study aims to assess the antioxidant, anti-inflammatory, and immunomodulatory effects of the methanolic extract of the aerial part of *J. phoenicea.*

RESULTS

Characterization of polyphenols by HPLC

Figure 1 represents the chromatograms of *J. phoenicea* extract and standards. Multiple compounds were identified in the methanolic extract of *J. phoenicea* which contained high concentrations of Gallic acid (5206.22 µg/g), hesperetin (4972.69 µg/g), catechin (4215.88 µg/g) and chlorogenic acid (3201.39 µg/g). However the kaempferol and ellagic acid were absent in this extract or not detectable. The Phytoconstituents concentrations in *J. phoenicea* extract are presented in the table 1.

Table 1. The Phytoconstituents concentrations of *J. phoenicea* extract.

Polyphenols	**Extract** (Concentration (µg/g))	**Standard** (Concentration (µg/ml))
Gallic acid	5206.22	302.26
Chlorogenic acid	3201.39	435.51
Catechin	4215.88	386.88
Methyl gallate	49.16	337.23
Caffeic acid	194.71	267.82
Syringic acid	353.64	302.37
Rutin	1297.54	367.40
Ellagic acid	ND	1016.95
Coumaric acid	593.03	681.46
Vanillin	162.99	411.03
Ferulic acid	1438.14	417.77
Naringenin	285.85	386.62
Rosmarinic acid	63.82	566.02
Daidzein	124.22	378.43
Querectin	13.42	299.16
Cinnamic acid	15.22	653.28
Kaempferol	ND	339.31
Hesperetin	4972.69	489.55

ND, non detected

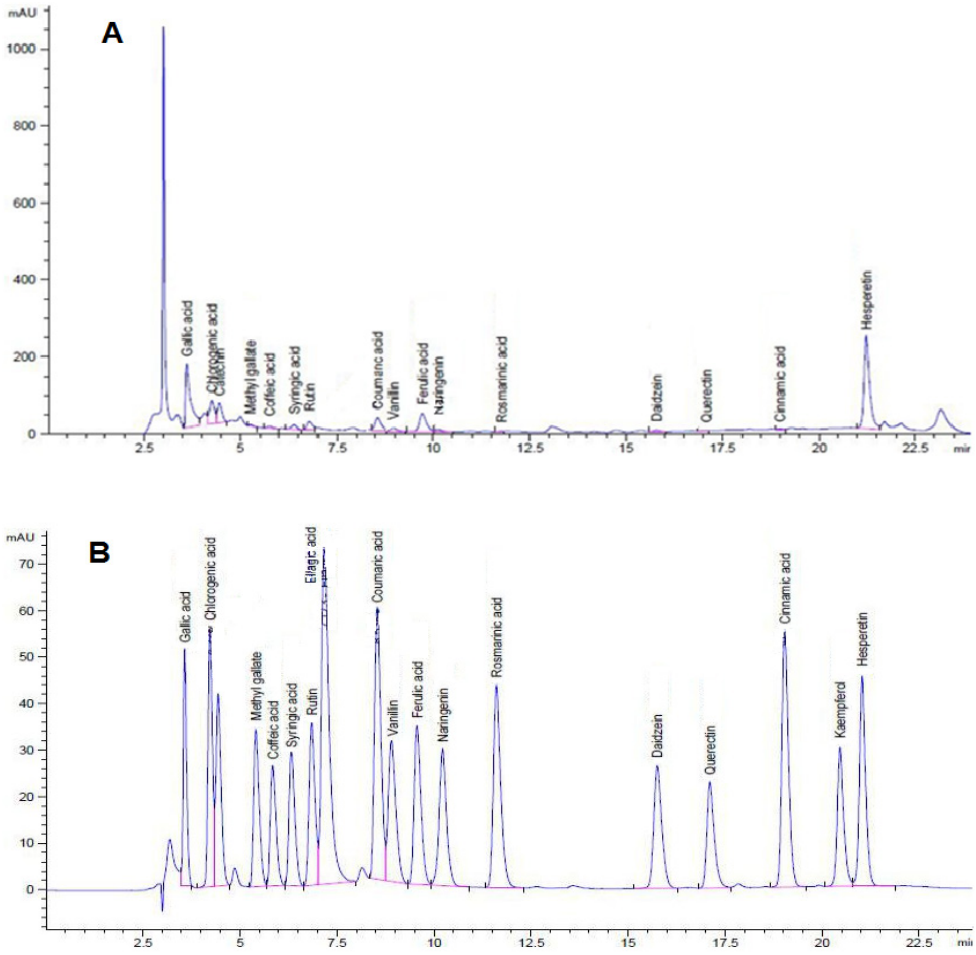

Figure 1. HPLC chromatograms; **A,** *J. phoenicea* extract;
B, Polyphenols standards.

Total polyphenol and flavonoid contents

The methanol extract of *J. phoenicea* produced a yield of 24.73%. The total polyphenol content was 138.15 ± 11.87 µg GAE/mg of dry extract, while the flavonoid content was 27.50 ± 1.20 µg QE/mg of dry extract.

Antioxidant activity

DPPH radical scavenging activity

DPPH free radical scavenging activity was determined by the IC_{50}values (IC_{50} represents the concentration of the sample required to inhibit 50% of the DPPH free radicals). The methanol extract of *J. phoenicea* demonstrated strong free radical scavenging activity with an IC_{50} value of 0.051 ± 0.002 mg/mL, in comparison to the synthetic antioxidant BHT (IC_{50} = 0.047 ± 0.0022 mg/mL).

Ferrous iron chelating effect

The capacity to chelate ferrous ions was expressed as the mean of the EC_{50} values (EC_{50} represents the effective concentration that chelates 50% of Fe^{2+}). The methanol extract of *J. phoenicea* showed an EC_{50} value of 3.61 ± 0.46 mg/mL. For comparison, EDTA showed an EC_{50} value of 3 ± 0.53 µg/mL.

Anti-hemolytic activity

The methanolic extract of *J. phoenicea* exhibited a strong ability to protect the erythrocyte membrane against hemolysis ($p < 0.001$) with HT_{50} = 74.93 ± 4.78 min compared to the negative control (AAPH) which reduced the hemolysis half-time (HT_{50} = 32.73 ± 1.83 min). Vitamin C served as standard (50 µg/mL) demonstrated an HT_{50} = 70.90 ± 6.43 min (Figure 2).

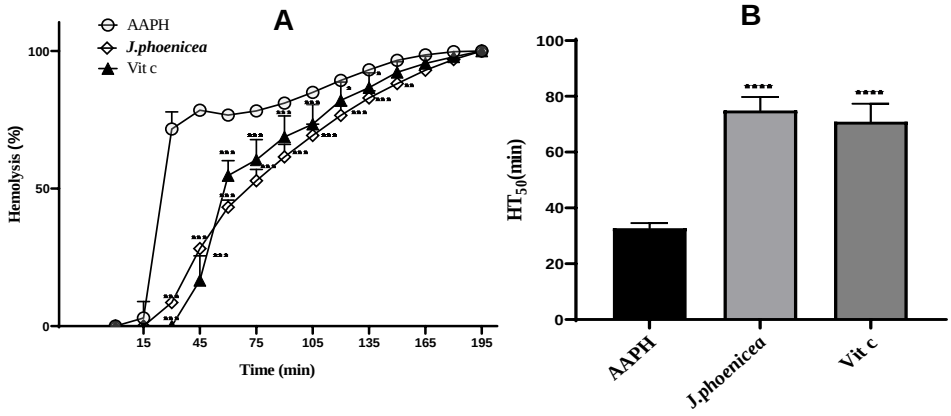

Figure 2. The kinetics of *J. phoenicea* extract and vitamin C action on AAPH-induced hemolysis of red blood cells (RBCs), (**A**). Half-Hemolysis Time (HT_{50}) for the analyzed compounds (**B**). Vit C: vitamin C. Values are presented as the mean ± SD (n=4). *p < 0.05, **p < 0.01, ***p < 0.001, ****p < 0.0001 when compared with the control.

Acute toxicity study

The oral administration of the methanolic extract of *J. phoenicea* (2000 and 5000 mg/kg) in mice demonstrated no signs of toxicity or mortality during the 14 days of the experiment. For the evaluation of the biological activities two doses were selected (200 and 400 mg/kg body weight).

Anti-inflammatory activity

Croton oil-induced ear edema in mice

Treating mice with the methanolic extracts of *J. phoenicea* (200 and 400 mg/kg) in croton oil-induced ear edema resulted in a significant reduction of edema ($p < 0.001$) after 6 hours (0.062 ± 0.009 mm, 0.026 ± 0.005 mm, respectively) compared to the control mice group, which showed an increase in the thickness of the right ear (0.138 ± 0.015 mm). Diclofenac at 50 mg/kg produced a significant reduction ($p < 0.001$) of edema (0.022 ± 0.007 mm) in comparison to the control group (Figure 3).

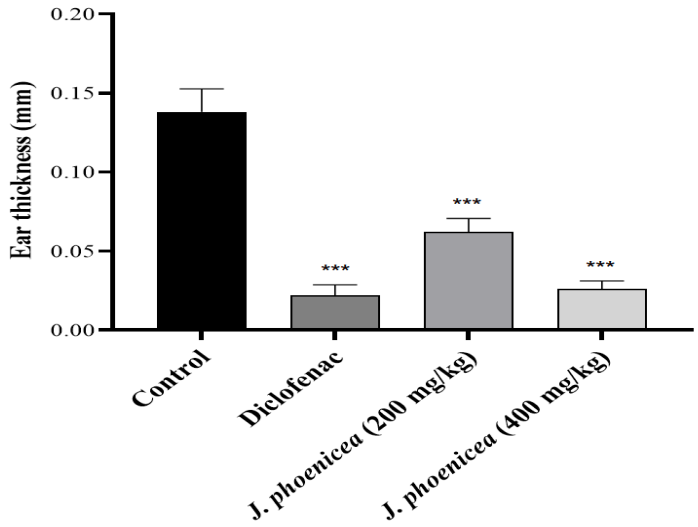

Figure 3. Effect of *J. phoenicea* extract on croton oil-induced ear edema in mice. Values are presented as the mean ± SEM (n=5), ***$p < 0.001$ when compared with the control group.

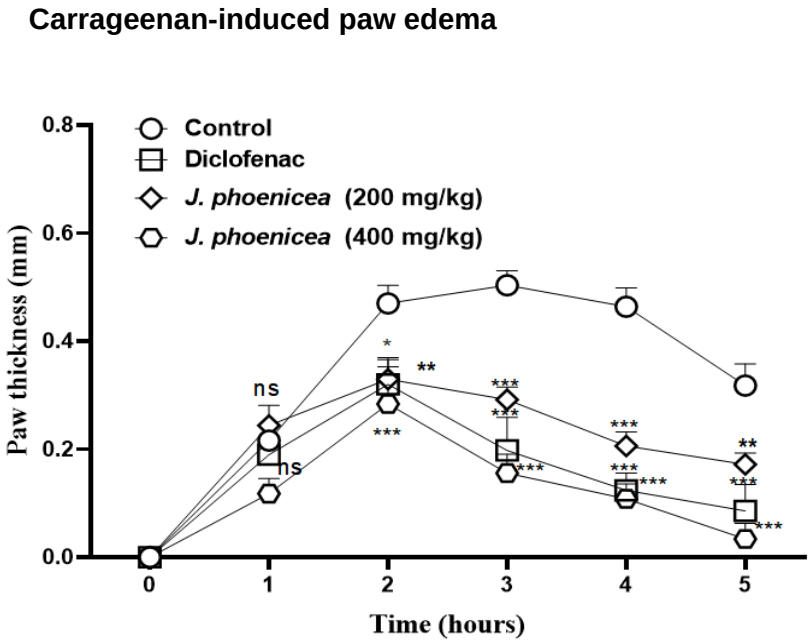

Figure 4. Effect of *J. phoenicea* extract on carrageenan-induced paw edema in mice. Values are presented as the mean ± SEM (n=5). ns: non-significant, *p < 0.05, **p < 0.01, ***p < 0.001 when compared with the control group.

Figure 4 represents the effect of *J. phoenicea* extract on carrageenan-induced paw edema in mice. The mice in the control group that received only the carrageenan solution showed an increase in paw thickness during the 1st, 2nd, and 3rd hour (0.216 ± 0.016 mm, 0.47 ± 0.033 mm, and 0.504 ± 0.027 mm, respectively), after the 3rd hour, which represents the peak of inflammation, a gradual decrease was observed (0.318 ± 0.040 in the 5th h). The group treated with *J. Phoenicea* extract at a dose of 200 mg/kg decreased paw thickness from the 2nd to the 5th h (0.33 ± 0.036 mm and 0.172 ± 0.021 mm, respectively), in comparison to the control group. The results demonstrated that the highest dose of the extract (400 mg/kg) was significantly ($p < 0.001$) more effective in reducing paw volume from the 2nd to the 5th hour (0.284 ± 0.069 mm and 0.034 ± 0.029 mm, respectively), relative to the control group. Diclofenac resulted in a significant reduction in paw edema from the 2nd to the 5th hour (0.32 ± 0.05 mm and 0.086 ± 0.049 mm, respectively), in comparison to the control group.

Humoral antibody response

Figure 5 represents the effect of *J. phoenicea* extract on antibody titer in mice. The results did not show any significant increase in the antibody titer when the methanolic extract of *J. phoenicea* was orally administered at doses of 200 and 400 mg/kg.

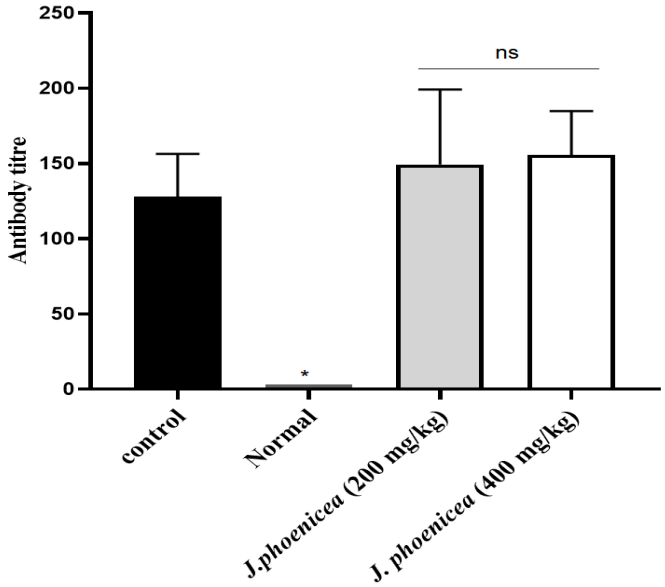

Figure 5. The effect of *J. phoenicea* extract on antibody titer in mice. Values are presented as the mean ± SEM (n = 6). ns: non-significant, *p < 0.05 when compared with the control group.

DISCUSSION

The use of natural antioxidants holds potential for the prevention of inflammation, cancer, diabetes and many other diseases [16]. Medicinal plants have demonstrated their importance as a primary source of biologically active compounds, or phytochemicals [17]. The bioactive compounds found in medicinal plants are predominantly polyphenols. The total phenolic and flavonoid contents of *J. phoenicea* were 138.15 ± 11.87 µg GAE/mg and

27.50 ± 1.20 µg QE/mg, respectively. The results obtained exceeded those reported by Bouassida et al. [18], who estimated the total phenolic and flavonoid contents of the hydroethanolic extract of *J. phoenicea* leaves from Boulifa northwestern part of Tunisia as follows 70.30 ± 0.2 mg GAE/g and 11.33 ± 0.05 mg QE/g, respectively. However, Keskes et al. [19] reported that the hexane and methanol extracts of the leaves of *J. phoenicea* in mid-west Tunisia contained higher phenolic and flavonoid contents than the results of the present study (265 ± 5.8 mg GAE/g, 176 ± 0.52 mg QE/g for the methanol extract and 162.3 ± 3.2 mg GAE/g, 96 ± 0.48 mg QE/g for the hexane extract, respectively). Furthermore, The study carried out by Zemmouli et al. [15] indicated that the aqueous extract of *J. phoenicea* leaves, collected from Biskra province in Algeria and obtained via decoction, reported total phenolic and flavonoid contents of 374.36 ± 0.1 mg GAE/g, 174.02 ± 2.79 mg QE/g, respectively. The amount and composition of phenolic compounds can be variable due to several factors such as the nature of the solvent, polarity, concentration of solvent and type of extraction [20], the season of the collection, the choice of parts and geographic origin [21].

The antioxidants that scavenge radicals to inhibit the initiation of the chain reaction and break the propagation phase are effective as primary antioxidants. However, the secondary antioxidants inhibit the formation of radicals [22]. In this context, two methods are used to assess primary and secondary antioxidant activity, the DPPH scavenging and the iron chelation tests, respectively.

The DPPH radical scavenging assay is intended to measure the ability of the extracts to neutralize the free radical 2,2'-diphenyl-1-picryl hydrazyl (DPPH) by donation of an electron or a hydrogen atom [19]. The ability of the plant extracts to scavenge DPPH is measured by the discoloration of DPPH, from purple to yellow color due to the formation of diphenyl picryl hydrazine. In this study, the methanolic extract of *J. phoenicea* exhibited high antioxidant activity (IC_{50}: 0.051 ± 0.0019 mg/mL). The IC_{50} of the methanolic extract was lower than those reported by Ghouti et al. [13] and Bouassida et al. [18], who assessed the ability of the Algerian Sahara *J. phoenicea* leaves hydroethanolic extract to scavenge the stable radical DPPH (IC_{50}: 12 ± 1 µg/mL), as well as Tunisian *J. phoenicea* leaves hydroethanolic extract (IC_{50}: 12.22 ± 0.02 µg/mL). Previous study have demonstrated a strong correlation between the content of polyphenols and the DPPH scavenging effect [23]. The antioxidant properties of polyphenols are attributed to their low redox potential and their ability to donate multiple electrons or hydrogen atoms [24]. A study conducted by Choi et al. [25] indicates that hesperetin, a flavonoid present in *J. phoenicea* extract demonstrated a strong DPPH free radical-scavenging effect.

Iron and other transition metals promote oxidation through their role as catalysts in radical reactions [26]. Chelating agents, known to form σ-bonds with metals, have been reported to work as secondary antioxidants because they stabilize the oxidized state of the metal ion [27]. In this study the results showed that the methanolic extract of *J. phoenicea* exhibited chelating properties and can bind ferrous ions before ferrozine, with an EC_{50} value of 3.614 ± 0.46 mg/mL. This extract showed a more marked chelating capacity than the results obtained by Taviano et al. [22] who evaluated the ability of Turkey *J. communis* and *J. oxycedrus* methanolic extracts to chelate ferrous ions (EC_{50}= 33.10 ± 0.4 mg/mL and EC_{50} = 6.82 ± 1.15 mg/mL, respectively). According to Taviano, Marino (22) and our findings, there is no correlation between the ferrous ion chelating ability of the extract and their polyphenol and flavonoid concentrations. This may suggest the presence of other compounds, including non-phenolic antioxidants responsible for metal chelation [28].

Erythrocytes hemolysis is commonly utilized as a model for studying oxidative damage to cell membranes induced by free radicals [29]. Peroxyl radicals are produced through the thermal degradation of AAPH, a water-soluble azo-based compound, under oxygen-rich condition [30]. These radicals target the membranes of erythrocytes to trigger lipid peroxidation and lead to hemolysis [29]. The methanolic extract of *J. phoenicea* exhibited strong anti-hemolytic activity by prolonging the duration required for 50% hemolysis of RBCs. These results are in agreement with those of Zemmouli et al. [15] which showed that the aqueous extract of Algerian *J. phoenicea* leaves collected from Biskra exhibited high protection of erythrocytes. Anti-hemolytic effect of *J. phoenicea* extract can be due to the different phenolic compounds which neutralize free radicals by their antioxidant properties and enhance erythrocytes' resistance to oxidative stress [31]. Furthermore, polyphenols bind to membrane phospholipids and shield them against lipid degradation [32]. Catechin, a type of flavonoid found in *J. phoenicea* extract has previously exhibited strong protection against AAPH-induced damage, according to Grzesik et al. [33].

Acute or chronic inflammation stimulates the production of inflammatory mediators such as tumor necrosis factor-α (TNF-α), prostaglandin E2 (PGE2), and nitric oxide (NO). Excessive inflammation can contribute to the development of diseases, including atherosclerosis, cardiovascular disease, and immune dysfunction [34].

In this study, croton oil and carrageenan-induced inflammatory models are used to evaluate the anti-inflammatory activity of our extract. The topical application of croton oil induces an inflammatory response. Tetradecanoyl-phorbol acetate (TPA) represents the primary irritant in croton oil which activates protein kinase C (PKC), phospholipase A2, lipoxygenase enzyme and induces the expression of COX-2, and pro-inflammatory cytokines [35]. The oral

administration of *J. phoenicea* at doses of 200 and 400 mg/kg exhibited a strong reduction of ear edema. This reduction may be due to chlorogenic acid and hesperetin identified in the *J. phoenicea* extract. Chlorogenic acid participates in modulating enzyme activity such as lipoxygenase and cycloxygenase [35]. As for hesperetin that inhibits the activity of the COX-1 and COX-2 reactions [36].

The carrageenan-induced paw edema serves as a model for acute inflammation biphasic [37]. The initial phase is mediated by serotonins, kinins, and histamines and the later phase is characterized by overproduction of prostaglandin [38]. Our results show that the methanolic extract of *J. phoenicea* at the doses of 200 and 400 mg/kg exhibited a strong reduction of paw edema in the later phase. These results are in agreement with those of Lafraxo et al. [39] which showed that the hydroethanolic extract of *J. phoenicea* leaves from Morocco reduced carrageenan-induced paw edema in rats. The anti-inflammatory effect can be due to Gallic acid and hesperetin which represent the major components of *J. phoenicea* extract [39 ,25].In this context, previous studies showed that hesperetin reduced the levels of NO and PGE2 [25] and gallic acid has been demonstrated to exhibit potent anti-inflammatory effects by targeting the MAPK (mitogen-activated protein kinase) and NF-κB (nuclear factor kappa B) signaling pathways [34].

Immunomodulators are a class of drugs that modify the activity of the immune system, either increasing or reducing its normal functions [40].The immune system can be regulated by various plant extracts. In this regard, the effect of *J. phoenicea* extract on humoral response was tested by hemagglutination test. This response is mediated by antibody molecules secreted by plasma cells [41]. The oral administration of both doses of *J. phoenicea* did not show any significant increase or decrease in the antibody titer. However, a previous study by Ali et al. [42], which determined the effect of the methanolic extract of *J. squamata* (100 and 200 mg/kg) on cell-mediated immunity (Delayed type hypersensitivity (DHT)), showed a significant change in DTH response.

CONCLUSIONS

The findings of the current study demonstrated that the methanolic extract of *J. phoenicea* exhibited strong *in vitro* antioxidant and *in vivo* anti-inflammatory effects. Nevertheless, no significant increase in the antibody titer was observed with this extract. These results suggest that the plant extract analyzed could serve as a potential natural alternative for treating inflammatory diseases.

EXPERIMENTAL SECTION

Chemicals, reagents and equipment

Folin-Ciocalteu reagent, sodium carbonate, gallic acid, trichloride aluminum, quercetin, 2,2'-diphenyl-1-picryl-hydrazyl (DPPH), butylated hydroxytoluene (BHT), methanol, ferrozine, $FeCl_2$, ethylene diamine tetraacetic (EDTA), 2, 2′,-azobis (2 amidinopropane) dihydrochloride (AAPH), phosphate-buffered saline (PBS), acetone , croton oil, carrageenan, NaCl and Alsever's solution were used in this study. All chemicals and reagents were of analytical grade.The extract was concentrated using a rotary evaporator (BÜCHI, Germany). Spectrophotometric measurements were performed using a DRAWELL (DV-8000) spectrophotometer. The AAPH-induced oxidative hemolysis was monitored at 630 nm using a 96-well microplate reader (ELX 800, BioTek Instruments, Winooski, VT, USA).

Plant material

J. phoenicea was collected from the region of Ouled Tebben (Setif), northeast of Algeria (35° 48′ 46″ north, 5° 06′ 05″ east), in July 2023 and identified by Pr. Hocine Laouer (Laboratory of Valorization of Natural and Biological Resources, Setif 1 Ferhat Abbas University, Algeria). A voucher specimen was deposited in the Department of Vegetal Biology and Ecology (DVBE0054:2023). The aerial part of *J. phoenicea* was washed and air-dried at room temperature in the dark. The dried material was then ground to powder using an electric grinder.

Preparation of extract

The methanolic extract of *J. Phoenicea* was prepared using the method described by Arrar et al. [43]. The powder of the aerial part (600g) was extracted with 6 L of absolute methanol in a sealed vessel at room temperature for 7 then 5 days. The crude extract was obtained by filtering the extract through Whatman filter paper then evaporated using a rotary evaporator at 45°C. It was desiccated until dryness in an oven. Finally, the extract was stored at 4°C until use.

Animals

Adult female NMRI mice weighing 25–30 g obtained from Pasteur Institute of Algeria (Algiers) were utilized for the study. Before the experiments, the animals were kept in clean plastic cages for 7 days in normal laboratory conditions (temperature, 20 – 22°C; relative humidity, 50 – 70 %, and 12/12 h light/ dark cycle). The animal experiments adhered to the guidelines and procedural details outlined in the Guide for the Care and use of Laboratory Animals (NIH Publication No. 86-23, 1985). Permission for experimental use was obtained from the Laboratory of Applied Biochemistry, Setif 1 Ferhat Abbas University.

Characterization of polyphenols by HPLC

Chemical analysis of the aerial part extract from *J. phoenicea* was performed by high-performance liquid chromatography (HPLC), which was conducted using an Agilent 1260 series. A Zorbax Eclipse Plus C8 column (4.6 mm x 250 mm i.d., 5 µm) was employed for the separation of constituents. A mixture of water (A) and 0.05% trifluoroacetic acid in acetonitrile (B) with a flow rate of 0.9 mL/min served as the mobile phase, which was applied in a linear gradient progression, as follows: 0 min (82% A); 0–1 min (82% A); 1-11 min (75% A); 11-18 min (60% A); 18-22 min (82% A); 22-24 min (82% A). The eluted samples and standards were monitored using a multi-wavelength detector at 280 nm. The injection volume was 5 µL and the column temperature was kept at 40°C.

Determination of total polyphenol and flavonoid contents

The total phenolic content of the methanolic extract was estimated using the Folin-Ciocalteu method according to Amraoui et al. [44]. Briefly, 0.1 mL of methanolic extract of *J. phoenicea* or standard was added to 0.5 mL of Folin-Ciocalteu reagent diluted to 1/10 (v/v) and incubated for 4 minutes at room temperature, then 0.4 mL of sodium carbonate (7.5%) solution was added and the mixture was incubated again at room temperature for 90 min in the dark. Then the absorbance was measured at 765 nm. A calibration curve was created using Gallic acid and the total polyphenol concentration was determined and expressed as micrograms of Gallic acid equivalent per milligram dry weight of extract (µg GAE/mg DW).

The concentration of flavonoid in the methanolic extract of *J. phoenicea* was quantified using aluminum chloride reagent, using the method described by Amraoui et al. [44]. A volume of 0.5 mL of the sample or standard was mixed with 0.5 mL of trichloride aluminum solution (2% in methanol). The mixture was incubated at room temperature in the dark for 10 min then the absorbance was read at 430 nm. The flavonoid content was expressed as microgram of quercetin equivalents per milligram dry weight of extract (µg QE/mg).

Antioxidant activity

DPPH radical scavenging activity

The DPPH (2,2'-diphenyl-1-picryl-hydrazyl) radical scavenging assay was evaluated according to Amraoui et al. [45], by mixing 50 µL of the extract at various concentrations with 1250 µL of a 0.004% DPPH solution (in methanol). The mixture was incubated at room temperature in the dark for 30 min then the absorbance was measured at 517 nm. Butylated hydroxytoluene (BHT) served as the standard. The DPPH radical scavenging activity was evaluated using the following equation:

$$I\ \% = 100 \times (Abs\ control - Abs\ sample)/Abs\ control \quad (1)$$

where: Abs control refers to the absorbance of the DPPH solution, Abs sample represents the absorbance in the presence of the extract or standard. IC_{50} is the concentration of an antioxidant-containing substance required to scavenge 50% of the initial DPPH radicals. The lower the IC_{50} value, the more potent is the substance at scavenging DPPH and this implies a higher antioxidant activity.

Ferrous iron chelation assay

The ferrous iron chelation assay of *J. phoenicea* extract was evaluated by the ferrozine method described by Guemmaz et al. [46]. A volume of 250 µL of different concentrations of extract was mixed with 50µL of $FeCl_2$ (0.6 Mm in H_2O) and 450 µL of methanol. After incubation at room temperature for 5 min, a volume of 50 µL ferrozine (5 Mm) was added to the mixture, which was then incubated again for 10 min at room temperature. The absorbance of the solution was read at 562 nm and EDTA (Ethylene diamine tetraacetic) served as the standard. The chelating effect of samples was calculated using the following equation:

$$Chelating\ power\ (\%) = 100\ x\ (Ac- As)/\ Ac \quad (2)$$

where: Ac: absorbance of the control (absence of chelator), As: absorbance in the presence of extract or EDTA.

Anti-hemolytic activity

The anti-hemolytic activity of *J. phoenicea* extract was evaluated using the method described by Guemmaz et al. [47]. In this test 2, 2′,-azobis (2 amidinopropane) dihydrochloride (AAPH) was used as a free radical generator, which damages the membranes of red blood cells (RBCs) and induces hemolysis. Mice blood was collected in tubes EDTA centrifuged and washed with phosphate-buffered saline (PBS; 10 mM, pH 7.4) three times. Blood cells were adjusted to a concentration of 2%. 80 µL of 2% erythrocyte suspension (in PBS) was added to 20 µL of extract or standard in a microplate then a volume of 136 µL of AAPH dissolved in PBS (300 mM) was added to the mixture. After incubation at 37°C, the absorbance was read at 630 nm, using a 96-well microplate reader. Erythrocytes resistance to radical attack was indicated by the time needed for the lysis of 50% of the erythrocytes (half Hemolysis Time in min: HT_{50}). Vitamin C was used as a standard. The negative control consists of RBCs and AAPH.

Acute toxicity evaluation

The acute oral toxicity of the methanolic extract of *J. phoenicea* was assessed according to the Organization for Economic Corporation and Development (OECD 425) guidelines [48], with slight modifications. The mice were divided into three groups of three each. Group 1 represents the negative control (received only distilled water) and two groups received *J. phoenicea* extract (2000 and 5000 mg/kg body weight), through oral administration. The mice were observed for 14 days for Indicators of toxicity such as changes in general behavior, body weight changes and mortality.

Anti-inflammatory activity

Croton oil-induced ear edema

Croton oil-induced mice ear edema was carried out using the method described by Amraoui et al. [49]. The mice were grouped into four sets of five each; group 1 was used as a negative control which was treated with an aqueous solution, group 2 represented the positive control (treated with Diclofenac (50 mg/ kg)) and two groups were treated with the methanolic extract of *J. phoenicea* (200 and 400 mg/kg). Ear edema was induced by applying 20 µL of a solution containing 80 µg of croton oil prepared in acetone-water solution (1:1 V/V) to the inner surface of each mouse's right ear one hour after oral administration of the extract or Diclofenac. The thickness of the right ear was measured using a digital caliper before and six hours after the croton oil application.

Carrageenan-induced paw edema

Carrageenan-induced paw edema assay was used to evaluate the anti-inflammatory activity of *J. phoenicea* extract according to the method of Amraoui et al. [45]. The mice were divided into four groups of five each. Group 1 represents the negative control which was treated with an aqueous solution, group 2 was used as a positive control (treated with Diclofenac 50 mg/ kg), and two groups were treated with the *J. phoenicea* extract (200 and 400 mg/kg). Mice were injected with 0.02 mL of carrageenan suspension (1% in NaCl 0.9%) at the subplantar region in the right paw of each mouse one hour after oral administration of the extract or Diclofenac. The thickness of the paws was measured using a digital caliper before and after carrageenan application at 1, 2, 3, 4, and 5 h.

Humoral antibody response

The humoral response to sheep red blood cells (SRBC) was assessed using the hemagglutination test according to the method described by Aichour et al. [50], with slight modifications. Sheep red blood cells (SRBC)

were mixed with Alsever's solution, washed two times with 0.9% NaCl and centrifuged each time. The red blood cells were adjusted to a concentration of 10^9 cells/mL. The mice were divided into four groups of six each. Group1 represents the healthy control (non-immune), group 2 was used as a negative control, both were treated with an aqueous solution, and two groups were treated with the *J. phoenicea* extract (200 and 400 mg/kg) on days -3, -2, -1, 0, 1, 2 and 3. Groups 2, 3, and 4 were immunized intraperitoneally (i.p) on day 0 with 10^9 cells/mL SRBC. Blood samples were collected from each mouse on day 8. A volume of 50 µL of serum samples was diluted two fold in microtitration plates and mixed with 50 µL of SRBC suspension (1%), then incubated for one hour. The antibody titer represents the final dilution of serum samples that caused hemagglutination.

Statistical analysis

The data are presented as the mean of triplicates ± SD for *in vitro* experiments, whereas *in vivo* results are expressed as the mean ± SEM. Statistical differences were analyzed using ANOVA, followed by Dunnett's test for multiple comparisons, utilizing GraphPad Prism software (version 8.0). A significance threshold of $p \leq 0.05$ was applied.

Funding
The authors have no funding to report.

Conflict of Interest
The authors declare no competing interests.

REFERENCES

1. L. Ali; S. Khan; M. Nazir; N. Raiz; S. Naz; G. Zengin; M. Mukhtar; S. Parveen; N. Shazmeen; M. Saleem; *S. Afr. J. Bot.*, **2021**, *140*, 189-193.
2. A. Tauffenberger; P. J. Magistretti; *Neurochem. Res.*, **2021**, *46*, 77-87.
3. D. Pandey; A. Joshi; S. Mishra; K. Sairam; S. Hemalatha; *Indian J. Exp. Biol.*, **2018**, *56*, 646-656.
4. S. Reuter; S. C. Gupta; M. M. Chaturvedi; B. B. Aggarwal; *Free Radic. Biol. Med.*, **2010**, *49*, 1603-1616.
5. S. Chandra; P. Chatterjee; P. Dey; S. Bhattacharya; *Asian Pac. J. Trop. Biomed.*, **2012**, *2*, S178-S180.
6. N. Karim; I. Khan; W. Khan; I. Khan; A. Khan; S. A. Halim; H. Khan; J. Hussain; A. Al-Harrasi; *Front. Immunol.*, **2019**, *10*, 581.
7. O. Mahamat; H. Flora; C. Tume; A. Kamanyi; *Evid. Based Complement. Alternat. Med.*, **2020**, *2020*, 5248346.

8. M. El-Zahabi; *Al-Azhar J. Pharm. Sci.*, **2021**, *64*, 41-68.
9. M. Strzelec; J. Detka; P. Mieszczak; M. K. Sobocińska; M. Majka; *Front. Immunol.*, **2023**, *14*, 1127704.
10. K. D. Moudgil; S. H. Venkatesha; *Int. J. Mol. Sci.*, **2022**, *24*, 95.
11. M. R. Kachmar; Y. O. El Majdoub; A. P. Oliveira; A. Bouymajane; H. N. Mrabti; T. Bouddine; N. Mir; N. N. Mrabti; H. Lhoussain; Z. Haloui; *Phytomed. Plus.*, **2024**, *4*, 100528.
12. P. Arulselvan; M. T. Fard; W. S. Tan; S. Gothai; S. Fakurazi; M. E. Norhaizan; S. S. Kumar; *Oxid. Med. Cell. Longev.*, **2016**, *2016*, 5276130.
13. D. Ghouti; W. Rached; M. Abdallah; T. C. Pires; R. C. Calhelha; M. J. Alves; L. H. Abderrahmane; L. Barros; I. C. Ferreira; *Food Funct.*, **2018**, *9*, 4664-4672.
14. G. F. Abdel Raoof; H. Mahmoud; *Egypt. J. Chem.*, **2023**, *66*, 963-972.
15. N. Zemmouli; F. Ramdane; N. Guezzoun; *Chem. Afr*, **2024**, 1-17.
16. H. Tohma; İ. Gülçin; E. Bursal; A. C. Gören; S. H. Alwasel; E. Köksal; *J. Food Meas. Charact.*, **2017**, *11*, 556-566.
17. R. A. Dar; M. Shahnawaz; M. A. Ahanger; I. u. Majid; *J. Phytopharmacol.*, **2023**, *12*, 189-195.
18. K. Zouari Bouassida; S. Makni; A. Tounsi; L. Jlaiel; M. Trigui; S. Tounsi; *Biomed. Res. Int.*, **2018**, *2018*, 3785487.
19. H. Keskes; K. Mnafgui; K. Hamden; M. Damak; A. El Feki; N. Allouche; *Asian Pac. J. Trop. Biomed.*, **2014**, *4*, S649-S655.
20. T. Prashant; K. Bimlesh; K. Mandeep; K. Gurpreet; K. Harleen; *Int. Pharm. Sci.*, **2011**, *1*, 98-106.
21. V. Papageorgiou; C. Gardeli; A. Mallouchos; M. Papaioannou; M. Komaitis; *J. Agric*. *Food Chem*., **2008**, *56*, 7254-7264.
22. M. F. Taviano; A. Marino; A. Trovato; V. Bellinghieri; T. M. La Barbera; A. Güvenç; M. M. Hürkul; R. D. Pasquale; N. Miceli; *Pharm*. *Biol*., **2011**, *49*, 1014-1022.
23. S. Aryal; M. K. Baniya; K. Danekhu; P. Kunwar; R. Gurung; N. Koirala; *Plants*, **2019**, *8*, 96.
24. M. E. Zujko; A. M. Witkowska; *Int. J. Food Prop*., **2011**, *14*, 300-308.
25. S.-S. Choi; S.-H. Lee; K.-A. Lee; *Antioxidants*, **2022**, *11*, 1618.
26. A. M. Hamad; M. A. Altaiaf; *Magna Scientia Adv*. *Res*. *Rev*., **2021**, *2*, 060-066.
27. A. Kumaran; R. J. Karunakaran; *LWT – Food Sci*. *Technol*., **2007**, *40*, 344-352.
28. J. Lee; M. Renita; R. J. Fioritto; S. K. St. Martin; S. J. Schwartz; Y. Vodovotz; *J. Agric*. *Food Chem*., **2004**, *52*, 2647-2651.
29. W. Liao; Z. Ning; L. Chen; Q. Wei; E. Yuan; J. Yang; J. Ren; *J. Agric*. *Food Chem*., **2014**, *62*, 8648-8654.
30. A. Banerjee; A. Kunwar; B. Mishra; K. Priyadarsini; *Chem*. *Biol*. *Interact*., **2008**, *174*, 134-139.
31. S. Kherbachı; M. Khenıche; M. Tacherfıout; *Int*. *J*. *Plant Based Pharm*., **2022**, *2*, 210-219.
32. M. Derouich; E. D. T. Bouhlali; M. Bammou; A. Hmidani; K. Sellam; C. Alem; *Scientifica*, **2020**, *2020*, 3971041.

33. M. Grzesik; K. Naparło; G. Bartosz; I. Sadowska-Bartosz; *Food Chem*., **2018**, *241*, 480-492.
34. J. Bai; Y. Zhang; C. Tang; Y. Hou; X. Ai; X. Chen; Y. Zhang; X. Wang; X. Meng; *Biomed. Pharmacother*., **2021**, *133*, 110985.
35. E. S. Santos; C. D. de Morais Oliveira-Tintino; D. B. Correia; C. D. C. de Alencar; M. de Fátima Sousa; C. N. F. Lima; S. T. de Sousa Machado; A. D. S. Gomes; F. A. de Oliveira Garcia; I. R. A. Menezes; *Phytomed. Plus*., **2021**, *1*, 100110.
36. H. Parhiz; A. Roohbakhsh; F. Soltani; R. Rezaee; M. Iranshahi; *Phytother. Res*., **2015**, *29*, 323-331.
37. I. Igbe; G. Inarumen; *Br. J. Pharm. Res*., **2013**, *3*, 391.
38. N. Zammel; M. Saeed; N. Bouali; S. Elkahoui; J. M. Alam; T. Rebai; M. A. Kausar; M. Adnan; A. J. Siddiqui; R. Badraoui; *Foods*, **2021**, *10*, 1383.
39. S. Lafraxo; A. Metouekel; F. E.-Z. Amrati; O. Zouirech; T. Chelouati; A. Drioiche; A.-R. Z. Gaafar; S. Ibenmoussa; A. A. Alsahli; M. Bourhia; *Pharmacogn. Mag*., **2024**, 09731296241281500.
40. S. Singh; R. Pradhan; R. Upadhyay; N. Singh; B. Ratha; *Panacea J. Med. Sci.*, **2024**, *14*, 249–254.
41. S. Farhath; P. Vijaya; M. Vimal; *Avicenna J. Phytomed.*, **2013**, *3*, 224.
42. R. Ali; N. Sajjad; S. Qureshi; S. Hassan; M. Ahmad; S. A. Ganie; R. Hamid; *Free Radic. Antioxid.*, **2018**, *8*, 111-119.
43. L. Arrar; N. Benzidane; I. Krache; N. Charef; S. Khennouf; A. Baghiani; *Pharmacogn. Commn.*, **2013**, *3*, 70.
44. N. Amraoui; N. Mayouf; N. Charef; A. Baghiani; L. Arrar; *Trop. J. Pharm. Res.*, **2019**, *18*, 1499-1506.
45. N. Amraoui; H. Laroui; N. Charef; A. Baghiani; L. Arrar; *Ann. Rom. Soc. Cell Biol.*, **2022**, *26*, 2912-23.
46. T. Guemmaz; L. Arrar; A. Baghiani; *J. Drug Deliv. Ther.*, **2020**, *10*, 39-44.
47. T. Guemmaz; F. Zerargui; S. Boumerfeg; L. Arrar; S. Aouachria; S. Khennouf; N. E. Charef; A. Baghiani; *J. Drug Deliv. Ther.*, **2018**, *24*, 1-12.
48. OECD; Co-operation, Organisation for Economic Co-operation and Development; Test No. 425: Acute Oral Toxicity: Up-and-Down Procedure, OECD Publishing, Paris, 2008, pp. 1–24.
49. N. Amraoui; Z. Boutefaha; N. Belattar; L. Arrar; *Arch. Biol. Sci.*, **2024**, *76*, 15-25.
50. R. Aichour; N. Charef; A. Baghiani; L. Arrar; *Int. J. Pharm. Pharm. Sci.*, **2016**, *8*, 51-54.

STUDIA UBB CHEMIA, LXXI, 1, 2026 (p. 193-208)
(RECOMMENDED CITATION)
DOI:10.24193/subbchem.2026.1.12

CHEMICAL COMPOSITION, ANTIMICROBIAL AND MOSQUITO LARVICIDAL ACTIVITIES OF THE ESSENTIAL OIL OF *CHLORANTHUS ERECTUS* COLLECTED IN VIETNAM

Le T. HUONG[a], Do N. DAI[b,*], Nguyen T. L. QUYEN[b], Nguyen H. HUNG[c,d], Bui B. THINH[e,*]

ABSTRACT. *Chloranthus erectus*, a subshrub native to South and Southeast Asia, has traditionally been used for its medicinal properties. This study investigated the chemical composition of the essential oil extracted from the aerial parts of *C. erectus* collected in Vietnam and evaluated its antimicrobial and mosquito larvicidal activities. The essential oil was obtained by hydrodistillation with a yield of 0.21% (v/w) and analyzed using gas chromatography coupled with flame ionization detection and mass spectrometry (GC–FID/MS). The major constituents identified were (*E*)-β-ocimene (13.41%), myrcene (12.85%), spathulenol (12.55%), and bicyclogermacrene (12.01%). Antimicrobial activity was assessed by determining the minimum inhibitory concentration (MIC) and half-maximal inhibitory concentration (IC_{50}) against selected bacterial and fungal strains. The essential oil showed antimicrobial activity, particularly against *Candida albicans* (MIC: 16 µg/mL; IC_{50}: 8.96 µg/mL), as well as against Gram-positive bacteria, including *Bacillus cereus* and *Enterococcus faecalis*. Larvicidal assays demonstrated toxicity against larvae of *Aedes aegypti*, *Aedes albopictus*, and *Culex quinquefasciatus*, with lethal concentration (LC_{50} and LC_{90}) values below 100 µg/mL after 24 and 48 h of exposure. These results highlight the bioactive potential of *C. erectus* essential oil for pharmaceutical and environmentally friendly mosquito control applications.

Keywords: *Chloranthus erectus, essential oil, antimicrobial activity, Candida albicans, mosquito larvicidal activity*

[a] *Faculty of Biology, College of Education, Vinh University, Nghe An Province, Vietnam.*
[b] *Faculty of Agriculture, Forestry and Fishery, Nghe An University, Nghe An Province, Vietnam.*
[c] *Center for Advanced Chemistry, Institute of Research and Development, Duy Tan University, Da Nang, Vietnam.*
[d] *Department of Pharmacy, Duy Tan University, Da Nang, Vietnam.*
[e] *Biotechnology Center of Ho Chi Minh City, Ho Chi Minh City, Vietnam.*
[*] *Corresponding authors: daidn23@gmail.com; buibaothinh9595@gmail.com*

INTRODUCTION

The genus *Chloranthus* (family Chloranthaceae) comprises approximately 14 recognized species of perennial herbs and subshrubs, predominantly distributed across tropical and subtropical regions of Asia [1]. These species are commonly found in countries such as China, Vietnam, Japan, India, and Malaysia, where they typically inhabit forested, humid, and mountainous ecosystems [1]. Many *Chloranthus* species have a long history of use in traditional Asian medicine. Ethnobotanical records document their application in the treatment of various ailments, including inflammation, fever, pain, and infected wounds [1]. These traditional uses have stimulated extensive phytochemical investigations, revealing that *Chloranthus* species are rich sources of structurally diverse secondary metabolites. To date, several classes of bioactive compounds have been identified within the genus, notably sesquiterpenoids, diterpenoids, flavonoids, and lignans [2, 3]. These metabolites exhibit a broad spectrum of biological activities, including anti-inflammatory, antioxidant, antimicrobial, and cytotoxic effects, thereby supporting both their traditional applications and pharmacological potential [2, 3].

Among the less-studied members of the genus is *Chloranthus erectus*, a species native to forested and montane regions of South and Southeast Asia [4]. It occurs in countries such as Vietnam and China, where it has traditionally been used for wound healing and the treatment of skin infections. Despite its ethnopharmacological relevance, the phytochemical and biological profiles of *C. erectus* remain relatively underexplored compared with other *Chloranthus* species. Preliminary investigations have reported the presence of various phytochemical constituents, including alkaloids, flavonoids, terpenoids, saponins, quinones, glycosides, and steroids, some of which have demonstrated antimicrobial, antioxidant, antipyretic, and anti-inflammatory properties [5–8]. However, studies focusing specifically on the essential oil composition of *C. erectus* remain scarce. Essential oils are volatile and aromatic plant-derived compounds that frequently exhibit potent biological activities [9]. In other *Chloranthus* species, essential oils have demonstrated antimicrobial, antioxidant, and anti-inflammatory effects [10–14]. A study conducted in Malaysia reported that germacrone was the major constituent of *C. erectus* essential oil, accounting for 36.62% of the total composition [15]. The oil also exhibited antifungal activity against *Ceratocystis fimbriata* [15].

To date, this Malaysian report remains the only published study describing the essential oil composition of *C. erectus*. Importantly, essential oil composition is strongly influenced by geographic origin, environmental conditions, and genetic variability, often resulting in distinct chemotypes [16, 17]. Therefore, findings obtained from Malaysian populations cannot be assumed to represent plants growing in other ecological regions. To the best of our

knowledge, no previous study has characterized the essential oil composition of *C. erectus* collected in Vietnam, nor has any investigation evaluated its larvicidal activity against mosquito vectors. This represents a significant knowledge gap, particularly given Vietnam's distinct climatic and ecological conditions, which may give rise to a unique chemotype with different biological properties.

The increasing prevalence of antimicrobial resistance (AMR) and the resurgence of mosquito-borne diseases represent major global public health challenges [18, 19]. The overuse and misuse of synthetic antibiotics have accelerated the emergence of multidrug-resistant bacterial and fungal pathogens, thereby compromising treatment efficacy [18]. Concurrently, the extensive use of synthetic insecticides has led to resistance in major mosquito vectors, including *Aedes aegypti*, *Aedes albopictus*, and *Culex quinquefasciatus*, which transmit diseases such as dengue, chikungunya, Zika, and lymphatic filariasis [19]. Moreover, synthetic agents pose environmental risks due to their persistence and toxicity toward non-target organisms. These challenges underscore the urgent need for alternative and environmentally sustainable solutions. In this context, essential oils have emerged as promising candidates for antimicrobial and vector control applications [20–22]. Due to their complex mixture of bioactive constituents and multifaceted mechanisms of action, essential oils may reduce the likelihood of resistance development [20, 21]. Additionally, many have demonstrated larvicidal activity against disease-vector mosquitoes, offering biodegradable and comparatively safer options for integrated vector management strategies [22].

Given the limited data available on *C. erectus* essential oil, particularly from Vietnam, the present study aimed to investigate its potential as a source of bioactive compounds. Notably, this study provides the first report describing both the chemical composition and the larvicidal activity of *C. erectus* essential oil from a Vietnamese population. The specific objectives were to: (1) characterize the chemical composition of essential oil extracted from the aerial parts of *C. erectus* collected in Vietnam using gas chromatography with flame ionization detection and mass spectrometry (GC–FID/MS); (2) evaluate its antimicrobial activity against selected bacterial and fungal pathogens; and (3) assess, for the first time, its larvicidal activity against larvae of *Ae. aegypti*, *Ae. albopictus*, and *Cx. quinquefasciatus*.

RESULTS AND DISCUSSION

Chemical composition of Chloranthus erectus essential oil

The essential oil extracted from *C. erectus* was obtained with a yield of 0.21% ± 0.01 (v/w) and analyzed by GC–FID/MS (Fig. S1). A total of 92.95% of the oil composition was identified, comprising several groups of

compounds (Table 1). Monoterpene hydrocarbons were the predominant class, accounting for 39.63% of the total oil, followed by sesquiterpene hydrocarbons (27.10%), oxygenated sesquiterpenes (19.35%), and oxygenated monoterpenes (5.12%), while other minor constituents contributed 1.75%. The principal components were (*E*)-β-ocimene (13.41%), myrcene (12.85%), spathulenol (12.55%), and bicyclogermacrene (12.01%), which together represented a substantial proportion of the total composition (Table 2). Other notable constituents included cis-β-elemene (4.80%), camphene (3.41%), α-pinene (3.22%), α-phellandrene (2.13%), elemol (2.07%), and bornyl acetate (2.04%). Compound identification was performed by comparison of retention indices (RI), calculated relative to a homologous series of *n*-alkanes on an HP-5ms column, together with mass spectral matching against the NIST library and published data. Although minor RI deviations were observed for certain sesquiterpenes, identification was confirmed by consistent agreement between RI values and MS fragmentation patterns, ensuring the analytical reliability of the reported composition. Overall, the chemical diversity of this essential oil indicates potential applications in the fragrance and pharmaceutical industries, largely attributable to the presence of bioactive terpenes and oxygenated derivatives.

Table 1. Distribution of chemical classes in the essential oil of *Chloranthus erectus*

Chemical class	Percentage (%)
Monoterpene hydrocarbons	39.63
Oxygenated monoterpenes	5.12
Sesquiterpene hydrocarbons	27.10
Oxygenated sesquiterpenes	19.35
Other compounds	1.75
Total identified	92.95

Notably, the chemical profile observed in this study differs markedly from the only previously reported analysis of *C. erectus* essential oil from Malaysia, where germacrone (36.62%) was the predominant compound [15]. In contrast, germacrone was absent in our sample. Such variation may result from environmental influences, genetic diversity, or differences in extraction and analytical methodologies [16, 17]. Since sesquiterpenes like germacrone are synthesized via the mevalonate pathway, its absence may reflect ecological or seasonal modulation of terpene biosynthesis [23].

Table 2. Chemical composition of the essential oil from *Chloranthus erectus*

Compound name [a]	RT [b]	RI [c]	RI [d]	Area (%)
α-Pinene	9.79	939	932	3.22
Camphene	10.28	955	946	3.41
Sabinene	10.98	978	969	0.13
β-Pinene	11.15	984	974	1.09
Myrcene	11.41	993	988	12.85
α-Phellandrene	11.97	1010	1002	2.13
o-Cymene	12.63	1029	1022	1.42
Limonene	12.78	1034	1024	0.99
β-Phellandrene	12.83	1035	1025	0.24
(*Z*)-β-Ocimene	12.93	1038	1032	0.56
(*E*)-β-Ocimene	13.32	1050	1044	13.41
Terpinolene	14.84	1094	1086	0.18
Rosefuran	15.02	1099	1094	0.15
Linalool	15.13	1102	1095	1.13
Perillene	15.19	1104	1102	0.31
Linalyl acetate	20.54	1257	1254	0.71
Geranial	21.15	1275	1264	0.15
Bornyl acetate	21.79	1294	1284	2.04
Safrole	21.93	1298	1285	1.11
δ-Elemene	23.58	1347	1335	0.35
α-Terpinyl acetate	23.88	1356	1346	0.63
Cyclosativene	24.72	1382	1369	0.63
α-Copaene	24.93	1388	1374	0.54
cis-β-Elemene	25.41	1403	1385	4.80
(*E*)-Caryophyllene	26.44	1436	1417	0.93
γ-Elemene	26.72	1444	1434	1.21
Aromadendrene	27.07	1456	1439	0.33
cis-Muurola-3,5-diene	27.38	1465	1448	0.30
α-Humulene	27.53	1470	1452	0.29
9-*epi*-(*E*)-Caryophyllene	27.76	1478	1664	0.38
epi-Zonarene	28.06	1487	1480	0.26
Valencene	28.13	1489	1483	0.19
Germacrene D	28.37	1497	1484	0.65
β-Selinene	28.56	1503	1489	1.18
Asaricin (= Sarisan)	28.67	1507	1495	0.64
Bicyclogermacrene	28.88	1514	1500	12.01
γ-Cadinene	29.41	1531	1513	0.61
δ-Cadinene	29.55	1536	1522	0.85
Zonarene	29.66	1540	1528	0.20

Compound name [a]	RT [b]	RI [c]	RI [d]	Area (%)
Elemol	30.37	1564	1548	2.07
E-Nerolidol	30.57	1570	1561	1.99
Germacrene B	30.77	1577	1562	1.39
Spathulenol	31.39	1598	1577	12.55
Caryophyllene oxide	31.57	1604	1582	0.76
1-*epi*-Cubenol	32.76	1646	1627	0.39
γ-Eudesmol	32.89	1650	1630	0.22
epi-α-Cadinol	33.19	1661	1638	0.28
β-Eudesmol	33.49	1672	1649	0.55
α-Eudesmol	33.56	1674	1652	0.54
Unidentified	42.38	2015	−	1.57

[a]Elution order on HP-5ms column. [b]Retention time (min). [c]Retention indices on HP-5ms column. [d]Literature retention indices.

Comparative analyses with other species in the *Chloranthus* genus further highlight interspecific metabolic divergence. For instance, *C. serratus* essential oil is dominated by cycloisolongifolene, 8,9-dehydro-9-formyl- (23.3%), 4-hydroxy-β-ionone (11.4%), curzerene (9.6%), and eremanthin (9.4%)-compounds not prevalent in *C. erectus* [11]. Likewise, bornyl acetate, which is a major component in *C. japonicus* (30.98%) and *C. multistachys* (35.99%), is present at a much lower concentration (2.04%) in *C. erectus* [10].

The essential oil profile of *C. elatior* shows partial similarity to *C. erectus*, with both containing bicyclogermacrene (*C. erectus*: 12.01%; *C. elatior*: 11.3%) [13]. However, *C. elatior* is also characterized by high levels of bicycloelemene (11.2%), (*Z*)-β-ocimene (7.8%), and *allo*-ocimene (6.3%) [13], whereas *C. erectus* contains a higher proportion of (*E*)-β-ocimene (13.41%). These differences underscore the influence of genetic and ecological factors on terpene profiles, even among closely related species [16, 17].

Intraspecific variation is also evident within *C. spicatus*, whose essential oil composition varies with geographic origin and plant part analyzed. For example, Vietnamese leaf oil is dominated by α-cadinol (10.0%), bicyclogermacrene (9.1%), and bicycloelemene (8.2%), while stem oil is rich in guaiol (16.9%), bicycloelemene (6.0%), and α-humulene (5.6%) [13]. A separate Vietnamese study by Tesso *et al.* reported (*Z*)-β-ocimene (6.3%), *allo*-aromadendrene (6.2%), sarisane (4.2%), and selina-4(15), 7(11)-diene (6.4%) as dominant components [12]. In contrast, *C. spicatus* from China exhibited a distinctly different profile, with 1,5,5-trimethyl-6-methylenecyclohexene (14.58%) as the most abundant compound, along with bicyclogermacrene (11.12%) and others [14].

Overall, the observed differences in essential oil composition of *C. erectus* and other *Chloranthus* species can be attributed to a combination of genetic, environmental, and methodological factors [16, 17]. The absence of germacrone in *C. erectus* from our study, despite its dominance in the Malaysian sample, highlights the need for further research into the role of ecological conditions in essential oil biosynthesis. Likewise, intraspecific variations, as seen in *C. spicatus* from different geographical regions, suggest that external factors such as climate, soil nutrients, and seasonal fluctuations play a critical role in determining the chemical profile of *Chloranthus* essential oils. These findings underscore the importance of continued investigations into the chemotaxonomic and pharmacological significance of *Chloranthus* essential oils.

Antimicrobial activity of Chloranthus erectus essential oil

The essential oil of *C. erectus* demonstrated antimicrobial activity against several tested bacterial and fungal strains, with minimum inhibitory concentration (MIC) values ranging from 16 to 64 µg/mL and half-maximal inhibitory concentration (IC_{50}) values from 8.96 to 24.15 µg/mL (Table 3). The oil inhibited the growth of *Candida albicans* with a MIC of 16 µg/mL and an IC_{50} of 8.96 µg/mL, showing activity comparable to the reference antifungal agent cycloheximide. Among the bacterial strains evaluated, *Bacillus cereus* and *Enterococcus faecalis* showed MIC values of 32 µg/mL, with corresponding IC_{50} values of 9.21 and 15.34 µg/mL, respectively. *Staphylococcus aureus* and *Pseudomonas aeruginosa* were inhibited at a MIC of 64 µg/mL, with IC_{50} values of 24.15 and 20.34 µg/mL, respectively. No inhibitory effect was observed against *Escherichia coli* and *Salmonella enterica*, whereas the positive control streptomycin inhibited these strains with MIC values of 256 µg/mL. Overall, the findings indicate that *C. erectus* essential oil displays antimicrobial activity against Gram-positive bacteria and yeast under the tested conditions.

Table 3. Antimicrobial activity of the essential oil from *Chloranthus erectus*

Microorganisms	Essential oil		Positive control [c]
	MIC [a]	IC_{50} [b]	MIC [a]
Enterococcus faecalis ATCC 299212	32	15.34	32
Staphylococcus aureus ATCC 25923	64	24.15	64
Bacillus cereus ATCC 14579	32	9.21	32
Escherichia coli ATCC 25922	–	–	256
Pseudomonas aeruginosa ATCC 27853	64	20.34	256
Salmonella enterica ATCC 13076	–	–	256
Candida albicans ATCC 10231	16	8.96	16

[a]Minimum inhibitory concentration (µg/mL). [b]Half-maximal inhibitory concentration (µg/mL).
[c]The positive controls for bacteria and yeast were streptomycin and cycloheximide, respectively.

Compared to previous studies, the antimicrobial potency observed in this work appears more pronounced. In an earlier report, the essential oil of *C. erectus* collected in Malaysia showed antifungal activity against *Ceratocystis fimbriata* but was ineffective against *Colletotrichum* and *Fusarium* species [15]. This discrepancy may reflect differences in chemical composition. The Malaysian sample was dominated by germacrone [15], while the present oil contains high levels of (*E*)-β-ocimene, myrcene, spathulenol, and bicyclogermacrene—compounds with well-established antimicrobial properties [24–27].

Essential oils from other *Chloranthus* species have also demonstrated significant antimicrobial activity. For example, the oil of *C. japonicus* showed strong antibacterial effects against *B. cereus* (MIC = 0.39 mg/mL), while *C. multistachys* was effective against both *B. cereus* and *Candida lipolytica* (MIC = 0.78 mg/mL) [10]. Moreover, the essential oil of *C. spicatus* has been reported to inhibit a broader spectrum of microorganisms, including *Bacillus subtilis*, *S. aureus*, *P. aeruginosa*, and *E. coli*, suggesting a wider antimicrobial range than that observed for *C. erectus* [14].

The antimicrobial effects of *C. erectus* essential oil can be attributed to both the major and minor constituents, and their potential synergistic interactions [28]. Among the dominant compounds, (*E*)-β-ocimene and myrcene are monoterpene hydrocarbons known to compromise microbial membrane integrity by increasing permeability and inducing intracellular leakage [29, 30]. Spathulenol, an oxygenated sesquiterpene, exerts antimicrobial effects through membrane destabilization and enzyme inhibition [31]. Bicyclogermacrene, a sesquiterpene hydrocarbon, has also been linked to bacteriostatic activity, likely through interference with membrane structure and energy pathways [32]. Although these major components likely contribute significantly to the observed bioactivity, minor constituents such as *cis*-β-elemene, camphene, α-pinene, and bornyl acetate may enhance the overall effect. These compounds may act synergistically by promoting membrane disruption, enhancing solubility or cellular uptake, or inhibiting microbial efflux systems [25]. This complex interaction among components supports the widely accepted notion that essential oils act through multifaceted mechanisms, often exhibiting greater efficacy as whole mixtures than as isolated compounds [33].

The higher susceptibility of Gram-positive bacteria to *C. erectus* essential oil, as compared to Gram-negative strains, can be explained by fundamental differences in cell wall architecture [34]. Gram-positive bacteria possess a thick but porous peptidoglycan layer that facilitates the penetration of lipophilic molecules such as terpenes [34]. In contrast, the outer membrane of Gram-negative bacteria, rich in lipopolysaccharides, acts as a selective barrier that limits the entry of hydrophobic compounds, thereby reducing the

antimicrobial efficacy of essential oils [35]. These differences in membrane architecture likely account for the variation in susceptibility and highlight the importance of targeting membrane structure in the development of plant-based antimicrobial agents.

Mosquito larvicidal activity of Chloranthus erectus essential oil

The insecticidal properties of essential oils have been widely documented, particularly in their effectiveness against mosquito vectors [36]. In this study, the larvicidal activity of *C. erectus* essential oil was assessed against the larvae of three mosquito species: *Ae. aegypti*, *Ae. albopictus*, and *Cx. quinquefasciatus* (Table 4). After 24 h of exposure, the essential oil produced LC_{50} values of 50.51 µg/mL for *Ae. aegypti*, 48.36 µg/mL for *Ae. albopictus*, and 45.66 µg/mL for *Cx. quinquefasciatus*, with corresponding LC_{90} values of 67.32 µg/mL, 67.19 µg/mL, and 60.11 µg/mL, respectively. Under the same conditions, the positive control permethrin yielded LC_{50} values of 0.000643 µg/mL (*Ae. aegypti*), 0.0024 µg/mL (*Ae. albopictus*), and 0.0165 µg/mL (*Cx. quinquefasciatus*), and LC_{90} values of 0.00246 µg/mL, 0.0042 µg/mL, and 0.0305 µg/mL, respectively. Following 48 h of exposure, the *C. erectus* essential oil showed reduced lethal concentration values, with LC_{50} values of 42.67 µg/mL for *Ae. aegypti*, 43.14 µg/mL for *Ae. albopictus*, and 41.21 µg/mL for *Cx. quinquefasciatus*, while the corresponding LC_{90} values were 67.02 µg/mL, 60.01 µg/mL, and 64.70 µg/mL, respectively. This time-dependent increase in toxicity aligns with previous findings on botanical larvicides and underscores the cumulative effects of essential oil components upon extended exposure [37–39].

Table 4. Mosquito larvicidal activity of the essential oil from *Chloranthus erectus* against *Aedes aegypti*, *Aedes albopictus* and *Culex quinquefasciatus* (µg/mL)

Time	Mosquitoes	LC_{50} (95% limits)	LC_{90} (95% limits)	χ^2	*p*
24 h	*Aedes aegypti*	50.51 (47.90−53.39)	67.32 (61.47−80.96)	0.903	0.825
	Aedes albopictus	48.36 (45.44−51.24)	67.19 (61.57−77.87)	0.122	0.941
	Culex quinquefasciatus	45.66 (42.46−48.08)	60.11 (56.06−68.37)	0.248	0.970
48 h	*Aedes aegypti*	42.67 (39.50−45.95)	67.02 (60.72−76.72)	0.743	0.863
	Aedes albopictus	43.14 (40.09−45.89)	60.01 (55.62−67.03)	1.317	0.518
	Culex quinquefasciatus	41.21 (38.13−44.42)	64.70 (58.65−73.89)	2.582	0.461

The enhanced toxicity observed over time may be associated with the progressive bioaccumulation of active compounds and their sustained interference with vital larval systems such as the nervous and respiratory systems. Key constituents of *C. erectus* essential oil—including (*E*)-β-ocimene, myrcene, spathulenol, and bicyclogermacrene—have been reported in previous studies to exhibit neurotoxic and cytotoxic effects [40–44]. Based on literature evidence, these compounds may contribute to larval mortality through mechanisms such as disruption of ion channels, inhibition of acetylcholinesterase, and impairment of mitochondrial function [45, 46]. Their lipophilic nature is generally considered to facilitate penetration through the larval cuticle, thereby enhancing bioavailability and potentially prolonging toxic effects [45, 46].

In addition to the individual bioactivity of these compounds, the observed larvicidal efficacy may also be influenced by synergistic interactions among multiple constituents. Previous research has suggested that combinations of monoterpenes and sesquiterpenes can exert greater toxicity than their isolated counterparts [47, 48]. Such synergism has been proposed to involve enhanced membrane permeability, inhibition of detoxifying enzymes, and prolonged persistence of toxic effects [45]. Hence, the larvicidal potential of *C. erectus* essential oil is likely attributable to the collective action of its complex chemical matrix rather than any single dominant component.

Species-specific differences in susceptibility were also apparent. *Cx. quinquefasciatus* showed slightly higher sensitivity, particularly after 24 h of exposure. This variation may reflect inherent differences in larval cuticle composition, metabolic rate, or detoxification capacity, which can influence the uptake and metabolism of xenobiotics [45]. Such interspecies variability emphasizes the need for evaluating botanical insecticides across multiple vector species to better understand their spectrum of activity and potential for targeted control.

Compared to other plant-based larvicides, the essential oil of *C. erectus* demonstrates comparable, if not superior, efficacy. The LC_{50} values reported here fall well within the generally accepted threshold of <100 µg/mL for effective botanical larvicides [47, 48]. Given the limited prior research on the insecticidal potential of this species, these findings offer a novel contribution and highlight *C. erectus* as a promising candidate for mosquito control.

Overall, the data indicate that *C. erectus* essential oil may serve as a promising candidate for the development of eco-friendly larvicidal formulations. The demonstrated time-dependent toxicity, broad-spectrum activity, and synergistic interactions among its constituents support its application in integrated vector management (IVM) strategies. Future studies should aim to isolate and characterize the active principles, investigate their specific mechanisms of action, and evaluate environmental safety to facilitate the development of effective and sustainable mosquito control products.

CONCLUSIONS

The essential oil extracted from *C. erectus* contained a diverse array of bioactive terpenoids, with (*E*)-β-ocimene, myrcene, spathulenol, and bicyclogermacrene identified as the major constituents. This chemical profile differs markedly from that previously reported for Malaysian populations, in which germacrone was the dominant compound, suggesting the presence of a distinct Vietnamese chemotype. The essential oil showed antimicrobial activity against several tested microorganisms, including Gram-positive bacteria and *C. albicans*, and also displayed larvicidal activity against three mosquito vectors—*Ae. aegypti*, *Ae. albopictus*, and *Cx. quinquefasciatus*.

Importantly, this study represents the first report of the larvicidal activity of *C. erectus* essential oil and the first characterization of its essential oil composition from Vietnam, thereby substantially expanding the current phytochemical and biological knowledge of the species. These findings underscore the potential of *C. erectus* essential oil as a natural source of antimicrobial and insecticidal agents. Further studies are warranted to isolate key bioactive constituents, elucidate their mechanisms of action, and evaluate formulation stability and environmental safety to support potential applications in pharmaceutical development and integrated vector control strategies.

MATERIALS AND METHODS

Plant material

The aerial parts of *C. erectus* were collected in August 2023 during a field expedition in Pu Luong Nature Reserve, Thanh Hoa province, Vietnam (20°28'43'' N, 105°6'52'' E, elevation: 667 m) (Fig. S2). The identification of the plant was conducted by Assoc. Prof. Dr. Le Thi Huong from Vinh University, Vietnam. A voucher specimen (LTH42L) was deposited at the university's herbarium for future reference. To maintain the integrity of bioactive compounds, the freshly collected plant material was transported directly to the laboratory for extraction.

Essential oil extraction

Essential oil extraction was performed using hydrodistillation in a Clevenger-type apparatus, following standard procedures outlined in the Vietnamese Pharmacopoeia [49] and previous studies [50, 51]. A total of 6 kg of *C. erectus* aerial parts was processed in three independent extractions, each using 2 kg of plant material. The distillation process was conducted at

atmospheric pressure for 4 h. After collection, the essential oil was dried over anhydrous sodium sulfate to remove residual moisture. The oil was then stored in sterilized glass vials at 4°C for up to one month before further analysis.

Essential oil analysis

The chemical composition of the essential oil was analyzed by GC–FID/MS [52]. For GC–FID analysis, an Agilent Technologies HP 7890A Plus gas chromatograph equipped with an HP-5ms capillary column (30 m × 0.25 mm i.d., 0.25 μm film thickness) and a flame ionization detector was employed. Hydrogen was used as the carrier gas at a flow rate of 1.0 mL/min. The oven temperature was programmed from 60°C (held for 2 min) to 220°C at a rate of 4°C/min, followed by a final hold of 10 min. The injector and detector temperatures were set at 250°C and 260°C, respectively, with a split ratio of 10:1. Relative percentages of the individual components were calculated by peak area normalization without the use of correction factors and are therefore presented as semi-quantitative values.

GC–MS analysis was performed under identical chromatographic conditions using an HP 5973 mass selective detector. Helium served as the carrier gas at a flow rate of 1.0 mL/min. The mass spectrometer operated in electron ionization mode at 70 eV with an emission current of 40 mA, scanning over a mass range of m/z 35–350 at a rate of 1 scan/s. Retention indices (RI) were calculated relative to a homologous series of *n*-alkanes (C_8–C_{25}) analyzed under the same experimental conditions. Compound identification was achieved by comparing calculated RI values with published data and by matching mass spectra with those in the NIST and Wiley libraries [53, 54].

Antimicrobial assay

The antimicrobial activity of the essential oil was evaluated against seven microbial strains: three Gram-positive bacteria (*E. faecalis* ATCC 299212, *S. aureus* ATCC 25923, *B. cereus* ATCC 14579), three Gram-negative bacteria (*E. coli* ATCC 25922, *P. aeruginosa* ATCC 27853, *S. enterica* ATCC 13076), and one yeast strain (*C. albicans* ATCC 10231). These strains were obtained from the American Type Culture Collection (ATCC, Manassas, USA).

The MIC and IC_{50} values were determined using the broth microdilution method [37, 38]. Bacterial strains were cultivated on Mueller-Hinton Agar, while fungal assays were conducted on Sabouraud Agar. The essential oil was dissolved and serially diluted in dimethyl sulfoxide (DMSO) to obtain the desired test concentrations prior to addition to 96-well microtiter plates. Bacterial suspensions were standardized to 5×10^5 CFU/mL in Mueller-Hinton broth, while fungal suspensions were adjusted to 1×10^3 CFU/mL in Sabouraud

dextrose broth. DMSO served as a negative control, while streptomycin and cycloheximide served as positive controls for antibacterial and antifungal assays, respectively. Plates were incubated at 37°C for 24 h (bacteria) and at 30°C for 24 h (fungi), and microbial growth was assessed by measuring optical density at 600 nm using a Spectramax 190 microplate reader. IC_{50} values were determined based on turbidity reduction using an EPOCH2C spectrophotometer.

Mosquito larvicidal assay

The larvicidal activity of the essential oil was tested against third instar larvae of *Ae. aegypti*, *Ae. albopictus*, and *Cx. quinquefasciatus* following standardized protocols [37, 38]. Larvae were collected and reared under controlled laboratory conditions at Duy Tan University, Vietnam. A 1% stock solution of the essential oil was prepared in DMSO, followed by serial dilutions to obtain test concentrations of 3.125, 6.25, 12.5, 25, 50, and 100 µg/mL. Each bioassay consisted of twenty larvae placed in 300 mL beakers containing the respective concentrations. Experiments were conducted at room temperature (25°C) with three replicates per concentration. Permethrin served as a positive control, while DMSO acted as a negative control. Larval mortality was recorded at 24 and 48 h post-exposure, and the lethal concentration values (LC_{50} and LC_{90}) were calculated using log-probit analysis.

Statistical analysis

All experiments were performed in triplicate. IC_{50} values for antimicrobial assays were derived using non-linear regression modeling of the dose-response curve. LC_{50} and LC_{90} values for the larvicidal assay were determined through log-probit regression analysis with 95% confidence intervals. Data analysis was conducted using Minitab 19.2020.1 (State College, PA, USA) and GraphPad Prism 9.5.1.733 (GraphPad Software Inc., San Diego, CA, USA).

REFERENCES

1. Y.Y. Liu; Y.Z. Li; S.Q. Huang; H.W. Zhang; C. Deng; X.M. Song; D.D. Zhang; W. Wang; Arab. J. Chem., **2022**, *15*(11), 104260. https://doi.org/10.1016/j.arabjc.2022.104260
2. A.R. Wang; H.C. Song; H.M. An; Q. Huang; X. Luo; J.Y. Dong; Chem. Biodivers., **2015**, *12*(4), 451-473. https://doi.org/10.1002/cbdv.201300376
3. Y.J. Xu; Chem. Biodivers., **2013**, *10*(10), 1754-1773. https://doi.org/10.1002/cbdv.201200066

4. H. Tag; N.D. Namsa; A.K. Das; P. Kalita; S.C. Mandal; J. Ethnopharmacol., **2009**, *126*(2), 371-374. https://doi.org/10.1016/j.jep.2009.08.015
5. N.A. Hasan; S. Ariffin; A.M. Azzeme; N.I. Hasbullah; M.Z. Nawahwi; I.H.B. Zemry; Mater. Today: Proc., **2023**, *88*(2), 6-9. https://doi.org/10.1016/j.matpr.2023.01.365
6. H. Tag; N.D. Namsa; M. Mandal; P. Kalita; A.K. Das; S.C. Mandal; Indian J. Pharmacol., **2010**, *42*(5), 273-276. https://doi.org/10.4103/0253-7613.70083
7. A.F. Musayyaf; International Journal of Medical Science and Clinical Research Studies, **2024**, *4*(12), 2418-2422. https://doi.org/10.36490/journal-jps.com.v8i3.950
8. I.H. Zemry; N.A. Hasan; N.I. Hasbullah; M.Z. Nawahwi; A.M. Azzeme; D.A. Siti Noor; S. Ariffin; J. Exp. Biol. Agric. Sci., **2023**, *11*(1), 75-80. http://dx.doi.org/10.18006/2023.11(1).75.80
9. F. Bakkali; S. Averbeck; D. Averbeck; M. Idaomar; Food Chem. Toxicol., **2008**, *46*(2), 446-475. https://doi.org/10.1016/j.fct.2007.09.106
10. J.F. Kang; Y. Zhang; Y.L. Du; Z.Z. Wang; Z. Naturforsch. C, **2010**, *65*(11-12), 660-666. https://doi.org/10.1515/znc-2010-11-1205
11. J. Zhu; R. Jia; P. Lai; Chem. Nat. Compd., **2017**, *53*, 159-161. https://doi.org/10.1007/s10600-017-1936-0
12. H. Tesso; W.A. König; P.T. Son; P.M. Giang; Flavour Fragr. J., **2006**, *21*(4), 592-597. https://doi.org/10.1002/ffj.1528
13. T.D. Thang; D.N. Dai; I.A. Ogunwande; Chem. Nat. Compd., **2016**, *52*, 149-151. https://doi.org/10.1007/s10600-016-1575-x
14. L. Chen; Y.M. Huang; M.Y. Sun; M. Zhao; Y.X. Wu; Z.B. Wan; X. Su; C.H. Zhao; J. Northeast For. Univ., **2021**, *49*(12), 52-57. https://doi.org/10.13759/j.cnki.dlxb.2021.12.021
15. J. Mailina; W.A.W.M. Azrul; M.A.N. Azah; S.S. Husni; J.A. Majid; L. Sahrim; Z.P.M. Faridz; C.C.K. Richard; A.L. Nurliyana; A. Noorsiha; Volatile composition and antifungal properties of *Chloranthus erectus* leaves oil, in *Proceedings of the 15th Seminar on Medicinal and Aromatic Plants*, Malaysia, **2018**.
16. A.C. Figueiredo; J.G. Barroso; L.G. Pedro; J.J. Scheffer; Flavour Fragr. J., **2008**, *23*(4), 213-226. https://doi.org/10.1002/ffj.1875
17. A. Barra; Nat. Prod. Commun., **2009**, *4*(8), 1147-1154. https://doi.org/10.1177/1934578X0900400827
18. L. Serwecińska; Water, **2020**, *12*(12), 3313. https://doi.org/10.3390/w12123313
19. Y. Zhang; M. Wang; M. Huang; J. Zhao; Front. Microbiol., **2024**, *15*, 1488106. https://doi.org/10.3389/fmicb.2024.1488106
20. B.F.M.T. Andrade; L.N. Barbosa; I.D.S. Probst; A.F. Júnior; J. Essent. Oil Res., **2014**, *26*(1), 34-40. https://doi.org/10.1080/10412905.2013.860409
21. S. Chouhan; K. Sharma; S. Guleria; Medicines, **2017**, *4*(3), 58. https://doi.org/10.3390/medicines4030058
22. R. Pavela; Ind. Crops Prod., **2015**, *76*, 174-187. https://doi.org/10.1016/j.indcrop.2015.06.050
23. J. Gershenzon; R.B. Croteau; Terpenoid biosynthesis: the basic pathway and formation of monoterpenes, sesquiterpenes, and diterpenes, in *Lipid Metabolism in Plants*, CRC press, **2018**, pp. 339-388.

24. A. Koziol; A. Stryjewska; T. Librowski; K. Salat; M. Gawel; A. Moniczewski; S. Lochynski; Mini-Rev. Med. Chem., **2014**, *14*(14), 1156-1168. https://doi.org/10.2174/1389557514666141127145820
25. N.A. Mahizan; S.K. Yang; C.L. Moo; A.A.L. Song; C.M. Chong; C.W. Chong; A. Abushelaibi; S.H.E. Lim; K.S. Lai; Molecules, **2019**, *24*(14), 2631. https://doi.org/10.3390/molecules24142631
26. K.A. Wojtunik-Kulesza; K. Kasprzak; T. Oniszczuk; A. Oniszczuk; Chem. Biodivers., **2019**, *16*(12), e1900434. https://doi.org/10.1002/cbdv.201900434
27. H.Y. Li; W.Q. Yang; X.Z. Zhou; F. Shao; T. Shen; H.Y. Guan; J. Zheng; L.M. Zhang; Biomolecules, **2022**, *12*(9), 1271. https://doi.org/10.3390/biom12091271
28. M. Angane; S. Swift; K. Huang; C.A. Butts; S.Y. Quek; Foods, **2022**, *11*(3), 464. https://doi.org/10.3390/foods11030464
29. M. Donati; A. Mondin; Z. Chen; F.M. Miranda; B.B. do Nascimento Jr; G. Schirato; P. Pastore; G. Froldi; Nat. Prod. Res., **2015**, *29*(10), 939-946. https://doi.org/10.1080/14786419.2014.964709
30. O.A. Oyedeji; A.J. Afolayan; J.N. Eloff; S. Afr. J. Bot., **2005**, *71*(1), 114-116. https://doi.org/10.1016/S0254-6299(15)30160-5
31. I.R. da Silva; C.C. Fernandes; D.S. Gonçalves; C.H. Martins; M.L. Miranda; Nat. Prod. Res., **2024**, *38*(19), 3476-3480. https://doi.org/10.1080/14786419.2023.2249584
32. A. Shafaghat; M. Shafaghatlonbar; Nat. Prod. Commun., **2011**, *6*(2), 1934578X1100600230. https://doi.org/10.1177/1934578X1100600230
33. I.H.N. Bassolé; H.R. Juliani; Molecules, **2012**, *17*(4), 3989-4006. https://doi.org/10.3390/molecules17043989
34. F. Nazzaro; F. Fratianni; L. De Martino; R. Coppola; V. De Feo; Pharmaceuticals, **2013**, *6*(12): 1451-1474. https://doi.org/10.3390/ph6121451
35. O. Lüderitz; M.A. Freudenberg; C. Galanos; V. Lehmann; E.T. Rietschel; D.H. Shaw; Lipopolysaccharides of gram-negative bacteria, in *Current topics in membranes and transport*, Academic Press, **1982**, pp. 79-151. https://doi.org/10.1016/S0070-2161(08)60309-3
36. M. Gupta; D. Gupta; J. Drug Deliv. Ther., **2022**, *12*(3), 193-201. http://dx.doi.org/10.22270/jddt.v12i3.5313
37. V.V. Khoa; D.N. Dai; L.T. Huong; B.B. Thinh; Nat. Prod. Commun., **2024**, *19*(11), 1934578X241299995. https://doi.org/10.1177/1934578X241299995
38. D.N. Dai; N.T. Thao; L.T. Huong; N.H. Hung; V.T. Thuong; B.B. Thinh; J. Essent. Oil Bear. Plants, **2024**, *27*(5), 1334-1346. https://doi.org/10.1080/0972060X.2024.2414866
39. L.T. Huong; D.N. Dai; N.H. Hung; B.B. Thinh; Chem. Biodivers., **2026**, *23*(2), e01348. https://doi.org/10.1002/cbdv.202501348
40. J.M.S. de Sousa; T.A.L. Nunes; R.R.L. Rodrigues; J.P.A. de Sousa; M.C.A. Val; F.A.R. Coelho; A.L.S. dos Santos; N.B. Maciel; V.M.R. de Souza; Y.A.A. Machado; P.S.A. Sousa; A.R. de Araújo; J.A. Rocha; D.P. de Sousa; M.V. da Silva; D.D.R. Arcanjo; K.A. da Franca Rodrigues; Pharmaceuticals, **2023**, *16*(2), 183. https://doi.org/10.3390/ph16020183

41. X. Bai; J. Tang; Nat. Prod. Commun., **2020**, *15*(9), 1934578X20961189. https://doi.org/10.1177/1934578X20961189
42. V.P. de Almeida; S.E.L. Tolouei; M. Minteguiaga; D.S.A. Chaves; G. Heiden; S.I. Khan; J. Trott; M. Wang; E. Dellacassa; V. Raman; P.V. Farago; I.A. Khan; A.G. Junior; J. Manfron; Chem. Biodivers., **2023**, *20*(10), e202300862. https://doi.org/10.1002/cbdv.202300862
43. S.S. Grecco; E.G.A. Martins; N. Girola; C.R. de Figueiredo; A.L. Matsuo; M.G. Soares; B.C. Bertoldo; P. Sartorelli; J.H.G. Lago; Pharm. Biol., **2015**, *53*(1), 137-143. https://doi.org/10.3109/13880209.2014.912238
44. J. Calva; M.B. Cuenca; A. León; Á. Benítez; Molecules, **2025**, *30*(13), 2712. https://doi.org/10.3390/molecules30132712
45. S. Senthil-Nathan; Front. Physiol., **2020**, *10*, 473482. https://doi.org/10.3389/fphys.2019.01591
46. M. Jankowska; J. Rogalska; J. Wyszkowska; M. Stankiewicz; Molecules, **2017**, *23*(1), 34. https://doi.org/10.3390/molecules23010034
47. T.R.S.A. Luz; L.S.S. de Mesquita; F.M.M. do Amaral; D.F. Coutinho; Acta Tropica., **2020**, *212*, 105705. https://doi.org/10.1016/j.actatropica.2020.105705
48. C.N. Dias; D.F.C. Moraes; Parasitol. Res., **2014**, *113*, 565-592. https://doi.org/10.1007/s00436-013-3687-6
49. Vietnamese Pharmacopoeia; Medical Publishing House, Hanoi, Vietnam, **2009**.
50. B.B. Thinh; D.B. Thin; I.A. Ogunwande; Nat. Prod. Commun., **2024**, *19*(3), 1934578X241239477. https://doi.org/10.1177/1934578X241239477
51. B.B. Thinh; L.D. Chac; J. Essent. Oil Bear. Plants, **2024**, *27*(2), 574-583. https://doi.org/10.1080/0972060X.2024.2324347
52. D.N. Dai; L.T. Thuy; D.T. Xuyen; N.T. Viet; L.T. Huong; B.B. Thinh; J. Essent. Oil Bear. Plants, **2025**, *28*(1), 147-157. https://doi.org/10.1080/0972060X.2025.2463480
53. National Institute of Science and Technology; NIST Chemistry Webbook. *Data from NIST Standard Reference Database*, **2018**, p. 69.
54. R.P. Adams; Identification of essential oil components by gas chromatography/ mass spectroscopy. *Allured Publishing Corporation*, Carol Stream, **2007**.

STUDIA UBB CHEMIA, LXXI, 1, 2026 (p. 209-222)
(RECOMMENDED CITATION)
DOI:10.24193/subbchem.2026.1.13

ANTICANCER EFFECTS OF HUMAN BREAST MILK-DERIVED PEPTIDES ON MCF-7 CELLS: OMICS – GUIDED EVALUATION

Begüm Gürel GÖKMEN[a], Merve GURBOGA[b], Ozlem BINGOL OZAKPINAR[b], Gonca ALTIN[c], Tuğba TUNALI-AKBAY[a*]

ABSTRACT. This study evaluated the anticancer potential of peptides from enzymatically hydrolyzed human breast milk on MCF-7 breast cancer cells, focusing on protein expression alterations associated with cell death. Human breast milk was enzymatically hydrolyzed under controlled conditions to simulate gastrointestinal processing, generating bioactive peptides. The hydrolysate was applied to MCF-7 cells for 24 hours, and proteomic changes were characterized using LC-MS/MS-based analysis. Application of the hydrolysate to MCF-7 cells led to notable proteomic alterations, particularly in proteins regulating apoptosis, cell survival, and cancer-related signalling pathways. In silico docking analyses identified three abundant peptides (AGFAGDDAPR, LAADDFR, and DAEAWFNEK) predicted to interact with key regulatory proteins, including myeloid cell leukemia-1, Ras suppressor protein-1, and galectin-3. These peptides showed favorable docking scores, which may indicate their potential involvement in apoptosis- and metastasis-related pathways. Omics-guided evaluation highlights these peptides as promising lead candidates for peptide-based anticancer strategies. This integrative approach demonstrates the utility of combining enzymatic hydrolysis, proteomic profiling, and computational analyses to identify human-derived bioactive molecules with therapeutic potential.

Keywords: *Bioactive peptides, bioinformatic analysis, breast milk, breast cancer*

[a] *Marmara University, Faculty of Dentistry, Department of Basic Medical Sciences, Istanbul, Türkiye*
[b] *Marmara University, Faculty of Pharmacy, Department of Biochemistry, Istanbul, Türkiye*
[c] *Bioanalysis Laboratory, TUBITAK National Metrology Institute, Kocaeli, Türkiye*
** Corresponding author: ttunali@marmara.edu.tr*

INTRODUCTION

Breast cancer raises from the uncontrolled proliferation of epithelial cells within ducts or lobules of the breast [1]. The development and homeostasis of mammary ductal epithelial cells are regulated by growth factors, differentiation signals, and the balance between pro- and anti-apoptotic pathways [2]. Consequently, modern therapy targets multiple molecular pathways, and research into novel compounds that influence apoptosis remains active [3]. Studies have shown that different types of milk have antiproliferative and apoptotic effects on cancer cells. The majority of these studies focused on the antiproliferative and apoptotic mechanisms of cow's milk, camel's milk, and goat's milk-based proteins [4-6]. Different recombinant casein forms (κ and α – casein) have also been found to stimulate the apoptotic signalling pathway by reducing cell growth in the breast cancer cell lines [7, 8]. Svanborg et al have found the anticancer properties of α-lactalbumin-oleic acid, a natural compound derived from breast milk (BM). This complex, known as human alpha-lactalbumin made lethal to tumor cells (HAMLET), was identified during their research on antiadhesive components in human milk [9]. In recent years, the studies related to bioactive peptides in cancer treatment have increased [10].

Bioactive peptides are encrypted within parent proteins and become functional only after *in vitro* or *in vivo* digestion [11]. Their immuno-modulatory, antihypertensive, antithrombotic, antioxidant or anticancer activities depend on their amino-acid sequence and three-dimensional conformation [12]. In this study, BM-based bioactive peptides were used to investigate their effects on breast cancer cell line.

Human BM is a complex fluid known for its nutritive, immunomodulatory, and developmental roles [13]. Although some studies have suggested potential anticancer properties, BM is primarily designed to support infant growth and immune development rather than to exhibit strong anticancer effects. However, specific bioactive components, such as peptides, may carry therapeutic potential, and their individual functions warrant further investigation [14]. Studies have indicated that BM-based bioactive peptides have immunoregulatory [15], antimicrobial [16], antihypertensive [17], antithrombotic [18], anticancer [19], and antioxidant [20] properties.

In parallel with *in vitro* studies, *in silico* approaches have become essential tools for predicting peptide bioactivity and potential molecular targets [21]. Previous research has employed computational methods to investigate transcriptional regulation and apoptotic mechanisms in breast cancer cells [22-24].

This study aims to evaluate the antiproliferative potential of bioactive peptides derived from enzymatically digested human BM on MCF-7 breast cancer cells, with a particular focus on their molecular mechanisms of action.

RESULTS AND DISCUSSION

LC-MS/MS analysis of the *in vitro* digested BM identified 94 peptides. Subsequent toxicity screening using the ToxinPred program revealed that none of these peptides possessed toxic potential. Furthermore, 14 of the identified peptides were predicted to exhibit significant biological activity (Table 1).

Table 1. Sequences of potential bioactive BM peptides

Peptide	Master Protein Accession Number	Potential Bioactive Peptide Sequences*	Amino Acid Length	Peptide Ranker Scores
1	P35908	HGGGGGGFGGGGFGSR	16	0.86
2	P35527	SGGGGGGGLGSGGSIR	16	0.83
3	P13929-1	FGANAILGVSLAVCK	15	0.77
4	P07602-1	SLPCDICK	8	0.76
5	P35908	GGSISGGGYGSGGGK	15	0.64
6	P01857	GPSVFPLAPSSK	12	0.64
7	P04745	HMWPGDIK	8	0.60
8	P07602-1	LGPGMADICK	10	0.58
9	P35527	QGVDADINGLR	11	0.58
10	P60709	AGFAGDDAPR	10	0.56
11	P02533	LAADDFR	8	0.54
12	P13645	DAEAWFNEK	9	0.53
13	P01614	FSGSGSGTDFTLK	13	0.53
14	Q32P51	SHFEQWGTLTDCVVMR	16	0.51

*Potential bioactive peptides were evaluated by the Peptide Ranker ($p>0.5$)

Bioactivity predictions performed through the BIOPEP-UWM database have revealed various potential functionalities for the identified peptides. These include inhibitory activities against angiotensin-converting enzyme (ACE), dipeptidyl peptidase III (DPP-III), dipeptidyl peptidase IV (DPP-IV), and α-glucosidase. Furthermore, the peptides are predicted to possess antioxidant, antithrombotic, and hypotensive effects, as well as the ability to stimulate glucose uptake and influence various enzyme activities such as phosphoglycerate kinase.

Several identified peptides originated from master proteins not classically classified as milk proteins, including cytoskeletal (e.g., keratins, actin), immune-related (e.g., immunoglobulins, β2-microglobulin), and regulatory proteins (e.g., annexin A1). This observation is consistent with previous proteomic studies demonstrating that human breast milk is a complex biological fluid containing not only secreted milk proteins but also cellular and immune components derived from mammary epithelial cells, immune cells, and extracellular vesicles. Enzymatic digestion of these proteins can generate bioactive peptide fragments, some of which have been reported to exhibit regulatory or signalling-related biological activities.

MTT assay results revealed that BM hydrolysate exhibited significant cytotoxic activity on MCF-7 breast cancer cells (Figure 1A). Interestingly, the most potent inhibition was observed at lower concentrations, particularly 5 µg/mL; at this concentration, cell viability was significantly reduced by approximately 18% compared to the control group ($p<0.001$). As the concentration increased above 25 µg/mL, the inhibitory effect remained statistically significant but showed a slight plateau ($p<0.05$); this suggests a non-linear dose-response relationship typical of complex biological hydrolysates. On the other hand, Real-Time Cell Assay (RTCA) growth curves (Figure 1B) also confirmed the MTT findings, demonstrating that the antiproliferative effect began shortly after treatment. Lower concentrations (0.31-5 µg/mL) of BM hydrolysate showed a significant divergence from the control curve, with the 5 µg/mL concentration consistently maintaining a lower Cell Index value throughout the 96-hour period. At higher concentrations (5-100 µg/mL) of BM hydrolysate, the growth curves initially showed fluctuations, followed by a gradual decrease in Cell Index towards the end of the 96-hour incubation period; this indicates that BM hydrolysate maintains inhibitory suppression for an extended period without significant cell recovery.

The 18% decrease in viability observed in MCF-7 cells following treatment with BM hydrolysate, along with a plateau-type dose-response pattern at higher concentrations, reflects the characteristic biochemical behavior of complex food-derived peptide mixtures. Such plateau-type responses are frequently reported in studies investigating bioactive protein hydrolysates [25, 26]. This non-linear profile can primarily be explained by concentration-dependent intermolecular hydrophobic interactions that promote peptide aggregation at high doses (50–100 µg/mL). Peptide aggregation can reduce the effective concentration of biologically active monomers and limit further biological activity by sterically inhibiting their interaction with cellular target [27]. Consistent with the nature of food-derived bioactive peptides, such hydrolysates typically function not as aggressive cytotoxic agents, but as modulator molecules capable of exhibiting maximum biological activity at lower concentration ranges, sometimes displaying hormetic-like dynamics [25, 26].

Importantly, no IC_{50} value could be determined in the tested concentration range, indicating that BM hydrolysate does not cause strong acute cytotoxicity under the current conditions. However, the observed moderate but statistically significant and reproducible effect supports the conclusion that BM-derived peptides exhibit a sustained growth inhibitory effect. Taken collectively, these findings suggest that BM hydrolysate has potential not as a conventional chemotherapeutic agent, but rather as a long-term protective or adjuvant bioactive component, requiring further fractionation and mechanistic characterization.

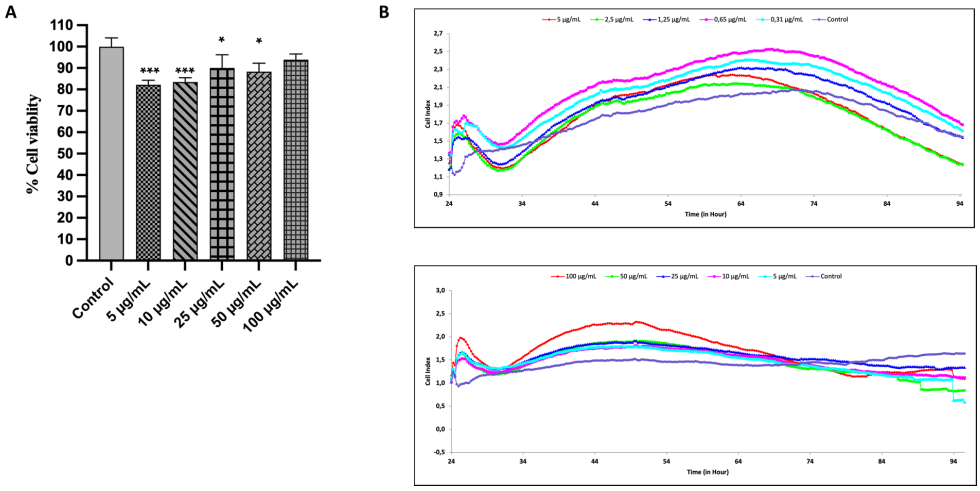

Figure 1. The dose-dependent antiproliferative effects of BM hydrolysate on MCF-7 cells. A) MTT results, B) Impedance-based cell index results. ***p<0.001 and *p<0.05 compared to control group.

Proteomic analysis BM-treated MCF-7 cells revealed differential expression of 160 proteins, with 80 upregulated (2- to 32-fold) and 80 downregulated (2- to 43-fold) compared to untreated MCF-7 cells. These proteins were found to be associated with cytosolic signal transduction, apoptosis regulation, and stress responses.

Table 2 presents the HPepDock interaction scores (kcal/mol) for bioactive BM peptides and differentially expressed proteins in MCF-7 cells. Lower values indicate stronger binding affinity.

Table 2. HPepDock docking scores of BM hydrolysate peptides and up-regulated or down-regulated proteins of BM-treated MCF-7 cells

Peptide	HPepDock Docking Scores (kcal/mol)	Galectin-3	Ras suppressor protein-1	Myeloid cell leukemia-1	Apoptosis-inducing factor-1
1	HGGGGGGFGGGGFGSR	-177.7	-190.8	-222.6	-192.8
2	SGGGGGGGLGSGGSIR	-148.5	-164.8	-176.1	-167.4
3	FGANAILGVSLAVCK	-189.0	-176.5	-209.5	-179.4
4	SLPCDICK	-143.1	-124.7	-165.5	-139.7
5	GGSISGGGYGSGGGK	-159.5	-193.0	-201.1	-183.2
6	GPSVFPLAPSSK	-169.2	-172.1	-212.7	-189.1
7	HMWPGDIK	-170.1	-178.9	-209.9	-204.1
8	LGPGMADICK	-156.1	-154.6	-173.9	-159.1
9	QGVDADINGLR	-165.0	-157.7	-162.1	-156.3
10	AGFAGDDAPR	-163.8	-166.2	-171.4	-180.2
11	LAADDFR	-160.8	-161.1	-169.1	-172.2
12	DAEAWFNEK	-180.8	-172.7	-172.0	-166.9
13	FSGSGSGTDFTLK	-174.8	-169.1	-188.01	-186.6
14	SHFEQWGTLTDCVVMR	-194.0	-213.6	-222.2	-216.0

Peptide 14 exhibited the most favorable docking scores with both the downregulated protein Galectin-3 (1A3K; −194.0 kcal/mol) and the upregulated protein Ras suppressor protein-1 (7D2S_A; −231.6 kcal/mol). Peptide 1 showed the most favorable docking scores with the downregulated protein Myeloid cell leukemia-1 (Mcl-1) (8G3S; −222.6 kcal/mol), while peptide 14 also demonstrated comparatively favorable interaction scores with the upregulated protein Apoptosis-inducing factor-1 (AIF-1) (4LII; −216.0 kcal/mol) (Table 2).

Table 3 shows the AutoDock Vina docking scores of bioactive peptides with the same set of up- and downregulated MCF-7-associated proteins*. In silico* docking analysis was performed to explore potential interactions between the identified peptides and selected target proteins associated with cancer-related pathways. Several peptides demonstrated docking scores indicating potential interactions with Ras suppressor protein-1 (7D2S-A) and Apoptosis-inducing factor-1 (4LII). These results suggest that certain peptides may interact with these proteins, although further experimental validation is required.

Table 3. Molecular docking scores of BM peptides and BM-treated MCF-7 cells

Peptide	Molecular docking scores (kcal/mol)	Galectin-3	Ras suppressor protein-1	Myeloid cell leukemia-1	Apoptosis-inducing factor-1
1	HGGGGGGFGGGGFGSR	-6	-6.1	-6.5	-8
2	SGGGGGGGLGSGGSIR	-6.1	-5.3	-7	-5.9
3	FGANAILGVSLAVCK	-5.7	-5.9	-7.3	-6.5
4	SLPCDICK	-5.2	-6	-7.1	-6.1
5	GGSISGGGYGSGGGK	-4.9	-6.5	-7.9	-6.6
6	GPSVFPLAPSSK	-6	-6.6	-7.8	-6.4
7	HMWPGDIK	-5.8	-6.1	-8	-6.5
8	LGPGMADICK	-5	-5.9	-7.9	-5.8
9	QGVDADINGLR	-5.3	-4.9	-7.4	-6.5
10	AGFAGDDAPR	-5.4	-6.8	-8.1	-5.7
11	LAADDFR	-5.8	-5.7	-8.5	-7.8
12	DAEAWFNEK	-6.3	-6.6	-8	-9.1
13	FSGSGSGTDFTLK	-6	-6.5	-7.4	-6.8
14	SHFEQWGTLTDCVVMR	-6	-6.3	-6.6	-6.3

Binding site analysis indicated specific amino acid residues involved in peptide–protein interactions. For Galectin-3 (1A3K), DAEAWFNEK (peptide 12) yielded the most favorable docking score (−6.3 kcal/mol) and was predicted to interact with ARG144, ASP148, ARG162, GLY165, LYS176, TRP181, GLY235, SER237, and GLY238 (Figure 2).

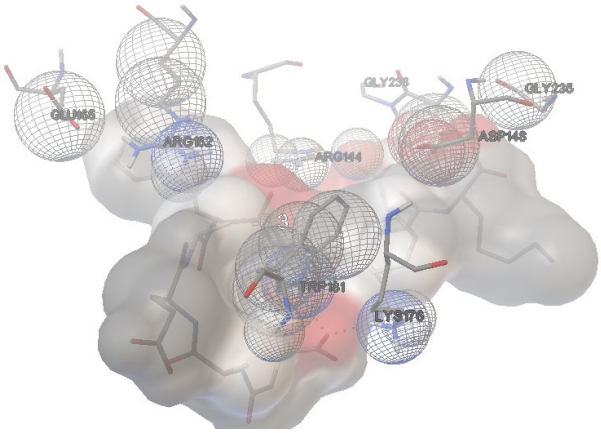

Figure 2: Autodock visualization of Galectin-3 and DAEAWFNEK peptide (Peptide 12)

Galectin-3, typically associated with cancer progression and apoptosis resistance, was found to be downregulated in BM-treated MCF-7 cells. In silico docking analyses indicated that several peptides particularly DAEAWFNEK, could potentially interact with galectin-3. These observations may be related to alterations in apoptosis-associated pathways; however, further experimental validation is required [28].

Ras suppressor protein-1, a protein involved in cell-matrix adhesion and tumor suppression, was upregulated in BM-treated MCF-7 cells. The AGFAGDDAPR peptide showed one of the most favorable docking scores with Ras suppressor protein-1 which may influence adhesion-related signalling and metastasis [29].

Peptide 10 (AGFAGDDAPR) showed a favorable docking score with Ras suppressor protein-1 (−6.8 kcal/mol), and predicted to interact with residues such as HIS49, ASN69, PHE71, and HIS186 (Figure 3).

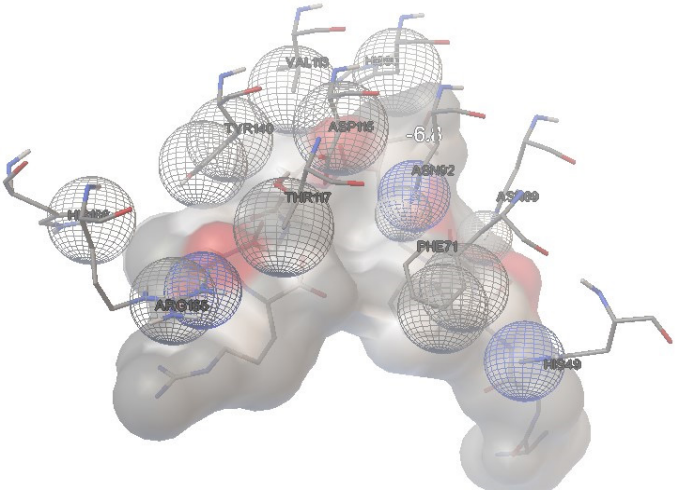

Figure 3: Autodock visualization of Ras suppressor protein-1 and AGFAGDDAPR (Peptide 10).

Mcl-1, an anti-apoptotic protein from the Bcl-2 family, was downregulated in BM-treated MCF-7 cells. Its inhibition has been associated with suppressed tumor growth and enhanced apoptosis in breast cancer [30, 31].

LAADDFR (Peptide 11) (−8.5 kcal/mol) showed one of the most favorable binding affinities toward Mcl-1 and was predicted to interact with residues ARG130, GLN139, and ARG300 (Figure 4).

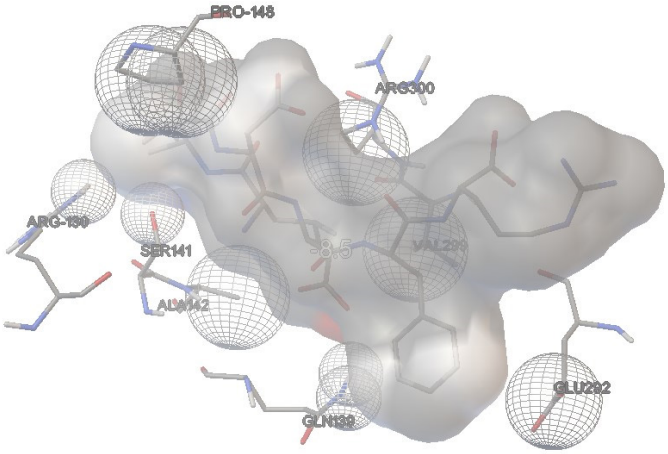

Figure 4: Autodock visualization of Mcl-1 and LAADDFR (Peptide 11)

AIF-1 expression was found to be upregulated in BM-treated MCF-7 cells following peptide treatment. DAEAWFNEK (Peptide 12) demonstrated the most favorable docking score with AIF-1 (−9.1 kcal/mol), and was predicted to interact with residues including ARG172, PHE284, and LEU497 (Figure 5).

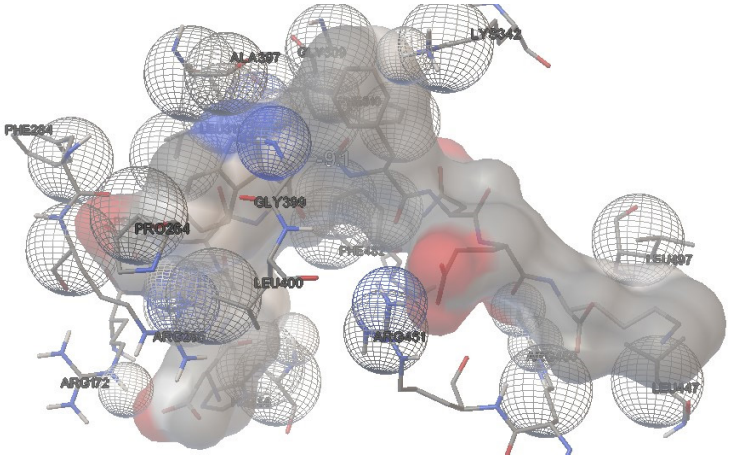

Figure 5: Autodock visualization of AIF-1 and DAEAWFNEK (Peptide 12)

In silico docking analysis revealed favorable docking score between AIF-1 and the peptide 12 (DAEAWFNEK), suggesting potential interactions **with the lowest docking score.** Since AIF-1 is known to induce caspase-

independent cell death [32], this *in silico* observation may be relevant to the apoptosis-related changes observed in BM-treated MCF-7 cells; however, no direct functional inference can be drawn without further experimental validation.

CONCLUSION

Docking analyses indicated that the peptides AGFAGDDAPR (peptide 10), LAADDFR (peptide 11), and DAEAWFNEK (peptide 12) exhibited favorable docking scores with several regulatory proteins and may influence the apoptotic regulation and cancer cell survival in MCF-7 cells. This study highlights the potential of combining enzymatic hydrolysis, proteomic profiling, and computational analyses to identify bioactive peptides that may be relevant to anticancer related pathways, providing a basis for the development of novel peptide-based therapeutic strategies.

EXPERIMENTAL SECTION

Breast Milk Collection

Human BM collection was approved by the Marmara University School of Medicine Ethics Committee (Approval no: 09.2019.893, Date: 04.10.2019). Eight volunteer mothers signed informed consent before donation. Samples were expressed via pump, pooled, and stored at −80 °C until use.

Gastrointestinal Digestion of BM

The simulated *in vitro* gastrointestinal digestion was performed by the method of Brodkorb et al. [33]. Simulated digestion fluids were prepared for the stomach and intestinal stages by the method of Minekus et al. [34]. Before digestion, milk was skimmed by centrifugation at 5000xg for 15 min at 4º C.

In oral stage, BM was mixed with equal volume of simulated salivary fluid (pH 7.0) and incubated at 37 ºC for 2 min.

In gastric stage, oral mixture was mixed with simulated gastric fluid. pH was adjusted to 3.0 and then 150 mg/mL pepsin was added to the mixture and incubated at 37°C for 2 hours.

In intestinal stage, gastric chyme was treated with simulated intestinal fluid. The pH was adjusted to 7.0. Pancreatin (2mg/mL) and bile salts (2mg/mL) were added to the mixture. And incubated at 37 ºC for 2 h. Digestion was stopped by adjusting pH to 9.0.

For epithelial barrier simulation, samples were dialyzed using a 100–500 Da molecular weight cut-off (MWCO) membrane against water for 2 h, then overnight at 4 °C to remove low–molecular-weight digestion products. After dialysis, the retentate fraction containing peptides above the MWCO was collected, filtered (Whatman No.1), and freeze-dried.

LC-MS/MS Analysis of BM Peptides

The resulting hydrolysate was then processed using the FASP kit (ab270519, Germany) for sample clean up and preparation prior to LC-MS/MS analysis. Peptides were analyzed using LC-MS/MS (Thermo Scientific Q Exactive HF, UltiMate 3000 RSLC). Data analysis was carried out using Proteome Discoverer 2.4 software with the Sequest HT search algorithm [35].

In Silico Prediction of Peptide Bioactivity and Toxicity

Peptide bioactivity was predicted using PeptideRanker [36]. The PeptideRanker program ranks peptides according to their potential for bioactivity on a scale of 0 to 1. Toxicity was assessed with ToxinPred [37]. Peptides with bioactivity scores >0.5 were further analyzed using BioPep for functional classification [38]. These peptides were examined for interactions with proteins differentially expressed in MCF-7 cells.

Assessment of Antiproliferative Effects of BM hydrolysate

MCF-7 cells (ATCC HTB22) were used in this study to investigate the antiproliferative effects of BM hydrolysate. The cells were cultured in a DMEM medium supplemented with 10% FBS and 1% penicillin-streptomycin at 37 °C and 5% CO_2 atmosphere. The antiproliferative effects of BM hydrolysate were evaluated using two complementary methods: The colorimetric MTT (3-(4,5-dimethylthiazol-2-yl)-2,5-diphenyltetrazolium bromide) assay for metabolic activity assessment and the xCELLigence Real-Time Cell Assay (RTCA) (ACEA Bioscience) system for label-free, continuous monitoring of cell viability.

For the MTT assay, the cells (1×10^4 cells/well) were seeded in 96-well plates and cultured for 24 h prior to treatment. The next day, the cells were treated with different concentrations (5-100 µg/mL) of BM hydrolysate for 24 h. After incubation, 10 µL MTT solution was added, and the cells were incubated in a CO_2 incubator for 4 h. The optical density (OD) was read at 570 nm using 630 nm as reference wavelength on a multiwell plate reader (Biotech Instruments, Winooksi, VT, USA). All experiments were repeated twice, and each treatment was run in triplicate. The percentage of cell viability was calculated using the equation:

[mean (OD) of treated cells/mean OD of control cells] × 100

To evaluate the real-time antiproliferative profile of BM hydrolysate, MCF-7 cells were monitored using the xCELLigence RTCA platform. Baseline resistance was recorded by adding 100 µL of medium to 16 wells of an e-plate. Following a 24-hour pre-incubation period for cellular equilibration, cells were exposed to various concentrations of BM hydrolysate. Each treatment was performed in triple replicates, and cellular behavior was continuously monitored for 96 hours. Proliferation profiles were determined via the Cell Index (CI), reflecting changes in electrical impedance proportional to cell viability, adhesion, and density.

Proteomic Profiling of MCF-7 Cell Proteins

Cell lysates were prepared using RIPA buffer [39] and proteins were digested via FASP for LC-MS/MS analysis. The same instrumentation and software were used as for BM peptides. Proteomic alterations were analyzed to identify up-/down-regulated proteins.

In Silico *Analysis of Protein-Peptide Interactions*

In silico analysis of the biochemical pathways and the locations of the up-regulated and down-regulated proteins of MCF-7 cell lines were determined by using the Reactome software program [40].

Galectin-3 (P17931), Ras suppressor protein-1 (Q15404), Mcl-1 (Q07820), and AIF-1 (O95831) were selected based on their relevance to apoptosis, metastasis, and cell differentiation. Their 3D structures (PDB IDs: 1A3K, 7D2S_A, 8G3S, 4LII) were prepared in Maestro 13.7 (Schrödinger Release 2023-4: Maestro, Schrödinger, LLC, New York, NY, 2023).

Docking studies were performed using HPepDock (http://huanglab.phys.hust.edu.cn/hpepedock/), a program that evaluates protein-peptide interactions and validated with AutoDock Vina 1.1.2 [41]. The docking result was visualized by AutoDock Tools (version 1.5.6). The binding modes with the lowest binding free energy and the most cluster members were chosen for the optimum docking conformation.

Statistical Analysis

Data generated in this study were presented as mean ± standard deviation (SD). Data were analyzed using one-way analysis of variance (ANOVA) followed by Tukey's multiple comparison test. Differences were considered statistically significant at $*p<0.05$ and $***p<0.001$. For cell culture experiments, at least six replicate experiments were carried out. Statistical analyses were conducted using GraphPad Prism 5.0 software (GraphPad Software, San Diego, CA, USA).

ACKNOWLEDGMENTS

This study was financially supported by TUBITAK (Project ID:321S097) and Marmara University Scientific Research Project Department (Project ID: TDK-2021-10306).

REFERENCES

1. Feng Y., Spezia M., Huang S., Yuan C., Zeng Z., Zhang L., Ji X., Liu W., Huang B., Luo W., et al.; *Genes Dis*, **2018**, *5*, 77-106.
2. Francis N., Borniger J.C.; *Trends Neurosci*, **2021**, *44*, 903-14.
3. Tufail M., Cui J., Wu C.; *Am J Cancer Res*, **2022**, *12*, 2920-49.
4. Davoodi H., Esmaeili S., Mortazavian A.; *Compr Rev Food Sci Food Saf*, **2013**, *12*, 249-64.
5. Kim K.-U., Kim W.-H., Jeong C.H., Yi D.Y., Min H.; *Int J Mol Sci*, **2020**, *21*, 7327.
6. Krishnankutty R., Iskandarani A., Therachiyil L., Uddin S., Azizi F., Kulinski M., Bhat A.A., Mohammad R.M.; *Asian Pac J Cancer Prev* **2018**, *19*, 3501.
7. Garner K.E., Hull N.J., Sims A.H., Lamb R., Clarke R.B.; *J Mammary Gland Biol Neoplasia*, **2019**, *24*, 245-56.
8. Wohlfromm F., Richter M., Otrin L., Seyrek K., Vidaković-Koch T., Kuligina E., Richter V., Koval O., Lavrik I.N.; *Front Cell Dev Biol*, **2021**, *8*, 617762.
9. Svanborg C., Agerstam H., Aronson A., Bjerkvig R., Düringer C., Fischer W., Gustafsson L., Hallgren O., Leijonhuvud I., Linse S., et al.; *Adv Cancer Res*, **2003**, *88*, 1-29.
10. Marqus S., Pirogova E., Piva T.J.; *J Biomed Sci*, **2017**, *24*, 1-15.
11. Meisel H., Schlimme E.; *Trends Food Sci Technol*, **1990**, *1*, 41-3.
12. Wang L., Dong C., Li X., Han W., Su X.; *Oncol Rep*, **2017**, *38*, 637-51.
13. Ballard O., Morrow A.L.; *Pediatr Clin*, **2013**, *60*, 49-74.
14. Liao Y., Alvarado R., Phinney B., Lönnerdal B.; *J Proteome Res*, **2011**, *10*, 5409-15.
15. Blaurock N., Schmerler D., Hünniger K., Kurzai O., Ludewig K., Baier M., Brunkhorst F.M., Imhof D., Kiehntopf M.; *Mediators Inflamm*, **2016**, *2016*.
16. Porta A., Petrone A.M., Morello S., Granata I., Rizzo F., Memoli D., Weisz A., Maresca B.; *Cell Microbiol*, **2017**, *19*, e12645.
17. Dabarera M.C., Athiththan L.V., Perera R.P.; *Ayuverda*, **2015**, *36*, 214.
18. Shiratsuchi E., Ura M., Nakaba M., Maeda I., Okamoto K.; *J Peptide Sci*, **2010**, *16*, 652-8.
19. Zhou J., Yang X., Zhang W., Wang J., Wei C., Gu F., Lei T., Qin Y.; *Anticancer Agents Med Chem*, **2017**, *17*, 635-43.
20. Kongcharoen A., Poolex W., Wichai T., Boonsombat R.; *Biotechnol Lett*, **2016**, *38*, 1195-201.
21. Zhang Y., Wang C., Zhang W., Li X.; *Biomater Transl*, **2023**, *4*, 5-17.

22. Yigitoglu B., Uctepe E., Yigitoglu R., Gunduz E., Gunduz M.; *Concise Rev Mol Pathol Breast Cancer*, **2015**, *175*.
23. Fujii Y.R.; *Med One*, **2019**, *4*, e190023.
24. Cortesi M., Liverani C., Mercatali L., Ibrahim T., Giordano E.; *Sci Rep*, **2020**, *10*, 12976.
25. Udenigwe C.C., Aluko R.E.; *Journal of food science*, **2012**, *77*, R11-R24.
26. Hartmann R., Meisel H.; *Current opinion in biotechnology*, **2007**, *18*, 163-9.
27. Wang W.; *International journal of pharmaceutics*, **2005**, *289*, 1-30.
28. Zhang H., Liang X., Duan C., Liu C., Zhao Z.; *PLoS One*, **2014**, *9*, e103482.
29. Gkretsi V., Louca M., Stylianou A., Minadakis G., Spyrou G.M., Stylianopoulos T.; *Int J Mol Sci*, **2019**, *20*, 163.
30. Campbell K.J., Dhayade S., Ferrari N., Sims A.H., Johnson E., Mason S.M., Dickson A., Ryan K.M., Kalna G., Edwards J.; *Cell Death Dis*, **2018**, *9*, 19.
31. Young A.I., Law A.M., Castillo L., Chong S., Cullen H.D., Koehler M., Herzog S., Brummer T., Lee E.F., Fairlie W.D.; *Breast Cancer Res*, **2016**, *18*, 1-15.
32. Kim E.-A., Jang J.-H., Lee Y.-H., Sung E.-G., Song I.-H., Kim J.-Y., Kim S., Sohn H.-Y., Lee T.-J.; *Apoptosis*, **2014**, *19*, 1165-75.
33. Brodkorb A., Egger L., Alminger M., Alvito P., Assunção R., Ballance S., Bohn T., Bourlieu-Lacanal C., Boutrou R., Carrière F.; *Nat Protoc*, **2019**, *14*, 991-1014.
34. Minekus M., Alminger M., Alvito P., Ballance S., Bohn T., Bourlieu C., Carrière F., Boutrou R., Corredig M., Dupont D.; *Food Funct*, **2014**, *5*, 1113-24.
35. Eng J.K., McCormack A.L., Yates J.R.; *J Am Soc Mass Spectrom*, **1994**, *5*, 976-89.
36. Mooney C., Haslam N.J., Pollastri G., Shields D.C.; *Plos One*, **2012**, *7*, e45012.
37. Gupta S., Kapoor P., Chaudhary K., Gautam A., Kumar R., Raghava G.P.S.; *Plos One*, **2013**, *8*, e73957.
38. Minkiewicz, Iwaniak, Darewicz; *Int J Mol Sci*, **2019**, *20*, 5978.
39. Wiśniewski J.R., Zougman A., Nagaraj N., Mann M.; *Nat Methods*, **2009**, *6*, 359-62.
40. Gillespie M., Jassal B., Stephan R., Milacic M., Rothfels K., Senff-Ribeiro A., Griss J., Sevilla C., Matthews L., Gong C., et al.; *Nucleic Acids Res*, **2021**, *50*, D687-D92.
41. Eberhardt J., Santos-Martins D., Tillack A.F., Forli S.; *J Chem Inf Mode*, **2021**, *61*, 3891-8.

STUDIA UBB CHEMIA, LXXI, 1, 2026 (p. 223-244)
(RECOMMENDED CITATION)
DOI:10.24193/subbchem.2026.1.14

THREE-WAY DATA ANALYSIS OF COPPER-PARACETAMOL COMPLEX FORMATION FOR THE QUANTIFICATION OF PARACETAMOL IN PHARMACEUTICAL MATRICES

İbrahim TEĞİN[a], Gurbet CANPOLAT[a], Zehra Ceren ERTEKİN[b], Nihat GÜÇLÜ[a], Erdal DİNÇ[b,*]

ABSTRACT. We present a chemometric strategy to study complex formation reactions using parallel factor analysis (PARAFAC) of three-way spectral data.UV spectra of PAR, $CuSO_4$, and their complex were recorded at five different pH levels. Reorganizing the spectra produced a wavelength × sample × pH array, to be decomposed by PARAFAC into spectral, pH, and concentration modes. This strategy achieved the resolution of contributing species and their profiles without requiring advanced instrumentation. PAR quantification was achieved using the relative concentration mode of the PARAFAC model. The calibration curve showed linearity in the range of $1.10x10^{-5}$ M-$8.90x10^{-5}$M, and standard-addition validation yielded recoveries of 96.70-99.00% for tablets and 96.48-99.67% for syrups. Crucially, this strategy achieved accurate quantification of PAR in syrup formulation even with uncalibrated interferences in syrup matrix. The application of PARAFAC to the pH-dependent UV dataset acquired according to Job's method revealed a 1:1 stoichiometric ratio between PAR and Cu^{2+}. Overall, the results demonstrate that three-way decomposition of pH-resolved UV measurements offers a practical and reliable alternative for studying Cu-PAR complex formation and quantifying PAR in different pharmaceutical matrices. To the best of our knowledge, this is the first PARAFAC application to study PAR-Cu complex formation for accurate quantification of PAR in the presence of uncalibrated interferences.

Keywords: *chemometrics, paracetamol, spectral analysis, ultraviolet spectrophotometry*

[a] *Siirt University, Faculty of Arts and Sciences, Department of Chemistry, 56100, Siirt, Türkiye.*
[b] *Ankara University, Faculty of Pharmacy, Department of Analytical Chemistry, 06560 Ankara, Türkiye.*
[*] *Corresponding author: dinc@ankara.edu.tr*

INTRODUCTION

Paracetamol (PAR), chemically named N-acetyl-p-aminophenol, consists of a phenol ring substituted with an amide group at the para position, forming a conjugated system (Figure 1). It is widely recognized as an effective analgesic and antipyretic for both adults and children. PAR is the principal active pharmaceutical ingredient in numerous over-the-counter and prescription medications, either alone or in combination with other active substances [1]. Although paracetamol is generally safe at therapeutic doses, intentional or accidental overdoses can lead to severe hepatotoxicity and other adverse effects. Therefore, its accurate determination in pharmaceutical formulations for quality control and in biological fluids for overdose monitoring is of critical importance [2].

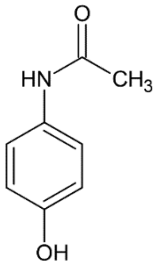

Figure 1. Molecular structure of paracetamol

There is an increasing interest in metal-drug complexes due to their potential biological, pharmaceutical, and catalytic applications. Several studies have reported the ability of PAR to form complexes with metal ions through coordination involving the hydroxyl and amide functional groups [3-6]. It has been shown that PAR exhibits affinity for transition metals via the lone pairs on the carbonyl oxygen, hydroxyl oxygen, or amide nitrogen atoms [7]. Recently, Al-Abbasi and co-workers characterized a Cu-PAR complex using potentiometric, conductometric, spectrophotometric, and computational techniques [8, 9]. In the present study, we aim to investigate the spectroscopic characteristics of the Cu-PAR complex using a chemometric approach and to exploit three-way data analysis for the quantification of PAR in different pharmaceutical formulations.

Chromatographic techniques such as high-performance liquid chromatography (HPLC) have been extensively employed for the analysis of complex samples across a wide range of disciplines including analytical chemistry, pharmaceuticals, medicine, food, agriculture, and environmental sciences. Numerous studies have reported the determination of paracetamol

using HPLC [10-13] and high-performance thin-layer chromatography (HPTLC) [13-15]. However, chromatographic techniques often require extensive method development for optimal separation, time-consuming optimization processes, dependence on organic solvents, and the use of costly and sophisticated instrumentation.

In contrast, ultraviolet-visible (UV-Vis) spectrophotometry is widely favored due to its simplicity, rapidity, cost-effectiveness, and minimal sample preparation requirements. UV-Vis methods have been commonly used to quantify PAR in relatively simple pharmaceutical matrices [16-20]. However, traditional UV-Vis techniques may not suffice when dealing with complex mixtures containing multiple active and inactive components due to spectral overlap. Thus, alternative analytical strategies are needed to address these challenges in a cost-effective and efficient manner.

To overcome the limitations of classical analytical methods, multi-way data analysis offers a promising alternative for identifying spectral features, monitoring reaction kinetics, and evaluating complex formation between drugs and metal ions. In chemometrics, multi-way analysis techniques have gained considerable attraction for addressing complex analytical challenges. Spectrophotometric measurements inherently generate multidimensional data without the need for sophisticated or expensive instrumentation. The spectral characteristics of metal complexes vary depending on analyte concentration and solution pH. These data can be structured as three-way arrays, encompassing wavelength, pH, and concentration dimensions, making them ideally suited for multi-way analysis. Integrating such methods with studies of metal-drug interactions can provide valuable insights into system behavior, chelation mechanisms, and ligand specificity, with potential implications for chelation therapy and drug development [21].

Among multi-way techniques, parallel factor analysis (PARAFAC) has emerged as a powerful tool for resolving overlapping signals and extracting meaningful information from complex datasets. The theoretical framework of PARAFAC has been well-documented [22-24] and its applications in spectroscopic data analysis include multicomponent quantification [25-29], spectral characterization [29-34], and kinetics, [35-38] and complexation studies [39].

In this study, we developed a novel analytical strategy based on three-way UV spectral data analysis to investigate Cu-PAR complex formation and to quantify PAR in commercial tablet and syrup formulations. Calibration, validation, and commercial sample solutions containing varying concentrations of PAR and $CuSO_4$ at different pH levels were prepared. Cu^{2+} precipitation as $Cu(OH)_2$ in alkaline conditions was avoided by using a methanol-aqueous buffer mixture. Under these co-solvent conditions, all solutions remained

clear up to pH 10, with no turbidity. Metal-ligand complexation was facilitated via sonication followed by vortex mixing. The resulting UV absorbance spectra were assembled into a three-way data array and decomposed using PARAFAC to resolve the individual spectral, concentration, and pH profiles of PAR, $CuSO_4$, and the Cu-PAR complex. The validity of the proposed strategy was confirmed using independent validation samples, yielding satisfactory recovery results. Application of the PARAFAC model to real pharmaceutical samples demonstrated accurate and reliable quantification of PAR in both tablet and syrup formulations.

RESULTS AND DISCUSSION

The proposed spectrophotometric method for the determination of paracetamol is based on its complexation with copper(II), followed by spectral three-way analysis, without the need for extraction or chromatographic separation. The application of the PARAFAC model as a three-way data analysis tool to the pH-dependent absorbance dataset provides an effective strategy for resolving spectral interferences. This approach enables accurate quantification of paracetamol in pharmaceutical formulations, offering a low-cost, rapid, and reliable alternative to conventional analytical techniques.

Construction of spectral datasets

The proposed PARAFAC calibration method for monitoring complex formation and quantifying paracetamol (PAR) in pharmaceutical formulations began with the construction of a calibration matrix composed of PAR and $CuSO_4$. As previously described in the Experimental section, the calibration set included 40 different sample solutions, combining five pH conditions with eight concentration levels. The UV spectrum of a solution containing a metal ion, a ligand, and their corresponding coordination complex yields a vector of absorbance values as a function of wavelength. When spectra of the analyte at varying concentrations are recorded, they can be arranged into a two-dimensional matrix. Because complex formation reactions are pH-dependent, acquiring spectra at different pH values enables the generation of a three-way data array (tensor), which enhances the system's modeling capacity. Figure 2 illustrates the pH-dependent UV absorbance matrices for the calibration samples across increasing paracetamol concentrations. These matrices were organized into a three-way calibration dataset with dimensions of 231×8×5 (wavelength × concentration × pH), which served as the input for PARAFAC modeling.

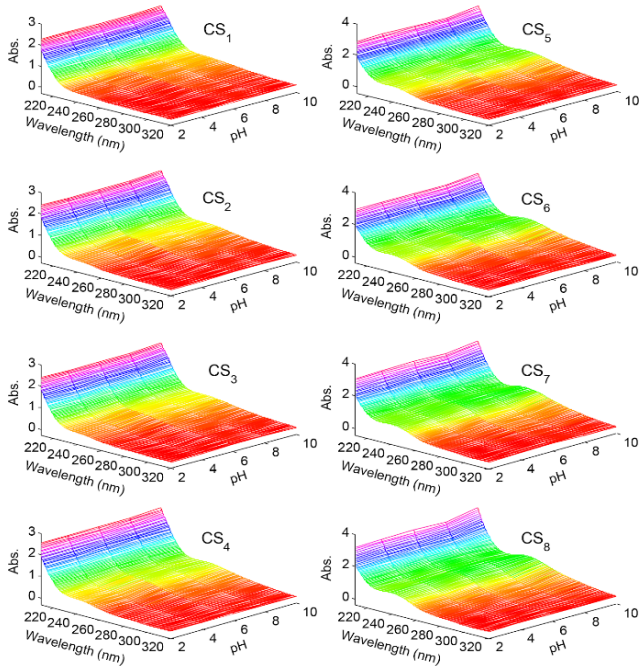

Figure 2. Three-dimensional representation of the pH-dependent UV absorbance matrices of calibration samples prepared at increasing paracetamol concentrations (8 levels) across five pH conditions. The dataset forms the basis of the calibration tensor used in PARAFAC modeling (231×8×5; wavelength×concentration×pH).

In this study, two independent datasets were constructed and analyzed using PARAFAC to quantify PAR in two types of pharmaceutical formulations: tablet and syrup formulations. Unlike tablet excipients, which were not expected to produce observable signals in the UV region, the excipients in the syrup formulations were anticipated to contribute additional spectral components and thus appear as distinct factors in the PARAFAC model. For the tablet analysis, a three-way dataset was constructed using eight calibration samples, four tablet standard addition samples, and five commercial tablet samples, at each pH conditions. These were combined into a data tensor of dimensions 231×17×5 (wavelength × sample × pH). The UV absorbance matrices corresponding to the five tablet samples at different pH conditions are shown in Figure 3a. Similarly, the syrup dataset was composed of the same eight calibration samples, four syrup standard addition samples, and five syrup samples at each pH level. This data was also structured as a tensor with dimensions 231×17×5, as shown in Figure 3b. These tensors enabled the simultaneous decomposition of spectral, pH, and sample modes, facilitating selective quantification of paracetamol even in the presence of complex excipient backgrounds.

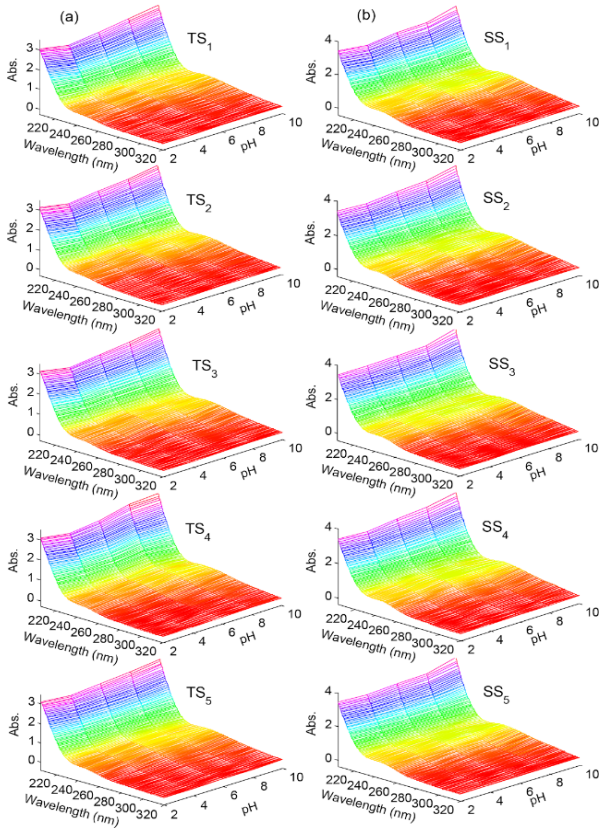

Figure 3. pH-dependent UV absorbance matrices of (a) tablet samples (TS_1-TS_5) and (b) syrup samples (SS_1-SS_5) recorded at five different pH levels. These matrices were used to construct the sample mode of the three-way data tensors for PARAFAC analysis.

Application of PARAFAC model

The three-way dataset constructed from the tablet analysis was subjected to PARAFAC modeling using the alternating least squares (ALS) algorithm. A three-component model was selected based on explained variance and residual analysis, and non-negativity constraints were applied to all modes to ensure chemical interpretability. The decomposition of the tensor yielded three distinct profiles:

- the relative spectral profile across the wavelength dimension (Figure 4a),
- the relative pH distribution profile (Figure 4b), and
- the relative concentration profile across the sample dimension (Figure 4c).

These profiles corresponded to three chemical species: paracetamol (PAR), $CuSO_4$, and the Cu-PAR complex. As shown in Figure 4a, the spectral

profile of PAR estimated by the model closely aligned with the experimental spectrum of pure PAR (represented by a dashed line), confirming the validity of the model. In Figure 4b, the Cu-PAR complex signal was found to intensify with increasing pH, indicating that complex formation is favored under alkaline conditions. The relative concentrations of the three species across samples, shown in Figure 4c, were used for the quantitative determination of PAR in tablet samples.

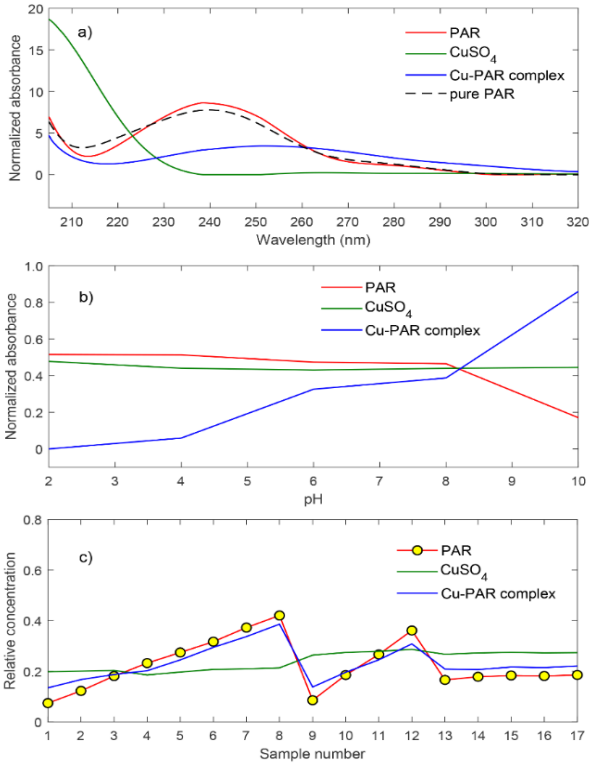

Figure 4. PARAFAC model results (three-component solution) for the tablet dataset: (a) Relative spectral profiles of PAR, $CuSO_4$, and Cu-PAR complex across the 205-320 nm range; the dashed line shows the experimental spectrum of pure PAR for comparison. (b) pH-dependent absorbance contributions of each component (pH 2-10) (c) Relative concentration profiles of the three species across 17 samples (8 calibration, 4 standard addition, and 5 tablet samples).

In contrast, the three-way dataset obtained from the syrup analysis required a four-component PARAFAC model to adequately explain the variance and capture additional sample complexity. Non-negativity constraints were also

applied. Figure 5a-5c illustrate the decomposed profiles from this four-component model. In addition to PAR, $CuSO_4$, and the Cu-PAR complex, a fourth profile was extracted corresponding to syrup excipients, which was not observed in the tablet dataset.

This additional component is a clear manifestation of the second-order advantage of the PARAFAC model, enabling the isolation and resolution of uncalibrated interferents without prior standardization. The presence of this excipient profile did not hinder the accurate resolution of PAR, demonstrating the model's robustness and selectivity. Figure 5c shows the relative concentration profiles of all four species across the syrup samples, from which the PAR concentrations were quantitatively predicted.

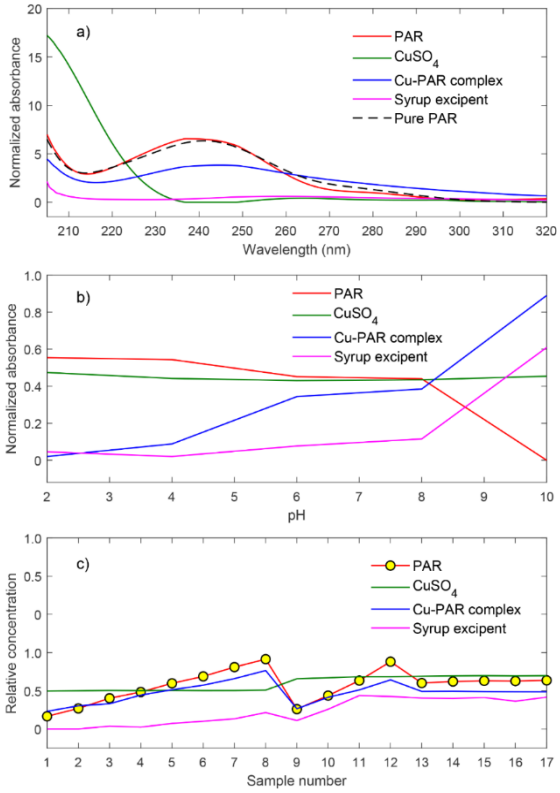

Figure 5. PARAFAC model results (four-component solution) for the syrup dataset: (a) Estimated spectral profiles of PAR, $CuSO_4$, Cu-PAR complex, and syrup excipient. (b) Corresponding pH profiles showing signal variation across (pH 2-10) (c) Relative concentration profiles of the four species across 17 samples (8 calibration, 4 standard addition, and 5 syrup samples). The fourth component, attributed to syrup excipients, illustrates the model's ability to resolve interfering matrix effects.

For both datasets, alternating least squares (ALS) algorithm was used for PARAFAC modeling applying non-negativity constraints. While unconstrained models can sometimes reveal deeper insights into mathematical interactions, UV absorbance and concentration values of chemical species in the sample are inherently non-negative physical quantities, meaning they are impossible to have a negative value in the physical world. Hence, applying non-negativity constraints ensured physically realistic and chemically interpretable PARAFAC solutions.

To ensure solution uniqueness and avoid convergence to local minima, the PARAFAC models were initialized multiple times using different random starting points. Specifically, the tablet dataset was subjected to 172 independent initializations, while the more complex syrup dataset required 1420 initializations to ensure stable convergence. The presence of rotational ambiguity or degeneracy was assessed by evaluating the chemical interpretability of the resolved profiles. In particular, the spectral profile of paracetamol (PAR) resolved by the model (solid red line) showed close agreement with the experimentally recorded spectrum of pure PAR (dashed line). If significant rotational ambiguity were present, such precise spectral recovery would be highly unlikely.

Model parameters were optimized by systematically testing different numbers of components (two to six) guided by chemical knowledge of the system and evaluating the explained variance and residual structure. Although core consistency diagnostics are widely used for component validation, they were not relied upon in this study because matrix heterogeneity and complexation-induced non-idealities may lead to misleading core consistency values despite chemically valid solutions. The final number of components was selected based on the best compromise between model simplicity, variance explained, and chemically interpretable profiles.

For the tablet dataset, three components corresponding to paracetamol (PAR), $CuSO_4$, and the Cu-PAR complex were considered chemically meaningful. Models with three or more components were evaluated, and increasing the number of components beyond three did not yield interpretable or chemically relevant profiles. The explained variance reached 99.8788% for the tablet dataset using a three-component model.

For the syrup dataset, which exhibits higher matrix complexity due to excipients, a four-component model was required, achieving an explained variance of 99.9300%. In addition to matrix effects, the metal–drug complexation reaction itself further increased system complexity by introducing strongly pH-dependent and overlapping spectral contributions, which can adversely affect conventional diagnostic metrics.

PARAFAC model enabled the resolution of three chemical species (PAR, $CuSO_4$, and Cu-PAR complex) in both datasets. Unlike the tablet dataset, the syrup dataset required an additional component attributed to syrup

excipients, indicating the presence of uncalibrated interferences. Despite this added complexity, the model successfully separated the contributions of all components, allowing reliable interpretation of the identified chemical species. The validity of the resolution was confirmed by the close agreement between the spectral profile of PAR obtained by PARAFAC and the experimentally recorded spectrum of pure PAR, as shown in Figures 4 and 5.

Calibration and Quantitative Analysis Based on PARAFAC Profiles

Quantitative calibration and prediction of paracetamol (PAR) were performed using the relative concentration values obtained from the PARAFAC model. Specifically, the PAR signal extracted from the sample mode (Figure 4c for tablets, Figure 5c for syrup) was used as the dependent variable in a least-squares regression against the nominal concentrations of PAR in the calibration set (first 8 samples).

To evaluate the validity of the proposed method, the linearity of the calibration model was assessed. A highly linear regression equation was obtained with a correlation coefficient (R) of 0.9994, confirming the strong agreement between the actual and estimated values. The independent variable was the known PAR concentrations ranging from 1.67 µg/mL to 13.44 µg/mL, and the dependent variable was the corresponding PARAFAC-derived relative concentration values.

The calibration parameters, including the slope, intercept, and correlation coefficient of the regression equation, along with their associated standard errors, are summarized in Table 1. The computed values of limit of detection (LOD) and limit of quantitation (LOQ) were also given in the same table. They were calculated by the equations $LOD = (3 \times SD)/m$ and $LOD = (10 \times SD)/m$, where SD represents the standard deviation of the intercept and m is the slope of the calibration curve.

These results validate the robustness and accuracy of the PARAFAC-assisted quantification strategy and confirm its suitability for routine application in pharmaceutical analysis.

Table 1. Linear regression analysis of tablet and syrup formulation

Parameter	Tablet	Syrup
slope	0.0291	0.0252
intercept	0.0305	0.0258
correlation coefficient	0.9994	0.9992
standard deviation of slope	4.11×10^{-4}	4.13×10^{-4}
standard deviation of intercept	3.49×10^{-3}	3.50×10^{-3}
standard deviation of correlation coefficient	5.76×10^{-3}	6.68×10^{-3}
limit of detection (µg/mL)	0.36	0.42
limit of quantitation (µg/mL)	1.20	1.39

Calibration and prediction of the analyte were based on the relative concentration values of PAR in the corresponding profile after PARAFAC decomposition. A least-squares regression was performed with the estimated relative concentration values and the nominal concentration values from the calibration set (first 8 samples in Figure 4c and 5c).

Analysis of Standard Addition Samples

In the next step of validation, the PARAFAC model was applied to the analysis of standard addition samples in order to evaluate the effect of excipients from both tablet and syrup formulations on the accuracy of drug quantification. As detailed in the Experimental section, standard addition samples were prepared at three concentration levels by spiking known amounts of paracetamol (3.49 µg/mL, 6.99 µg/mL, and 10.48 µg/mL) into fixed volumes of tablet or syrup samples, containing approximately 1.68 and 2.67 µg/mL of paracetamol for tablet and syrup, respectively.

In this validation approach, the prediction of total paracetamol concentration in standard addition samples (samples 9-13 in Figure 4c and 5c) was carried out using the relative concentration values obtained from PARAFAC decomposition and the calibration equations derived in Table 1. The added recovery values were calculated by subtracting the estimated PAR concentration of the non-spiked commercial sample (sample 9 in Figure 4c and 5c) from the total PAR concentration of the spiked samples at the three respective levels (samples 10-12 in Figure 4c and 5c). The results of these analyses are summarized in Table 2.

Table 2. Analysis results and recovery values of standard addition samples

PFT*	Spiked sample no	Added (µg/mL)	Found (µg/mL)	Added recovery (%)
tablet	1	3.49	3.43	98.3
	2	6.99	6.92	99.0
	3	10.48	10.13	96.7
syrup	1	3.49	3.48	99.67
	2	6.99	6.95	99.50
	3	10.48	10.11	96.48

*PFT: Pharmaceutical form type

The data in Table 2 show that excipients in both tablet and syrup formulations did not affect the accuracy of paracetamol determination. Although the tablet formulation did not exhibit significant spectral interference, the syrup formulation presented a noticeable interference signal due to the presence of excipients. Nevertheless, the PARAFAC model successfully resolved the contributions of all components, including the interfering excipient illustrated as the pink line in Figure 7, across the spectral, pH, and concentration dimensions. As the contribution of syrup excipients was extracted efficiently

by PARAFAC, the relative concentration profile of PAR in Figure 7 was free from interferences. This ability to correctly quantify analytes in the presence of uncalibrated and unknown interfering species is a characteristic of the second-order advantage. It allows for accurate, selective estimation of the analyte without requiring any preliminary separation or extraction steps.

Furthermore, the added recovery values for all standard addition levels in both formulations were found to be close to 100%, confirming the selectivity and reliability of the developed method. The strong agreement between predicted and actual concentrations, further validates the robustness of the method. These results demonstrate that the proposed PARAFAC-based spectrophotometric strategy is highly effective for the analysis of paracetamol in complex pharmaceutical matrices.

Quantitative Estimation of Paracetamol in Commercial Samples

The proposed PARAFAC-based spectrophotometric methods were applied to the determination of paracetamol (PAR) in commercial tablet and syrup formulations to evaluate their practical applicability. Sample preparation procedures for both dosage forms were performed as described in Section 2.3.5 (tablet) and 2.3.6 (syrup). The corresponding pH-dependent UV spectral datasets, recorded using a UV-Vis spectrophotometer, are shown in Figure 3a and Figure 3b.

PARAFAC decomposition of the datasets for both formulations was carried out as previously described in Section 3.2. Application of the PARAFAC Model. The estimated relative concentration values of PAR from the PARAFAC concentration profiles for five commercial samples (samples #13-17 in Figure 4c and 5c, for tablet and syrup, respectively) were used to compute the predicted concentrations using the calibration equations (see Table 1).

The calculated concentrations of paracetamol in the analyzed pharmaceutical products are listed in Table 3, along with the corresponding recovery values, which were calculated based on the label claims of the respective products.

Table 3. Amount of paracetamol for tablet and syrup samples obtained by PARAFAC model

Sample No.	Tablet assay (mg/tablet)	Recovery (%)	Syrup assay (mg/5mL)	Recovery (%)
1	492.8	98.56	127.5	106.25
2	507.8	101.56	127.4	106.17
3	525.2	105.04	128.3	106.92
4	507.8	101.56	126.3	105.25
5	506.2	101.24	128.9	107.42
Average	507.96	101.59	127.68	106.4
Standard deviation	11.5	2.30	1.0	0.82
Relative standard deviation	2.27	2.27	0.77	0.77

The results demonstrated excellent agreement with the expected values. Specifically, the mean recovery was found to be 101.59% for tablets and 106.4% for syrups, with corresponding relative standard deviations (RSD) of 2.27% and 0.77%, respectively (Table 3). Although the mean recovery of commercial syrup samples (106.4%) is slightly above the commonly accepted range for pharmaceutical assays (approximately 95-105%), this deviation may arise from sample preparation and dilution steps (e.g., minor pipetting errors) and/or matrix effects associated with liquid formulations containing excipients. The standard-addition recoveries (96.48-99.67%) confirm that the method is accurate and does not demonstrate a positive bias. These findings confirm the accuracy and precision of the developed method for the routine quantification of paracetamol in commercial formulations, including those containing potentially interfering excipients.

Multi-way analysis techniques such as PARAFAC provide a powerful strategy for investigating metal-drug interactions by enabling the simultaneous resolution of spectral, environmental (e.g., pH), and concentration-dependent variations. In the context of chelation therapy, this capability allows the direct extraction of the spectral signature of the metal-drug complex from overlapping contributions of the free metal ion and ligand, without requiring physical separation. Such information is critical for understanding complex stability, formation conditions, and environmental sensitivity (e.g., pH dependence, which are key factors in evaluating chelation efficiency and selectivity in situ.

In syrup samples, the total contributions of all individual excipients were modelled as a single additional component. On the other hand, no extra component was required for the tablet dataset, indicating that tablet excipients did not contribute significantly to the spectral, pH, or concentration modes. The explained variance reached its maximum with three components for the tablet dataset, while a four-component model was required for the syrup dataset. The presence of fourth component in the syrup dataset demonstrates the increased complexity of the formulation and the necessity of three-way analysis in spectroscopy for selectively resolving the drug and drug-metal complex in such matrices. The successful extraction of this excipient-related profile indicates that future studies can reliably analyze syrup and similar liquid formulations even without prior knowledge of the specific additives in the formulation.

Since the proposed method was shown to resolve the uncalibrated interferences in real samples, it may be extended to different types of pharmaceutical formulations. However, if a matrix component exhibits spectral behavior that is fully collinear with the analyte across all modes, mathematical resolution would not be feasible. Other limitations might occur depending on the formulation. For example, semi-solid formulations such as creams and

ointments would likely require an extraction step to create a clear solution suitable for UV spectrophotometric measurements, as turbidity and light scattering effects cause non-linear behavior that violates the trilinear model assumption. On the other hand, the application of PARAFAC to nasal sprays and eye drops formulations would be similar to application on syrup formulation described in this work. Nevertheless, the presence of excipients with strong and pH-dependent UV absorbance may still hinder accurate component resolution.

Application of the PARAFAC Model to the Job Plot Method

To determine the stoichiometry of Cu-PAR complex, the Job's method of continuous variation was applied. Based on the spectral behavior observed within the pH range of 2-10, it was assumed that only one type of complex species is predominantly formed, making the application of Job's method appropriate under these conditions.

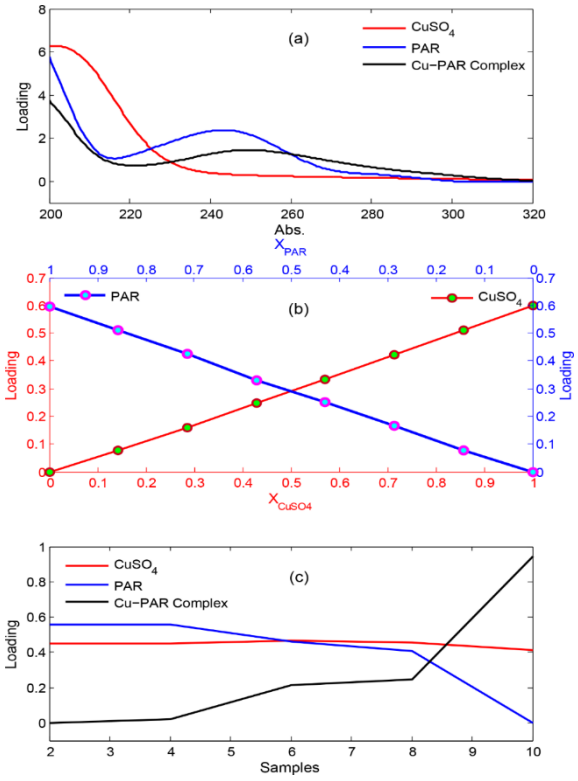

Figure 6. (a) Spectral profile, (b) mole fraction profile, and (c) relative concentration profile obtained by PARAFAC decomposition using Job's plot method

Eight solutions containing Cu(II) and PAR were prepared with a constant total molar amount of 7.0×10^{-4} mmol, but varying molar fractions of the two components. The pH of each solution was adjusted using Britton-Robinson (BR) buffer to fall within the 2-10 range. The UV absorption spectra of the resulting mixtures were recorded over the 200-320 nm range.

The spectral dataset was arranged into a three-way tensor and subjected to PARAFAC decomposition. The resulting component profiles, including the mole fraction contributions, are shown in Figure 6. As illustrated in Figure 6b, the Job plot obtained from the PARAFAC concentration mode exhibits a clear maximum at a molar fraction of 0.5, indicating a 1:1 stoichiometric ratio between PAR and Cu(II) ions as reported in the literature [8, 9].

In addition to the PARAFAC-based interpretation, the Job method was also applied using the classical univariate approach. For this purpose, absorbance values at the characteristic wavelength were recorded for a series of solutions with constant total molar concentration of Cu(II) and PAR but varying molar fractions. The corresponding Job plot is shown in Figure 7, where absorbance is plotted as a function of the molar fraction of paracetamol.

As seen in Figure 7, the plot exhibits a clear maximum at a molar fraction of 0.5, which corresponds to a 1:1 stoichiometric ratio between PAR and Cu(II). This result is fully consistent with the PARAFAC-based Job plot analysis, confirming that one paracetamol molecule coordinates with one copper ion to form the Cu-PAR complex. The agreement between the classical and multiway approaches provides additional confidence in the validity of the complexation model proposed in this study.

The formation of a single dominant complex over pH 2-10 was assumed in this work. The assumption was justified by symmetrical Job's plot and the analysis of the residuals. The Job's plots (both classical and PARAFAC-based) exhibit a clear, symmetric maximum at exactly 0.5 molar fraction. The presence of higher-order species (e.g., 1:2 or 2:1) would typically cause a shift in the peak position or asymmetry in the plot. In addition, the tablet and syrup datasets were adequately described by three- and four-component PARAFAC models, respectively. If significant higher-order species were present, high residuals would be observed, or inclusion of an additional component would be required to model the data. Furthermore, to prevent the formation of hydroxo complexes such as $Cu(OH)_2$, a mixed methanol–aqueous buffer system was employed. Under these conditions, solutions remained optically clear even at pH 10, supporting the negligible presence of insoluble hydroxo species and the assumption of a single dominant Cu-PAR complex.

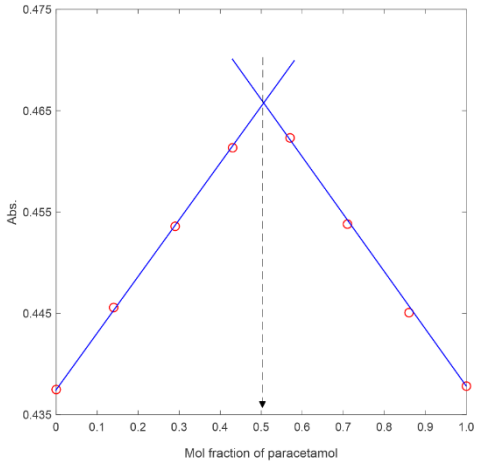

Figure 7. Classical Job plot for the Cu-PAR system.

CONCLUSIONS

In this study, a chemometric method based on three-way analysis of pH-dependent UV absorbance data was developed and successfully applied for the quantification of paracetamol in commercial tablet and syrup formulations. The approach combines simple UV measurements with PARAFAC decomposition of wavelength × sample × pH tensors, enabling resolution of overlapping signals and reliable estimation of PAR concentrations without chromatographic separation. The method demonstrated high accuracy with recovery rates between 96.48% and 99.67% in standard addition validation. LOD values 0.36 µg/mL for tablets and 0.42 µg/mL for syrups were reported. While HPLC can often achieve lower LODs, the sensitivity in this work is sufficient for pharmaceutical quality control where PAR is a major active ingredient. The main advantages of the PARAFAC approach over traditional chromatography are its efficiency and green profile while proving sufficient sensitivity. The second-order advantage, which enables accurate quantification even with uncalibrated interferences, provide mathematical separation of components in the sample. Whereas traditional chromatographic methods require extensive method development as well as more time, effort, and consumables to physically separate components to achieve the accurate quantification. The method exhibited excellent selectivity for both solid and liquid dosage forms. In tablet samples, no excipient-related component was detected in the PARAFAC model, confirming that the excipients do not significantly contribute to the studied spectral region. In syrup samples, an additional factor attributable to excipients or additives was clearly identified, yet the model was still able to selectively isolate the PAR signal and

accurately quantify the drug. The ability to separate the Cu-PAR complex absorbance from excipient-related signals illustrates the selectivity and second-order advantage of the three-way PARAFAC approach.

Furthermore, the stoichiometry of the Cu-PAR complex was investigated using both PARAFAC-assisted and classical Job plots, and in both cases a 1:1 complex was confirmed. The study reveals that the Cu-PAR complex signal intensifies with increasing pH, indicating that complex formation is favored under alkaline conditions. The 1:1 ratio confirmed by Job's method implies a specific binding mechanism. A plausible explanation is the involvement of the deprotonated phenolic group of paracetamol, given its higher availability in alkaline conditions, although further mechanistic studies would be required to confirm this hypothesis. This pH-dependence has practical implications for both complex stability and analytical selectivity, and it underlies the effectiveness of the second-order advantage exploited by the PARAFAC model. Overall, the proposed three-way modeling strategy provides a reliable, cost-effective, and chromatography-free alternative for the quantification of paracetamol, particularly in syrup formulations where classical UV methods often fail due to matrix interferences. Its simplicity and efficiency make it a promising tool for routine quality control in pharmaceutical analysis.

EXPERIMENTAL SECTION

Apparatus and Software

A Perkin Elmer Lambda 750 UV dual-beam spectrophotometer with a constant slit width (0.5 nm) and equipped with a 1.00 cm optical path quartz cell was used for all absorbance measurements. The scan was carried out in the range of 205 to 320 nm at 0.5 nm intervals. PARAFAC modelling performed through N-way Toolbox [40] in Matlab platform (MathWorks, MA, USA). The pH values were measured on a Mettler Toledo pH meter, with glass electrode.

Chemicals and Reagents

Paracetamol standard material was supplied from Nobel Pharmaceuticals. Copper (II) sulfate pentahydrate ($CuSO_4 \cdot 5H_2O$) (≥98%), and ACS spectrophotometric grade methanol (MeOH) were procured from Sigma-Aldrich (St. Louis, Missouri, USA). CH_3COOH, H_3BO_3, H_3PO_4, and NaOH were of analytical grade. For real sample analysis two commercial pharmaceutical formulations, Parol Tablet (produced by Atabay Kimya, Türkiye, containing 500 mg of paracetamol per tablet) and Parol Oral Suspension (produced by Atabay Kimya, Türkiye, containing 120 mg of paracetamol per 5 mL) were procured from a local pharmacy in Siirt, Türkiye.

Buffer solutions

Buffer solutions at five pH levels (2, 4, 6, 8, and 10) were prepared by adjusting a mixture of 0.04 M CH_3COOH, 0.04 M H_3BO_3 and 0.04 M H_3PO_4 with 0.1 M NaOH, while monitoring the pH value with the pH meter.

Stock solutions

PAR stock solution ($1.0x10^{-3}$ M, equivalent to 151 µg/mL) was prepared in methanol due to its limited solubility in water. $CuSO_4$ solution was prepared in ultrapure water at a concentration of $1.0x10^{-3}$ M. All stock solutions were freshly prepared and protected from light prior to use.

Experimental design for complex formation

The solution sets were designed to investigate the complexation between copper(II) sulfate ($CuSO_4$) and paracetamol (PAR) under varying pH conditions and analyte concentrations. For the preparation of sample sets, five pH levels and eight PAR concentration levels were planned. The complexation of PAR with Cu(II) was monitored by an increasing amount of PAR while $CuSO_4$ concentration, buffer concentration, and methanol: aqueous solution ratio was kept constant.

For each solution:

- 5.00 mL of the appropriate buffer solution (corresponding to pH 2-10) was first introduced into a conical polypropylene tube.
- Sequentially, 0.90 mL of $CuSO_4$ stock solution and required volume of PAR stock solution (0.00 to 0.80 mL) were added.
- Since the PAR solution was prepared in methanol, additional methanol was added to ensure that the total MeOH content in each solution was fixed at 0.80 mL.
- 0.10 mL PAR + 0.70 mL MeOH
- 0.20 mL PAR + 0.60 mL MeOH
- …
- 0.80 mL PAR + 0.00 mL MeOH
- Then, 2.30 mL of ultrapure water was added to each tube to reach a total volume of 9.0 mL.

Samples were prepared in the order of increasing pH, and each was manually shaken for 1 minute to ensure complete mixing. Immediately after mixing, UV absorption spectra were recorded over the range 205.0–320.0 nm with an increment of 0.5 nm. Each spectrum, corresponding to a vector of 231 elements was transferred to a Microsoft Excel file as a column vector, resulting in a matrix with wavelength and sample dimensions. Each pH condition was organized in a separate worksheet as the third dimension.

The precipitation of Cu^{2+} as $Cu(OH)_2$ in alkaline media was prevented by the use of a mixed medium of methanol and aqueous buffer. To ensure a constant matrix composition, Cu(II) concentration (1.0×10^{-4} M) and MeOH concentration (~8.9% *v/v*) were kept constant across all solutions within the pH range of 2-10. The fixed methanol content was sufficient to dissolve paracetamol in all solutions without significantly affecting pH or Cu^{2+} speciation. Under these controlled co-solvent conditions, all solutions remained optically clear even at pH 10 (no turbidity or baseline lift in the 205–320 nm range), and the spectra were highly reproducible.

Preparation of calibration set

A total of 40 calibration samples were systematically designed across five pH values (2, 4, 6, 8, and 10), with eight different PAR concentrations evaluated at each pH. Required volumes of buffer, methanol, water, stock solutions of $CuSO_4$ and PAR to prepare the portion of calibration set with pH 2 is presented in Table 4. The design was replicated with pH=4, pH=6, pH=8, and pH=10 conditions resulting in 40 calibration solutions.

Table 4. The composition of calibration set at the level of pH 2

Sample	Buffer		$CuSO_4$	PAR	MeOH	Water	Total	PAR
no	pH	mL	mL	mL	mL	mL	mL	µg/mL
1	2	5.0	0.90	0.10	0.70	2.30	9.00	1.68
2	2	5.0	0.90	0.20	0.60	2.30	9.00	3.36
3	2	5.0	0.90	0.30	0.50	2.30	9.00	5.04
4	2	5.0	0.90	0.40	0.40	2.30	9.00	6.72
5	2	5.0	0.90	0.50	0.30	2.30	9.00	8.40
6	2	5.0	0.90	0.60	0.20	2.30	9.00	10.08
7	2	5.0	0.90	0.70	0.10	2.30	9.00	11.76
8	2	5.0	0.90	0.80	0.00	2.30	9.00	13.44

Solutions of tablet formulation

A tablet stock solution was prepared in order to be used for PAR determination in tablet samples and tablet standard addition studies. Ten tablets with a label claim of 500 mg PAR were weighed to calculate the average weight of one tablet. The tablets were finely powdered in a mortar, and a mass theoretically containing $1x10^{-3}$ mol (151 mg) paracetamol was weighed and dissolved in 100 mL of methanol in a volumetric flask. After 30 min of mechanical shaking, the solution was filtered by Whatman No. 42 filter paper. The filtered solution was diluted to a ratio of 1:10 to obtain a tablet stock solution. Considering the label claim, PAR concentration of tablet stock solution was $1.0x10^{-3}$ M, equivalent of 151 µg/mL PAR.

Tablet sample solutions were prepared in a similar manner with calibration set samples across five pH values (2, 4, 6, 8, and 10). For each pH value, five replicate solutions were prepared by mixing 5.00 mL buffer, 0.90 mL $CuSO_4$ stock solution, 0.30 mL tablet stock solution, 0.50 mL methanol and 2.30 mL water. Required volumes of stock solutions to prepare a representative tablet sample set of each pH level is presented in Table 5. The design was replicated with five different buffers (pH=2, pH=4, pH=6, pH=8, and pH=10) resulting in 25 tablet sample solutions.

Table 5. Experimental design for the tablet sample solutions

Sample No	Buffer (mL)	$CuSO_4$ (mL)	Tablet stock (mL)	MeOH (mL)	Water (mL)	Total volume (mL)
1	5.0	0.90	0.30	0.50	2.30	9.00
2	5.0	0.90	0.30	0.50	2.30	9.00
3	5.0	0.90	0.30	0.50	2.30	9.00
4	5.0	0.90	0.30	0.50	2.30	9.00
5	5.0	0.90	0.30	0.50	2.30	9.00

In order to determine whether the excipients in the tablet formulation have an impact on the determination of the drug, standard addition technique was used. A portion of tablet standard addition solutions was designed as depicted in Table 6. All tablet standard addition solutions contained a fixed volume of tablet stock solution (0.10 mL), increasing volume of PAR stock solution (0.00 mL, 0.20 mL, 0.40 mL, 0.60 mL). The same table was used to prepare 5 tablet solutions in each pH value resulting in 20 tablet standard addition solutions.

Table 6. Experimental design of the tablet standard addition samples

Exp. no	Buffer (mL)	$CuSO_4$ (mL)	Tablet stock (mL)	PAR (mL)	MeOH (mL)	Water (mL)	Total volume (mL)
1	5.0	0.90	0.10	0.00	0.70	2.30	9.00
2	5.0	0.90	0.10	0.20	0.50	2.30	9.00
3	5.0	0.90	0.10	0.40	0.30	2.30	9.00
4	5.0	0.90	0.10	0.60	0.10	2.30	9.00

Solutions of syrup formulation

A syrup stock solution was prepared in order to be used for PAR determination in syrup formulation and syrup standard addition studies. The oral suspension formulation was prepared by adding distilled water to the marked line and hand mixing for 2 minutes. PAR concentration in the suspension was 120 mg/5 mL (0.159 M) according to the label claim. A portion of 2 mL from the suspension was diluted to 100 mL with methanol, mechanically

stirred for 10 minutes then diluted to a ratio of 1:10. The diluted solution was filtered through a syringe filter (Merck Millipore, USA) to obtain the syrup stock solution, approximately containing 240 µg/mL PAR (1.59 $x10^{-3}$ M) according to the label claim.

Syrup sample solutions were prepared in a similar manner with tablet sample solutions across five pH values (2, 4, 6, 8, and 10). For each pH value, five replicate solutions were prepared by mixing 5.00 mL buffer, 0.90 mL $CuSO_4$ stock solution, 0.30 mL syrup stock solution, 0.40 mL methanol and 2.30 mL water. The total number of syrup sample solutions were 25.

The effect of excipients in syrup formulation was studied by standard addition technique. A set of syrup standard addition solutions was designed similar to the tablet standard addition set. All syrup standard addition solutions contained a fixed volume of syrup stock solution (0.10 mL), and an increasing volume of PAR stock solution (0.00 mL, 0.20 mL, 0.40 mL, 0.60 mL) at each pH level.

ACKNOWLEDGMENTS

This work was supported by the Research Fund of Siirt University with Project Number: 2015-SİUFEB-32

REFERENCES

1. M. Jóźwiak-Bebenista; J. Z. Nowak; Acta Pol. Pharm., **2014**, *71*, 11–23.
2. M. E. Bosch; A. R. Sánchez; F. S. Rojas; C. B. Ojeda; J. Pharm. Biomed. Anal., **2006**, *42*, 291–321.
3. S. M. El-Megharbel; R. Z. Hamza; M. S. Refat; Spectrochim. Acta A, **2014**, *131*, 534–544.
4. I. Ledeti; G. Simu; G. Vlase; G. Savoiu; T. Vlase; L.-M. Suta; C. Popoiu; A. Fulias; Rev. Chim. (Bucharest), **2013***, 64*, 1127–1130.
5. A. Lawal; J. Obaleye; Biokemistri, **2007**, *19*, 19.
6. A. Chandrathilaka; O. Ileperuma; C. Hettiarachchi; J. Natl. Sci. Found. Sri Lanka, **2013**, *41*, 337-344.
7. R. A. L. A. Salam; H. A. L. N. Taghreed; Anal. Sci. Technol., **2022**, *35*, 143–152.
8. A. Al-Abbasi; M. Zidan; N. Shnin; B. Aldoori; J. Turk. Chem. Soc. A: Chem., **2023**, *10*, 703–718.
9. A. Al-Abbasi; N. A. Belkher; K. Ahmida; M. Zidan; J. Turk. Chem. Soc. A: Chem., **2023**, *10*, 325–338.
10. S. Abbasi; S. A. Haeri; S. Sajjadifar; Microchem. J., **2019**, *146,* 106–114.
11. A. Dewani; B. Barik; V. Chipade; R. Bakal; A. Chandewar; S. Kanungo; Arabian J. Chem., **2014**, *7*, 811–816.
12. N. S. Rashed; O. M. Abdallah; R. S. Farag; S. S. Awad; Adv. Anal. Chem., **2014**, *4*, 1–8.

13. E. A. Abdelaleem; I. A. Naguib; E. S. Hassan; N. W. Ali; J. Pharm. Biomed. Anal., **2015**, *114*, 22–27.
14. N. F. Farid; E. A. Abdelaleem; J. Chromatogr. Sci., **2016**, *54*, 647–652.
15. M. I. Gadallah; H. R. H. Ali; H. F. Askal; G. A. Saleh; Microchem. J., **2019**, *150*, 104093.
16. S. S. Abed; Al-Nahrain J. Sci., **2009**, *12*, 46–53.
17. S. Glavanović; M. Glavanović; V. Tomišić; Spectrochim. Acta A, **2016**, *157*, 258–264.
18. O. A. Lawrence; A. Olufemi; O. D. Alex; S. T. Kayode; J. Res. Environ. Sci. Toxicol., **2012**, *1*, 251–257.
19. G. P. Kumar; G. B. Kumar; T. C. Sekhar; S. B. Murthy; Int. J. Res. Chem. Environ., **2012**, *2*, 231–235.
20. A. M. Saeed; Int. J. Pharm. Sci. Rev. Res., **2017**, *42*, 53–57.
21. S. Berto; E. Alladio; Front. Chem., **2020**, *8*, 614171.
22. R. Bro; Chemom. Intell. Lab. Syst., **1997**, *38*, 149–171.
23. G. Tomasi; R. Bro; Comput. Stat. Data Anal., **2006**, *50*, 1700–1734.
24. R. Bro; J. J. Workman JR; P. R. Mobley; B. R. Kowalski; Appl. Spectrosc. Rev., **1997**, *32*, 237–261.
25. Z. Wang; P. Wu; Y. Zhao; X. Li; D. Kong; Spectrochim. Acta A, **2025**, *328*.
26. H. Liu; L. Zhang; G. Cai; Z. Zhang; J. Li; L. Zhao; J. Li; J. Fluoresc., **2025**, *35*, 3649–3666.
27. F.-X. Wang; Y. Chen; Y.-M. Liang; M. Yang; C. Kang; Spectrochim. Acta A, **2023**, *290*, 122293.
28. M. C. Barreto; R. G. Braga; S. G. Lemos; W. D. Fragoso; Food Chem., **2021**, *364*, 130407.
29. E. Dinç; N. Ünal; Z. C. Ertekin; Anal. Lett., **2020**, *53*, 1871-1887.
30. L. Zhao; Y. Zhang; C. Du; B. Jiang; L. Wei; Y. Li; Environ. Sci. Pollut. Res., **2021**, *28*, 17928–17941.
31. H. Xu; G. Yu; L. Yang; H. Jiang; J. Hazard. Mater., **2013**, *263*, 412–421.
32. M. L. Miranda; H. Osterholz; H. A. Giebel; P. Bruhnke; T. Dittmar; O. Zielinski; Spectrochim. Acta A, **2020**, *230*, *118027*.
33. Z. Lujun; C. Nuo; H. Xiaodong; F. Xinmin; G. Juanjuan; G. Jin; L. Sensen; W. Yan; W. Chunyan; J. Fluoresc., **2025**, *35,* 1819–1832.
34. F. Selimoğlu; N. Ünal; Z. C. Ertekin; E. Dinç; Spectrochim. Acta A, **2021**, *248*, 119253.
35. L. N. Rosa; A. Coqueiro; P. H. Março; P. Valderrama; Food Chem., **2019**, *273*, 52–56.
36. E. Dinç; A. Üçer; N. Ünal; J. Food Drug Anal., **2023**, *31*, 326–337.
37. X. Wang; X. Wang; W. Zhu; L. Ding; X. Liang; R. Wu; H. Jia; X. Huang; X. Guo; Sci. Total Environ., **2024**, *913*, 169427.
38. E. Dinç; A. Üçer; N. Ünal; J. Food Compos. Anal., **2023**, *123*, 105600.
39. Y. Yan; T. Zhao; W. Huang; D. Fang; X. Zhang; L. Zhang; P. Huo; K. Xiao; Y. Zhang; Y. Zhang; Atmos. Environ., **2022**, *287*, *119247*.
40. C. A. Andersson; R. Bro; Chemom. Intell. Lab. Syst., **2000**, *52*, 1–4.

STUDIA UBB CHEMIA, LXXI, 1, 2026(p. 245-256)
(RECOMMENDED CITATION)
DOI:10.24193/subbchem.2026.1.15

ANTIOXIDANT ACTIVITY AND DFT STUDIES OF ETHYL 2-(2-((6-METHYL-4-OXO-4*H*-CHROMEN-3-YL) METHYLENE)HYDRAZINYL)THIAZOLE-4-CARBOXYLATE

Adriana GROZAV[a], Gabriel MARC[a*], Cristina AZAROV[a], Violeta NECULA[b], Smaranda ONIGA[c], Tamas LOVASZ[d], Ovidiu CRIȘAN[a]

ABSTRACT. The microwave-assisted improved synthesis of ethyl 2-(2-((6-methyl-4-oxo-4*H*-chromen-3-yl)methylene)hydrazinyl)thiazole-4-carboxylate is described. The antioxidant potential of the target compound was evaluated using spectrophotometric methods, including the DPPH• and ABTS•$^+$ radical scavenging assays, as well as three additional electron-transfer assays employing metal-based oxidizing agents. The title compound exhibited good antioxidant activity compared to reference antioxidants. For the title compound theoretical quantum chemical (DFT) calculations were performed.

Keywords: *microwave-assisted synthesis, antioxidant activity, DFT calculation, chromene, thiazole;*

1. INTRODUCTION

Free radicals are highly reactive molecular species that result from metabolic processes in the body and contain an unpaired electron. They can be neutralized by the body's natural defense systems, but when the regulatory capacity is exceeded, a condition known as oxidative stress occurs, in which free radicals attack biomolecules, causing their deterioration. Antioxidant

[a] *"Iuliu Haţieganu" University of Medicine and Pharmacy, Faculty of Pharmacy, Department of Organic Chemistry, 8 Victor Babes, Cluj-Napoca, RO-400012, Romania.*
[b] *"Iuliu Haţieganu" University of Medicine and Pharmacy, ENT Department Cluj-Napoca, Romania.*
[c] *"Iuliu Haţieganu" University of Medicine and Pharmacy, Faculty of Pharmacy, Department of Therapeutical Chemistry, 12 Ion Creangă, Cluj-Napoca, RO-400010, Romania.*
[d] *Babeş-Bolyai University, Faculty of Chemistry and Chemical Engineering, 11 Arany Janos str., RO-400028, Cluj-Napoca, Romania.*
* *Corresponding author: marc.gabriel@umfcluj.ro*

compounds neutralize free radicals and are considered essential for maintaining health, reducing the risk of developing various diseases. The most well-known mechanism through which this effect is achieved consists in donating a hydrogen atom to the free radicals, eliminating the unpaired electron and transforming them into non-reactive species [1],[2],[3].

Compounds containing thiazole or hydrazinothiazole unit have been widely reported in the literature to exhibit a broad spectrum of biological activities, including antitumor [4,5], antimicrobial [6], and antioxidant activities [7–9].

In addition, chromone (benzo-γ-pyrone) and its derivatives are versatile molecular scaffolds capable of interacting with various receptors, exhibiting diverse biological activities, including notable antioxidant properties [10–12].

This study aimed to integrate the two moieties into a single molecular entity using an improved approach by means of a microwave-assisted synthesis. Based on the aforementioned premises, the synthesized chromene–thiazole hybrid compound was subsequently evaluated for its antioxidant activity using multiple assays.

2. RESULTS AND DISCUSSION

2.1. Chemical synthesis

2-((6-Methyl-4-oxo-4H-chromen-3-yl)methylene) thiosemicarbazone (**1**) [13,14] was subjected to a Hantzsch-type cyclization with ethyl 3-bromo-2-oxopropanoate under microwave-assisted conditions. The reaction was performed in DMF at 50°C, 50W for 30 min. Under these experimental conditions, microwave-assisted synthesis lead to the obtention of ethyl 2-(2-((6-methyl-4-oxo-4H-chromen-3-yl)methylene) hydrazinyl)thiazole-4-carboxylate (**2**) in a substantially shorter reaction time than the conventional approach previously reported by our group [15].

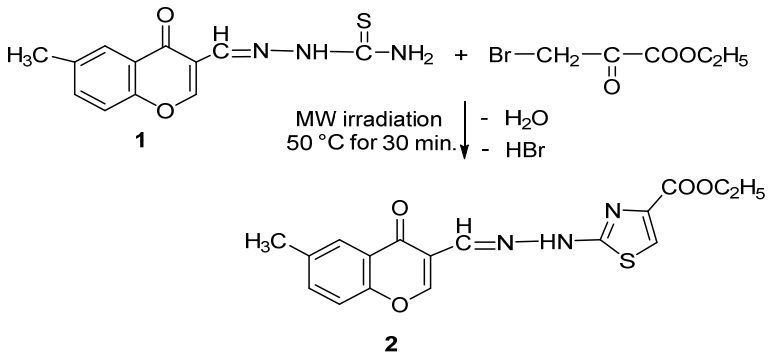

1 **2**

Scheme 1. Synthesis of ethyl-2-(2-((6-methyl-4-oxo-4H-chromen-3-yl)methylene)hydrazineyl)thiazole-4-carboxylate (**2**)

2.2. Antioxidant activity evaluation

The determination of in vitro antioxidant activity of compound **2** was carried out using standard spectrophotometric methods based on the ability of compounds to scavenge free radicals or reduce metal-based oxidizing agents. The antioxidant potential of the newly synthesized chromone–thiazole derivative was evaluated using the following methods: DPPH (1,1-diphenyl-2-picrylhydrazyl), ABTS (2,2′-azino-bis(3-ethylbenzothiazoline-6-sulfonate)), FRAP (Ferric Reducing Antioxidant Power), RP (Reducing Power), and TAC (Total Antioxidant Capacity), which are based on hydrogen transfer mechanisms and electron transfer, respectively. The results of the antioxidants assays are presented in Tables 1 and 2.

Table 1. The antioxidant activity of compound 2 determined in the DPPH and ABTS radical scavenging assays expressed as IC50 (μM)

Compound	$DPPH^{\bullet}$ scavenging	$ABTS^{\bullet+}$ scavenging
2	64.38	18.92
Trolox	36.23	14.68

The results presented in Table 1 show a higher IC_{50} (64.38 μM) for compound 2 compared to the standard IC_{50} (36.23 μM), indicating an approximately twofold lower antioxidant potential in the DPPH radical scavenging method. On the other hand, the ABTS assay reveals a comparable antioxidant activity of compound 2 IC_{50} (18.92 μM) to that of the standard IC_{50} (14.68 μM).

Table 2. The antioxidant activity of compound 2 determined in the FRAP, RP and TAC assays, expressed as molar equivalents of reference agents – ascorbic acid, trolox and butylated hydroxytoluene, respectively

FRAP			RP			TAC		
AAE	**TE**	**BHTE**	**AAE**	**TE**	**BHTE**	**AAE**	**TE**	**BHTE**
1.78	0.57	0.86	0.49	0.62	0.47	0.36	0.57	0.78

AAE: Ascorbic Acid Equivalent Mol, **TE:** Trolox Equivalent Mol, **BHTE:** Butylated Hydroxytoluene Equivalent Mol

In the FRAP assay, compound 2 had the highest activity, particularly in ascorbic acid equivalents (1.78 AAE). This value surpasses the corresponding trolox (0.57 TE) and BHT equivalents (0.86 BHTE), suggesting that compound 2 exhibits a strong electron-donating capacity, more comparable to ascorbic acid than to the other reference antioxidants.

In the RP assay the reducing power values are lower and more uniform across standards, ranging from 0.47 to 0.62. Compound 2 displayed a moderate reducing ability, with slightly higher activity relative to trolox (0.62 TE). The title compound, under these conditions, had a stable but not exceptionally high reducing capacity, but approximately a half of the activity of the reference antioxidants.

The TAC assay yields the lowest values overall (0.36–0.78 molar equivalents), highlighting a reduced total antioxidant capacity compared to FRAP. However, compound 2 demonstrates relatively stronger activity when expressed in BHT equivalents (0.78 BHTE), suggesting that its efficiency in this assay may be influenced by radical scavenging mechanisms or by interactions specific to the assay's reaction environment.

A comparison of the three methods shows that FRAP provides the strongest antioxidant potential for compound 2, whereas TAC reveals the weakest. This variability underscores that the antioxidant behavior of compound 2 is highly dependent on the redox system evaluated in each specific reaction environment.

2.3. DFT Calculations

DFT calculations were performed to evaluate some molecular properties and the frontier molecular orbital energies (HOMO and LUMO) in vacuum and in three solvents, to evaluate how the solvation environment may interact with compound **2**. The results are presented in Tables 3 and 4.

Table 3. Molecular properties of compound 2.

Area (Å^2)	Polar Surface Area (Å^2)	Volume (Å^3)	LogP	Dipole moment (D)
358.85	69.068	334.96	2.59	4.01

The calculated molecular properties of compound 2 indicate a balanced distribution between polar and nonpolar regions. The molecular volume (334.96 Å^3) is consistent with a compact structure, typical for molecules of this size. The calculated LogP value of 2.59 denotes moderate lipophilicity,

implying that the compound can interact with both hydrophobic and hydrophilic environments, favoring membrane permeability. The dipole moment of 4.01 D reflects a moderate molecular polarity, which may contribute to favorable solvation in polar media while maintaining a hydrophobic character. The polar regions of the molecule electron-deficient were identified where electronegative atoms are found (the two chromone oxygen atoms, the oxygen atoms from the carboxylic ester, the azomethine nitrogen atom, the thiazole nitrogen atom), while the electron-rich regions are in the N-H group and in the position 5 of the thiazole. The graphical depiction of the aforementioned data is presented in Figure 1.

Table 4. The energy levels of HOMO and LUMO, across the four environments studied for compound 2 (eV).

Vacuum			Nonpolar solvent (ε=7.43)			Polar solvent (ε=37.22)			Water		
HOMO	**LUMO**	**gap**	**HOMO**	**LUMO**	**gap**	**HOMO**	**LUMO**	**gap**	**HOMO**	**LUMO**	**gap**
-6.03	-1.87	4.16	-6.01	-1.92	4.09	-6.01	-1.94	4.07	-6.01	-1.94	4.07

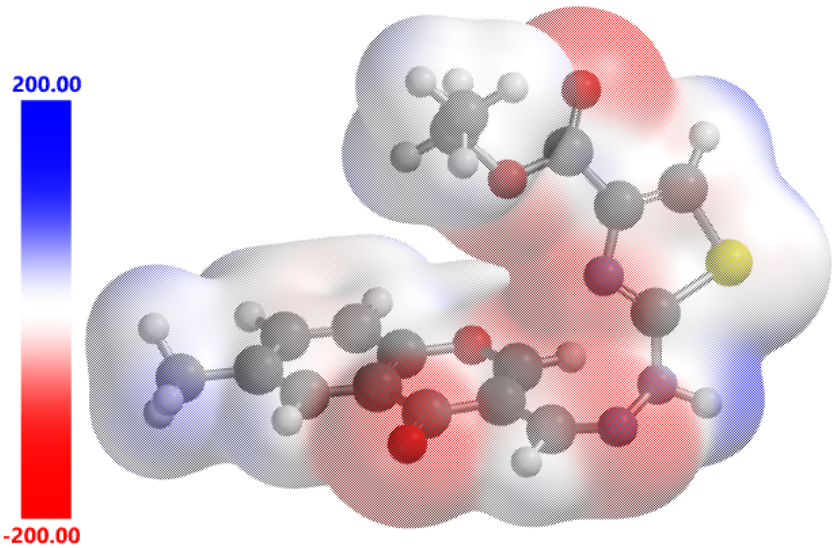

Figure 1. The electrostatic potential map for compound 2

In the studied compound, HOMO is found across the hydrazone and the thiazole ring and slight on the pyrone moiety from chromone, while LUMO is found across the whole chromone moiety (Figure 2). HOMO and LUMO energies show minimal variation across different environments. The HOMO level remains nearly constant at around −6.0 eV, while the LUMO decreases slightly (from −1.87 eV in vacuum to −1.94 eV in polar solvents). This indicates that solvent induced effect, even in nonpolar, polar or high polar media such as water, has some effect on the frontier orbital energies of the molecule, reducing the gap between the two frontier molecular orbitals. The respective effect is attributed mainly to the variation of LUMO energy levels and less to the change of the HOMO energy levels. The low change in HOMO levels, indicate a low variability of the antioxidant properties of the molecule 2 in different solvents with different electronic properties. The small stabilization of LUMO in solvents suggests a weak solvent–solute electronic interaction and limited charge delocalization upon solvation.

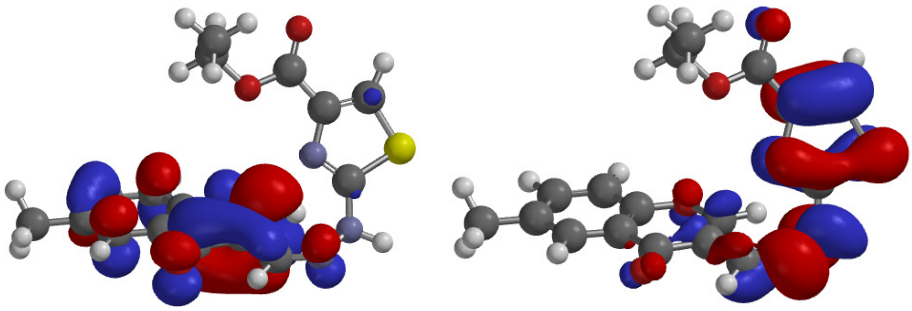

Figure 2. The graphical depiction of frontier molecular orbitals HOMO (left), LUMO (right) of compound 2.

The compound exhibited a good radical-scavenging activity against DPPH• and a very good against ABTS•+, together with a good reducing power in all three assays when compared to the reference compounds. These findings indicate that the conjugated π-system created through the hydrazone bridge effectively facilitates electron transfer—a key process involved in antioxidant reactions. The reducing character suggests that the molecule can readily donate electrons to stabilize oxidative species, which aligns with the behavior of other chromone-based antioxidants reported in the literature.

To better understand these results at a molecular level, DFT calculations were per-formed, which indicated the pyrone-hydrazone-thiazole being the moieties redox active in the present compound. These theoretical insights supported the experimental data by revealing that the electron-rich regions of the molecule—particularly those located across the extended aromatic system—play a central role in radical neutralization, consistent with the orbital distribution observed in previous studies on similar heterocyclic antioxidants. According to the distribution of electrons across the molecule, the substituent from the position 4 of the thiazole ring have no evident contribution to the antioxidant activity of the studied compound.

Overall, the combination of experimental assays and computational analysis highlights the potential of this chromone–thiazole hydrazone scaffold as a promising antioxidant candidate. Considering its favorable redox properties and structural versatility, future research should explore structural modifications aimed at further enhancing electronic delocalization, as well as biological evaluations in cellular oxidative stress models. These directions could provide deeper insight into structure–activity relationships and expand the applicability of this hybrid system in medicinal or materials chemistry.

3. CONCLUSIONS

The microwave-assisted synthesis of the ethyl-2-(2-((6-methyl-4-oxo-4H-chromen-3-yl)methylene)hydrazineyl)thiazole-4-carboxylate proved to be an efficient and advantageous approach, enabling the preparation of the chromene–thiazole derivative within a significantly reduced reaction time (30 minutes) compared to the conventional classical synthesis, which requires approximately 24 hours. The synthesized compound exhibited antioxidant activity comparable to that of the reference standards used (ascorbic acid, Trolox, and BHTE), highlighting its relevant biological potential. The experimental findings were further supported and validated by theoretical studies based on Density Functional Theory (DFT) calculations, which confirmed the correlation between structural properties and the observed antioxidant activity. Overall, these results emphasize the utility of microwave-assisted synthesis and the relevance of the obtained chromene–thiazole derivative as a potential candidate for future applications.

4. EXPERIMENTAL SECTION

4.1. Chemical synthesis

All reagents, solvents and chemicals were obtained from commercial sources (Sigma-Aldrich and Riedel-de Haënand used as received without further purification. The uncorrected melting point was measured with a

Buchi M-560 device (BÜCHI Labortechnik AG, Flawil, Switzerland). Colorimetric measurements were recorded with a UV-VIS Jasco V-530 spectrophotometer (Jasco International Co., Tokyo, Japan) at room temperature against specific blank samples. Thin-layer chromatography (TLC) was performed on 0.2 mm silica gel 60 plates (Fluka, Merck KGaA, Darmstadt, Germany). The microwave-assisted synthesis experiments were performed using the CEM Discover Microwave Synthesizer system (CEM Corporation, Matthews, NC, USA).

4.1.1. Microwave assisted synthesis of ethyl-2-(2-((6-methyl-4-oxo-4H-chromen-3-yl)methylene)hydrazineyl)thiazole-4-carboxylate (compound 2)

A mixture of 2-((6-methyl-4-oxo-4H-chromen-3-yl)methylene) thiosemicarbazone (87 mg, 0.33 mmol) and ethyl 3-bromo-2-oxopropanoate (60 mg, 0.33 mmol) in DMF (2 mL) was irradiated under microwave conditions for 30 min at 50 °C and 50 W. The progress of the reaction was monitored by thin-layer chromatography (TLC) using heptane/ ethyl acetate/ethanol (7:3:0.5, v/v/v) as the eluent on silica gel plates. After completion, the reaction mixture was neutralized to pH 7 with an aqueous $NaHCO_3$ solution (10%). The resulting precipitate was filtered, dried under reduced pressure, and recrystallized from DMF (5 mL) to afford a pale yellow powder (77 mg, 65% yield). Compound 2 was identified by melting point determination (m.p. = 248°C) in accordance with reported literature data [15] and mass spectrometry (m/z = 358.0874, APCI, $[M+H]^+$).

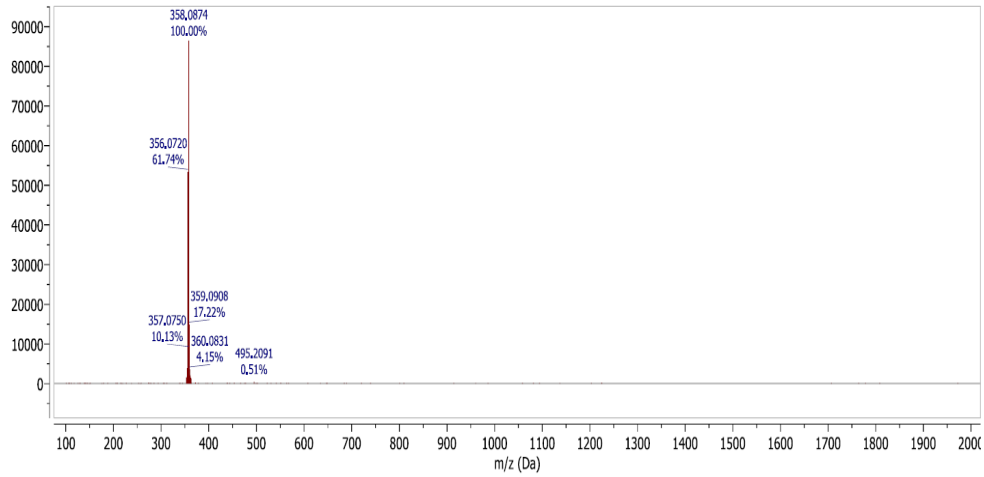

Figure 3. APCI mass spectra recorded for compound 2 (positive ionization mode).

4.2. Antioxidant activity evaluation

The protocols used for the antiradical assays and for the electron transfer assays were previously reported by our group in our previous papers [16]. Briefly, the respective assays will be presented in the following subsections [4].

4.2.1. Antiradical assays

For evaluation of the antiradical properties of the compound 2, two radical scavenging assays were employed - DPPH• and ABTS•+. The reducing of the absorbance of the two radicals was calculated using the following equation:

$$\text{radical scavenging (\%)} = (\text{control absorbance-sample absorbance})/(\text{control absorbance})\times 100 \quad (1)$$

The 1,1-diphenyl-2-picrylhydrazyl (DPPH•) scavenging test relies on the ability of the investigated compound to donate a hydrogen atom to the intensely colored DPPH• radical, which contains an unpaired electron and exhibits a characteristic absorption peak at 517 nm. A reduction in the absorbance of the reaction mixture indicates radical neutralization, and the scavenging activity was quantified using the presented equation.

The 2,2'-azino-bis(3-ethylbenzothiazoline-6-sulfonic acid) (ABTS•+) scavenging assay was carried out in a 0.1 M potassium phosphate buffer (pH=7.4) after generating the ABTS•+ radical with MnO_2. The reduction of absorbance at 734 nm was measured spectrophotometrically, and the percentage of radicals quenched was calculated according to the presented equation.

4.2.2. Electron transfer assays

All electron-transfer–based assays were carried out using equimolar amounts of the tested compound 2 and the corresponding reference antioxidants, under specific experimental conditions for each method [17].

The activity of compound 2, expressed relative to the activity of an equimolar quantity of the standard compound, was determined according to the following equation in the three following assays:

$$\text{\% of control activity} = (\text{sample absorbance})/(\text{reference absorbance})\times 100$$

The Ferric Reducing Antioxidant Power (FRAP) assay followed the procedure originally described by Benzie and Strain, with minor modifications [18]. In this method, the analyte reduces Fe^{3+} from the reagent to Fe^{2+}, which subsequently forms an intense blue complex with a chromogenic ligand, exhibiting maximal absorbance at 593 nm.

Total Antioxidant Capacity (TAC) was assessed by monitoring the reduction of the phosphomolybdate reagent by the test compounds upon heating, resulting in the formation of a green-colored complex with an absorption peak at 695 nm.

For the Reducing Power (RP) assay, the principle involves the reduction of $[Fe(CN)_6]^{3-}$ to $[Fe(CN)_6]^{4-}$ by the electron-donating activity of the sample. The generated ferrocyanide reacts with ferric ions to produce a blue complex, which absorbs maximally at 700 nm.

4.3. DFT Calculations

To investigate the electronic and structural characteristics of the compound 2 in silico DFT calculations were performed with the B3LYP functional method and the 6-311G(2D,P) basis set using Spartan 24 1.3.1 (Wavefunction, Inc., Irvine, CA, USA) under Microsoft Windows 10, on a machine with Intel 12700KF CPU. The calculations were performed under vacuum, in a nonpolar solvent (ε = 7.43), a polar solvent (ε = 37.22), and in water.

Abbreviations

The following abbreviations are used in this manuscript:

ABTS 2,2′-azino-bis(3-ethylbenzothiazoline-6-sulfonate)
DFT Density Functional Theory
DMF Dimethylformamide
DPPH 1,1-diphenyl-2-picrylhydrazyl
FRAP Ferric Reducing Antioxidant Power
HOMO Highest Occupied Molecular Orbital
LUMO Lowest Unoccupied Molecular Orbital
MP Melting Point
RP Reducing Power
TAC Total Antioxidant Capacity

REFERENCES

1. Chelliah, R.; Banan-MwineDaliri, E.; Oh, D.-H. Screening for Antioxidant Activity: Total Antioxidant Assay. In; 2022; pp. 459–460.
2. Theodosis-Nobelos, P.; Tziona, P.; Poptsis, A.; Athanasekou, C.; Kourounakis, P.N.; Rekka, E.A. Activity. *Med. Chem. Res.* **2017**, *26*, 461–472, doi:10.1007/s0044-016-1767-8.
3. K. Ahmouda and M. T. Oucif Khaled, *Plant Physiol. Biochem*., **2025,** *222,* 109723 doi: 10.1016/j.plaphy.2025.109723.
4. A. Grozav, I.-D. Porumb, L. Găină, L. Filip, and D. Hanganu, *Molecules*, **2017**, *22(2)*, 260. doi: 10.3390/molecules22020260.
5. O. Sabin, *R. M. Pop, I. C. Bocșan,V.S. Chedea, F. Ranga, A.Grozav, A. M. Levai, A. D. Buzoianu*, *Molecules*, **2024**, *29(15),* 3448. doi: 10.3390/molecules29153448.
6. A. Grozav, L. I. Găină, V. Pileczki, O. Crisan, L. Silaghi-Dumitrescu, B. Therrien, V. Zaharia and I. Berindan-Neagoe. *Int. J. Mol. Sci.*, **2014**, *15(12),* 22059–22072. doi: 10.3390/ijms151222059.
7. A. Grozav, V. Miclaus, O. Vostinaru, S. Ghibu, C. Berce, I. Rotar, C. Mogosan, B. Therrien, F. Loghin, D.-S. Popa*. Regul. Toxicol. Pharmacol.*, **2016**, *80*, 233–240. doi: 10.1016/j.yrtph.2016.06.018.
8. A. Grozav, V. Zaharia, C. Cristea, N. I. Fit, *Studia UBB Chemia*, **2015**, *60(3)*, 283-289.
9. G. Kumari, S. Dhillon, P. Rani, M. Chahal, D. K. Aneja, and M. Kinger, *ACS Omega*, **2024**, 9(17), 18709–18746, doi: 10.1021/acsomega.3c10299.
10. S.S Shatokhin; V.A. Tuskaev; S.C. Gagieva; D.I. Pozdnyakov; E.T Oganesyan, Pharm. Pharmacol. 2021, 9, 367–376, doi:10.19163/2307-9266-2021-9-5-367-376.
11. S.P. Pawar, D.D. Kondhare, P.K. Zubaidha, *Med. Chem. Res.* **2013**, *22*, 753–757, doi:10.1007/s00044-012-0069-z.
12. E. Csepanyi, P. Szabados-Furjesi, A. Kiss-Szikszai, L.M. Frensemeier, U. Karst, I. Lekli, D.D. Haines, A. Tosaki, I. Bak, *Molecules* **2017**, *22*, 588, doi:10.3390/molecules22040588.
13. U. Salar, K. M. Khan, A. Jabeen, S. Hussain, A. Faheem, F. Naqvi and S. Perveen Lett. Drug Des. Discov., vol. 17, no. 5, pp. 547–555, May **2020**, doi: 10.2174/1570180816666190611155218.
14. M. J. Saadh, Z. N.Jawad, S. M. Dhia Younis, W. K. Mohammed, M.K. Sultan, J. Rizaev, U. S. Altimari, M. J. Naser, M. L. Shaghnab, H. K. Shareef, I. Ahmad, A. Alawadi J. Mol. Struct., vol. 1338, p. 142093, Aug. **2025**, doi: 10.1016/j.molstruc.2025.142093.
15. A. Grozav, C. Azarov, G. Marc, A. Pîrnău, S. Manolov, O. Oniga and O. Crișan, *Molbank*, vol. **2026,** no. 1, p. M2127, Jan. 2026, doi: 10.3390/M2127.

16. G. Marc, A. Stana, M. Tertiş, C. Cristea, A. Ciorîţă, Ș.M. Drăgan, V. A. Toma, R. Borlan, M. Focșan, A. Pîrnău, L. Vlase, S. Oniga, O. Oniga, *Int. J. Mol. Sci*. **2023**, *24*, 13277, doi:10.3390/ijms241713277.
17. M. N. Alam, N.J. Bristi, M. Rafiquzzaman. *Saudi Pharm. J*. **2013**, *21*, 143–152, doi:10.1016/j.jsps.2012.05.002.
18. I. F. Benzie, J. J. Strain, *Methods Enzymol*. **1999**, *299*, 15–27, doi:10.1016/S0076-6879(99)99005-5.